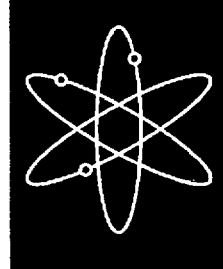


SCDAP/RELAP5/MOD 3.3 Code Manual



MATPRO - A Library of Materials Properties for Light-Water-Reactor Accident Analysis



Idaho National Engineering and Environmental Laboratory



U.S. Nuclear Regulatory Commission Office of Nuclear Regulatory Research Washington, DC 20555-0001





AVAILABILITY OF REFERENCE MATERIALS IN NRC PUBLICATIONS

NRC Reference Material

As of November 1999, you may electronically access NUREG-series publications and other NRC records at NRC's Public Electronic Reading Room at www.nrc.gov/NRC/ADAMS/index.html.

Publicly released records include, to name a few, NUREG-series publications; Federal Register notices; applicant, licensee, and vendor documents and correspondence; NRC correspondence and internal memoranda; bulletins and information notices; inspection and investigative reports; licensee event reports; and Commission papers and their attachments.

NRC publications in the NUREG series, NRC regulations, and *Title 10, Energy*, in the Code of *Federal Regulations* may also be purchased from one of these two sources.

- The Superintendent of Documents U.S. Government Printing Office P. O. Box 37082 Washington, DC 20402–9328 www.access.gpo.gov/su_docs 202–512–1800
- The National Technical Information Service Springfield, VA 22161–0002 www.ntis.gov 1–800–533–6847 or, locally, 703–805–6000

A single copy of each NRC draft report for comment is available free, to the extent of supply, upon written request as follows:

Address: Office of the Chief Information Officer,

Reproduction and Distribution

Services Section

U.S. Nuclear Regulatory Commission

Washington, DC 20555-0001

E-mail: DISTRIBUTION@nrc.gov

Facsimile: 301-415-2289

Some publications in the NUREG series that are posted at NRC's Web site address www.nrc.gov/NRC/NUREGS/indexnum.html are updated periodically and may differ from the last printed version. Although references to material found on a Web site bear the date the material was accessed, the material available on the date cited may subsequently be removed from the site.

Non-NRC Reference Material

Documents available from public and special technical libraries include all open literature items, such as books, journal articles, and transactions, *Federal Register* notices, Federal and State legislation, and congressional reports. Such documents as theses, dissertations, foreign reports and translations, and non-NRC conference proceedings may be purchased from their sponsoring organization.

Copies of industry codes and standards used in a substantive manner in the NRC regulatory process are maintained at—

The NRC Technical Library Two White Flint North 11545 Rockville Pike Rockville, MD 20852–2738

These standards are available in the library for reference use by the public. Codes and standards are usually copyrighted and may be purchased from the originating organization or, if they are American National Standards, from—

American National Standards Institute 11 West 42nd Street New York, NY 10036–8002 www.ansi.crg 212–642–4900

The NUREG series comprises (1) technical and administrative reports and books prepared by the staff (NUREG-XXXX) or agency contractors (NUREG/CR-XXXX), (2) proceedings of conferences (NUREG/CP-XXXX), (3) reports resulting from international agreements (NUREG/IA-XXXX), (4) brochures (NUREG/BR-XXXX), and (5) compilations of legal decisions and orders of the Commission and Atomic and Safety Licensing Boards and of Directors' decisions under Section 2.206 of NRC's regulations (NUREG-0750).

DISCLAIMER: This report was prepared as an account of work sponsored by an agency of the U.S. Government. Neither the U.S. Government nor any agency thereof, nor any employee, makes any warranty, expressed or implied, or assumes any legal liability or responsibility for any third party's use, or the results of such use, of any information, apparatus, product, or process disclosed in this publication, or represents that its use by such third party would not infringe privately owned rights.

SCDAP/RELAP5/MOD 3.3 Code Manual

MATPRO - A Library of Materials Properties for Light-Water-Reactor Accident Analysis

Manuscript Completed: August 2000

Date Published: January 2001

Prepared by

L. J. Siefken, E. W. Coryell, E. A. Harvego,

J. K. Hohorst

Idaho National Engineering and Environmental Laboratory P.O. Box 1625 Idaho Falls, ID 83415-3129

S. A. Arndt, NRC Project Manager

Prepared for Division of Systems Technology Office of Nuclear Regulatory Research U.S. Nuclear Regulatory Commission Washington, DC 20555-0001 NRC Job Code W6095



ABSTRACT

The SCDAP/RELAP5 code has been developed for best-estimate transient simulation of light water reactor coolant systems during a severe accident. The code models the coupled behavior of the reactor coolant system and reactor core during severe accidents as well as large and small break loss-of-coolant accidents, operational transients such as anticipated transient without SCRAM, loss of offsite power, loss of feedwater, and loss of flow. The coolant system behavior is calculated using a two-phase model allowing for unequal temperatures and velocities of the two phases of the fluid, and the flow of fluid through porous debris and around bockages caused by reactor core damage. The reactor core behavior is calculated using models for the ballooning and oxidation of fuel rods, the meltdown of fuel rods and control rods, fission product release, and debris formation. The code also calculates the heatup and structural damage of the lower head of the reactor vessel resulting from the slumping of reactor core material. A generic modeling approach is used that permits as much of a particular system to be modeled as necessary. Control system and secondary system components are included to permit modeling of plant controls, turbines, condensers, and secondary feedwater conditioning systems.

This volume, Volume 4, describes the material properties correlations and computer subroutines (MATPRO) used by SCDAP/RELAP5. Formulation of the materials properties are generally semi-empirical in nature. The materials property subroutines contained in this document are for uranium, uranium dioxide, mixed uranium-plutonium, dioxide fuel, zircaloy cladding, zirconium dioxide, stainless steel, stainless steel oxide, silver-indium-cadmium alloy, cadmium, boron carbide, Inconel 718, zirconium-uranium-oxygen melts, fill gas mixtures, carbon steel, and tungsten. This document also contains descriptions of the reaction and solution rate models needed to analyze a reactor accident. Revision 2 includes changes incorporated since the manuals were released in July 1998.

CONTENTS

ABS	TRACT		111
FIGU	JRES		xv
TAB	LES		xxv
EXE	CUTIVE	SUMMARY	xxxi
ACK	NOWLE	EDGMENTS	xxxiii
1.	INTR	ODUCTION	1-1
	1.1	General Code Capabilities	1-1
	1.2	Relationship to Other NRC-Sponsored Software	
	1.3	Quality Assurance	1-2
	1.4	Organization of the SCDAP/RELAP5 Manuals	1-2
	1.5	Organization of Volume 4	1-3
	1.6	References	1-4
2.	URA:	NIUM DIOXIDE/MIXED OXIDES	2-1
	2.1	Melting Temperature and Heat of Fusion (FHYPRP)	
		2.1.1 Melting Temperature	2-1
		2.1.2 UO ₂ and (U, Pu)O ₂ Heat of Fusion	2-2
		2.1.3 References	
	2.2	Specific Heat Capacity and Enthalpy (FCP, FENTHL)	2-2
		2.2.1 Summary	2-3
		2.2.2 Literature Review	2-4
		2.2.3 Model Development	2-5
		2.2.4 Model Comparisons with Data	2-11
		2.2.5 Model Uncertainty	2-11 2-11
		2.2.6 References	
	2.3	Thermal Conductivity (FTHCON)	
		2.3.1 Summary	2-15
		2.3.2 Literature Review: Theory and Available Data	
		2.3.3 Model Development	
		2.3.4 Model Uncertainty	2-40 2./13
		2.3.5 References	
	2.4	Emissivity (FEMISS)	
		2.4.1 Summary	
		2.4.2 Emissivity Data	2-40
		2.4.3 Model Development	2-47 2-17
		2.4.4 References	
	2.5	Thermal Expansion and Density (FTHEXP, FDEN)	
		2.5.1 Summary (FTHEXP)	2-48

	2.5.2	Literature Review (FTHEXP)	
	2.5.3	Model Development (FTHEXP)	
	2.5.4	Model Data Comparison and Uncertainty (FTHEXP)	2-5
	2.5.5	Implementation (FTHEXP)	
	2.5.6	Density (FDEN)	
	2.5.7	References	2-50
2.6	Elastic	Moduli (FELMOD, FPOIR)	2-58
	2.6.1	Summary (FELMOD)	2-58
	2.6.2	Survey of Available Data (FELMOD)	
	2.6.3	Model Development (FELMOD)	2-6
	2.6.4	Model Uncertainty (FELMOD)	2-66
	2.6.5	Poisson's Ratio (FPOIR)	2-6
	2.6.6	References	
2.7	Creep	(FCREEP)	
	2.7.1	Summary	
	2.7.2	Model Development	2-73
	2.7.3	Evaluation of Constants and Data Comparison	
	2.7.4	References	
2.8	Densif	ication (FUDENS)	2-84
	2.8.1	Summary	2-85
	2.8.2	Uranium Dioxide and Mixed Oxide Densification Data and Models	
	2.8.3	Model Development	
	2.8.4	References	
2.9	Swellin	ng (FSWELL)	2-97
	2.9.1	Summary	2-97
	2.9.2	Solid Fission Product Swelling Model	2-97
	2.9.3	Fission Gas Swelling Model	2-99
	2.9.4	References	2-101
2.10	Pressu	re Sintering (FHOTPS)	2-103
	2.10.1	Summary	2-104
	2.10.2	Pressure Sintering Process and Data	2-105
	2.10.3	Model Development and Uncertainties	2-111
	2.10.4	References	2-114
2.11	Restruc	cturing (FRESTR)	2-115
	2.11.1	Summary	2-115
		Restructuring Data	
		Model Development	
		References	
2.12	Fractur	e Strength (FFRACS)	2-125
		Summary	
	2.12.2	Out-of-Pile Uranium Dioxide Deformation	2-126
	2.12.3	Uranium Dioxide Fracture Strength Model	
	2.12.4	References	2-132
2.13		ty (FVISCO)	2_133
	1 100001	67 14 T 40/2007 I 4444444444444444444444444444444444	/-1**

		2.13.1 Summary		2-134
		2.13.2 Fuel Viscosity Data		2-135
		2.13.3 Model Development and	Uncertainty	2-138
		2.13.4 References		2-140
	2.14	Vapor Pressure (FVAPRS)		2-141
		2.14.1 Summary		2-142
		2.14.2 Vapor Pressure Data		2-144
		2.14.3 Model Development		2-152
		2.14.4 References		2-161
	2.15			
		2.15.1 Summary		2-166
		2.15.2 Review of Literature		2-166
		2.15.3 Model Development		2-167
		2.15.4 Description of the FOXY	and FOXYK Subcodes	2-170
		2.15.5 References		2-171
3.	URAI	IIUM ALLOYS		3-1
	3.1		lpy (UCP, UENTHL)	
			JCP)	
		3.1.2 Enthalpy (UENTHL)		3-5
		3.1.3 References		3-7
	3.2		T)	
		3.2.1 Model Development		3-7
		3.2.2 References		3-9
	3.3	Thermal Expansion and Density (UTHEXP, UDEN)	3-9
		3.3.1 Thermal Expansion (UTF	1EXP)	3-9
		3.3.2 Density (UDEN)		3-12
		3.3.3 Reference		3-12
	3.4		XD, UOXWTK)	
		3.4.2 Comparison With Data		3-15
		3.4.3 Summary		3-16
		3.4.4 References		3-16
1.	ZIRCALOY			
	4.1		n Temperatures (CHYPRP)	
			-	
		4.1.2 Reference		4-5
	4.2	Temperature Required to Prevent of Hydrogen in Zircalov (CTSOI	Hydriding of a Given Concentration	4-5
	4.2		t of Hydride Solution on Cladding	
	4.3	Specific Heat and Futhalny (CCF	P, CHSCP, CENTHL)	4-6
		42.1 Consider Heat (CCD)	, CIBCI, CEI(IIII)	4_6
		4.3.1 Specific Heat (CCP)	n (CHSCP)	4-10
		4.J.Z EHECL OF TRAINE SOURIN	H (CIED)	

	4.3.3	Uncertainties in Specific Heat Predictions	
	4.3.4	Zircaloy Enthalpy (CENTHL)	4-13
	4.3.5	References	4-16
4.4	Therm	nal Conductivity (CTHCON)	4-16
	4.4.1	Summary	4-17
	4.4.2	Literature Review	4-18
	4.4.3	Model Development	4-23
	4.4.4	References	4-24
4.5	Therm	al Expansion, Density and Their Relation to Texture (CTHEXP, CDEN).	4-25
	4.5.1	Summary (CTHEXP)	
	4.5.2	Literature Review (CTHEXP)	4-28
	4.5.3	Model Development (CTHEXP)	4-31
	4.5.4	Model Data Comparison and Uncertainty (CTHEXP)	4-40
	4.5.5	Density (CDEN)	
	4.5.6	References	
4.6	Elastic	: Moduli (CELMOD, CSHEAR, AND CELAST)	4-43
	4.6.1	Summary	4-43
	4.6.2	Review of Available Data	
	4.6.3	Model Development	
	4.6.4	Comparison of Models and Data Base	
	4.6.5	Expected Standard Error of the CELMOD and CSHEAR Codes	
	4.6.6	References	
4.7	Axial (Growth (CAGROW)	4-65
	4.7.1	Summary	4-65
	4.7.2	Background and Approach	4-67
	4.7.3	Review of Experimental Data.	4-67
	4.7.4	The Effect of Texture on Axial and Circumferential Growth	4-69
	4.7.5	Analysis of Irradiation-Induced Growth Factors Other Than Texture	
	4.7.6	Evaluation of the Model and Its Uncertainty	
	4.7.7	References	
4.8	Creep	(CCSTRN, CCSTRS, CABTP, CTP)	4-80
	4.8.1	Summary	4-81
	4.8.2	Survey of Available Data	4-84
	4.8.3	Model Development	4-88
	4.8.4	Model Uncertainty	4-98
	4.8.5	References	4-99
4.9	Plastic	Deformation (CSTRES, CSTRAN, CSTRNI, CANISO, CKMN)	4-101
	4.9.1	Summary	4-101
	4.9.2	Available Data	4-109
	4.9.3	Model Development	
	4.9.4	Comparison to Burst Test Data	
	4.9.5	Uncertainties	
	4.9.6	References	
4.10	Anneal	ing (CANEAL)	1 112

	4.10.1 Summary	4-143
	4.10.2 Available Data	4-145
	4.10.3 Model Development	4-151
	4.10.4 Comparison of Annealing Models to Data	4-163
	4.10.5 References	4-166
4.11	Mechanical Limits and Embrittlement (CMLIMT, CBRTTL)	
	4.11.1 Summary (CMLIMT)	4-167
	4.11.2 Available Data	4-169
	4.11.3 Model Development	4-173
	4.11.4 Application of the Failure Criterion to Determine	
	Cladding Shape After Burst	4-180
	4.11.5 Summary (CBRTTL)	4-186
	4.11.6 Literature Review	4-188
	4.11.7 Model Development	4-189
	4.11.8 Model for Fast Cooled Cladding	4-190
	4.11.9 Model for Slow Cooled Cladding	4-193
	4.11.10 Model Uncertainties	4-194
	4.11.11 References	4-194
4.12	Cyclic Fatigue (CFATIG)	4-197
	4.12.1 Summary	4-198
	4.12.2 Basis for High-Cycle Fatigue Material Constants	4-199
	4.12.3 Basis for Low-Cycle Fatigue Material Constants	4-201
	4.12.4 References	4-202
4.13	Collapse Pressure (CCLAPS)	
	4.13.1 Model Development	4-203
	4.13.2 References	4-203
4.14	Meyer Hardness (CMHARD)	4-204
	4.14.1 Model Development	4-204
	4.14.2 References	4-205
4.15	Zircaloy Oxidation in Water and Steam (CORROS, COBILD,	
	COXIDE, COXWTK, COXTHK)	
	4.15.1 Summary	4-206
	4.15.2 Zircaloy Oxidation Literature and Data	4-212
	4.15.3 Model Development	4-214
	4.15.4 Description of the CORROS, COBILD, COXIDE, COXWTK,	
	and COXTHK Subcodes	
	4.15.5 References	4-231
4.16	Cladding Hydrogen Uptake (CHUPTK)	
	4.16.1 Summary	4-234
	4.16.2 Background and Approach	4-236
	4.16.3 Out-of-Pile Basis for the Model	4-236
	4.16.4 Generalization to an In-Pile Model	4-238
	4.16.5 References	4-239
4.17	Young's Modulus and Poisson's Ratio (CELMDR)	4-240

		4.17.1	Reference	4-240
	4.18	Zircal	oy and Zirconium Heats of Fusion (PHYPRP)	4-241
		4.18.1	References	4-241
	4.19	Zircor	nium Transformation Temperature (PHYPRP)	4-241
			Reference	
5.	ZIRC	ALOY (OXIDES	5-1
	5.1	Meltir	ng and Phase Transformation Temperatures (ZOPRP)	5-1
		5.1.1	Model Development	5-1
		5.1.2	Reference	5-3
	5.2	Specif	fic Heat Capacity and Enthalpy (ZOCP, ZONTHL)	5-3
		5.2.1	Specific Heat (ZOCP)	
		5.2.2	Enthalpy (ZONTHL)	
		5.2.3	References	
	5.3	Therm	nal Conductivity (ZOTCON)	•
		5.3.1	Model Development	5-8
		5.3.2	References	
	5.4	Surfac	ee Emissivity (ZOEMIS)	5-15
		5.4.1	Summary	
		5.4.2	Literature Review	
		5.4.3 5.4.4	Model Development	
		5.4.5	References	
	5.5	Therm	nal Expansion and Density (ZOTEXP, ZODEN)	
		5.5.1	Thermal Expansion (ZOTEXP)	5-25
		5.5.2	Density (ZODEN)	
		5.5.3	References	5-28
	5.6	Elastic	: Moduli (ZOEMOD, ZOPOIR)	5-29
		5.6.1	Young's Modulus (ZOEMOD)	5-29
		5.6.2	Poisson's Ratio (ZOPOIR)	
		5.6.3	Reference	5-31
	5.7	Mecha	mical Limits and Embrittlement (ZORUP)	5-31
		5.7.1	Model Development	
		5.7.2	Reference	5-32
6.	CONT	ROL RO	DD CLADDING	6-1
	6.1	Meltin	g Temperatures (SHYPRP)	6-1
		6.1.2	Reference	6-1
	6.2	Specifi	ic Heat Capacity and Enthalpy (SCP, SENTHL)	6-1
		6.2.1	Model Development	6-1
		6.2.2	References	6-3

	6.3	Therm	Thermal Conductivity (STHCON)	
		6.3.1 6.3.2	Model Development	6-3 6-5
	6.4	Therm	nal Expansion and Density (STHEXP, SDEN)	6-5
		6.4.1	Model Development	
		6.4.2	References	6-6
	6.5	Stainle	ess Steel Oxidation in Steam (SOXIDE, SOXWGN, SOXTHK)	6-6
		6.5.1	Model Development	6-7
		6.5.2	References	6-9
7.	STAI	NLESS S	STEEL OXIDES	7-1
	7.1	Specifi	ic Heat Capacity and Enthalpy (SOCP, SONTHL)	7-1
		7.1.1	Specific Heat Capacity (SOCP)	7-1
		7.1.2	Enthalpy (SONTHL)	7-7
		7.1.3	Reference	
	7.2	Therm	nal Conductivity (SOTCON)	
		7.2.1	Model Development	7-9
		7.2.2	Reference	
	7.3		nal Expansion and Density (SOTHEX, SODEN)	
		7.3.1	Thermal Expansion (SOTHEX)	7-11 7.11
		7.3.2 7.3.3	Density (SODEN)	7-11 7-13
^	3.000.0			
8.			BSORBERS (SILVER-INDIUM-CADMIUM CONTROL RODS N CARBIDE CONTROL BLADES)	8-1
	11112	8.0.1	References	
	0.1		rg Temperature (AHYPRP)	
	8.1			
		8.1.1 8.1.2	Model Development	8-1 8-1
	8.2		ic Heat Capacity and Enthalpy (ACP, AENTHL)	
	0.2	8.2.1	Specific Heat Capacity of Ag-In-Cd (ACP)	8-2
		8.2.2	Specific Heat Capacity for Boron Carbide(ACP)	8-3
		8.2.3	Enthalpy of Ag-In-Cd (AENTHL)	8-4
		8.2.4	Enthalpy of Boron Carbide (AENTHL)	
		8.2.5	References	
	8.3		al Conductivity (ATHCON)	
		8.3.1	Thermal Conductivity of Ag-In-Cd (ATHCON) Thermal Conductivity of Boron Carbide (ATHCON)	8-6 2.7
		8.3.2 8.3.3	References	8-7 8-8
	8.4		al Expansion and Density (ATHEXP, ADEN)	
	0.4	8.4.1	Thermal Expansion Strain of Ag-In-Cd	
		8.4.2	Thermal Expansion Strain of Ag-III-Cu	8-11
		8.4.3	Density Calculations for Ag-In-Cd and Boron Carbide	8-11

		8.4.4 References	8-13		
	8.5	Surface Tension (ASTEN)	8-13		
		8.5.1 Model Development	8-13		
		8.5.2 Reference			
	8.6	Viscosity (AVISC)			
		8.6.1 Viscosity of Ag-In-Cd			
		8.6.3 Reference			
9.	CADI	MIUM	9-1		
	9.1	Specific Heat (CDCP)	9-1		
		9.1.1 Reference	9-1		
	9.2	Thermal Conductivity (CDTCON)	9-1		
		9.2.1 Reference	9-2		
	9.3	Density (CDDEN)	9-2		
		9.3.1 Reference			
	9.4	Enthalpy (CDENTH)	9-3		
		9.4.1 Reference	9-4		
10.	GRID SPACER MATERIAL (INCONEL)				
	10.1	Melting Temperatures (HPROP)	10-1		
	10.2	Enthalpy Correlations (USERP)	10-1		
	10.3	Thermal Conductivity (USERP)	10-2		
	10.4	Density (USERP)	10-2		
		10.4.1 References	10-3		
11.	ZIRCONIUM-URANIUM COMPOUNDS				
		11.0.1 References	11-4		
	11.1	Zirconium Uranium Oxygen Compound Melting, Solution, and			
		Precipitation (PSOL, PLIQ, ZUSOLV, COEF)			
		11.1.1 Introduction			
		11.1.3 Model Development	11-17		
		11.1.4 References			
	11.2	Specific Heat Capacity and Enthalpy (ZUCP, ZUNTHL, ZUCP1, ZUNTH1)	11-29		
		11.2.1 Zirconium-Uranium-Oxygen Compounds			
		11.2.2 Core Component Compounds			
	11.3	Thermal Conductivity (ZUTCON, ZUTCO1)			
		11.3.1 Zirconium-Uranium-Oxygen Compounds			
		11.3.2 Core Component Compounds			

		11.3.3 References	11-43
	11.4	Thermal Expansion and Density (ZUTEXP, ZUDEN, ZUTEX1, ZUDEN1)	11-43
		11.4.1 Zirconium-Uranium-Oxygen Compounds11.4.2 Core Component Compounds11.4.3 Reference	11-49
	11.5	Zirconium-Uranium-Oxygen Compounds Coefficients of Friction (ZUFRIC)	
	11.6	Zirconium-Uranium-Oxygen Compounds Interfacial Surface Tension (ZUSTEN	
	11.7	Zirconium-Uranium-Oxygen Compounds Viscosity (ZUVISC)	
		11.7.1 Model Development	11-55
	11.8	Heat of Solution of Uranium Dioxide by Zirconium-Uranium-Oxygen Compounds (ZUSOLN)	11-57
		11.8.1 Model Development	11-57 11-59
	11.9	Heat of Fusion of Zirconium-Uranium-Oxygen Compounds (ZUFUSN)	11-59
	11.10	Coefficient of Thermal Expansion of Liquefied Mix (ZUBET1)	11-59
	11.11	Position of Advancing Zr-UO ₂ Interface (PSUZ)	11-60
		11.11.1 Summary	11-60 11-61
	11.12	UO ₂ Solubility in Oxygen Stabilized Zircaloy (PSLV)	
		11.12.1 Summary	11-61
	11.13	Rate of Dissolution of UO2 in Zr-U-O (UO2DIS, UO2SOL)	
		11.13.1 Introduction	11-62 11-64 11-67
12.	HYDR	CONDENSABLE GASESHELIUM, ARGON, KRYPTON, XENON, ROGEN, NITROGEN, OXYGEN, CARBON MONOXIDE, SON DIOXIDE, WATER MIXTURES	12-1
	12.1	Thermal Conductivity, Gas Conductance, and Jump Distance (GASCON, GTHCON, GJUMP)	12-1
		12.1.1 Summary	12-1
		12.1.2 Gas Thermal Conductivity and Accommodation Coefficient Data	12-5 12 - 9
		12.1.3 Model Development and Uncertainty Estimates	12-20
	12.2	Viscosity (GVISCO)	
		12.2.1 Model Development	12-22
		12.2.2 References	12-24

13.	VESS	EL AND COOLANT SYSTEM MATERIALS	13-1
	13.1	Rupture Time and the Creep Damage Term Calculations (RUPTUR, TRUPT, CALTAV)	13-1
		13.1.1 Model Description	13-4
14.	TUNG	GSTEN	14-1
	14.1	Specific Heat (TUNGCP)	14-1
	14.2	Thermal Conductivity (TUNGK)	14-1
	14.3	Density Correlations (TUNGRO)	14-2
		14.3.1 Reference	14-2
15.	DIFF	USIVITIES	15-1
	15.1	Diffusion of Oxygen in Oxidic Layer	15-1
	15.2	Diffusion of Oxygen in Metallic Layer	15-1
	15.3	Alternative Correlations for Diffusion of Oxygen in Oxidic and Metallic Layer	ers 15-1
	15.4	Correlation for binary diffusivity in H2O + H2 mixture	15-2
	15.5	References	15-3
16.	UTILI	ITIES	16-1
	16.1	Linear Interpolation (POLATE, POL8)	16-1
	16.2	Cladding Texture Factors (CTXTUR)	16-1
		16.2.1 Model Description	
	16.3	Collected Heats of Fusion (QFUSON)	16-5
		16.3.1 Model Development	
	16.4	Mass Fraction Mole Fraction Conversions (PMOLE, PMASS)	16-6
	16.5	Integral of the Reciprocal of Thermal Conductivity (ZUINT)	16-7
	16.6	Atomic Fraction (ATOMFR)	

FIGURES

Figure 2-1.	Specific heat capacity as a function of temperature and oxygen-to-metal ratio for UO ₂	2-8
Figure 2-2.	Specific heat capacity as a function of temperature and oxygen-to-metal ratio for $(U_{0.8}Pu0_{0.2})O_2+x$	2-9
Figure 2-3.	Enthalpy of UO ₂ as a function of temperature to 4,000 K	
Figure 2-4.	Specific heat capacity of UO ₂ from three experimenters compared with the FCP correlation (solid line) for UO ₂	2-12
Figure 2-5.	Specific heat capacity of PuO ₂ from Kruger and Savage compared with the FCP correlation (solid line) for PuO ₂	2-12
Figure 2-6.	Specific heat capacity of $(U_{0.8} Pu O_{0.2})O_2$ from three experimenters compared with the FCP correlation (solid line) for mixed oxides	2-13
Figure 2-7.	Model prediction for thermal conductivity of 0.99% TD UO ₂ compared to data from specimens with densities in the range 0.985 to 0.995% TD	2-41
Figure 2-8.	Model prediction for thermal conductivity of 0.98% TD UO ₂ compared to data from specimens with densities in the range 0.975 to 0.985% TD	2-41
Figure 2-9.	Model prediction for thermal conductivity of 0.96% TD UO ₂ compared to data from specimens with densities in the range 0.955 to 0.965% TD	2-42
Figure 2-10.	Model prediction for thermal conductivity of 0.95% TD UO ₂ compared to data from specimens with densities in the range 0.945 to 0.955% TD	2-42
Figure 2-11.	Emissivity data and corresponding FEMISS predictions.	2-48
Figure 2-12.	Correlation for the thermal expansion strain of UO ₂ compared with its data base	2-54
Figure 2-13.	Correlation for the thermal expansion strain of PuO ₂ compared with its data base	2-55
Figure 2-14.	Comparisons of the UO ₂ , PuO ₂ , and (U _{0.8} , PuO _{0.2})O ₂ correlations from 0 to 2,000 K	2-55
Figure 2-15.	Theoretical density of UO ₂ .	2-56
Figure 2-16.	Young's modulus for stoichiometric UO ₂ fuel at several temperatures and fractions of theoretical density.	2-60
Figure 2-17.	Young's modulus for (U, Pu)O ₂ with various oxygen-to-metal ratios	2-61
Figure 2-18.	Young's modulus data and least-squares linear fit for stoichiometric UO ₂ fuel at room temperature and several different densities	2-62
Figure 2-19.	Ratio of Young's modulus for stoichiometric and nonstoichiometric fuels measured at room temperature compared to values predicted by de Novion's correlation.	2-64
Figure 2-20.	Poisson's ratio as a function of temperature	
Figure 2-21.	Comparison of unirradiated UO ₂ experimental data with corresponding calculated values from FCREEP.	
Figure 2-22.	Comparison of irradiated UO ₂ experimental data with corresponding calculated values from FCREEP.	

Figure 2-23.	Comparison of (U,Pu)O ₂ experimental data with corresponding calculated values from FCREEP.	2-80
Figure 2-24.	Comparison of UO ₂ strain data of Rod 3C with corresponding calculated values from FCREEP.	2-81
Figure 2-25.	Comparison of UO ₂ strain data of Capsule 2 with corresponding calculated values from FCREEP.	2-82
Figure 2-26.	The effect of burnup and fission rate on the fuel density change for EPRI fuel types 1, 2, and 4	2-87
Figure 2-27.	Change in fuel stack length of Halden fuel as a function of burnup	2-89
Figure 2-28.	Fuel stack length changes for 92% TD UO2 processed by different techniques.	2-90
Figure 2-29.	Graphical solution of Rolstad's model, where TD is percent of theoretical density, TS is sintering temperature (oC), and BU is burnup.	2-93
Figure 2-30.	FUDENS calculations using EPRI fuel fabrication parameters and resintering values correlated with experimental EPRI in-pile data	2-95
Figure 2-31.	Unrestrained fission gas swelling.	
Figure 2-32.	Fuel volume changes calculated by FSWELL compared with experimental fuel swelling data.	. 2-100
Figure 2-33.	Urania pressure sintering rates calculated using the FHOTPS model compared with data	. 2-112
Figure 2-34.	Mixed-oxide pressure sintering rates calculated using the	. 2-113
Figure 2-35.	Threshold of columnar grain growth with temperature gradient of 4.0 x 105 K/m.	. 2-123
Figure 2-36.	Comparison of Equation (2-128) in the elastic behavior regime with out-of-pile UO ₂ fracture strength data normalized to 10-mm grain size and 95% TD.	
Figure 2-37.	Comparison of Equation (2-129) in the elastic behavior regime with out-of-pile UO ₂ fracture strength data normalized to 10-mm grain size and 95%TD.	. 2-130
Figure 2-38.	Least squares regression fit of UO ₂ fracture strength in the elastic plastic regime to out-of-pile data of Cannon et al	
Figure 2-39.	Calculated curves showing the predictions of FFRACS as a function of temperature for two fuel densities.	
Figure 2-40.	Uranium dioxide viscosities measured as a function of temperature	
Figure 2-41.	Data from uranium dioxide samples compared with least-squares fit	
Figure 2-42.	Viscosities calculated with Equation (2-130) (solid line) and upper and lower uncertainty estimates (dashed lines) compared with data	2-141
Figure 2-43.	Urania vapor pressure data	
Figure 2-44.	Plutonia vapor pressure data.	
Figure 2-45.	Mixed oxide vapor pressure data.	
Figure 2-46.	FVAPRS calculations (solid line) compared to urania data	2-157
Figure 2-47.	FVAPRS calculations (solid line) compared to plutonia data	2-158

Figure 2-48.	FVAPRS calculations (solid line) compared to mixed oxide data.	
	An oxygen-to-metal ratio of 2.0 was used in the FVAPRS calculations	2-159
Figure 2-49.	FVAPRS hypostoichiometric oxygen vapor pressure calculations	
· ·	(UOXVAP) compared to the data.	2-161
Figure 2-50.	FVAPRS hyperstoichiometric oxygen vapor pressure calculations	
	(DIOVAP) compared to the data	2-162
Figure 2-51.	FVAPRS vapor pressure calculations of plutonia (PUOVAP),	
	urania (UO2VAP), mixed oxides (VAPMIX), and monatomic oxygen	0.160
	over urania (UOXVAP), using an oxygen-to-metal ratio of 2.0.	2-162
Figure 2-52.	Computed weight gain as a function of temperature for constant time	2 160
	step size	2-109
Figure 2-53.	Computed weight gain as a function of time step size for constant	2-170
T: 0.1	temperature.	
Figure 3-1.	Specific heat capacity for uranium metal calculated by the function UCP.	
Figure 3-2.	Enthalpy change for uranium metal calculated by UENTHL	
Figure 3-3.	Thermal conductivities calculated by UTHCON.	3-9
Figure 3-4.	Thermal expansion strain as a function of temperature calculated	3-13
T: 2 E	by UTHEXP	5-15
Figure 3-5.	Density calculated by UDEN using the thermal strain calculated by UTHEXP.	3-13
Figure 3-6.	Parabolic rate constant for the uranium-steam reaction as a function of	
8	temperature.	3-16
Figure 4-1.	Zircaloy solidus and liquidus temperatures	
Figure 4-2.	Specific heat of zircaloys as calculated by CCP for alloys without hydride	
Figure 4-3.	Available data, MATPRO expressions for specific heat, and estimated	
J	uncertainty of the MATPRO expression for temperatures from	
	300 to 1,000 K	4-9
Figure 4-4.	Available data, MATPRO expressions for specific heat, and estimated	
	uncertainty of the MATPRO expression for temperatures from 1,000 to	4.0
	2,000 K	4-9
Figure 4-5.	Data base for MATPRO prediction of the effect of hydride solution on specific heat, Scott's proposed curve for the specific heat of zirconium,	
	and the MATPRO predictions for the effect of 28 and 300 ppm of	
	hydrogen on the specific heat curve	4-12
Figure 4-6.	MATPRO predictions for apparent zircaloy specific heat for several	
riguic 4-0.	hydrogen concentrations compared with the curve measured with	
	as-received zircaloy-2.	4-13
Figure 4-7.	Derivation of Equation (4-21)	
Figure 4-8.	Zircaloy enthalpy as a function of temperature.	
Figure 4-9.	Thermal conductivity data, least squares fit, and the two standard	
-6	deviation limits	4-18
Figure 4-10.	Comparison of CTHEXP prediction with Douglass' data in the axial	
•	direction.	4-28

rigure 4-11.	circumferential direction	4-29
Figure 4-12.	Comparison of CTHEXP prediction with Kearns' model in the axial direction.	
Figure 4-13.	Comparison of CTHEXP prediction with Kearns' model in the circumferential direction.	
Figure 4-14.	Angles and orientation of the unit cell of zircaloy relative to a system of coordinates fixed in the lab frame of reference.	
Figure 4-15.	Elastic moduli for isotropic material compared to corresponding moduli for typical PWR cladding.	
Figure 4-16.	Reference directions selected for CELMOD/CSHEAR/CELAST analysis.	4-54
Figure 4-17.	Measured values of axial Young's modulus compared to values predicted by the CELAST subcode for several oxygen concentrations and temperatures in the range of 300 to 1,500 K.	
Figure 4-18.	Measured values of circumferential Young's modulus compared to values predicted by the CELAST subcode for several oxygen concentrations and temperatures in the range of 300 to 1,500 K.	
Figure 4-19.	Comparison of the Young's modulus predicted with the CELAST code to the beta phase zirconium data of Padel and Groff, and Armstrong and Brown.	
Figure 4-20.	Model predictions and measured values of zircaloy tube axial growth as a function of fast neutron fluence, irradiation temperature, cold work, and texture coefficient, fz.	
Figure 4-21.	The growth of schematic unit cells in a grain.	
Figure 4-22.	Model predictions and measured values of the growth of zircaloy tubes adjusted to a common texture coefficient of $fz = 0.05$.	
Figure 4-23.	Zircaloy growth versus square root of fast neutron fluence for data adjusted to a common tube texture coefficient of fz = 0.05 with linear least-squares fits superimposed.	
Figure 4-24.	Zircaloy growth versus square root of fast neutron fluence for data adjusted to a common tube texture coefficient of $fz = 0.05$ and to a common temperature of 300° C with linear least squares fits superimposed	l
Figure 4-25.		
Figure 4-26.	Radial displacement of cladding surface at 200 hours in Hobson's test 269-4	
Figure 4-27.		
Figure 4-28.	Average tangential creep strain as a function of time at 14.48 MPa differential pressure	
Figure 4-29.		<i>1</i> -95

Steady-state creep rates reported by Fidleris for Tests R-6 and	
	4-98
Increase of the strain anisotropy constant A1E as a function of	4-116
Padial compressive strain in two tests.	
Strain rate sensitivity exponent as a function of temperature	4-117
function of strain rate based on Chung, Garde, and Kassner's data	4-118
Base data, MATPRO prediction, and uncertainty estimate for strain hardening exponent of annealed tubes.	4-119
Base data, MATPRO prediction, and uncertainty estimate for	
strain coefficient of annealed, isotropic cladding	.4-120
Data and least squares fit to strength coefficients as a function	
of cold work and irradiation at room temperature.	4-122
Data and analytical functions for strain hardening coefficient	
as a function of cold work and irradiation at room temperature	. 4-124
Calculated ratios of the strength coefficients of zircaloy, containing	
oxygen (K) and the strength coefficients of as fabricated zircaloy (Ko)	
as a function of oxygen concentration for several temperatures	. 4-130
Calculated curve and data showing the rate of change of the zircaloy	
strength coefficient with oxygen content as a function of temperature	. 4-130
Calculated ratios of the strain hardening exponents of zircaloy containing	
oxygen (n) and the strain hardening exponents of as-fabricated	
zircaloy (no) as a function of oxygen concentration for several	4 122
temperatures	.4-132
Calculated curve and data showing the rate of change of the zircaloy	1 122
strain hardening exponent as a function of temperature	. 4-133
Strain rate sensitivity exponent, m, data as a function of oxygen concentration from Chung.	. 4-135
The ratio m/mo as a function of oxygen concentration showing	
Chung data and the line used to fit these data	. 4-135
Zircalov oxygen phase diagram, taken from Chung	. 4-136
Stress as a function of strain at a strain rate of 10-3/s for two oxygen	
concentrations at 600 K.	. 4-137
Stress as a function of strain at a strain rate of 10-3/s for two oxygen	
concentrations at 1,400 K.	. 4-138
concentrations at 600 K.	. 4-138
Measured diametral strain versus MATPRO predictions for two initial	
values of cold work in tests conducted by Hardy at heating rates of 25 K/s	.4-139
Measured diametral strain versus MATPRO predictions for	
Chung's test at 1,023 K and 5.2 MPa.	. 4-140
	Rx-14 compared to model predictions for steady-state creepdown rates derived from these data. Increase of the strain anisotropy constant A1E as a function of radial compressive strain in two tests. Strain rate sensitivity exponent as a function of temperature and strain rate. Increase of the strain rate sensitivity exponent at 1,173 K as a function of strain rate based on Chung, Garde, and Kassner's data. Base data, MATPRO prediction, and uncertainty estimate for strain hardening exponent of annealed tubes. Base data, MATPRO prediction, and uncertainty estimate for strain coefficient of annealed, isotropic cladding. Data and least squares fit to strength coefficients as a function of cold work and irradiation at room temperature. Data and analytical functions for strain hardening coefficient as a function of cold work and irradiation at room temperature. Calculated ratios of the strength coefficients of zircaloy, containing oxygen (K) and the strength coefficients of zircaloy, containing oxygen (K) and the strength coefficients of as fabricated zircaloy (Ko) as a function of oxygen concentration for several temperatures. Calculated curve and data showing the rate of change of the zircaloy strength coefficient with oxygen content as a function of temperature. Calculated ratios of the strain hardening exponents of zircaloy containing oxygen (n) and the strain hardening exponents of as-fabricated zircaloy (no) as a function of oxygen concentration for several temperatures. Calculated curve and data showing the rate of change of the zircaloy strain hardening exponent as a function of temperature. Calculated ourse and data showing the rate of change of the zircaloy strain hardening exponent as a function of oxygen concentration from Chung. The ratio m/mo as a function of oxygen concentration showing Chung data and the line used to fit these data. Zircaloy oxygen phase diagram, taken from Chung. Stress as a function of strain at a strain rate of 10-3/s for two oxygen concentrations at 1,400 K. Stress

Figure 4-50.	Local radial strains at burst versus temperature.	4-175
Figure 4-51.	Average circumferential strains at failure versus temperature	
Figure 4-52.	Local tangential stress at failure versus temperature.	
Figure 4-53.	Base data and MATPRO correlation for effect of temperature	
	variation on average circumferential elongation.	4-182
Figure 4-54.	Schematic cross-sections of cladding at burst.	4-183
Figure 4-55.	Typical average circumferential strains predicted by the MATPRO	
	correlations for typical engineering burst stress, true burst stress, and	
	typical strain distributions at three different temperature differences	
Figure 4-56.	Hobson-Rittenhouse isothermal data for fast cooled cladding compared	
T: 4.55	with the 0.65 and 0.70 wt% and the 90 and 95% filled criteria.	4-191
Figure 4-57.	Hobson-Rittenhouse and PBF data for fast-cooled rods compared with	
	the critical fractional wall thickness as calculated from the 0.65 and	4 100
Figure 4-58.	0.70 wt% and the 90 and 95% filled criteria. Comparison of the Argonne data for slow-cooled cladding with the	4-192
1 iguic 4-36.	criterion that at least 0.3 mm of zircaloy with less than 1 wt% oxygen	
	is required to survive thermal shock.	4-193
Figure 4-59.	Values of the CMHARD correlation and its data base	
Figure 4-60.	Idealized schematic of a uranium dioxide pellet in contact with the	205
J	cladding, showing the layered structure	4-209
Figure 4-61.	Schematic of post-transition oxide, showing an intact, rate-determining	
	layer of varying thickness, with another oxide layer that does not	
	affect the oxidation rate	4-216
Figure 4-62.	Estimates of enhancements over out-of-pile oxidation rates when	
T	cladding is irradiated in typical BWR and PWR environments	4-219
Figure 4-63.	Comparison of the predicted oxide layer thickness with the base data	
	from average values of six Shippingport zircaloy-2 rods in a PWR environment at 277 oC.	4 221
Figure 4-64.		4-221
11guic 4-04.	Comparison of the predicted oxide layer thickness with the base data from Saxton zircaloy-4 rods in a PWR at 340 oC.	4 221
Figure 4-65.	Comparison of the predicted oxide layer thickness with the base data	4-221
- 18 mile : 000	from zircaloy-2 rods irradiated in the Vallecitos and Dresden BWRs	
	at 286 oC.	4-222
Figure 4-66.	Comparison of calculated (solid lines) and measured ZrO2 thickness	
	for six temperatures	4-223
Figure 4-67.	Data used by Urbanic and Heidrick to determine high temperature	
	zircaloy oxidation rates.	4-224
Figure 4-68.	Growth of Zr(O) and Zr(O)b layers as a function of temperature	
	from Hofmann and Politis. 4.15-16	4-225
Figure 4-69.	Linear power generation for a rod of initial diameter of 1.25 x 10-2 m	
T'	as a function of temperature for various initial oxide thicknesses	
Figure 5-1.	Zircaloy oxide solidus and liquidus temperatures.	
Figure 5-2.	Zircaloy oxide specific heat capacity as a function of temperature	5-6

Figure 5-3.	Zircaloy oxide enthalpy as a function of temperature.	5-8
Figure 5-4.	Zircaloy oxide thermal conductivity data and correlations	
Figure 5-5.	Zircaloy oxide thermal conductivity as a function of temperature	
Figure 5-6.	Total hemispherical emittance of zircaloy-4 versus time at	
J	temperature in steam.	5-18
Figure 5-7.	ZOEMIS calculations compared with the data base of the model	5-22
Figure 5-8.	Expected standard errors of emissivity for temperatures below 1,500 K and at 1,573 K	5-24
Figure 5-9.	Zircaloy oxide thermal strain.	5-26
Figure 5-10.	Zircaloy oxide density as a function of temperature	5-26
Figure 5-11.	Zircaloy oxide thermal strain data compared to code prediction	5-28
Figure 5-12.	Data and calculated values of Young's modulus for zircaloy oxide	5-30
Figure 5-13.	Zircaloy oxide failure stress data and correlations versus temperature	
Figure 5-14.	Zircaloy oxide failure stress calculated with the ZORUP function	5-33
Figure 6-1.	Stainless steel specific heat capacity at constant pressure.	
Figure 6-2.	Stainless steel thermal conductivity.	
Figure 6-3.	Stainless steel thermal expansion strain.	
Figure 6-4.	Stainless steel density	
Figure 6-5.	Parabolic constant for oxygen weight gain.	6-10
Figure 6-6.	Parabolic constant for oxide layer thickness	6-10
Figure 6-7.	Average power per meter during 1 second for a 1.25 x 10-2 m stainless steel rod with no initial oxide layer	
Figure 6-8.	Oxygen uptake after 1 second with no initial oxidation.	
Figure 6-9.	Oxide layer thickness after 1 second with no initial oxidation	
Figure 7-1.	Specific heat capacity for stainless steel oxide calculated by SOCP	
Figure 7-2.	Enthalpy change for stainless steel oxide calculated by SONTL.	
Figure 7-3.	Thermal conductivities for stainless steel oxide calculated by SOTCON	
Figure 7-4.	Thermal expansion strain as a function of temperature calculated by SOTHEX.	
Figure 7-5.	Density calculated by SODEN using the thermal strain calculated	
	by SOTHEX.	7-12
Figure 8-1.	Silver-indium-cadmium absorber heat capacity.	
Figure 8-2.	Boron carbide absorber heat capacity.	8-4
Figure 8-3.	Silver-indium-cadmium absorber enthalpy.	8-5
Figure 8-4.	Boron carbide absorber enthalpy.	8-5
Figure 8-5.	Thermal conductivity of silver-indium-cadmium alloy.	8-7
Figure 8-6.	Thermal conductivity of silver-indium-cadmium absorber	
Figure 8-7.	Thermal conductivity of boron carbide absorber.	
Figure 8-8.	Thermal expansion strain of silver-indium-cadmium absorber	
Figure 8-9.	Thermal expansion strain of boron carbide absorber.	
Figure 8-10.	Density of silver-indium-cadmium absorber	

Figure 8-11.	Density of boron carbide absorber.	8-12
Figure 8-12.	Viscosity of silver-indium-cadmium absorber.	8-15
Figure 8-13.	Viscosity of boron carbide absorber	
Figure 11-1.	Compositions of Zr-U-O compounds on a Gibbs triangle plot	11-2
Figure 11-2.	Zirconium-zirconium dioxide phase diagram	
Figure 11-3.	Uranium oxygen phase diagram.	
Figure 11-4.	Solidus and liquidus temperatures of uranium oxides according to Latta and Fryxell.	11-9
Figure 11-5.	Oxygen saturated, alpha phase zirconium uranium dioxide isopleth	11-10
Figure 11-6.	Uranium dioxide zirconium dioxide quasi-binary phase diagram	11-11
Figure 11-7.	Uranium zirconium system liquidus and solidus	11-12
Figure 11-8.	Phases of the Zr-U-O system at 1,273 K.	
Figure 11-9.	Phases of the Zr-U-O system at 1,773 K.	
Figure 11-10.	Phases of the Zr-U-O system at 1,873 K.	
Figure 11-11.	Phases of the Zr-U-O system at 2,073 K.	11-14
Figure 11-12.	Phases of the Zr-U-O system at 2,178 K.	11-15
	Phases of the Zr-U-O system at 2,223 K.	
Figure 11-14.	Phases of the Zr-U-O system at 2,273 K	11-16
Figure 11-15.	Points that are connected to form the ternary Zr-O-U system liquidus lines.	11-17
Figure 11-16.	Points that are connected to form the ternary Zr-O-U system solidus lines	
Figure 11-17.	Solid and liquid phase boundaries with tie lines connecting compositions on the boundaries as they are represented for 2,500 K in the ZUSOLV code	
Figure 11-18.	Specific heat capacity calculated for a 0.2 UO2-0.8 ZrO2 weight fraction compound.	
Figure 11-19	Enthalpy calculated for a 0.2 UO2-0.8 ZrO2 weight fraction compound.	
	Thermal conductivity calculated for a 0.2 UO2-0.8 ZrO2 weight fraction compound.	
Figure 11-21.	Thermal strain calculated for a 0.2 UO2-0.8 ZrO2 weight fraction compound.	
Figure 11-22.	Density calculated for a 0.2 UO2-0.8 ZrO2 weight fraction compound	11.46
	Coefficient of friction calculated with the ZUFRIC function.	
	Viscosity of a compound composed of 0.33 mol% zirconium and 0.67 mol% uranium dioxide	
Figure 11-25.	Effect of solvent composition of heat required to dissolve a kilogram of uranium dioxide.	
Figure 11-26	Zirconium-zirconium dioxide phase diagram.	
	Uranium-oxygen phase diagram.	
	Oxygen saturated alpha phase zirconium - uranium dioxide isopleth	

Figure 11-29.	Quasi binary phase diagram for the ZrO2-UO2 system	
	from Reference 11.13-6.	
Figure 11-30.	Zr-U-O isothermal section at 2,273 K according to Hofmann and Politis.	11-67
Figure 11-31.	Points connected to form the ternary Zr-U-O system.	11-68
	Zr-U-O isothermal section at 2,273 K according to Hofmann	
_	and Politis (revised).	
Figure 12-1.	Thermal conductivity of helium as a function of temperature	12-11
Figure 12-2.	Thermal conductivity of argon as a function of temperature	12-11
Figure 12-3.	Thermal conductivity of krypton as a function of temperature	12-12
Figure 12-4.	Thermal conductivity of xenon as a function of temperature	12-12
Figure 12-5.	Thermal conductivity of hydrogen as a function of temperature	12-13
Figure 12-6.	Thermal conductivity of nitrogen as a function of temperature	12-14
Figure 12-7.	Thermal conductivity of oxygen as a function of temperature	12-14
Figure 12-8.	Thermal conductivity of carbon monoxide as a function of temperature	12-15
Figure 12-9.	Thermal conductivity of carbon dioxide as a function of temperature	12-16
Figure 12-10.	Thermal conductivity of helium xenon mixtures at 793 K.	12-16
Figure 12-11.	Gas viscosity as a function of temperature for pure helium, a binary	
•	mixture of helium and xenon, and for an equal molar mixture of	
	helium, argon, krypton, and xenon.	12-24
Figure 13-1.	Master creep rupture curve for A-508, Class 2 carbon steel	
Figure 13-2.	Master creep rupture curve for 316 stainless steel	
Figure 13-3.	Master creep rupture curve for Inconel 600.	13-9
Figure 13-4.	Master creep rupture curves for SA533B carbon steel with 95%	
	certainty bounds, T > 1000 K.	13-9
Figure 13-5.	Master creep rupture curve for SA533B carbon steel with 95%	
	certainty bounds, T < 1000 K.	13-10
Figure 16-1.	Schematic illustration showing the relation between basal pole	
	intensity at one orientation (h,u) and the plotted value of the intensity	16-2
160	at (r,u) on a pole figure.	10-2 16 2
Figure 16-2.	Input grid for CTXTUR subcode.	10-3
Figure 16-3.	Relation between angles used in the definition of Kearn's texture factor (fu) and angles averaged by CTXTUR subcode	16_5
	Tactor (10) and angles averaged by CIAIUK Subcode	10-3

TABLES

Table 2-1.	Constants used in UO2 and PuO2 heat capacity and enthalpy correlations.	2-3
Table 2-2.	UO ₂ data from Christensen. ^{2.3-21}	2-21
Table 2-3.	UO ₂ data from Godfrey et al. ^{2.3-18}	2-22
Table 2-4.	UO ₂ data from Bates (Reference 2.3-19) thermal diffusivity measurements	
Table 2-5.	UO2 data, Gibby's2.3-27 thermal diffusivity measurements	
Table 2-6.	UO ₂ data from Weilbacher's ^{2.3-26} thermal diffusivity measurements	
Table 2-7.	UO2 data from Goldsmith and Douglas'2.3-12 thermal	
	diffusivity measurements.	2-33
Table 2-8.	UO2 data from Hobson's 2.3-13 thermal diffusivity measurements	2-36
Table 2-9.	Values of b0 and b1 from various density groups	
Table 2-10.	Parameters used in UO2 and PuO2 solid phase thermal expansion	
	correlations	2-49
Table 2-11.	Summary of Young's moduli measured in nonstoichiometric fuel	2 63
m.11. 0.10	at room temperature.	2-03 2-66
Table 2-12.	Least squares constants for data of Figure 2-16 Pressure sintering data	2-00 2 ₋ 110
Table 2-13.		
Table 2-14.	UO ₂ viscosity data from Tsai and Olander 2.13-4	
Table 2-15.	UO2 viscosity data from Woodley.2.13-5	
Table 2-16.	Measured and calculated weight gain.	2_170
Table 2-17.	Glossary of FORTRAN names.	
Table 3-1.	Alpha phase uranium specific heat capacity data.	J-1 2 2
Table 3-2.	Beta phase uranium specific heat capacity data.	د-د
Table 3-3.	Gamma phase uranium specific heat capacity data	
Table 3-4.	Uranium metal thermal conductivity from Touloukian et al	3-/
Table 3-5.	Uranium thermal expansion data from Touloukian et al. for temperature < 942 K	3-10
Table 3-6.	Uranium thermal expansion data from Touloukian et al.,	
Table 3-7.	Uranium thermal expansion data from Touloukian et al.,3.3-1 T > 1,045 K.	
Table 3-8.	Parabolic rate law constants for the uranium steam reaction	3-15
Table 4-1.	Oxygen content parameters for zircaloy.	
Table 4-2.	Zircaloy specific heat capacities for CCP	
Table 4-3.	Specific heat as a function of temperaturebeta phase	
Table 4-4.	Uncertainties in specific heat of zircaloy.	4-13
Table 4-5.	Values of mass for zircaloy.	4-15
Table 4-6.	Uncertainty of zircaloy enthalpy.	
Table 4-7.	Zircaloy thermal conductivity data base	
Table 4-8.	Comparison of Mehan and Wiesinger plate expansion	
	with MATPRO model.	
Table 4-9.	Bunnell's circumferential thermal expansion data	4-35

Table 4-10.	Bunnell's axial thermal expansion data	4-36
Table 4-11.	Comparison of model predictions and Bunnell's alpha phase data in the diametral direction.	4-41
Table 4-12.	Comparison of model predictions and Bunnell's alpha phase data in the axial direction	4-41
Table 4-13.	Beta-phase zirconium Young's Modulus measured by Armstrong and Brown	4-47
Table 4-14.	Beta phase zirconium Young's Modulus measured by Padel and Groff	
Table 4-15.	Young's modulus measurements by Busby	
Table 4-16.	Young's Modulus measurements by Spasic et al.	
Table 4-17.	Young's Modulus measurement by Mehan.	4-51
Table 4-18.	Elastic moduli measurements by Northwood et al. 4.6-9	4-52
Table 4-19.	Relations between fourth-rank tensor elements and traditional matrix elements.	
Table 4-20.	Measurements of growth in zircaloy tubing	
Table 4-21.	Zircaloy growth data as a function of cold work and fluence	
Table 4-22.	Determination of cold work coefficient.	
Table 4-23.	Surface coordinates of probes which measure radial displacement	
Table 4-24.	Radial displacements at 200 hours in Hobson's Test 269-4 (10-3 mm)	
Table 4-25.	Strength coefficient calculated with data of L. S. Rubenstein.	
Table 4-26.	Rate of change of K/Ko with oxygen content	4-129
Table 4-27.	Rate of change of n/n ₀ with oxygen content	
Table 4-28.	Room temperature ultimate strengths of cladding annealed for 1 hour from Howe and Thomas	1-146
Table 4-29.	644 K test results for unirradiated transient annealed cladding. 4.10-2	
Table 4-30.	644 K test results for irradiated transient annealed cladding. 4.10-3	4-148
Table 4-31.	644 K test results for irradiated isothermally annealed cladding. 4.10-3	4-149
Table 4-32.	Strength and residual strength coefficients after isothermal anneals.	1 155
Table 4-33.	Strength and residual strength coefficients with modified cold work annealing model.	
Table 4-34.	Strength and residual strength coefficients after transient anneals (tests with equal maximum temperature)	
Table 4-35.	Strength and residual strength coefficients after transient anneals (test with equal heating rates).	
Table 4-36.	Comparison of model predictions of K and n with data base for unirradiated cladding	4-163
Table 4-37.	Comparison of model predictions of K and n with data base for transient anneals of irradiated cladding	
Table 4-38.	Comparison of model predictions of K and n with data base for isothermal anneals of irradiated cladding	4-166
Table 4-39.	Summary of multirod burst test data employed in CMLIMT.	
Table 4-40.	Summary of data from the Hobson-Rittenhouse tests	4_171

Table 4-41.	Summary of data from the Chung-Kassner tests.	4-172
Table 4-42.	Summary of data from the Bauer tests	
Table 4-43.	Uncertainties in digitized Argonne data	4-194
Table 4-44.	Crack growth rate versus stress intensity range from Rao	4-199
Table 4-45.	Low-cycle fatigue material parameters.	
Table 4-46.	Rate constants for oxidation by steam.	4-210
Table 4-47.	Rate constants for oxidation by UO2	4-210
Table 4-48.	90% joint confidence intervals for the parabolic rate constants	
	for oxide layer growth, alpha layer growth, and total oxygen uptake	4-223
Table 4-49.	Time temperature layer thickness data from Hoffman's	
	out of pile experiments	4-225
Table 4-50.	Rate equations for hydrogen uptake.	
Table 5-1.	Zircaloy cladding oxide specific heat capacity data from Gilchrist	
Table 5-2.	Stabilized zircaloy dioxide thermal conductivity data from Adams	
Table 5-3.	Zircaloy oxide thermal conductivity data reported by Maki	5-10
Table 5-4.	Zircaloy dioxide thermal conductivity data of Lapshov and	
	Bashkatov.	
Table 5-5.	Zircaloy oxide thermal conductivity data of Gilchrist	
Table 5-6.	Emissivity of thin oxide films as reported by Murphy and Havelock	
Table 5-7.	Emissivity data from Burgoyne and Garlick	
Table 5-8.	Emissivity versus oxide thickness from Juenke and Sjodahl's data	
Table 5-9.	Standard errors of ZOEMIS predictions	
Table 5-10.	Zircaloy dioxide thermal expansion data by Fulkerson	
Table 5-11.	Zircaloy dioxide thermal expansion data from Brassfield et al	
Table 5-12.	Zircaloy dioxide modulus of elasticity data from Brassfield et al	
Table 5-13.	Zircaloy dioxide tensile strength data from Brassfield et al	
Table 6-1.	Rate constants for use with Equation (6-12) to predict oxidation	
Table 7-1.	FeO specific heat capacity data	
Table 7-2.	Fe2O3 specific heat capacity data	
Table 7-3.	Fe3O4 specific heat capacity data	
Table 7-4.	Stainless steel oxide thermal conductivity from Touloukian	
Table 8-1.	Molar heat capacity constants for Equation (8-1) from Reference 8.2-1.	
Table 8-2.	Thermal conductivity values for Ag-In-Cd recommended by Cohen et al	
Table 9-1.	Cadmium specific heat as a function of temperature.	
Table 9-2.	Cadmium thermal conductivity as a function of temperature	
Table 9-3.	Cadmium density as a function of temperature.	9-3
Table 9-4.	Cadmium enthalpy as a function of temperature.	9-4
Table 10-1.	Enthalpy of Inconel as a function of temperature.	
Table 10-2.	Thermal conductivity of Inconel as a function of temperature	10-2
Table 11-1.	Solidus and liquidus temperatures of UO _{2+x} from Latta and Fryxell	
Table 11-2.	Correlations for liquidus compositions	

Table 11-3.	Correlations for solidus compositions.	11-20
Table 11-4.	Data used to produce liquidus correlations.	11-23
Table 11-5.	Data used to produce solidus correlations.	11-25
Table 11-6.	ZUNTHL calculations and Deem's data for a 0.2 UO ₂ -0.8 ZrO ₂	
	weight fraction compound.	11-32
Table 11-7.	ZUNTHL calculations and Deem's data for 0.32 UO ₂ -0.68 ZrO ₂	
	weight fraction compound.	11-33
Table 11-8.	ZUNTHL calculations and Deem's data for a 0.5 UO ₂ -0.5 ZrO ₂	
	•	11-34
Table 11-9.	ZUNTHL calculations and Deem's data for 0.94 UO ₂ -0.06 ZrO ₂	11.00
Table 11 10	weight fraction compound.	11-36
Table 11-10.	ZUTCON calculations and Deem's results for 0.2 UO ₂ -0.8 ZrO ₂ weight fraction compound.	11 20
Table 11-11.	ZUTCON calculations and Deem's results for 0.32 UO ₂ -0.68 ZrO ₂	11-30
Table 11-11.	weight fraction compound.	11-39
Table 11-12.	ZUTCON calculations and Deem's results for 0.5 UO2-0.5 ZrO2	11 37
	weight fraction compound.	11-40
Table 11-13.	ZUTCON calculations and Deem's results for a low-density 0.32	
	UO2-0.68 ZrO2 weight fraction compound	11-41
Table 11-14.	ZUTCON calculations and Deem's results for 0.94 UO2-0.06	
	ZrO ₂ weight fraction compound.	11-41
Table 11-15.	ZUTEXP calculations and Deem's data for a 0.2 UO ₂ -0.8 ZrO ₂	
	weight fraction compound.	11-47
Table 11-16.	ZUTEXP calculations and Deem's data for 0.32 UO ₂ -0.68 ZrO ₂	
T.1. 11 17		11-47
Table 11-17.	ZUTEXP calculations and Deem's data for a 0.5 UO ₂ -0.5 ZrO ₂	11 40
Table 11-18.	weight fraction compound.	11-48
14016 11-18.	ZUTEXP calculations and Deem's data for 0.94 UO ₂ -0.06 ZrO ₂ weight fraction compound.	11_40
Table 11-19.	· · · · · · · · · · · · · · · · · · ·	
Table 11-20.	Constants for thermal expansion strain.	
Table 11-21.	Input variable to the subroutine ZUBET1.	
Table 12-1.	Constants used in gas thermal conductivity correlations.	
Table 12-2.	Uncertainty of the gas thermal conductivity correlations.	
Table 12-3.	Surface accommodation coefficients.	
Table 12-4.	Pure gas conductivity references	
Table 12-1.	Creep parameter-to-stress correlations.	
Table 12-2.	Time to rupture from parameter definition.	
Table 12-3.	Creep rupture data of A-508 pressure vessel carbon steel.	
Table 12-4.	Stainless steel creep rupture data.	
Table 12-5.	Inconel 600 creep rupture data	
Table 12-6.	High temperature SA533B creen runture data	

Table 14-1.	Specific heat of tungsten as a function of temperature	14-1
Table 14-2.	Thermal conductivity of tungsten as a function of temperature	14-2
Table 16-1.	Heats of fusion calculated in QFUSON	16-6

EXECUTIVE SUMMARY

The specific features of SCDAP/RELAP5/MOD3.3 are described in this five volume set of manuals covering the theory, use, and assessment of the code for severe accident applications. This set replaces the SCDAP/RELAP5/MOD3.2 Code Manuals, NUREG/CR-6150, Rev. 1.

The SCDAP/RELAP5 computer code is designed to calculate for severe accident situations the overall reactor coolant system (RCS) thermal-hydraulic response, core damage progression, and reactor vessel heatup and damage. The code was developed at the Idaho National Engineering and Environmental Laboratory (INEEL) under the primary sponsorship of the Office of Nuclear Regulatory Research of the U.S. Nuclear Regulatory Commission (NRC). The code is the result of merging the RELAP5 and SCDAP codes. The models in RELAP5 calculate the overall RCS thermal-hydraulics, control system interactions, reactor kinetics, and the transport of noncondensable gases. The RELAP5 code is based on a two-fluid model allowing for unequal temperatures and velocities of the fluids and the flow of fluid through porous debris and around blockages caused by reactor core damage. The models in SCDAP calculate the progression of damage to the reactor core. These models calculate the heatup, oxidation and meltdown of fuel rods and control rods, the ballooning and rupture of fuel rod cladding, the release of fission products from fuel rods, and the disintegration of fuel rods into porous debris and molten material. The SCDAP models also calculate the heatup and structural damage of the reactor vessel lower head resulting from the slumping to the lower head of reactor core material with internal heat generation. Although previous versions of the code have included the analysis of fission product transport and deposition behavior, this capability has been removed from SCDAP/RELAP5, and the analysis of fission product behavior is now performed using the detailed fission product code, VICTORIA^a, in an effort to reduce duplicative model development and assessment.

The SCDAP/RELAP5 code includes many generic component models from which general systems can be simulated. The component models include fuel rods, control rods, pumps, valves, pipes, reactor vessel, electrical fuel rod simulators, jet pumps, turbines, separators, accumulators, and control system components. In addition, special process models are included for effects such as form loss, flow at an abrupt area change, branching, choked flow, boron tracking, and noncondensable gas transport. The code also includes a model for reactor kinetics.

Several new capabilities and improvements in existing capabilities were implemented into the MOD3.3 version of SCDAP/RELAP5. The new capabilities include; (1) an integral diffusion method to calculate oxygen and hydrogen uptake accounting in mechanistic manner for steam starvation and rapid changes in temperature, (2) calculation of the relocation in the circumferential direction of melted metallic cladding retained by the oxidic portion of cladding, (3) calculation of the re-slumping of cladding that previously slumped and froze, (4) calculation of heat transfer in porous debris using correlations specific to porous debris, (5) calculation of flow losses in porous debris locations based on Darcy's Law and applying relative permeabilities and passabilities based on local debris conditions and volume fractions of the liquid and vapor phases of the coolant, (6) calculation of oxidation of both intact and slumped cladding under reflood conditions, (7) calculation of the heatup of the lower core structures and its interaction with slumping core material, (8) calculation of the behavior of jets of core material penetrating into a pool of water, (9) calculation of the permeation of melted core plate material into porous debris in the lower head of reactor vessel and affect of this permeation on lower head heatup, and (10) calculation of heatup of lower head containing melted core material and accounting for whether the melted material is well-mixed

a. N. E. Bixler, "VICTORIA2.0: A Mechanistic model for Radionuclide Behavior in a Nuclear Reactor Coolant System Under Severe Accident Conditions," NUREG/CR-6131, SAND93-2301, December 1998.

or stratified into oxidic and metallic pools. The improvements in existing modeling capabilities include; (1) a semi-mechanistic stress-based model instead of a wholly empirical model for failure of the oxidic portion of cladding retaining melted metallic cladding, and (2) more simplistic but accurate models for calculating position, configuration, and oxidation of melted fuel rod cladding that slumped to a lower location and froze. The MOD3.3 version of the code retains all of the capabilities of the previous version, namely MOD3.2.

This volume, Volume 4, describes the material properties correlations and computer subroutines contained in MATPRO. Formulation of the material properties are generally semi-empirical in nature. The material property subroutines contained in this document are for uranium, uranium dioxide, mixed uranium-plutonium dioxide fuel, zircaloy, cladding, zirconium dioxide, stainless steel, stainless steel oxide, silver-indium-cadmium alloy, cadmium, boron carbide, Inconel 718, zirconium-uranium-oxygen melts, fill gas mixtures, carbon steel, and tungsten. This document also contains descriptions of the reaction and solution rate models needed to analyze a reactor accident.

ACKNOWLEDGMENTS

Acknowledgments are made to those who made significant contributions to this and earlier versions of SCDAP/RELAP5, B. D. Reagan, D. L. Knudson, F. Griffin, J. L. Rempe and M. Sohal. The authors also acknowledge the former RELAP5 development team, specifically R. A. Riemke and J. Tolli for their contributions to SCDAP/RELAP5.

The SCDAP/RELAP5 Program is indebted to the technical monitor, J. Schaperow and S. Arndt of the U. S. Nuclear Regulatory Commission who was responsible for directing the overall program. Finally, acknowledgment is made of those many code users who have been very helpful in stimulating correction of code deficiencies and suggesting improvements.

1. INTRODUCTION

The SCDAP/RELAP5/MOD3.3 computer code is designed to calculate for severe accident situations the overall reactor coolant system (RCS) thermal-hydraulic response, reactor core and vessel damage progression, and, in combination with VICTORIA, ¹⁻¹ fission product release and transport during severe accidents. The code was developed at the Idaho National Engineering and Environmental Laboratory (INEEL) under the primary sponsorship of the Office of Nuclear Regulatory Research of the U.S. Nuclear Regulatory Commission (NRC).

1.1 General Code Capabilities

The code is the result of merging the RELAP5/MOD3¹⁻² and SCDAP¹⁻³ models. The RELAP5 models calculate the overall RCS thermal-hydraulics, control system interactions, reactor kinetics, and transport of noncondensable gases. A model is also included in RELAP5 to calculate flow losses in porous debris. Although previous versions of the code have included the analysis of fission product transport and deposition behavior using models derived from TRAP-MELT, this capability has been replaced through a data link to the detailed fission product code, VICTORIA, as a result of an effort to reduce duplicative model development and assessment. The SCDAP models calculate the heatup and damage progression in the core structures and the lower head of the reactor vessel. The calculations of damage progression include calculations of the meltdown of fuel rods and structures, the fragmentation of embrittled fuel rods, convective and radiative heat transfer in porous debris, the formation of a molten pool of core material, and the slumping of molten material to the lower head.

SCDAP/RELAP5 is capable of modeling a wide range of system configurations from single pipes to different experimental facilities to full-scale reactor systems. The configurations can be modeled using an arbitrary number of fluid control volumes and connecting junctions, heat structures, core components, and system components. Flow areas, volumes, and flow resistances can vary with time through either usercontrol or models that describe the changes in geometry associated with damage in the core. System structures can be modeled with RELAP5 heat structures, SCDAP core components, or SCDAP debris models. The RELAP5 heat structures are one-dimensional models with slab, cylindrical, or spherical geometries. The SCDAP core components include representative light water reactor (LWR) fuel rods, silver-indium-cadmium (Ag-In-Cd) and B₄C control rods and/or blades, electrically heated fuel rod simulators, and general structures. A two-dimensional, finite element heat conduction model based on the COUPLE¹⁻⁴ code may be used to calculate the heatup of the lower head of the reactor vessel and the slumped material supported by the lower head. This model takes into account the decay heat and internal energy of newly fallen or formed debris and then calculates the transport by conduction of this heat in the radial and axial directions to the wall structures and water surrounding the debris. The most important use of this model is to calculate the heatup of the vessel lower head and the timing of its failure in response to contact with material that has slumped from the core region. Other system components available to the user include pumps, valves, electric heaters, jet pumps, turbines, separators, and accumulators. Models to describe selected processes, such as reactor kinetics, control system response, and tracking noncondensable gases, can be invoked through user control.

The development of the current version of the code was started in the spring of 1998. This version contains a number of new capabilities and improvements in existing models since the last version of the code, SCDAP/RELAP5/MOD3.2 was released. The new capabilities include; (1) an integral diffusion method to calculate oxygen and hydrogen uptake in the fuel cladding, (2) calculation of the relocation in the circumferential direction of melted metallic cladding retained by the oxidic portion of cladding,

(3) calculation of the re-slumping of cladding that previously slumped and froze, (4) calculation of heat transfer in porous debris using correlations specific to porous debris, (5) calculation of flow losses in porous debris based on Darcy's Law and applying relative permeabilities and passabilities based on local debris conditions and volume fractions of the liquid and vapor phases of the coolant, (6) calculation of oxidation of both intact and slumped cladding under reflood conditions, (7) calculation of the heatup of the lower core structure and its interaction with slumping core material, (8) calculation of the behavior of jets of core material penetrating into a pool of water, (9) calculation of the permeation of melted core plate material into porous debris in the lower head of a reactor vessel and the affect of this permeation on lower head heatup, and (10) calculation of heatup of lower head containing melted core material and accounting for whether the melted material is well-mixed or stratified into oxidic and metallic pools. The improvements in existing modeling capabilities include; (1) a semi-mechanistic stress-based model instead of a wholly empirical model for failure of the oxidic portion of cladding retaining melted metallic cladding, (2) more simplistic but accurate models for calculating position, configuration, and oxidation of melted fuel rod cladding that slumped to a lower location and froze. In addition to the above changes, the MOD3.3 version of the code retains all of the capabilities of its previous version, namely MOD3.2.

1.2 Relationship to Other NRC-Sponsored Software

SCDAP/RELAP5 and RELAP5 are developed in parallel and share a common configuration. Both codes share a common source deck. Separate codes are formed only prior to compilation, so changes made to the source deck are automatically reflected in both codes.

The development and application of the code is also related to several other NRC-sponsored software packages. Theoretical work associated with the development of PARAGRASS-VFP¹⁻⁶ has resulted in model improvements for fission product release. A data link to the VICTORIA code allows for the detailed treatment of phenomena such as fission product and aerosol transport, deposition, and resuspension. A link with PATRAN¹⁻⁷ and ABAQUS¹⁻⁸ provides the user with the means to calculate the details of lower head failure. Animated plant response displays are possible through links to the Nuclear Plant Analyzer (NPA)¹⁻⁹ display software, which gives the user an efficient way of analyzing the large amount of data generated. Detailed plant simulations from accident initiation through release of fission products to the atmosphere are made available through links to the CONTAIN¹⁻¹⁰ containment response and CRAC2¹⁻¹¹ or MACCS¹⁻¹² atmospheric dispersion consequence codes.

1.3 Quality Assurance

SCDAP/RELAP5 is maintained under a strict code configuration system that provides a historical record of the changes made to the code. Changes are made using an update processor that allows separate identification of improvements made to each successive version of the code. Modifications and improvements to the coding are reviewed and checked as part of a formal quality program for software. In addition, the theory and implementation of code improvements are validated through assessment calculations that compare the code-predicted results to idealized test cases or experimental results.

1.4 Organization of the SCDAP/RELAP5 Manuals

The specific features of SCDAP/RELAP5/MOD3.3 are described in a five-volume set of manuals covering the theory (Volume 2), user's guidelines and input manual (Volume 3), material properties (Volume 4), and assessment (Volume 5). Although Volume 1 describes (a) the overall code architecture,

(b) interfaces between the RELAP5 and SCDAP models, and (c) any system models unique to SCDAP/ RELAP5, the code user is referred to the companion set of six volumes which describe the RELAP5¹⁻² system thermal-hydraulics and associated models.

Volume 1 presents a description of SCDAP/RELAP5/MOD3.3-specific thermal-hydraulic models (relative to RELAP5/MOD3), and interfaces between the thermal-hydraulic models and damage progression models.

Volume 2 contains detailed descriptions of the severe accident models and correlations. It provides the user with the underlying assumptions and simplifications used to generate and implement the basic equations into the code, so an intelligent assessment of the applicability and accuracy of the resulting calculation can be made.

Volume 3 provides the user's guide and code input for the severe accident modeling. User guidelines are produced specifically for the severe accident code. The user should also refer to the RELAP5/MOD3 Code Manual Volume V: User Guidelines for a complete set of guidelines.

Volume 4 describes the material property library, MATPRO. It contains descriptions of the material property subroutines available for severe accident analysis.

Volume 5 documents the assessments of SCDAP/RELAP5/MOD3.3. It includes nodalization sensitivity studies and time-step sensitivity studies, assessments using standard PWR and BWR plant models, and assessments using code-to-data comparisons.

1.5 Organization of Volume 4

Publication of a set of materials properties descriptions intended to provide a common base for reactor analysis began in 1974. The descriptions have been revised from time to time, as required by new data or consideration of new materials and temperature ranges. ¹⁻¹³ to ¹⁻²⁰ This MATPRO document is the only formal description of the package published since the last release of the SCDAP/RELAP5 code manuals. ¹⁻²¹ This volume contains descriptions of all MATPRO subroutines used by SCDAP/RELAP5 (subroutines dealing with fission product transport and deposition have been replaced by a data link to VICTORIA). Also, material properties have been updated. The materials whose properties were updated include: uranium dioxide, uranium alloys, zircaloy, Inconel, and zirconium-uranium compounds. Furthermore, three new materials descriptions were added. They are cadmium, carbon steel, and tungsten.

The descriptive detail provided for the subroutines presented in this document varies because the subroutine documentation came from many different resources, including the MATPRO-11 Revision 2 document, ¹⁻¹³ a series of informal reports dealing with materials properties subroutines that have been incorporated into SCDAP/RELAP5, and previously undocumented materials properties subroutines that are contained in the SCDAP/RELAP5 computer code or in the MATPRO library of materials properties subroutines. The correlations used in MATPRO-11 Revision 2 were developed using an extensive literature search, whereas later correlations were developed as their need became evident or new and relevant experimental data became available, such as the dissolution model for UO₂ in zircaloy. A less extensive literature search was used to develop the correlations used to calculate the materials properties in the models developed after the publication of the MATPRO-11 Revision 2 document.

The cladding and fuel materials properties subprograms modified by Pacific Northwest National Laboratory (PNNL) for high burnup fuel during the development of the FRAPCON3 code for high burnup fuels are described in Appendix A. These high burnup specific materials properties subprograms were included in this release of MATPRO with a high burnup specific identifier. SCDAP/RELAP5/MOD3.3 does not apply these high burnup subprograms because an assessment of the code with the use of these high burnup subprograms has not been completed. Any future assessment of these high burnup models using SCDAP/RELAP5/MOD3.3 requires substitution of calls in the FORTRAN source to these high burnup subprograms in place of the calls to the existing standard subprograms.

1.6 References

- 1-1. T. Heames et al., VICTORIA: A Mechanistic Model of Radionuclide Behavior in the Reactor Coolant System Under Sever Accident Conditions, NUREG/CR-5545, SAND90-0756, Rev. 1, December 1992.
- 1-2. C. M. Allison, C. S. Miller, N. L. Wade (Eds.) *RELAP5/MOD3 Code Manual*, Volumes I through IV, NUREG/CR-5535, EGG-2596, June 1990.
- 1-3. C. M. Allison and G. H. Beers, "Comparisons of the SCDAP Computer Code with Bundle Data Under Severe Accident Conditions," Seventh International SMIRT Conference, Chicago, IL, August 22-26, 1983.
- 1-4. E. C. Lemmon, COUPLE/FLUID: A Two-Dimensional Finite Element Thermal Conduction and Advection Code, EGG-ISD-SCD-80-1, February 1980.
- 1-5. M. L. Corradini et al., SCDAP/RELAP5 Independent Peer Review, LA-12481, January 1993.
- 1-6. J. Rest and S A. Zawadzki, "FASTGRASS-VFP/PARAGRASS-VFP Version 50531, Users Guide," Argonne National Laboratory Quarterly Report, January-March 1983, Volume I, NUREG/CR-3689, ANL-83-85 Volume I, June 1983.
- 1-7. PATRAN Plus User's Manual, Release 2.4, PDA Engineering, Costa Mesa, California, 1987.
- 1-8. ABAQUS User's Manual, Version 4.6, Hibbitt, Karlsson & Sorensen, Inc., Providence, Rhode Island, 1987.
- 1-9. D. M. Snider, K. L. Wagner, and W. Grush, Nuclear Plant Analyzer (NPA) Reference Manual Mod1, EGG-EAST-9096, April 1990.
- 1-10. K. D. Bergeron et al., User's Manual for CONTAIN 1.0, A Computer Code for Severe Nuclear Reactor Accident Containment Analysis, NUREG/CR-4085, SAND84-1204, May 1985.
- 1-11. L. T. Ritchie et al., CRAC2 Model Description, NUREG/CR-2552, SAND82-0342, March 1984.
- 1-12. D. I. Chanin et al., MELCOR Accident Consequence Code System (MACCS Version 1.5), NUREG/CR-4691, SAND86-1562, July 1988, DRAFT.

- 1-13. D. L. Hagrman, G. A. Reyman, R. E. Mason, MATPRO-Version 11 (Revision 2), A Handbook of Materials Properties for Use in the Analysis of Light Water Reactor Fuel Rod Behavior, NUREG/CR-0479, TREE-1280, Revision 2, August 1981.
- 1-14. R. L. Miller, R. R. Hobbins, V. F. Baston, and W. A. Yuill, FRAP-T: A Computer Code for the Transient Analysis of Oxide Fuel Rods. Vol. 2, MATPRO Materials Properties Subcode, I-243-2, 1974.
- 1-15. P. E. MacDonald and L. B. Thompson (eds.), MATPRO A Handbook of Materials Properties for Use in the Analysis of Light Water Reactor Fuel Rod Behavior, ANCR-1263, February 1976.
- 1-16. P. E. MacDonald and L. B. Thompson (eds.), MATPRO-Version 09 A Handbook of Materials Properties for Use in the Analysis of Light Water Reactor Fuel Rod Behavior, TREE-NUREG-1005, December 1976.
- 1-17. G. A. Reymann (ed.), MATPRO-Version 10 A Handbook of Materials Properties for Use in the Analysis of Light Water Reactor Fuel Rod Behavior, TREE-NUREG-1180, February 1978.
- 1-18. D. L. Hagrman and G. A. Reymann (eds.), MATPRO-Version 11 A Handbook of Materials Properties for Use in the Analysis of Light Water Reactor Fuel Rod Behavior, NUREG/CR-0497, TREE-1280, February 1979.
- 1-19. D. L. Hagrman, G. A. Reymann, and R. E. Mason (eds.), MATPRO-Version 11 (Revision 1) A Handbook of Materials Properties for Use in the Analysis of Light Water Reactor Fuel Rod Behavior, NUREG/CR-0497, TREE-1280, Rev. 1, February 1980.
- 1-20. D. L. Hagrman, G. A. Reymann, and R. E. Mason (eds.), MATPRO Version 11 (Revision 2) A Handbook of Materials Properties for Use in the Analysis of Light Water Reactor Fuel Rod Behavior, NUREG/CR-0497, TREE-1280, Rev. 2, August 1981.
- 1-21. C. M. Allison et. al, *SCDAP/RELAP5/MOD3 Code Manual*, Volumes I through IV, NUREG/CR-5273, EGG-2555, September 1990.

2. URANIUM DIOXIDE/MIXED OXIDES

Sixteen materials properties of LWR fuel have been modeled for inclusion in MATPRO. The approaches range from (a) a least-squares fit to available data using a polynomial or other function having little or no theoretical basis to (b) a semiempirical correlation employing an analytical expression suggested by theory with constants determined by comparison with data. The intent of current and future work is to take the second approach wherever possible.

All 16 MATPRO fuel subcodes have temperature as an argument. In addition, many are functions of burnup, plutonia content, density, time, and other variables.

2.1 Melting Temperature and Heat of Fusion (FHYPRP)

2.1.1 Melting Temperature

The subroutine FHYPRP calculates the lowest temperature with a liquid phase (solidus) and the highest temperature with a solid phase (liquidus) of UO₂ and (U, Pu)O₂. These temperatures are calculated as a function of burnup and plutonia content.

2.1.1.1 Model Development. The equations used to calculate the UO₂ and (U, Pu)O₂ melting points utilize 3,113.15 K as the melting temperature of uranium (experimentally measured by Brassfield^{2,1-1}) and a least-squares fit to parabolic equations for the solidus and liquidus boundaries from the Lyon and Baily^{2,1-2} phase diagram for the stoichiometric (U, Pu)O₂ mixed oxide. The equations used are as follows:

For plutonia compositions > 0,

$$T_{sol} = 3,113.15 - 5.41395 C + 7.468390 \times 10^{-3} C^2 - 3.2 \times 10^{-3} FBu$$
 (2-1)

$$T_{liq} = 3,113.15 - 3.21660 \text{ C} - 1.448518 \times 10^{-2} \text{ C}^2 - 3.2 \times 10^{-3} \text{ FBu}$$
 (2-2)

For plutonia compositions = 0,

$$T_{sol} = 3{,}113.15 - 3.2 \times 10^{-3} \text{ FBu}.$$
 (2-3)

$$T_{i,q} = T_{sol} \tag{2-4}$$

where

 T_{sol} = the solidus temperature (K)

 T_{liq} = the liquidus temperature (K)

 $C = PuO_2$ content (wt%)

FBu = burnup (MWd/tU).

2.1.2 UO₂ and (U, Pu)O₂ Heat of Fusion

The two calorimetrically determined values for the heat of fusion of unirradiated UO_2 are in good agreement. Specifically, Hein and Flagella^{2.1-3} found a heat of fusion of 76.1 ± 2 kJ/mol, and Leibowitz^{2.1-4} reported a value of 74 kJ/mol. These results suggest that the heat of fusion of unirradiated UO_2 is adequately known from experimental analyses. The routine PHYPRP uses Leibowitz's calorimetry value of 2.74 x 10^5 J/kg for the heat of fusion of UO_2 .

Leibowitz^{2.1-5} determined a heat of fusion for mixed oxides of 67 kJ/mol from three tests. This 10% agreement between UO_2 and mixed oxide values for the heat of fusion is reasonable because of the similarity in crystal structure and atomic bonding. Therefore, unless conflicting data become available, the UO_2 value will be used for the heat of fusion of mixed oxides.

2.1.3 References

- 2.1-1 H. C. Brassfield et al., Recommended Property and Reactor Kinetics Data for Use in Evaluating a Light-Water-Coolant Reactor Loss-of-Coolant Incident Involving Zircaloy-4 or 304-SS-Clad UO₂, GEMP-482, April 1968.
- 2.1-2 W. F. Lyon and W. E. Baily, "The Solid-Liquid Phase Diagram for the UO₂-PuO₂ System," Journal of Nuclear Materials, 22, 332, 1967.
- 2.1-3 A. Hein and P. N. Flagella, Enthalpy Measurements of UO₂ and Tungsten to 3,260 K, GE-NMPO-578, February 1968.
- 2.1-4 L. Leibowitz et al., "Enthalpy of Liquid Uranium Dioxide to 3,500 K," Journal of Nuclear Material, 39, 1971, p. 115.
- 2.1-5 L. Leibowitz, D. F. Fischer, and M. G. Chasanov, *Enthalpy of Molten Uranium-Plutonium Oxide*, ANL-8082, February 1975.

2.2 Specific Heat Capacity and Enthalpy (FCP, FENTHL)

The specific heat capacity of nuclear fuel is needed for time dependent temperature calculations. The stored energy, or enthalpy, is calculated from the specific heat capacity. Stored energy is important in reactor transient analysis because the severity of the transient is greatly affected by the initial stored energy of the fuel.

2.2.1 Summary

The specific heat capacity and enthalpy of nuclear fuel are modeled empirically as functions of four parameters: temperature, composition, molten fraction, and oxygen to metal ratio. Since UO₂ and PuO₂ are the principal LWR fuels, they are the constituents considered. The correlations for fuel specific heat and enthalpy are valid for temperatures from 300 K to more than 4,000 K.

Equations for the specific heat and enthalpy of solid UO₂ and PuO₂ are assumed to have the same form, but with different constants. The basic equations are

$$FCP = \frac{K_1 \theta^2 e^{\left(\frac{\theta}{\overline{t}}\right)}}{T^2 \left[e^{\left(\frac{\theta}{\overline{t}}\right)} - 1\right]^2} + K_2 T + \frac{Y K_3 E_D}{2R T^2} e^{\left(\frac{-E_D}{RT}\right)}$$
(2-5)

and

FENTHL =
$$\frac{K_1 \theta}{e^{(\frac{\theta}{1})} - 1} + \frac{K_2 T^2}{2} + \frac{Y K_3 e^{\frac{-E_D}{RT}}}{2}$$
 (2-6)

where

and the constants are given in Table 2-1.

Table 2-1. Constants used in UO₂ and PuO₂ heat capacity and enthalpy correlations.

Constant	UO ₂	PuO ₂	Units
K ₁	296.7	347.4	J/kg•K

Table 2-1. Constants used in UO₂ and PuO₂ heat capacity and enthalpy correlations. (Continued)

Constant	UO_2	PuO_2	Units
K ₂	2.43 x 10 ⁻²	3.95 x 10 ⁻⁴	J/kg•K ²
K ₃	8.745×10^7	3.860×10^7	J/kg
θ	535.285	571.000	K
E_{D}	1.577 x 10 ⁵	1.967 x 10 ⁵	J/mol

The specific heat capacities of UO2 and PuO2 in the liquid state are given by

$$FCP = 503 \text{ J/kg} \bullet \text{K} . \tag{2-7}$$

For a mixture of UO₂ and PuO₂, the specific heat capacity of the solid is determined by combining the contribution from each constituent in proportion to its weight fraction. When the material is partially molten, the heat capacity is determined similarly with a weighted sum. The standard error of the UO₂ specific heat capacity correlation is ± 3 J/kg•K; and, for the mixed oxide specific heat capacity correlation, it is 6 to 10 J/kg•K, depending on the fraction of PuO₂. For nonstoichiometric fuels, these uncertainties are approximately doubled.

Inspection of Equations (2-5) and (2-6) shows that the fuel enthalpy correlation is simply the integral of fuel specific heat correlation from 0 K to T (K). Because the specific heat correlation is only valid above a fuel temperature of about 300 K, the fuel enthalpy correlation is not valid below a temperature of about 300 K. Therefore, it is necessary to calculate fuel enthalpy with respect to a reference temperature \geq 300 K. Thus, the fuel enthalpy at any desired temperature T, is calculated by evaluating Equation (2-6) at T and a reference temperature, T_{ref} , of 300 K and taking the difference [FENTHL (T) - FENTHL (T_{ref})]. For temperatures greater than 2 K below melting, the molten fraction and heat of fusion are used to interpolate between the enthalpy of unmelted fuel and just melted fuel at the melting temperature.

Section 2.2.2 is a review of the surveyed literature. The model development is presented in Section 2.2.3. Model predictions are compared with data in Section 2.2.4. An uncertainty analysis is given in Section 2.2.5.

2.2.2 Literature Review

An important source for fuel specific heat capacity data is the extensive review by Kerrisk and Clifton.^{2.2-1} Additional data from Kruger and Savage^{2.2-2} are used to find the parameters for PuO₂ in Equation (2-5). The heat capacity of liquid fuel is taken from Leibowitz.^{2.2-3} Literature relevant to the heat of fusion, which is used for the enthalpy model is discussed in Section 2.2.

2.2.2.1 Limitations of the Data Source. The data used by Kerrisk and Clifton cover a wide range of temperatures (483 to 3,107 K), but these data are restricted to nearly stoichiometric material

(oxygen to metal ratio between about 2.00 and 2.015). The data of Kruger and Savage are limited in that the highest reported temperature was only 1,400 K, which is well below the melting point of PuO₂, about 2,600 K. Their data are also restricted to approximately stoichiometric PuO₂. The oxygen-to-metal ratio has been shown to be significant by Gronvold^{2.2-4} and by Affortit and Marcon.^{2.2-5}

The specific heat capacity of liquid fuel taken from Leibowitz is applicable to UO_2 only. The assumption is made that the liquid UO_2 value is also valid for liquid PuO_2 . Although departures from stoichiometry were found to be significant for solid fuel, no experimental effort has been made to assess the importance of this parameter in the liquid state.

2.2.2.2 Other Data Sources. Several other data sources are used to estimate the uncertainty of the model but not in its development. These sources are cited in Section 2.2.5, where the uncertainty is analyzed.

2.2.3 Model Development

The most common technique of determining specific heat capacity is to measure the enthalpy of a sample by drop calorimetry and deduce the heat capacity by finding the rate of enthalpy change with temperature. Generally, the enthalpy data are fitted using an empirical function, often a simple polynomial equation. Whereas the accuracy of this approach is good, a function based on first principles is preferable because it allows the identification of the physical processes involved and can be extrapolated beyond its temperature base with some degree of confidence. This approach was used by Kerrisk and Clifton and is adopted here.

2.2.3.1 Specific Heat Capacity of a Typical Solid. The lattice specific heat capacity of solids at constant volume can be characterized theoretically quite well using the Debye model for specific heat. Except at low temperatures, a similar but simpler theory developed earlier by Einstein is also adequate. These theories are described in the most basic solid state textbooks, such as Kittel.^{2.2-6} The Einstein formulation is used here because of its simplicity. This formulation is

$$C_{v} = \frac{K_{1}\theta^{2}e^{\left(\frac{\theta}{\bar{T}}\right)}}{T^{2}\left[e^{\left(\frac{\theta}{\bar{T}}\right)} - 1\right]^{2}}$$
(2-8)

where

 C_v = specific heat capacity (J/kg•K)

 K_1 = constant to be determined (J/kg•K).

Equation (2-8) gives the specific heat capacity at constant volume. In most reactor situations, the specific heat capacity at constant pressure, C_p , is more appropriate. The relationship between the two is $^{2.2-7}$

$$C_{p} = C_{V} + \left(\alpha^{2} \frac{V}{\beta}\right) T \tag{2-9}$$

where

 α = coefficient of thermal expansion (K⁻¹)

 β = coefficient of compressibility (Pa⁻¹)

 $V = molar volume (m^3).$

The temperature dependence of α^2 (V/ β) in Equation (2-9) is complicated. The compressibility of a liquid or a solid is nearly constant with temperature, but the molar volume and the coefficient of thermal expansion change with temperature. However, expressing the quantity (C_p - C_v) as a function of a constant times temperature yields results well within the scatter of the data. Therefore, C_p is expressed as

$$C_p = C_v + K_2 T$$
 (2-10)

where C_v is given by Equation (2-8) and K_2 is a constant to be determined by comparison with data.

2.2.3.2 Defect Energy Contribution to the Specific Heat Capacity. At temperatures > 1,500 K, the specific heat capacity data show a rapid increase not described by Equation (2-10). This increase is generally attributed to the energy necessary to form Frenkel defects. $^{2.2-7,2.2-8,2.2-9}$ Some investigators $^{2.2-4,2.2-8}$ have suggested that Schottky defects may also contribute to this rapid increase. However, the assumption used in this model is that the rapid increase in specific heat capacity > 1,500 K is due to formation of Frenkel defects. The functional form of the extra term that should be added to Equation (2-10) may be found from the defect energy contribution to the enthalpy given by $^{2.2-6}$ and R and T were previously defined in Equation (2-5). To determine the defect contribution to the specific heat capacity, the derivative of H_D with respect to temperature, C_D is given by

$$H_D = K_3 e^{(-E_D \S RT)}$$
 (2-11)

where

 H_D = defect energy contribution to enthalpy (J)

 E_D = activation energy for Frenkel defects (J/mol)

 K_3 = constant to be determined (J)

and R and T were previously defined in Equation (2-5). To determine the defect contribution to the specific heat capacity, the derivative of H_D with respect to temperature, C_D is given by

$$C_{D} = \frac{K_{3}E_{D}}{RT^{2}}e^{\left(\frac{E_{D}}{RT}\right)}.$$
 (2-12)

Combining Equations (2-8), (2-10), and (2-12) gives the general expression for specific heat capacity

$$C_{p} = \frac{K_{1}\theta^{2}e^{\left(\frac{\theta}{T}\right)}}{T^{2}\left[e^{\left(\frac{\theta}{T}\right)} - 1\right]^{2}} + K_{2}T + \frac{K_{3}E_{D}}{RT^{2}}e^{\left(-\frac{E_{D}}{RT}\right)} . \tag{2-13}$$

2.2.3.3 Determination of the Constants in the Model. For UO_2 , the values of the five constants, K_1 , K_2 , K_3 , K_4 , and E_D , are taken from Kerrisk and Clifton. For PuO_2 , the constants are determined by fitting the data of Kruger and Savage. In both cases, the fuel was nearly stoichiometric. Data sources for pure PuO_2 are scarce. One potential source is the work of Affortit and Marcon. However, they give only correlations determined from fitting the data and not the actual data. Also, they do not present an uncertainty analysis. Without knowing the number or accuracy of the data on which their correlations are based, it is not possible to estimate what weight to give to their results. Therefore, their correlations were not used to determine the constants of Equation (2-13). However, their work was useful for the assessment of the effects of departure from stoichiometry.

It should be noted that the constants determined for Equation (2-13) are only valid at fuel temperatures > 300 K. Data < 300 K were not used to determine the constants of Table 2-1, and the Einstein formulation assumes temperatures above the Einstein temperature, θ .

2.2.3.4 Effect of Nonstoichiometry. Several investigators have found the oxygen-to-metal ratio of fuel to influence the specific heat capacity. ^{2.2-1}, ^{2.2-5}, ^{2.2-8}, ^{2.2-10} At temperatures > 1,300 K, departures from stoichiometry typical of those found in LWR fuel have caused changes in the specific heat capacity greater than the data scatter. The most complete analysis of this effect has been done by Affortit and Marcon. Even though their results are quantitatively different (see Figure 2-1 and Figure 2-2), made from their correlations) from sources used to develop this model, they illustrate well the qualitative aspects of this effect. Figure 2-1 is for UO₂, and Figure 2-2 is for mixed oxide fuels. These figures show that the

specific heat capacity increases as the oxygen-to-metal ratio becomes larger than 2.

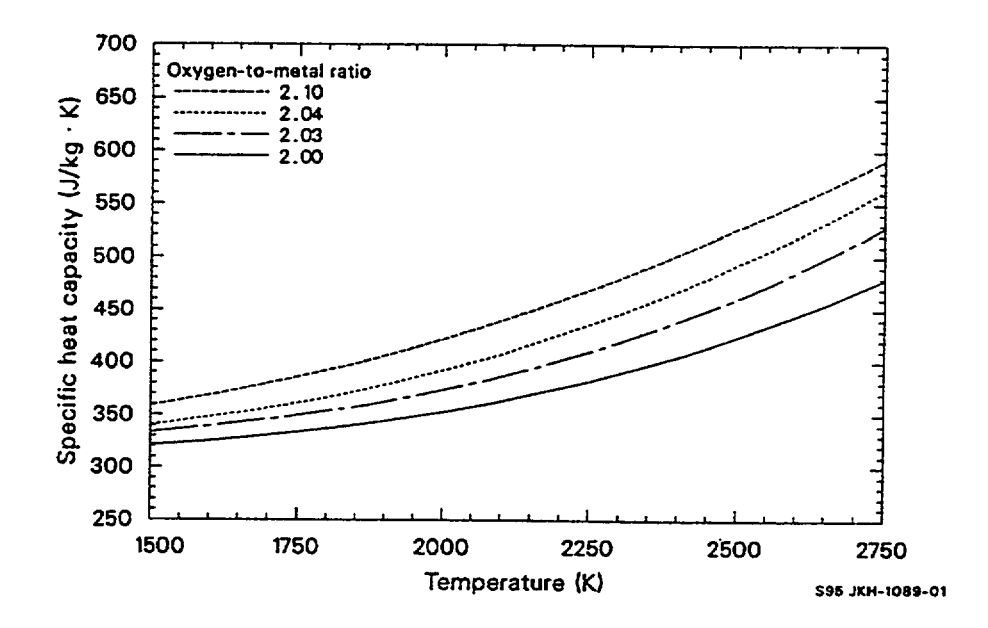


Figure 2-1. Specific heat capacity as a function of temperature and oxygen-to-metal ratio for UO₂.

Very hyperstoichiometric materials, such as U_4O_9 and U_3O_8 , have specific heat capacities considerably larger than that of UO_2 .^{2.2-4,2.2-11} In addition, these materials exhibit peaks in specific heat capacity at temperatures associated with phase transitions. However, the incidence of these states in LWR fuel is infrequent and their influence is neglected in this model.

In reactor fuel, nonstoichiometry is believed to be due to oxygen interstitials for hyperstoichiometric fuel and oxygen vacancies for hypostoichiometric fuel. 2.2-8 Excess oxygen tends to increase and an oxygen deficiency tends to decrease the probability of formation of Frenkel and Schottky defects, thereby changing the specific heat capacity. Thus, the logical adjustment to Equation (2-13) to account for the oxygen-to-metal ratio effect is in its last term, which includes the effect of defect formation. By multiplying the term by the oxygen-to-metal ratio divided by 2.0, the following desirable features are produced.

- 1. The correlation is unaffected for stoichiometric fuel.
- 2. The proper temperature dependence is obtained.
- 3. The specific heat capacity is increased for hyperstoichiometry and decreased for hypostoichiometry, in accordance with the data.

Therefore, this correction has been made to Equation (2-13), giving Equation (2-5). This is the model used for the specific heat capacity of solid UO_2 and PuO_2 .

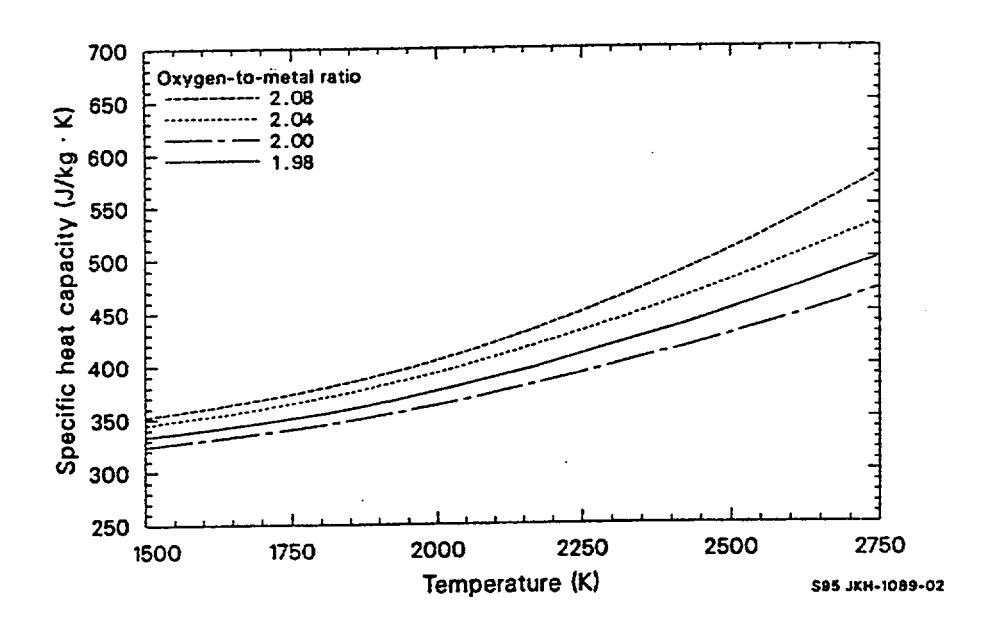


Figure 2-2. Specific heat capacity as a function of temperature and oxygen-to-metal ratio for $(U_{0.8}Pu_{0.2})O_{2+x}$.

If the fuel consists of a mixed oxide (MO₂) with a weight fraction of PuO₂ equal to FCOMP, then the specific heat capacity of the mixed oxide fuel is calculated by the expression

$$FCP_{MO_2} = FCP_{UO_2}(1 - FCOMP) + FCP_{PuO_2} \cdot FCOMP . (2-14)$$

If the fuel temperature is greater than the fuel melting temperature, FTMELT, plus the liquid solid coexistence temperature, then the fuel specific heat capacity is not calculated using Equation (2-5) but is set equal to the specific heat of liquid fuel, 503 J/kg•K, for both UO₂ and PuO₂ fuel. If the fuel temperature is equal to the fuel melting temperature, TMELT, then the specific heat capacity is calculated by the expression

$$FCP = (1.0 - R) FCP (T - TMELT) + R \bullet FCPMOL$$
(2-15)

where

R = fraction of fuel that is molten (unitless)

FCPMOL = specific heat capacity of liquid fuel (503 J/kg•K).

Fuel enthalpy, FENTHL, for solid fuel is found by integrating Equation (2-5) with respect to temperature over the interval 0 K to T K. The result of the integration is the expression

FENTHL =
$$\frac{K_1 \theta}{e^{\left(\frac{\theta}{T}\right)} - 1} + \frac{K_2 T^2}{2} + \frac{Y}{2} \left[K_3 e^{\left(-\frac{E_p}{RT}\right)} \right]$$
 (2-16)

Figure 2-3 shows the enthalpy of UO₂ versus temperature calculated using Equation (2-6).

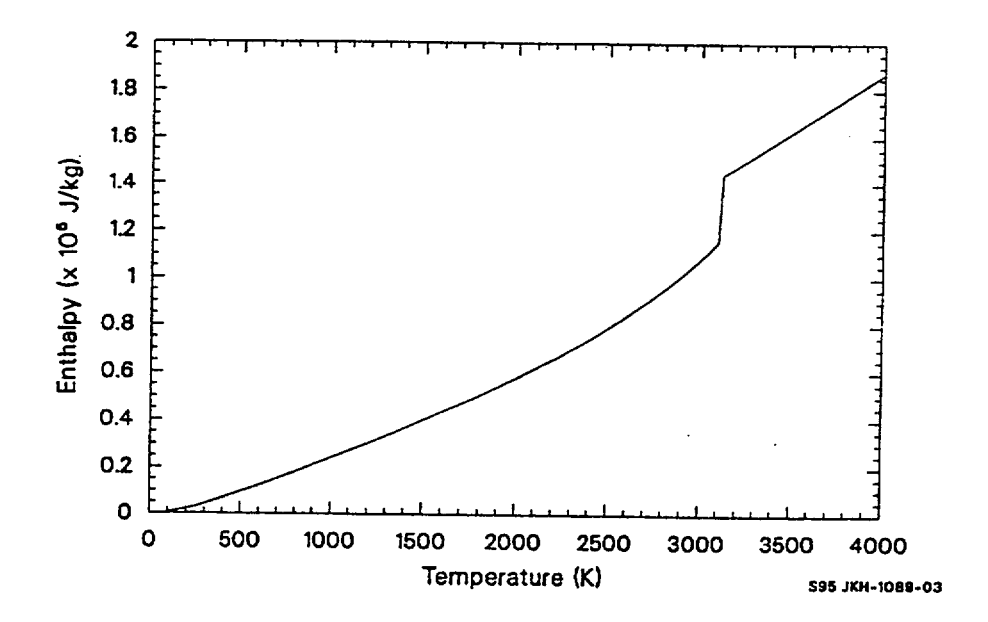


Figure 2-3. Enthalpy of UO_2 as a function of temperature to 4,000 K.

If the fuel consists of a mixed oxide with a weight fraction of PuO₂ equal to FCOMP, then the enthalpy of the mixed oxide fuel is calculated by the expression

$$FENTHL_{MO_2} = FENTHL_{UO_2}(1 - FCOMP) + FENTHL_{PuO_2} \cdot FCOMP . \qquad (2-17)$$

If the fuel temperature is equal to the fuel melting temperature, FTMELT, then the fuel enthalpy is calculated by the expression

$$FENTHL = FENTHL(FTMELT) + FHEFUS \cdot FACMOT$$
 (2-18)

where

FTMELT = melting temperature minus a vanishingly small increment (K)

FHEFUS = heat of fusion of the fuel (J/kg)

FACMOT = fraction of the fuel that is molten (unitless).

If the fuel temperature, FTEMPT, is greater than the fuel melting temperature, then the fuel enthalpy is calculated by the expression

where FCPMOL is the specific heat capacity of molten fuel (J/kg•K).

2.2.4 Model Comparisons with Data

Figure 2-4 shows the specific heat capacity correlation, FCP, for UO2 compared with data from three sources.^{2.2-4,2.2-12,2.2-13} These data were taken from experiments using stoichiometric UO₂. At the high end of the temperature interval (a few hundred K below the melting temperature), the data fall below the model calculations. (This is probably the result of partial melting due to a nonuniform temperature distribution within the sample.) For example, the measured specific heat capacity would be smaller because the specific heat capacity in a liquid is considerably lower than in a solid. A similar comparison is shown in Figure 2-5 for PuO2. In this instance, the correlation is compared with its own data base. This was necessary due to the lack of a broad data base for PuO2 fuel. A better test of the accuracy of the model is found by comparing its predictions with mixed oxide data, 2.2-5,2.2-10,2.2-14 as shown in Figure 2-6. None of the data shown in this figure were used in the development of the model. The agreement is relatively good except for the low values reported by Affortit and Marcon. Other experimenters^{2,2-3,2,2-10} have pointed out that the results of Affortit and Marcon are generally low when compared with their data and have excluded the Affortit and Marcon measurements from their data base. No one has proposed an adequate explanation for the discrepancy. On the other hand, at least one investigator^{2.2-9} has given considerable weight to the work done by Affortit and Marcon. In this document, the Affortit and Marcon results are used only in the analysis of the effect of departure from stoichiometry on the specific heat capacity.

2.2.5 Model Uncertainty

As would be expected, the accuracy of the FCP model when compared with its own data base is quite good. A better test was found by comparing the correlations with data not used during their development. The UO₂ and mixed oxide fuel correlations are analyzed separately in this section.

2.2.5.1 Uncertainty in UO_2 Model. Kerrisk and Clifton report an accuracy of \pm 3% for their correlation over the temperature range 300 to 3,000 K, with an approximately uniform distribution relative

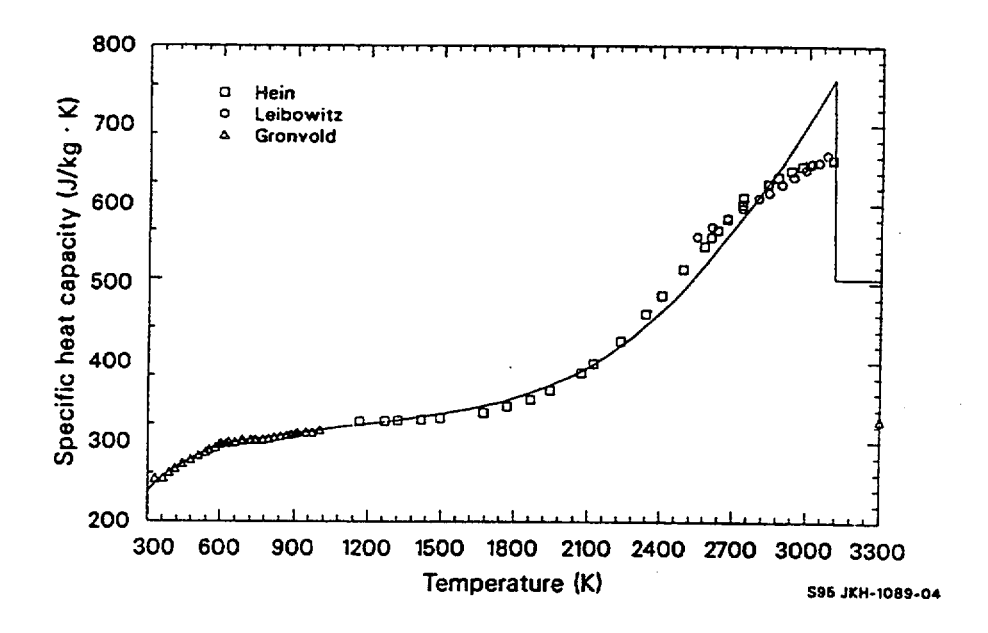


Figure 2-4. Specific heat capacity of UO₂ from three experimenters compared with the FCP correlation (solid line) for UO₂.

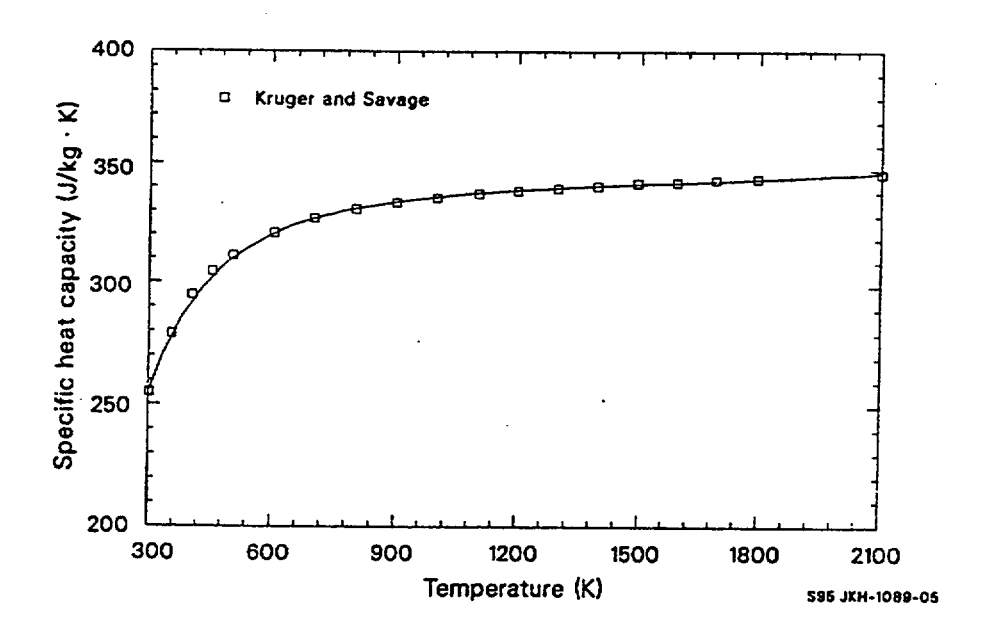


Figure 2-5. Specific heat capacity of PuO_2 from Kruger and Savage compared with the FCP correlation (solid line) for PuO_2 .

to temperature. When the calculations of the correlation are compared with the data of Gronvold for stoichiometric oxide, the agreement is even better, having a standard error of only 2.0 J/kg•K. This is a

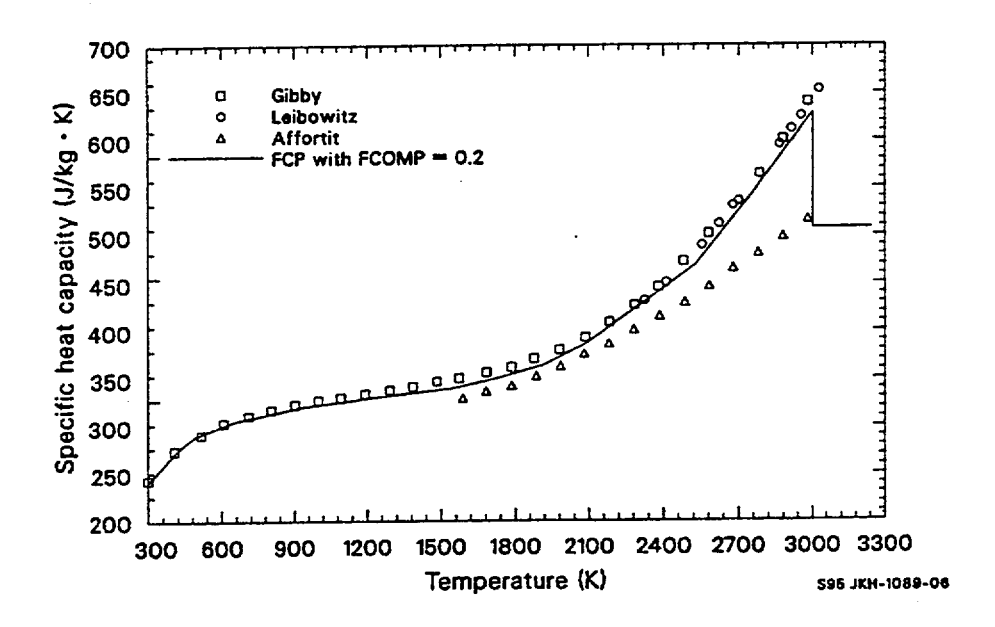


Figure 2-6. Specific heat capacity of $(U_{0.8} Pu_{0.2})O_2$ from three experimenters compared with the FCP correlation (solid line) for mixed oxides.

good test of the model, since these data were not used to develop the correlation. The paper by Affortit and Marcon gives correlations fit to their data. Arbitrarily taking 200 K intervals over their temperature range from 600 to 3,000 K and using their correlations, the standard error is 46 J/kg•K. Affortit and Marcon's predictions are smaller at all temperatures, and the residuals increase with temperature.

2.2.5.2 Uncertainty in the Mixed Oxide Model. Because of the limited number of data for PuO₂, the accuracy of the correlation for mixed oxide fuel was used as a test for this correlation. Data were taken from Leibowitz, ^{2.2-14} Gibby, ^{2.2-10} and Affortit and Marcon. ^{2.2-5} The model presented in this paper, using a weighted sum of the UO₂ and PuO₂ results, calculates specific heat capacities that are slightly larger than all but two of the 55 data points reported by Gibby and Leibowitz. At the highest and lowest applicable temperatures (3,000 and 300 K), the differences are negligible, < 1.0 J/kg•K. At intermediate temperatures, around 1,600 K, the residuals are approximately 10.0 J/kgK, falling off smoothly from this temperature. The standard error of the model relative to these three data sets is 5.6 J/kg•K. This is equivalent to a maximum percentage error of < 2.5%. Since these residuals are smaller than the scatter in the data, the model represents these data sets adequately. When the model is compared with that of Affortit and Marcon, again taking 200 K steps from 1,600 K to melting, the standard error is 46 J/kg•K. Affortit and Marcon always have the smaller value, and the residuals increase with increasing temperature, as with the UO₂ results. Because of the lack of actual data, the results of Affortit and Marcon are not included in

the standard error estimate.

2.2.6 References

- 2.2-1 J. F. Kerrisk and D. G. Clifton, "Smoothed Values of the Enthalpy and Heat Capacity of UO₂," Nuclear Technology, 16, December 1972, pp. 531-535.
- 2.2-2 O. L. Kruger and H. Savage, "Heat Capacity and Thermodynamic Properties of Plutonium Dioxide," *Journal of Chemical Physics*, 45, November 1968, pp. 4,540-4,544.
- 2.2-3 L. Leibowitz et al., "Enthalpy of Liquid Uranium Dioxide to 3,500 K," Journal of Nuclear Materials, 39, 1971, pp. 115-116.
- 2.2-4 F. Gronvold et al., "Thermodynamics of the UO_{2+x} Phase I. Heat Capacities of UO_{2.017} and UO_{2.254} from 300 to 1,000 K and Electronic Contributions," *Journal of Chemical Thermodynamics*, 2, 1970, pp. 665-679.
- 2.2-5 C. Affortit and J. Marcon, "Chaleur Specifique a Haute Temperature des Oxydes D'Uranium et de Plutonium," Revue Internationale des Hautes Temperatures et des Refractaires, 7, 1970, pp. 236-241.
- 2.2-6 C. Kittel, *Introduction to Solid State Physics*, 3rd Edition, New York: John Wiley and Sons, Inc., 1966.
- 2.2-7 D. R. Olander, Fundamental Aspects of Nuclear Reactor Fuel Elements, TID-26711-P1, 1976.
- 2.2-8 R. Szwarc, "The Defect Contribution to the Excess Enthalpy of Uranium Dioxide Calculation of the Frenkel Energy," *Journal of Chemistry and Physics of Solids*, 30, 1969, pp. 705-711.
- 2.2-9 E. A. Fscher, P. R. Kinsman, and R. W. Ohse, "Critical Assessment of Equations of State for UO₂," *Journal of Nuclear Materials*, 59, 1976, pp. 125-136.
- 2.2-10 R. L. Gibby et al., "Analytical Expressions for Enthalpy and Heat Capacity for Uranium-Plutonium Oxide," *Journal of Nuclear Materials*, 50, 1974, pp. 155-161.
- 2.2-11 H. Inaba, H. Shimizu, and K. Naito, "Lambda Type Heat Capacity Anomalies in U₃O₈," *Journal of Nuclear Materials*, 64, 1977, pp. 66-70.
- 2.2-12 R. A. Hein, L. H. Sjodahl, and R. Swarc, "Heat Content of Uranium Dioxide from 1,200 to 3,100 K," *Journal of Nuclear Materials*, 25, 1968, pp. 99-102.
- 2.2-13 L. Leibowitz, L. W. Mschler, and M. G. Chasanov, "Enthalpy of Solid Uranium Dioxide from 2,500 K to its Melting Point," *Journal of Nuclear Materials*, 29, 1969, pp. 356-358.

2.2-14 L. Leibowitz, D. F. Fischer, and M. G. Chasanov, "Enthalpy of Uranium Plutonium Oxides $(U_{0.8},Pu_{0.2})$ O_{1.07} from 2,350 to 3,000 K," *Journal of Nuclear Materials*, 42, 1972, pp. 113-116.

2.3 Thermal Conductivity (FTHCON)

In this section, a correlation is presented for the thermal conductivity of uncracked UO_2 and $(U, Pu)O_2$ fuels. This property and the closely associated models for the effect of fuel cracking on temperature distributions within the fuel are critical to accurate predictions of fuel rod behavior in both steady-state operation and off-normal transients because fuel rod behavior is strongly dependent on temperature.

2.3.1 Summary

The FTHCON subcode determines the fuel thermal conductivity and its derivative with respect to temperature as a function of temperature, density, oxygen to metal (O/M) ratio, and plutonium content of the fuel. Burnup is also required input but is used only to calculate the melt temperature.

The data base shows no significant effect of porosity at temperatures above about 1,600 K, probably because of the effects of radiation and gas conductivity, which increase pore conductivity at high temperatures. The thermal conductivity of liquid fuel was estimated from physical considerations because no data for the conductivity of molten fuel were found.

With the exception of minor modifications made to eliminate discontinuities in slope in the temperature range from 1,364 to 2,300 K, the expression used to model thermal conductivity of solid fuel is

$$k = \left[\frac{D}{1 + (6.5 - 0.00469T')(1 - D)}\right] \left[\frac{C_{V}}{(A + BT'')(1 + 3e_{th})}\right] + 5.2997 \times 10^{-3} Te^{\left[\frac{-13358}{T}\right]} \left\{1 + 0.169\left[\left(\frac{13358}{T}\right) + 2\right]^{2}\right\}$$
(2-20)

where

 $k = thermal conductivity (W/m \cdot K)$

D = fraction of theoretical density (unitless)

C_v = phonon contribution to the specific heat at constant volume (J/kg•K). The first term of the MATPRO correlation for fuel specific heat capacity is used for this factor^a

e_{th} = linear strain caused by thermal expansion when temperature is > 300 K (unitless). The MATPRO correlation for fuel thermal expansion is used for this factor

T =	fuel temperature (K)
-----	----------------------

T' = porosity correction for temperature < 1,364, T' = 6.50 - T* 4.69 * 10⁻³, for temperature > 1877, T" = -1. and for temperatures in the range 1,364 to 1,834 K, T is found by interpolation, as explained in Section 2.3.3

T" = fuel temperature if < 1,800 K. For temperatures > 2,300 K, T" is equal to 2,050 K; for temperatures in the range 1,800 to 2,300 K, T" is found by interpolation, as explained in Section 2.3.3

A = a factor proportional to the point defect contribution to the phonon mean free path (m•s/kg•K). The correlation used for this factor is 0.339 + 12.6 x absolute value (2.0 - O/M ratio)

B = a factor proportional to the phonon-phonon scattering contribution to the phonon mean free path (m•s/kg•K). The correlation used for this factor is 0.06867 x (1 + 0.6238 x plutonium content of fuel).

The first term of Equation (2-20) represents the phonon contribution to specific heat, and the second term represents the electronic (electron hole) contribution. The expression is valid only in the range 90 to 100% of theoretical density. When the fuel is molten, the first term is neglected.

The expected error of the thermal conductivity model has been estimated by computing the standard error of the model with respect to its data base. For stoichiometric UO_2 samples, the standard error was 0.2 (W/m•K); and for stoichiometric (U, Pu) O_2 with 2% Pu, the standard error was 0.3 (W/m•K). On the basis of these results, the following expression is used to calculate the expected standard error of the thermal conductivity of the solid fuel:

$$UK = [0.2(1 - COMP) + 0.7 COMP] \times (1.0 + |2 - OTM|10)$$
(2-21)

where

UK = expected standard error of solid fuel thermal conductivity (W/m⋅K)

COMP = PuO_2 content of the fuel (ratio of weight of PuO_2 to total weight)

OTM = O/M ratio of fuel (unitless).

$$C_{V} = \frac{296.7(535.285)^{2}}{T^{2} \left[e^{\left[\frac{535.285}{T}\right]} - 1\right]^{2}} \left[e^{\left[\frac{535.285}{T}\right]}\right] (1 - COMP) + \frac{COMP \cdot (347.4)(571)^{2}}{T^{2} \left[e^{\left[\frac{571}{T}\right]} - 1\right]^{2}} e^{\left[\frac{571}{T}\right]}$$

a. The analytical expression for $C_{\boldsymbol{v}}$ as a function of temperature, T, and plutonium content, COMP, is

The following subsection is a review of the general theories and data used to derive the model for thermal conductivity. Section 2.3.3 describes the development of the model, and Section 2.3.4 is a discussion of the uncertainty of the model.

2.3.2 Literature Review: Theory and Available Data

The mechanistic basis for a description of the thermal conductivity of solid unirradiated UO_2 and $(U, Pu)O_{2+x}$ is well documented.^{2.3-1} to ^{2.3-4} The thermal conductivity is the sum of contributions due to lattice vibrations, electron hole pairs, and radiant heat transfer. At temperatures below 1,500 K, the lattice component, k_p , [Equation (2-22)] is the most important contribution. At temperatures above 2,000 K, sufficient thermal energy exists to create significant numbers of electron hole pairs. These pairs contribute to the thermal conductivity ^{2.3-4} if the solid is not doped with donors or acceptors. The radiant heat transfer contribution to the thermal conductivity is small in polycrystalline fuel, ^{2.3-1} presumably because the material is transparent only at long wavelengths.

$$k_{p} = \rho C_{v} u \lambda / 3 \tag{2-22}$$

where

 k_p = lattice vibration (phonon) contribution to thermal conductivity (W/m•K)

 ρ = density of the solid (kg/m³)

 C_v = phonon contribution to the specific heat at constant volume (J/kg•K)

u = mean phonon speed (m/s)

 λ = phonon mean free path (m).

$$k_{e} = 2\left(\frac{k_{b}}{e}\right)^{2}T\left[\sigma + \frac{2\sigma_{e}\sigma_{h}}{\sigma}\left(\frac{E_{q}}{2k_{B}T} + 2\right)^{2}\right]$$
(2-23)

where

 k_e = electronic contribution to thermal conductivity (W/m•K)

 k_B = Boltzmann's constant, 1.38 x 10⁻²³ (J/K)

e = electron charge, 1.6×10^{-19} (coul)

 σ_e = electron contribution to electrical conductivity (1/ohm•m)

 σ_h = hole contribution to electrical conductivity (1/ohm•m)

 $\sigma = \sigma_e + \sigma_h [1/(ohm \cdot m)]$

 E_g = energy gap between conduction and valence bands (J)

T = temperature (K).

The application of Equation (2-23) is simplified by the existence of accurate measurements of the electrical conductivity of UO_2 . Bates, Hinman, and Kawada^{2.3-5} report electrical conductivities above 1,400 K to be given by

$$\sigma = 3.569 \times 10^7 e^{\left(\frac{E_g}{2k_BT}\right)} \tag{2-24}$$

where

 σ = electrical conductivity (1/ohm•m)

 E_g = energy gap between conduction and valence bands, 3.688 x 10^{-19} (J).

Equation (2-23) can be combined with Equation (2-24) to obtain

$$k_{e} = 2\left(\frac{k_{B}}{e}\right)^{2} (3.569 \times 10^{7} \text{T}) \left[e^{\left(\frac{E_{g}}{2k_{B}T}\right)} \right] \left[1 + \frac{2f}{(1+f)^{2}} \left(\frac{E_{g}}{2k_{B}T} + 2\right)^{2} \right]$$
(2-25)

where $f = \sigma_h / \sigma_e$ and the other symbols have been defined in conjunction with the two previous equations. Equation (2-25) contains only one undetermined parameter, the ratio of f.

Unfortunately, the application of Equation (2-22) for the lattice contribution to thermal conductivity is complex. C_v and ρ are available from the MATPRO routines for fuel specific heat and fuel thermal expansion and u is approximately the speed of sound in the lattice, but the phonon mean free path, λ , is not a directly measured quantity. For the purpose of applying Equation (2-22) to (U, Pu)O₂, it is sufficient to point out that the quantity $u\lambda/3$ in Equation (2-22) at temperatures in the range from 500 to 3,000 K is determined by two main contributions—the deflection or scattering of lattice vibrations from permanent defects in the regular lattice pattern and the scattering of lattice vibrations from each other. The first contribution is primarily a function of the O/M ratio and the impurity content of the fuel, and the second contribution is a function of temperature and the plutonium content of the fuel. When the two main

a. The interested reader will find detailed physical discussions in Reference 2.3-3 and Reference 2.3-4.

contributions to the phonon mean free path are incorporated in Equation (2-22), the appropriate expression for the lattice vibration contribution to the thermal conductivity of solid fuel is

$$k_{p} = \frac{\rho C_{V}}{A + BT} \tag{2-26}$$

where A is a function of the number of permanent defects in the lattice and B is a measure of the probability that lattice vibrations interfere with each other. The second term in the denominator is proportional to temperature because the density of lattice vibrations is proportional to temperature in the range of 500 to 3,000 K.

For porous materials, some modification of Equation (2-26) is required because the pores do not have the same conductivity as the lattice. This physical problem has been discussed extensively in the literature, 2.3-1,2.3-6 to 2.3-10 where the effect of porosity has been shown to be a function of the porosity fraction (volume of pores/total volume), the pore shape, the thermal conductivity of any gas trapped within the pores, and the emissivity of the lattice.

Unfortunately, the detailed mechanistic analysis presented in the literature cannot be applied to most of the published thermal conductivity data because the pore shape and the composition of the gas trapped within the pores are usually not reported. Most authors interested in obtaining usable expressions^{2,3-11 to}
^{2,3-14} have adopted some form of either the modified Loeb equation

$$\frac{\mathbf{k}}{\mathbf{k}_{100}} = 1 - \alpha \mathbf{P} \tag{2-27}$$

or the Maxwell-Eucken equation

$$\frac{k}{k_{100}} = \frac{1 - P}{1 + \beta P} \tag{2-28}$$

where

k = thermal conductivity of a porous sample (W/m•K)

 k_{100} = thermal conductivity of a sample with no pores (W/m•K)

P = volume of pores/total sample volume (unitless)

 α,β = factors depending on the shape and distribution of the pores (unitless).

These authors usually assume α or β to be linear functions of temperature and fit the linear functions to data from a limited set of samples.

None of the known previous studies of the effect of porosity on thermal conductivity has used the large collection of available experimental data. These data will be used in Section 2.3.3. The correlation will be based on the Maxwell-Eucken relation because from mechanistic studies both Marino^{2.3-6} and Ondracek^{2.3-10} recommend using this relation.

The remainder of this literature review discusses the available experimental measurements of thermal conductivity. Two general types of experiments will be encountered: the radial heat flow method and the transient heat pulse method. In the radial heat flow method, heat is supplied internally to a specimen and the thermal conductivity is deduced from measurements of the heat input and the steady-state temperature difference across the sample. In the transient heat pulse method, the measured quantity is the thermal diffusivity, 2.3-3

$$\alpha = \frac{k}{C_P \rho} \tag{2-29}$$

where

 α = thermal diffusivity (m²/s)

k = thermal conductivity (W/m•K)

 C_p = fuel specific heat at constant pressure (J/kg•K)

 ρ = fuel density (kg/m³).

The available UO₂ data are contained in Reference 2.3-11 through Reference 2.3-27. Several of these sources were not used in the present analysis: Hedge^{2.3-15} and Kingery^{2.3-16} used samples with densities between 70 and 75% theoretical density (TD) - far below those used in commercial fuel. Asamoto,^{2.3-14} Reiswig,^{2.3-23} Stora,^{2.3-24} and Hetzler^{2.3-17} employed radial heat flow methods in which the electrically heated center conductor may have been in contact with the oxide sample, so that Joule heating of the oxide could result and indicate anomalously high conductivity. The data of Hetzler and Asamoto also show unusually large scatter, probably because of cracking during the measurements. The data of Ferro^{2.3-25} show such large scatter that they were rejected for this reason alone. The temperature data of Lyons^{2.3-22} were derived from observation of post-irradiation grain growth and restructuring, a method considered less reliable than that used by other investigators. The data of Van Craeynest and Stora,^{2.3-11} and Lucks and Deem^{2.3-20} showed anomalously low conductivity compared to data from fuels with similar density. The low conductivity was probably caused by cracking before the reported data were taken.

Christensen's data^{2.3-21} are the most suspect of those used. The apparatus used in his radial heat flow experiment is not well described. Possibly the sharp increase in thermal conductivity at high temperature reported by Christensen is due to electrical contact with the heating element. Because of this possibility and because the specimen composition changed from UO_{2.01} to UO_{1.99} during the test, Christensen's data for temperatures above 1,800 K were not used. The data from Christensen that were used are listed in Table 2-2.

The data of Godfrey^{2.3-18} are the most reliable radial heat flow data reviewed in this section. Granular alumina insulation and careful positioning of the center heater were used to minimize electrical contact between the center heater and the sample. Runs which resulted in a change in the O/M ratio were reported as suspect and not used. Thermocouple errors were analyzed carefully, and runs at temperatures above 1,373 K were identified as not valid because of thermocouple problems.

Unfortunately, Godfrey used only samples of 93.4% TD. Also, the data were corrected to TD by dividing by the fraction of theoretical density. The unsatisfactory nature of this correction would no doubt have become evident if samples of varying density had been used. This correction was removed before the data were used to develop the model described here.

The data with the density correction removed are listed in Table 2-3. Several runs are represented, and there is no systematic variation from run to run. Data at temperatures below 500 K are not included in Table 2-3 because the low temperature data cannot be used with Equation (2-26). (The equation is valid only when temperatures are well above the Debye temperature.)

The remaining five sets of UO₂ data used were all obtained with the heat pulse method. Bates^{2.3-19} measured the thermal diffusivity of three samples, all with a density of 98.4% TD. Some data which correspond to runs taken when the samples had a metallic second phase at the grain boundaries were not used. Table 2-4 is a list of the values of thermal conductivity deduced from Bates' thermal diffusivity data, Equation (2-29), and the MATPRO expressions for fuel specific heat at constant pressure and for thermal expansion (see Section 2.2 and Section 2.5). Systematic variation does not occur in the data either from run to run or sample to sample.

Table 2-2. UO_2 data from Christensen. $^{2.3-21}$

Temperature (K)	Density (fraction of)	Thermal conductivity
.13120E+04	.9400E+00	.287000E+01
.13890E+04	.9400E+00	.287000E+01
.14320E+04	.9400E+00	.270000E+01
.14960E+04	.9400E+00	.272000E+01
.15520E+04	.9400E+00	.271000E+01
.15870E+04	.9400E+00	.256000E+01
.16120E+04	.9400E+00	.257000E+01

Table 2-2. UO_2 data from Christensen.^{2,3-21} (Continued)

Temperature (K)	Density (fraction of)	Thermal conductivity	
.16560E+04	.9400E+00	.280000E+01	
.17470 E+0 4	.9400E+00	.248000E+01	
.18380E+04	.9400E+00	.259000E+01	

Table 2-3. UO_2 data from Godfrey et al. $^{2.3-18}$

Temperature (K)	Density (fraction of theoretical)	Thermal conductivity [W/(m•K)]	Run number
.57400E+03	.9340E+00	.540400E+01	2
.67300E+03	.9340E+00	.475400E+01	2
.76700E+03	.9340E+00	.432200E+01	2
.87700E+03	.9340E+00	.390200E+01	2
.97600E+03	.9340E+00	.355900E+01	2
.10740E+04	.9340E+00	.326500E+01	2
.67500E+03	.9340E+00	.461000E+01	3
.87000E+03	.9340E+00	.379400E+01	3
.86900E+03	.9340E+00	.383200E+01	3
.97100E+03	.9340E+00	.348700E+01	3
.10720E+04	.9340E+00	.318200E+01	3
.11650E+04	.9340E+00	.298500E+01	3
.11730E+04	.9340E+00	.297500E+01	3
.12790E+04	.9340E+00	.277400E+01	3
.12820E+04	.9340E+00	.275500E+01	3
.57200E+03	.9340E+00	.518700E+01	4
.87000E+03	.9340E+00	.373700E+01	4
.87000E+03	.9340E+00	.369000E+01	4
.87200E+03	.9340E+00	.368100E+01	4
.11710E+04	.9340E+00	.288800E+01	4

Table 2-3. UO_2 data from Godfrey et al.^{2.3-18} (Continued)

Temperature (K)	Density (fraction of theoretical)	Thermal conductivity [W/(m•K)]	Run number
.11750E+04	.9340E+00	.287000E+01	4
.57000E+03	.9340E+00	.514000E+01	5
.57200E+03	.9340E+00	.511100E+01	5
.67300E+03	.9340E+00	.458900E+01	5
.67300E+03	.9340E+00	.455700E+01	5
.77400E+03	.9340E+00	.407700E+01	5
.77400E+03	.9340E+00	.409600E+01	5
.87500E+03	.9340E+00	.371100E+01	5
.87500E+03	.9340E+00	.373400E+01	5
.97300E+03	.9340E+00	.341600E+01	5
.97300E+03	.9340E+00	.341700E+01	5
.10710E+04	.9340E+00	.316900E+01	5
.10710E+04	.9340E+00	.316400E+01	5
.11730E+04	.9340E+00	.295000E+01	5
.12710E+04	.9340E+00	.275100E+01	5
.13230E+04	.9340E+00	.268200E+01	5
.57600E+03	.9340E+00	.523200E+01	6
.57600E+03	.9340E+00	.522900E+01	6
.67100E+03	.9340E+00	.469100E+01	6
.67100E+03	.9340E+00	.469100E+01	6
.67100E+03	.9340E+00	.470500E+01	6
.87400E+03	.9340E+00	.382100E+01	6

Table 2-4. UO_2 data from Bates (Reference 2.3-19) thermal diffusivity measurements.

Temperature (K)	Density (fraction of theoretical)	Thermal conductivity [W/(m•K)]	Sample	Cycle number
.53900E+03	.9840E+00	.650000E+01	RR1	3
.53900E+03	.9840E+00	.657000E+01	RR1	3
.75600E+03	.9840E+00	.482000E+01	RR1	3
.76100E+03	.9840E+00	.502000E+01	RR1	3
.89500E+03	.9840E+00	.411000E+01	RR1	3
.89100E+03	.9840E+00	.435000E+01	RR1	3
.99400E+03	.9840E+00	.383000E+01	RR1	3
.99500E+03	.9840E+00	.391000E+01	RR1	3
.11800E+04	.9840E+00	.328000E+01	RR1	3
.11850E+04	.9840E+00	.313000E+01	RR1	3
.13250E+04	.9840E+00	.285000E+01	RR1	3
.13250E+04	.9840E+00	.289000E+01	RR1	3
.14890E+04	.9840E+00	.251000E+01	RR1	3
.14910E+04	.9840E+00	.255000E+01	RR1	3
.16660E+04	.9840E+00	.240000E+01	RR1	3
.16550E+04	.9840E+00	.237000e+01	RR1	3
.17780E+04	.9840E+00	.224000E+01	RR1	3
.17800E+04	.9840E+00	.213000E+01	RR1	3
.18630E+04	.9840E+00	.219000E+01	RR1	3
.18660E+04	.9840E+00	.219000E+01	RR1	3
.19770E+04	.9840E+00	.210000E+01	RR1	3
.19720E+04	.9840E+00	.224000E+01	RR1	3
.20930E+04	.9840E+00	.232000E+01	RR1	3
.21020E+04	.9840E+00	.225000E+01	RR1	3
.21740E+04	.9840E+00	.226000E+01	RR1	3
.21870E+04	.9840E+00	.225000E+01	RR1	3

Table 2-4. UO_2 data from Bates (Reference 2.3-19) thermal diffusivity measurements. (Continued)

Temperature (K)	Density (fraction of theoretical)	Thermal conductivity [W/(m•K)]	Sample	Cycle number
.23730E+04	.9840E+00	.249000E+01	RR1	3
.23730E+04	.9840E+00	.264000E+01	RR1	3
.22800E+04	.9840E+00	.229000E+01	RR1	3
.22850E+04	.9840E+00	.242000E+01	RR1	3
.15990E+04	.9840E+00	.237000E+01	RR1	3
.16010E+04	.9840E+00	.249000E+01	RR1	3
.16090E+04	.9840E+00	.232000E+01	RR1	3
.13600E+04	.9840E+00	.283000E+01	RR1	4
.14530E+04	.9840E+00	.242000E+01	RR1	4
.15620E+04	.9840E+00	.248000E+01	RR1	4
.16490E+04	.9840E+00	.237000E+01	RR1	4
.17500E+04	.9840E+00	.239000E+01	RR1	4
.19070E+04	.9840E+00	.213000E+01	RR1	4
.20050E+04	.9840E+00	.210000E+01	RR1	4
.20070E+04	.9840E+00	.231000E+01	RR1	4
.21090E+04	.9840E+00	.219000E+01	RR1	4
.21040E+04	.9840E+00	.227000E+01	RR1	4
.21950E+04	.9840E+00	.235000E+01	RR1	4
.22950E+04	.9840E+00	.247000E+01	RR1	4
.23840E+04	.9840E+00	.242000E+01	RR1	4
.57100E+03	.9840E+00	.572000E+01	RR2	2
.57700E+03	.9840E+00	.603000E+01		
.57700E+03	.9840E+00	.616000E+01		
.66100E+03	.9840E+00	.533000E+01		
.68200E+03	.9840E+00	.541000E+01		
.78600E+03	.9840E+00	.448000E+01		
.78400E+03	.9840E+00	.445000E+01		

Table 2-4. UO_2 data from Bates (Reference 2.3-19) thermal diffusivity measurements. (Continued)

Temperature (K)	Density (fraction of theoretical)	Thermal conductivity [W/(m•K)]	Sample	Cycle number
.78500E+03	.9840E+00	.454000E+01		
.86600E+03	.9840E+00	.415000E+01		
.86700E+03	.9840E+00	.415000E+01		
.96100E+03	.9840E+00	.373000E+01		
.96100E+03	.9840E+00	.363000E+01		
.96100E+03	.9840E+00	.396000E+01		
.10690E+04	.9840E+00	.335000E+01		
.10710E+04	.9840E+00	.331000E+01		
.10690E+04	.9840E+00	.351000E+01		
.11710E+04	.9840E+00	.304000E+01		
.11740E+04	.9840E+00	.307000E+01		
.11730E+04	.9840E+00	.324000E+01		
.12700E+04	.9840E+00	.280000E+01		
.12690E+04	.9840E+00	.287000E+01		
.12700E+04	.9840E+00	.281000E+01		
.13610E+04	.9840E+00	.255000E+01		
.13610E+04	.9840E+00	.263000E+01		
.13610E+04	.9840E+00	.259000E+01		
.13610E+04	.9840E+00	.263000E+01		
.14710E+04	.9840E+00	.254000E+01		
.14720E+04	.9840E+00	.267000E+01		
.14690E+04	.9840E+00	.226000E+01		
.15690E+04	.9840E+00	.240000E+01		
.15710E+04	.9840E+00	.241000E+01		
.15690E+04	.9840E+00	.246000E+01		
.16830E+04	.9840E+00	.233000E+01		
.16830E+04	.9840E+00	.237000E+01		

Table 2-4. UO₂ data from Bates (Reference 2.3-19) thermal diffusivity measurements. (Continued)

Temperature (K)	Density (fraction of theoretical)	Thermal conductivity [W/(m•K)]	Sample	Cycle number
.17580E+04	.9840E+00	.230000E+01		
.17560E+04	.9840E+00	.219000E+01		
.17600E+04	.9840E+00	.228000E+01		
.67300E+03	.9840E+00	.553000E+01	RR3	3
.12830E+04	.9840E+00	.275000E+01		
.67300E+03	.9840E+00	.542000E+01		
.11000E+04	.9840E+00	.360000E+01	RR3	1
.10890E+04	.9840E+00	.340000E+01		
.10900E+04	.9840E+00	.354000E+01		
.10990E+04	.9840E+00	.341000E+01		
.81300E+03	.9840E+00	.486000E+01		
.79700E+03	.9840E+00	.480000E+01		
.50700E+03	.9840E+00	.646000E+01	RR3	2
.58300E+03	.9840E+00	.640000E+01		
.67600E+03	.9840E+00	.542000E+01		
.67900E+03	.9840E+00	.551000E+01		
.76300E+03	.9840E+00	.501000E+01		
.76400E+03	.9840E+00	.513000E+01		
.87300E+03	.9840E+00	.450000E+01		
.87600E+03	.9840E+00	.429000E+01		
.97900E+03	.9840E+00	.395000E+01		
.98100E+03	.9840E+00	.396000E+01		
.10650E+04	.9840E+00	.374000E+01		
.10720E+04	.9840E+00	.369000E+01		
.11880E+04	.9840E+00	.317000E+01		
.11870E+04	.9840E+00	.336000E+01		
.12770E+04	.9840E+00	.309000E+01		

Table 2-4. UO_2 data from Bates (Reference 2.3-19) thermal diffusivity measurements. (Continued)

			== ===================================	aromemo. (Commuca)	
•	Temperature (K)	Density (fraction of theoretical)	Thermal conductivity [W/(m•K)]	Sample	Cycle number
	.12850E+04	.9840E+00	.319000E+01		
	.12840E+04	.9840E+00	.328000E+01		
	.10710E+04	.9840E+00	.370000E+01		
	.88000E+03	.9840E+00	.457000E+01		
	.87900E+03	.9840E+00	.452000E+01		
	.87900E+03	.9840E+00	.452000E+01		
	.67800E+03	.9840E+00	.534000E+01		
	.57300E+03	.9840E+00	.618000E+01	RR3	3
	.58300E+03	.9840E+00	.589000E+01		
	.68000E+03	.9840E+00	.536000E+01		
	.68100E+03	.9840E+00	.524000E+01		
	.67800E+03	.9840E+00	.533000E+01		
	.77600E+03	.9840E+00	.488000E+01		
	.77500E+03	.9840E+00	.496000E+01		
	.89100E+03	.9840E+00	.417000E+01		
	.89500E+03	.9840E+00	.430000E+01		
	.96800E+03	.9840E+00	.388000E+01		
	.97300E+03	.9840E+00	.396000E+01		
	.10870E+04	.9840E+00	.345000E+01		
	.10810E+04	.9840E+00	.348000E+01		
	.11720E+04	.9840E+00	.328000E+01		
	.11730E+04	.9840E+00	.316000E+01		
	.12920E+04	.9840E+00	.285000E+01		
	.12910E+04	.9840E+00	.281000E+01		
	.13770E+04	.9840E+00	.265000E+01		
	.13800E+04	.9840E+00	.263000E+01		
	.14730E+04	.9840E+00	.254000E+01		

Table 2-4. UO₂ data from Bates (Reference 2.3-19) thermal diffusivity measurements. (Continued)

Temperature (K)	Density (fraction of theoretical)	Thermal conductivity [W/(m•K)]	Sample	Cycle number
.14770E+04	.9840E+00	.259000E+01	RR3	3
.15780E+04	.9840E+00	.230000E+01		
.15840E+04	.9840E+00	.245000E+01		
.16730E+04	.9840E+00	.223000E+01		
.16790E+04	.9840E+00	.220000E+01		
.17690E+04	.9840E+00	.209000E+01		
.17920E+04	.9840E+00	.224000E+01		
.17860E+04	.9840E+00	.219000E+01		
.15950E+04	.9840E+00	.206000E+01		
.15960E+04	.9840E+00	.241000E+01		
.14000E+04	.9840E+00	.261000E+01		
.13990E+04	.9840E+00	.256000E+01		
.11660e+04	.9840E+00	.329000E+01		
.10790E+04	.9840E+00	.344000E+01		
.10850E+04	.9840E+00	.350000E+01		
.84700E+03	.9840E+00	.443000E+01		
.84700E+03	.9840E+00	.445000E+01		
.57700E+03	.9840E+00	.598000E+01		
.55300E+03	.9840E+00	.622000E+01		

Gibby $^{2.3-27}$ reported the thermal diffusivity of a UO₂ sample as part of a study on the effect of plutonium additions. The sample had a density of 95.8% TD. The thermal conductivity data calculated from Gibby's diffusivities are shown in Table 2-5.

Weilbacher^{2.3-26} reported the thermal diffusivity of a UO₂ sample as part of a study of the effect thorium additions. The sample had a density of 98.0% TD. These data are important because they include temperatures up to melting and because the low temperature part of the data falls within the narrow scatter of the data reported by Bates for his samples of similar density. The close agreement of the Bates and Weilbacher data provide support for the idea that the thermal diffusivity data on uncracked samples are consistent. The thermal conductivity data calculated from Weilbacher's thermal diffusivity data using the same MATPRO expressions used with Bates' data are listed in Table 2-6.

The data of Goldsmith and Douglas^{2.3-12} provide more support for the idea that thermal diffusivity data on uncracked samples are consistent. When the MATPRO expressions for specific heat and thermal expansion are employed to convert the thermal diffusivity data of Goldsmith and Douglas to thermal conductivity, the resultant thermal conductivities fall within the scatter of the data of several authors who performed extensive measurements on a limited number of samples. The thermal conductivities obtained from Goldsmith and Douglas' data are presented in Table 2-7 The thermal conductivity data from 98.2 and 97.7% TD samples agree with the data of Bates and Weilbacher, the 95.1 and 95.8% dense sample data agree with the data of Gibby, the 95.2 and 94.7% dense sample data agree with the data of Hobson^{2.3-13} (which will be discussed in the next paragraph), and the 93.2 and 93.0% dense sample data agree with the data of Godfrey.^a

Table 2-5. UO₂ data, Gibby's^{2.3-27} thermal diffusivity measurements.

Temperature (K)	Density (fraction of theoretical)	Thermal conductivity [W/(m•K)]
.57500E+03	.9580E+00	.624000E+01
.57800E+03	.9580E+00	.636000E+01
.58600E+03	.9580E+00	.628000E+01
.58700E+03	.9580E+00	.587000E+01
.58800E+03	.9580E+00	.563000E+01
.66500E+03	.9580E+00	.512000E+01
.67500E+03	.9580E+00	.520000E+01
.67900E+03	.9580E+00	.531000E+01
.69000E+03	.9580E+00	.512000E+01
.84600E+03	.9580E+00	.430000E+01
.84600E+03	.9580E+00	.440000E+01
.85200E+03	.9580E+00	.453000E+01
.85300E+03	.9580E+00	.465000E+01
.86500E+03	.9580E+00	.430000E+01
.86500E+03	.9580E+00	.440000E+01
.89300E+03	.9580E+00	.429000E+01

a. The thermal conductivities determined from each author's data will be compared with each other and the MATPRO model in a series of figures presented in Section 2.3.4.

Table 2-5. UO_2 data, Gibby's^{2.3-27} thermal diffusivity measurements. (Continued)

Temperature (K)	Density (fraction of theoretical)	Thermal conductivity [W/(m•K)]
.90800E+03	.9580E+00	.429000E+01
.90700E+03	.9580E+00	.420000E+01
.96400E+03	.9580E+00	.384000E+01
.96400E+03	.9580E+00	.392000E+01
.96900E+03	.9580E+00	.402000E+01
.96900E+03	.9580E+00	.412000E+01
.10000E+04	.9580E+00	.370000E+01
.10310E+04	.9580E+00	.394000E+01
.10310E+04	.9580E+00	.384000E+01
.10710E+04	.9580E+00	.366000E+01
.10800E+04	.9580E+00	.347000E+01
.10800E+04	.9580E+00	.355000E+01
.12040E+04	.9580E+00	.324000E+01
.12040E+04	.9580E+00	.334000E+01
.12800E+04	.9580E+00	.313000E+01
.12880E+04	.9580E+00	.299000E+01
.12880E+04	.9580E+00	.292000E+01
.12890E+04	.9580E+00	.299000E+01
.13230E+04	.9580E+00	.301000E+01
.13350E+04	.9580E+00	.290000E+01
.13840E+04	.9580E+00	.292000E+01
.13900E+04	.9580E+00	.280000E+01
.13950E+04	.9580E+00	.270000E+01
.13990E+04	.9580E+00	.280000E+01
.14120E+04	.9580E+00	.295000E+01
.14910E+04	.9580E+00	.278000E+01
.15020E+04	.9580E+00	.244000E+01

Table 2-5. UO₂ data, Gibby's^{2,3-27} thermal diffusivity measurements. (Continued)

Temperature (K)	Density (fraction of theoretical)	Thermal conductivity [W/(m-K)]
.15080E+04	.9580E+00	.262000E+01
.15100E+04	.9580E+00	.266000E+01

Table 2-6. UO₂ data from Weilbacher's ^{2.3-26} thermal diffusivity measurements.

Temperature (K)	Density (fraction of theoretical)	Thermal conductivity [W/(m-K)]
.97400E+03	.9800E+00	.358000E+01
.97400E+03	.9800E+00	.381000E+01
.11710E+04	.9800E+00	.309000E+01
.11710E+04	.9800E+00	.325000E+01
.13770E+04	.9800E+00	.262000E+01
.13760E+04	.9800E+00	.285000E+01
.15750E+04	.9800E+00	.231000E+01
.15750E+04	.9800E+00	.251000E+01
.17780E+04	.9800E+00	.218000E+01
.17760E+04	.9800E+00	.239000E+01
.29790E+04	.9800E+00	.219000E+01
.19800E+04	.9800E+00	.233000E+01
.21800E+04	.9800E+00	.226000E+01
.21820E+04	.9800E+00	.239000E+01
.22810E+04	.9800E+00	.231000E+01
.22840E+04	.9800E+00	.245000E+01
.23790E+04	.9800E+00	.245000E+01
.23790E+04	.9800E+00	.254000E+01
.24840E+04	.9800E+00	.261000E+01
.24830E+04	.9800E+00	.273000E+01

Table 2-6. UO_2 data from Weilbacher's $^{2.3-26}$ thermal diffusivity measurements. (Continued)

Temperature (K)	Density (fraction of theoretical)	Thermal conductivity [W/(m-K)]
.25770E+04	.9800E+00	.274000E+01
.25770E+04	.9800E+00	.286000E+01
.26740E+04	.9800E+00	.291000E+01
.26740E+04	.9800E+00	.302000E+01
.27730E+04	.9800E+00	.310000E+01
.27730E+04	.9800E+00	.321000E+01
.28750E+04	.9800E+00	.332000E+01
.28750E+04	.9800E+00	.344000E+01
.30250E+04	.9800E+00	.366000E+01
.30270E+04	.9800E+00	.383000E+01

Table 2-7. UO₂ data from Goldsmith and Douglas'^{2,3-12} thermal diffusivity measurements.

Temperature (K)	Density (fraction of theoretical)	Thermal conductivity [W/m•K]
.67000E+03	.960E+00	.557000E+01
.67000E+03	.9860E+00	.553000E+01
.67000E+03	.9860E+00	.559000E+01
.67000E+03	.9820E+00	.531000E+01
.67000E+03	.9770E+00	.543000E+01
.67000E+03	.9610E+00	.519000E+01
.67000E+03	.9580E+00	.498000E+01
.67000E+03	.9520E+00	.485000E+01
.67000E+03	.9470E+00	.508000E+01
.67000E+03	.9320E+00	.455000E+01
.67000E+03	.9300E+00	.461000E+01
.67000E+03	.9060E+00	.440000E+01
.67000E+03	.9040E+00	.420000E+01

Table 2-7. UO₂ data from Goldsmith and Douglas' 2.3-12 thermal diffusivity measurements. (Continued)

Temperature (K)	Density (fraction of theoretical)	Thermal conductivity [W/m•K]
.87000E+03	.9860E+00	.468000E+01
.87000E+03	.9860E+00	.467000E+01
.87000E+03	.9860E+00	.470000E+01
.87000E+03	.9820E+00	.444000E+01
.87000E+03	.9770E+00	.460000E+01
.87000E+03	.9610E+00	.438000E+01
.87000E+03	.9580E+00	.410000E+01
.87000E+03	.9520E+00	.416000E+01
.87000E+03	.9470E+00	.426000E+01
.87000E+03	.9320E+00	.380000E+01
.87000E+03	.9300E+00	.388000E+01
.87000E+03	.9060E+00	.369000E+01
.87000E+03	.9040E+00	.349000E+01
.10700E+04	.9860E+00	.396000E+01
.10700E+04	.9860E+00	.394000E+01
.10700E+04	.9860E+00	.394000E+01
.10700E+04	.9820E+00	.375000E+01
.10700E+04	.9770E+00	.387000E+01
.10700E+04	.9610E+00	.370000E+01
.10700E+04	.9580E+00	.356000E+01
.10700E+04	.9520E+00	.346000E+01
.10700E+04	.9470E+00	.361000E+01
.10700E+04	.9320E+00	.324000E+01
.10700E+04	.9300E+00	.330000E+01
.10700E+04	.9060E+00	.310000E+01
.10700E+04	.9040E+00	.291000E+01
.12700E+04	.9860E+00	.327000E+01

Table 2-7. UO₂ data from Goldsmith and Douglas'^{2.3-12} thermal diffusivity measurements. (Continued)

Temperature (K)	Density (fraction of theoretical)	Thermal conductivity [W/m•K]
.12700E+04	.9860E+00	.326000E+01
.12700E+04	.9860E+00	.332000E+01
.12700E+04	.9820E+00	.316000E+01
.12700E+04	.9770E+00	.323000E+01
.12700E+04	.9610E+00	.312000E+01
.12700E+04	.9580E+00	.301000E+01
.12700E+04	.9520E+00	.295000E+01
.12700E+04	.9470E+00	.301000E+01
.12700E+04	.9320E+00	.266000E+01
.12700E+04	.9300E+00	.275000E+01
.12700E+04	.9060E+00	.259000E+01
.12700E+04	.9040E+00	.246000E+01

The final set of UO_2 data to be discussed are those of Hobson et al.^{2.3-13} These authors have apparently measured the thermal diffusivity of a series of UO_2 samples. However, they reported only data from a single sample with a density of $10.40 \times 10^3 \text{ kg/m}^3$ (94.9% TD). Their thermal diffusivity data were converted to thermal conductivity and are listed in Table 2-8.

The data appropriate for modeling the thermal conductivity of mixed (U, Pu) $O_{2\pm x}$ include the (U, Pu) O_2 measurements that are available, 2.3-11,2.3-17,2.3-27 to 2.3-34 and $UO_{2\pm x}$ data with $x \neq 0.2.3-12,2.3-13,2.3-17$. The $UO_{2\pm x}$ data are important because the effect of nonstoichiometry in mixed oxide fuels is at least as important as the effect of variations in the weight fraction PuO_2 . Unfortunately, the resources available to produce the present model were too limited to allow for a careful review of the (U, Pu) $O_{2\pm x}$ or the $UO_{2\pm x}$ data. For that reason, the stoichiometric data from Reference 2.3-27 to Reference 2.3-30 and the model proposed by Olander 2.3-1 for the effect of O/M ratio variations will be adopted without modification.

Kim et al $^{2.3-35}$ provided the data which allow a calculation of the thermal conductivity of liquid fuel (UO₂ or UO₂-PuO₂ mixtures). They measured the thermal diffusivity of 0.813 and 1.219 mm layers of molten UO₂ in the temperature range of 3,187 through 3,315 K. The diffusivity values obtained of 1.90 x $^{10-6}$ to 3.23 x $^{10-6}$ m²/s can be used with specific heat and density measurements to calculate the thermal conductivity of liquid fuel.

2.3.3 Model Development

The development of the model for thermal conductivity of $(U, Pu)O_{2\pm x}$ was based directly on the theory and data which have just been reviewed. The first step in producing the model was the determination of an expression for the effect of density. The UO_2 data were grouped by density, with second degree polynomials in temperature fit to the data in each group. Inspection of the data regular pattern of decreasing thermal conductivity with decreasing density at low temperature but almost no density effect at high temperature. For this reason, the polynomials representing the thermal conductivity of the various groups were evaluated at 600 and 1,000 K and the average thermal conductivities obtained were used with Equation (2-28) to obtain linear functions of the form

$$\beta = \beta_0 + \beta_1 T \tag{2-30}$$

corresponding to pairs of porosity groups. The resultant values of β_0 and β_1 are listed in Table 2-9.

Table 2-8. UO₂ data from Hobson's^{2.3-13} thermal diffusivity measurements.

_	Temperature (K)	Density (fruition of theoretical)	Thermal conductivity [W/m-K]
	.54700E+03	.9490E+00	.576000E+01
	.60700E+03	.9490E+00	.541000E+01
	.64200E+03	.9490E+00	.533000E+01
	.73200E+03	.9490E+00	.496000E+01
	.78800E+03	.9490E+00	.463000E+01
	.83400E+03	.9490E+00	.445000E+01
	.88500E+03	.9490E+00	.426000E+01
	.94400E+03	.9490E+00	.413000E+01
	.99500E+03	.9490E+00	.401000E+01
	.10460E+04	.9490E+00	.386000E+01
	.10830E+04	.9490E+00	.375000E+01
	.11330E+04	.9490E+00	.362000E+01
	.11500E+04	.9490E+00	.351000E+01
	.11750E+04	.9490E+00	.353000E+01
	.12790E+04	.9490E+00	.323000E+01

a. The data and model predictions are illustrated in Section 2.3.4

Table 2-8. UO_2 data from Hobson's $^{2.3-13}$ thermal diffusivity measurements. (Continued)

Temperature (K)	Density (fruition of theoretical)	Thermal conductivity [W/m•K]
.13300E+04	.9490E+00	.315000E+01
.13920E+04	.9490E+00	.304000E+01
.14490E+04	.9490E+00	.297000E+01
.15000E+04	.9490E+00	.281000E+01
.15320E+04	.9490E+00	.284000E+01
.16210E+04	.9490E+00	.263000E+01
.16380E+04	.9490E+00	.269000E+01
.17490E+04	.9490E+00	.252000E+01
.17600E+04	.9490E+00	.258000E+01
.18070E+04	.9490E+00	.246000E+01
.18710E+04	.9490E+00	.260000E+01
.19130E+04	.9490E+00	.248000E+01
.19930E+04	.9490E+00	.245000E+01
.20160E+04	.9490E+00	.252000E+01
.20590E+04	.9490E+00	.247000E+01
.21540E+04	.9490E+00	.243000e+01
.21540E+04	.9490E+00	.249000E+01
.22430E+04	.9490E+00	.247000E+01
.23360E+04	.9490E+00	.251000E+01
.24120E+04	.9490E+00	.263000E+01
.25030E+04	.9490E+00	.266000E+01

The scatter in the values of β_0 and β_1 is caused by unknown variations of pore shape and content, as discussed in Section 2.3.2. In subsequent model development steps, all three sets of β_0 and β_1 , as well as their average values, were tested to determine which produced the model with the smallest standard error. Since very little difference was found, the average values of β_0 and β_1 were adopted.

The second step in the development of the model was the determination of the constants A and B of Equation (2-26). This determination was done with a least-squares-fit technique and the UO₂ thermal

conductivity data for temperatures between 500 and 1,000 K.^a The data were normalized to 100% TD with Equation (2-28) before the fit was carried out.

The third step in developing the UO_2 model was the determination of a value for the constant f in Equation (2-25) through the use of the high temperature data. Since Equation (2-25) models the electronic contribution to thermal conductivity, a value for f was determined with a least-squares fit to the difference between the experimental thermal conductivities and the lattice vibration contribution predicted with Equation (2-26). The factor (A + BT) in Equation (2-26) was limited to its value at T = 2,050 K because the mean free path of the phonons is about equal to the interatomic distance at this temperature. ^{2.3-1} No normalization for density was applied to the high temperature data.

Table 2-9. Values of β_0 and β_1 from various density groups.

Groups compared ^a	β_0	β ₁
2 and 5	9.6	-0.00946
2 and 7	4.1	-0.00281
4 and 7	5.8	-0.00181
AVERAGES	6.5	-0.00469

a. Group 2 contains densities between 0.975 and 0.985 of theoretical

The final steps in the development of the UO_2 model were a trivial smoothing of two discontinuities in the slope of the predicted thermal conductivities as a function of temperature and the provision of an estimate for liquid fuel. The discontinuities are caused by limiting β in Equation (2-28) to values larger than -1 and limiting the phonon mean free path to at least the interatomic distance. Each discontinuity was removed by replacing temperature with an interpolated temperature in a range above the cutoff value and requiring the interpolated temperature to produce continuous functions and slopes at the ends of the range. For liquid fuel, the lattice vibration contribution to thermal conductivity was set equal to zero.

Several preliminary assumptions have been made to provide at least an approximate model for effects of variations in the plutonium content and the O/M ratio of ceramic fuels:

- 1. The effects of variations in density of mixed oxide fuels have been assumed to be described by the porosity correction derived with UO₂ data.
- 2. The high temperature electronic contribution to thermal conductivity has been assumed to be the same for PuO₂, UO₂, and nonstoichiometric fuels.

Group 4 contains densities between 0.955 and 0.965 of theoretical.

Group 5 contains densities between 0.945 and 0.955 of theoretical.

Group 7 contains densities between 0.925 and 0.935 of theoretical.

a. Data below 500 K were not used because Equation (2-26) is not valid near the Debye temperature.

- 3. Variations in plutonium content have been assumed to affect only the phonon-phonon scattering term in Equation (2-26).
- 4. Variations in O/M ratio have been assumed to affect only the defect term of Equation (2-26).

The change in the phonon-phonon scattering term of Equation (2-26) was modeled by fitting reported thermal conductivities^{2.3-27 to 2.3-30,2.3-33} of (U, Pu)O₂ to Equation (2-26) with B replaced by

$$B' = B_{UO_2}(1 + b \cdot COMP) \tag{2-31}$$

where

B' = coefficient of temperature in Equation (2-26) for mixed oxides

 B_{UO_2} = coefficient of temperature in Equation (2-26) for UO_2

COMP = UO_2 content of the fuel (ratio of weight of PuO_2 to total weight)

b = constant to be determined.

The resultant value of b was 0.6238.

Olander's expression^{2,3-1} for the effect of O/M ratio on the defect term of Equation (2-26) was adopted to provide a preliminary model for the effect of variations from stoichiometry. The fractional change in the defect term was estimated by Olander to be

$$\frac{\Delta A}{A} = \frac{400x}{A'} \tag{2-32}$$

where

x = absolute value of (O/M ratio -2.0).

A' = defect term in Olander's version of Equation (2-26)

 $\frac{\Delta A}{A}$ = fractional change in the defect term of Equation (2-20).

The expression for A which resulted from this adaptation is given in Equation (2-20).

The thermal diffusivity values of 1.90×10^{-6} through 3.23×10^{-6} m²/s measured for the 0.813 and 1.219 mm layers of molten UO_2 in the temperature range of 3,187 through 3,315 K by Kim et al.^{2.3-35} can be used with specific heat and density measurements to calculate the thermal conductivity of molten UO_2 or UO_2 - PuO_2 mixtures from the relation

$$K = C_p \rho \alpha \tag{2-33}$$

where

K = thermal conductivity of molten UO_2 or $UO_2 - PuO_2(W/m \cdot K)$

 C_p = specific heat capacity (J/kg•K)

 ρ = density (kg/m³

 α = thermal diffusivity (m²/s).

Substitution of the MATPRO values for C_p and ρ at melting into Equation (2-33) yields thermal conductivities in the range 8.5 to 14.5 W/m•K.

Kim et al.^{2.3-35} interpret this unusually high conductivity as being due to internal infrared radiation heat transfer in the liquid UO_2 that is not allowed in the solid because of the effect of scattering centers, such as grain boundaries or voids. Although they caution that radiative thermal diffusivity depends on the thickness of the material as well as on the emissivity of the boundary surfaces, the variations they estimate are only 0.10 to 0.30 times the measured value. The constant 11.5 (W/m²•s) used for the thermal conductivity of liquid fuel (UO_2 or UO_2 - PuO_2 mixtures) in the FTHCON subroutine is the average of a range of values calculated from the data of Kim et al. An uncertainty of \pm 0.3 times the given liquid conductivity is estimated from the range of values measured.

2.3.4 Model Uncertainty

The standard error^a of the FTHCON model for thermal conductivity with respect to its UO_2 data base is \pm 0.20 W/m•K. The standard error with respect to the $(U,Pu)O_2$ data base is \pm 0.29 W/m•K. The first two terms of Equation (2-21), the expression of model uncertainty which has been added to the FTHCON subcode, were constructed to reproduce these uncertainties at 0 and 20% PuO_2 content. The third term of Equation (2-21) provides an engineering estimate of the increase in the error of the model for nonstoichiometric fuel.

a. The standard error was estimated with the expression (sum of squared residuals/number of residuals minus the number of constants used to fit the data) $^{1/2}$. Five constants were used for the UO₂ data, and six were used for the PuO₂ data.

Figure 2-7 through Figure 2-10 illustrate the model predictions and the UO_2 data base for several densities. Each figure shows data within \pm 0.005 of the fraction of theoretical density assumed for the model prediction. The UO_2 data of each investigator show scatter nearly as large as the standard error of the model. This fact suggests that this part of the model is complete.

Mixed oxide data have not been compared to the current model because the part of the model that applies to mixed oxide (fuel) is preliminary.

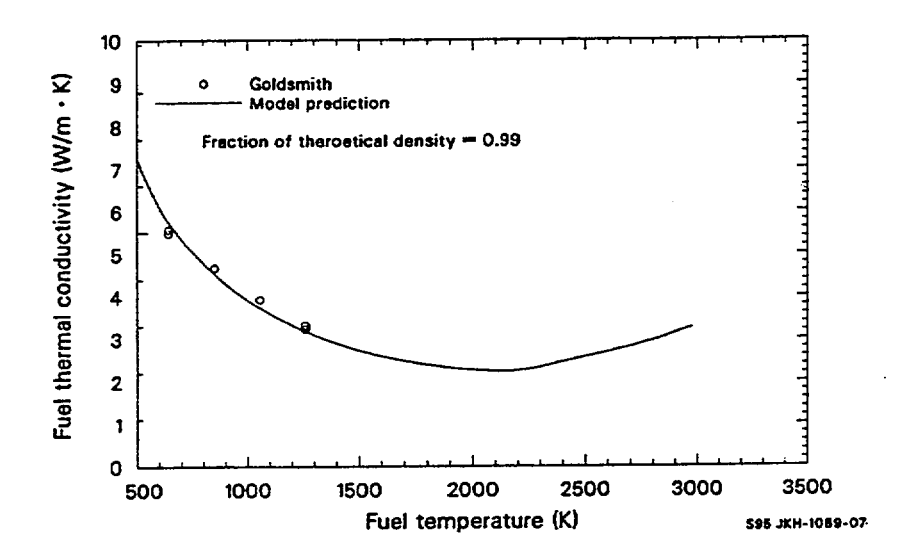


Figure 2-7. Model prediction for thermal conductivity of 0.99% TD UO₂ compared to data from specimens with densities in the range 0.985 to 0.995% TD.

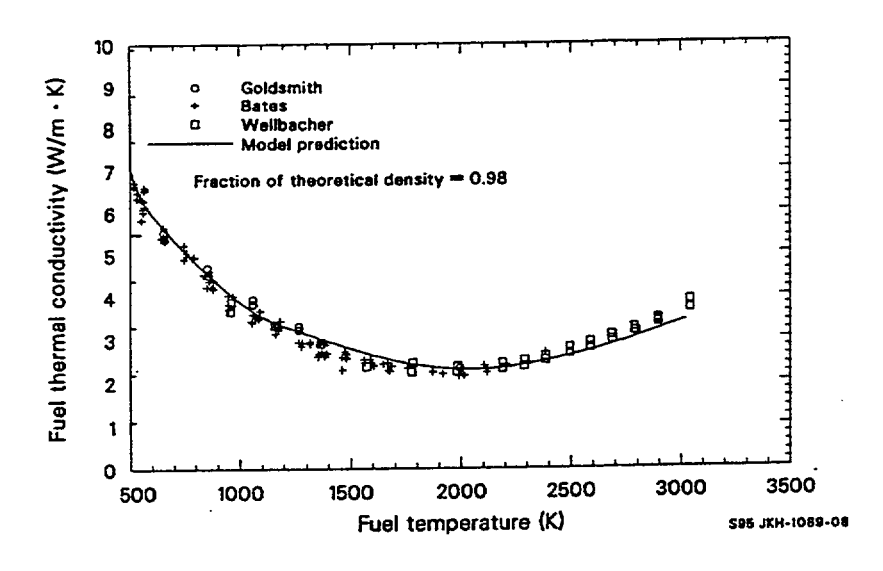


Figure 2-8. Model prediction for thermal conductivity of 0.98% TD UO₂ compared to data from specimens with densities in the range 0.975 to 0.985% TD.

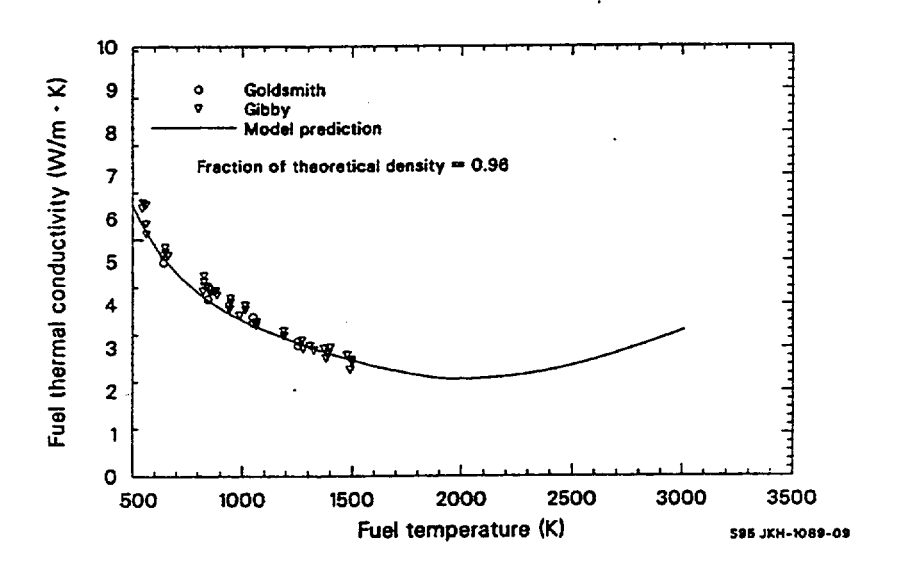


Figure 2-9. Model prediction for thermal conductivity of 0.96% TD $\rm UO_2$ compared to data from specimens with densities in the range 0.955 to 0.965% TD.

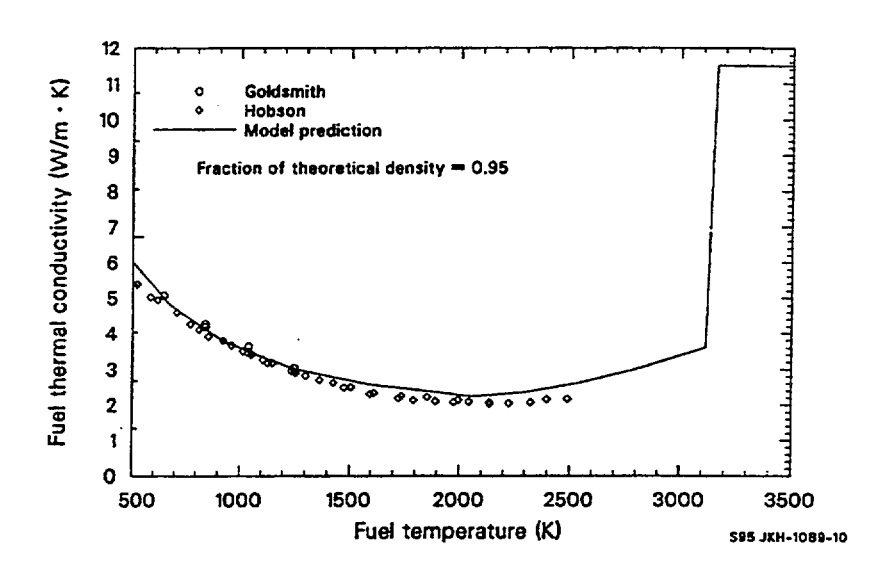


Figure 2-10. Model prediction for thermal conductivity of 0.95% TD UO₂ compared to data from specimens with densities in the range 0.945 to 0.955% TD.

2.3.5 References

- 2.3-1 D. R. Olander, Fundamental Aspects of Nuclear Reactor Fuel Elements, TID-26711-P1, 1976.
- 2.3-2 C. Kittel, Introduction to Solid State Physics, New York: John Wiley and Sons, Inc., 1956.
- 2.3-3 R. Berman, Thermal Conduction in Solids, Oxford: Clarendon Press, 1976.
- 2.3-4 H. J. Goldsmith, The Thermal Properties of Solids, New York: Dover Publications, Inc., 1965.
- 2.3-5 J. L. Bates, C. A. Hinman, T. Kawada, "Electrical Conductivity of Uranium Dioxide," *Journal of the American Ceramic Society, 50*, 1967, pp. 652-656.
- 2.3-6 G. P. Marino, "The Porosity Correction Factor for the Thermal Conductivity of Ceramic Fuels," Journal of the American Ceramic Society, 38, 1970, pp. 178-190.
- 2.3-7 A. L. Loeb, "Thermal Conductivity: A Theory of Thermal Conductivity of Porous Materials," Journal of the American Ceramic Society, 37, 1954, pp. 96-99.
- J. R. MacEwan, R. L. Stoute, and M. F. Notley, "Effect of Porosity on the Thermal Conductivity of UO₂," *Journal of Nuclear Materials*, 24, 1967, pp. 109-112.
- 2.3-9 A. Biancheria, "The Effect of Porosity on Thermal Conductivity of Ceramic Bodies," Transactions of the American Nuclear Society, 9, 1966, p. 15.
- 2.3-10 G. Ondracek and B. Schulz, "The Porosity Dependence of the Thermal Conductivity for Nuclear Fuels," *Journal of Nuclear Materials*, 46, 1973, pp. 253-258.
- 2.3-11 J. C. VanCraeynest and J. P. Stora, "Effect de la Porosite sur la Variation de Conductubilite Thermique du Bioxyde d'Uranium en Fonction de la Temperature," Journal of Nuclear Materials, 37, 1970, pp. 153-158.
- 2.3-12 L. A. Goldsmith and J. A. M. Douglas, "Measurements of the Thermal Conductivity of Uranium Dioxide at 670-1,270 K," *Journal of Nuclear Materials*, 47, 1973, pp. 31-42.
- 2.3-13 I. C. Hobson, R. Taylor, and J. B. Ainscough, "Effect of Porosity and Stoichiometry on the Thermal Conductivity of Uranium Dioxide," *Journal of Physics Section D: Applied Physics*, 7, 1974 pp. 1003-1015.
- 2.3-14 R. R. Asamoto, F. L. Anselin, and A. E. Conti, "The Effect of Density on the Thermal conductivity of Uranium Dioxide," *Journal of Nuclear Materials*, 29, 1969, pp. 67-81.
- 2.3-15 J. C. Hedge, Measurement of Thermal Conductivity of Uranium Dioxide, AECU-3881, September 20, 1956.

- 2.3-16 W. K. Kingery et al., "Thermal Conductivity X: Data for Several Pure Oxide Materials Corrected to Zero Porosity," *Journal of the American Ceramic Society, 37*, 1954, pp.107-110.
- 2.3-17 F. J. Hetzler et al., The Thermal Conductivity of Uranium and Uranium Plutonium Oxides, GEAP-4879, August 1967.
- 2.3-18 T. G. Godfrey et al., Thermal Conductivity of Uranium Dioxide and Armco Iron by an Improved Radial Heat Flow Technique, ORNL-3556, June 1964.
- 2.3-19 J. Lambert Bates, High Temperature Thermal Conductivity of "Round Robin" Uranium Dioxide, BNWL-1431, July 1970.
- 2.3-20 C. F. Lucks and H. W. Deem, "Thermal Conductivity and Electrical Conductivity of UO₂," *Progress Relating to Civilian Applications During June 1960*, BMI-1448, July1, 1960.
- 2.3-21 J. A. Christensen, et al., "Uranium Dioxide Thermal Conductivity," Transactions of the American Nuclear Society, 7, 1964, pp. 391-392.
- 2.3-22 M. F. Lyons et al., UO₂ Pellet Thermal Conductivity from Irradiations with Central Melting, GEAP-4624, July 1964.
- 2.3-23 R. D. Reiswig, "Thermal Conductivity of UO₂ to 2,100 °C," Journal of the American Ceramic Society, 44, 1961, pp. 8-49.
- 2.3-24 J. Stora et al., Thermal Conductivity of Sintered Uranium Oxide Under In-Pile Conditions, EURAEC 1095, CEA-R 2585, August 1964.
- 2.3-25 C. Ferro, C. Patimo, and C. Piconi, "Thermal Diffusivity of Mixed H_{1-x}, U_x Oxides and Some Materials to be Used as Reference in the Range 650 2,700 K," *Journal of Nuclear Materials*, 43, 1972 pp. 272-276.
- 2.3-26 J. C. Weilbacher, "Diffusivite Thermique de l'Oxyde d'Uranium et de l'Oxyde de Thorium a Haute Temperature," *High Temperatures--High Pressure*, 4, 1972, pp. 431-438.
- 2.3-27 R. L. Gibby, "The Effect of Plutonium Content on the Thermal Conductivity of (U, Pu)O₂ Solid Solutions," *Journal of Nuclear Materials*, 38, 1971, pp. 163-177.
- 2.3-28 R. L. Gibby, The Thermal Diffusivity and Thermal Conductivity of Stoichiometric, $(U_{0.8} Pu_{0.2})O_2$, BNWL-704, May 1968.
- 2.3-29 R. L. Gibby, The Effect of Oxygen Stoichiometry on the Thermal Diffusivity and Conductivity of $U_{0.75}$ $Pu_{0.25}$ O_{2-x} BNWL-927, January 1969.
- 2.3-30 L. A. Goldsmith and J. A. M. Douglas, "The Thermal Conductivity of Plutonium Uranium Dioxide at Temperatures up to 1,273 K," *Journal of Nuclear Materials*, 43, 1972, pp. 225-233.

- 2.3-31 M. Serizawa et al., "Thermal Diffusivity and Thermal Conductivity of Uranium Plutonium Dioxide," Journal of Nuclear Materials, 34, 1970, pp. 224-226.
- J. C. VanCraeynest and J. C. Weilbacher, "Etude de la Conductibility Thermique des Oxides Mixed d'Uranium et de Plutonium," *Journal of Nuclear Materials*, 26, 1968, pp. 132-136.
- 2.3-33 H. E. Schmidt, "Die Waermeleitfaehigkeit von Uran and Uran Plutonium Dioxyd bei Hohen Temperaturen," Forschung, Ingenieur-Wesen, 38, 1972, pp. 149-151.
- 2.3-34 H. E. Schmidt, "Die Waermeleitfaehigkeit von Uran and Uran Plutonium Dioxyd bei Hohen Temperaturen," High Temperatures--High Pressure, 3, 1971, p. 345.
- 2.3-35 C. S. Kim et Al., "Measurement of Thermal Diffusivity of Molten UO₂," Proceedings of the Seventh Symposium on Thermophysical Properties at the National Bureau of Standards, Gaithersberg, MD, May 10-12, 1977, CONF 770537-3, pp. 338-343.

2.4 Emissivity (FEMISS)

The fuel emissivity subcode FEMISS calculates total hemispherical UO₂ emissivity (emissivity integrated over all wavelengths) as a function of temperature. Fuel emissivity is defined as the ratio of radiant energy emitted from a material to that emitted by a black body at the same temperature. The subcode is used to calculate radiant energy transfer from fuel to cladding in conjunction with thermal conduction. Radiant energy transfer can be a significant heat transfer mechanism, depending on the gap size, temperature gradient across the gap, and plenum gas.

2.4.1 Summary

According to the Stefan-Boltzmann law, the total radiant power per unit area emitted by a body at temperature T is

$$P = e\sigma T^4 \tag{2-34}$$

where

P = radiant power per unit area (W/m^2)

e = total hemispherical emissivity (unitless)

σ = the Stefan-Boltzmann constant (5.672 x 10⁻⁸ W/m²•K)

T = temperature (K).

The expression used in the FEMISS subcode to describe total emissivity is

 $e = 0.7856 + 1.5263 \times 10^{-5} T$.

(2-35)

The standard error of estimate of Equation (2-35) with respect to its data base is \pm 6.8%. The emissivity data were measured at temperatures up to approximately 2,400 K, and use of FEMISS above this temperature is speculative because of possible high temperature effects that are not modeled. At the time of model development, there were no data to develop a (U, Pu)O₂ emissivity equation, so Equation (2-35) is also recommended for (U, Pu)O₂.

The data base for Equation (2-35) is discussed in Section 2.4.2. Model development is discussed in Section 2.4.3.

2.4.2 Emissivity Data

Emissivity data have been reported by Held and Wilder, ^{2.4-1} Cabannes, ^{2.4-2} Jones and Murchison, ^{2.4-3} Claudson, ^{2.4-4} Belle, ^{2.4-5} and Ehlert and Margrave. ^{2.4-6}

Held and Wilder reported hemispherical spectral (emissivity at one wavelength) emissivity data of UO₂. These data are also documented by Touloukian and Dewitt. They determined the emissivity of UO₂ having O/M ratios between 1.95 and 2.29 and bulk densities between 8 x 10^3 and 10.6 x 10^3 kg/m³. The measurements were taken at wavelengths of 0.656 and 0.7 μ m and at temperatures between 450 and 2,400 K. The data show no observable emissivity trend as a function of the fuel O/M ratio or density, but scatter of the data is large (\pm 10%) and may obscure trends. Their data indicate that emissivity increases with temperature between 450 and 2,200 K and then drops a few percent at temperatures near 2,400 K. Whether or not the emissivity continues to drop at higher temperatures is uncertain because of lack of data. Since this decrease in emissivity at high temperatures is less than the scatter of the data, the trend cannot be considered to continue until more high temperature data are obtained.

Cabannes measured reflectance (1.0 - emissivity) of UO_2 up to 2,200 K as a function of wavelength and temperature. He found that the emissivity approaches 1.0 at wavelengths above 20 μ m but remains between 0.9 and 0.8 for wavelengths below 10 μ m. He also found that emissivity did not change with thermal cycling. Since a polished surface normally deteriorates during thermal cycling, the study implies little sensitivity of emissivity data to the surface polish of the UO_2 samples.

Jones and Murchison reported reflectivity of UO_2 at wavelengths between 0.4 and 0.7 μ m. The emissivity of the samples varied between 0.81 and 0.84. They found emissivity to be smallest (0.81) at a wavelength of about 0.5 μ m. It increased 1 to 3% for wavelengths other than 0.5 μ m. Emissivity also varied less than 3% for O/M ratios between 2.003 and 2.203.

Data reported by Claudson and Belle indicate that emissivity decreases from 0.85 to 0.37 as temperature increases from 1,000 to 2,200 K. This decrease with decreasing temperature is in direct contradiction to the Held and Wilder, Cabannes, and Jones and Murchison data. Cabannes has reviewed Claudson's data and concludes that the discrepancy is possibly due to an error in Claudson's measurement technique.

Ehlert and Margrave reported two data points from UO_2 pellets. They measured the emissivity of UO_2 at 2,073 K and approximately 3,000 K and found the emissivities to be 0.416 and 0.40, respectively.

2.4.3 Model Development

The subcode FEMISS calculates total emissivity of fuel at a particular temperature. The hemispherical spectral data of Held and Wilder and the emissivity data of Cabannes and Jones and Murchison were used in developing the FEMISS model. Data of Claudson and Ehlert and Margrave were not used because of possible errors in measurement technique.^{2,4-2}

Spectral emissivity data were also used to develop the total emissivity subcode FEMISS for the following reasons. Jones and Murchison indicate that spectral emissivities do not vary more than 2 or 3% at wavelengths between 0.4 and 0.7 μ m, well within the uncertainty of the data. The Cabannes data show that UO₂ emissivity is about 0.85 at all wavelengths below 10 μ m. Since spectral data measured at wavelengths smaller than 10 μ m do not vary more than a few percent as wavelength varies, spectral data can be used to develop a total emissivity correlation. This assumption is valid in general for FEMISS calculations, since the radiation emitted from a black body or any material has maximum intensities at wavelengths smaller than 10 μ m at temperatures for which radiant energy transfer is important.

Besides the emitted wavelength, emissivity can be a function of material properties, such as density, porosity, surface finish, O/M ratio, and temperature. Analysis of the data showed no dependence of emissivity on any of the above properties except temperature. The Held and Wilder data and the Cabannes data were used in a linear regression program to obtain Equation (2-35). A standard error of estimate of \pm 6.8% was also determined using Equation (2-35) and the data base.

The emissivity data of Held and Wilder and Cabannes are shown in Figure 2-11 as a function of temperature. The emissivity predictions of FEMISS at temperatures between 300 and 3,000 K are shown as a solid line in the figure. The dashed lines in the figure represent predicted $\pm \sigma$ values. The decreasing emissivities of the Held and Wilder data at temperatures near 2,400 K can be seen in Figure 2-11. There are no data past this temperature to determine whether the drop is a real effect or experimental error. If the trend is real, no data exist to indicate what happens to the emissivity beyond 2,400 K; so until more data at higher temperatures are obtained, the drop of the Held and Wilder data near 2,400 K is assumed to be experimental error.

2.4.4 References

- 2.4-1 P. C. Held and D. R. Wilder, "High Temperature Hemispherical Spectral Emittance of Uranium Oxides at 0.65 and 0.70 µm," *Journal of the American Ceramic Society, 52,* 1969.
- 2.4-2 M. M. F. Cabannes, J. P. Stora, and J. Tsakiris, "ORTIQUE-MOLECULAIRE-Fracteurs de re'flexion et d'e'mission de UO₂ a' haute Temperature," C. R. Acad. Sc. Paris, t. 264, January 1967.
- 2.4-3 J. M. Jones and D. G. Murchison, "Optical Properties of Uranium Oxides," *Nature*, 205, 4972, 1965, pp. 663-665.

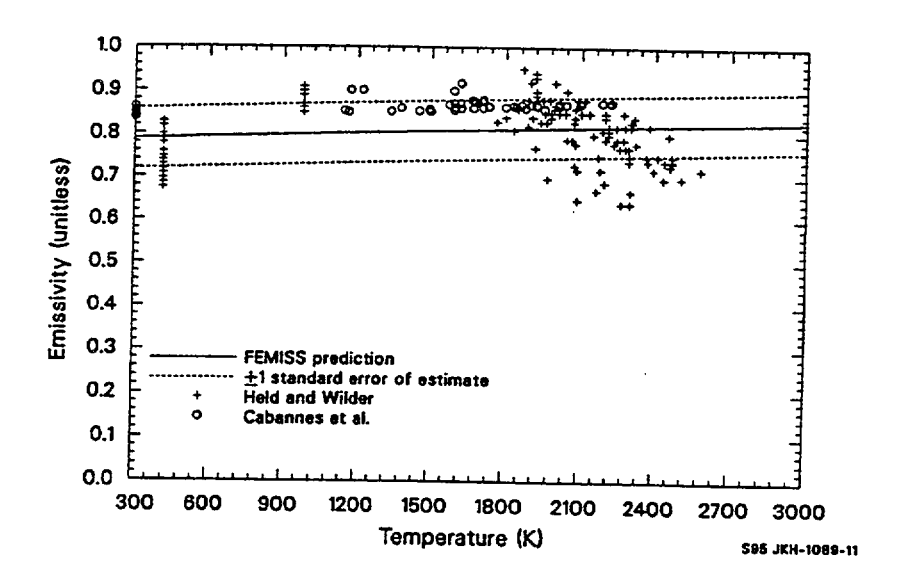


Figure 2-11. Emissivity data and corresponding FEMISS predictions.

- 2.4-4 T. T. Claudson, Emissivity Data for Uranium Dioxides, HW-55414, November 5, 1958.
- 2.4-5 J. Belle (ed.), Uranium Dioxide: Properties and Nuclear Applications, TID-7546, 1961.
- 2.4-6 T. C. Ehlert and J. L. Margrave, "Melting Point and Spectral Emissivity of Uranium Dioxide," Journal of the American Ceramic Society, 41, 1958, p. 330.
- 2.4-7 Y. S. Touloukian and D. P. Dewitt, "Thermal Radiative Properties of Nonmetallic Solids," *Thermophysical Properties of Materials*, 8, New York-Washington: IFI/Plemung, 1972.

2.5 Thermal Expansion and Density (FTHEXP, FDEN)

The FTHEXP function models dimensional changes in unirradiated fuel pellets caused by changes in temperature. It is capable of dealing with any combination of UO₂ and PuO₂ in solid, liquid, or states with both phases and includes expansion due to the solid liquid phase change. The FDEN function determines the theoretical density of UO₂ using room temperature data and thermal expansion strains calculated by the FTHEXP subcode.

Fuel dimensional changes affect the pellet to cladding gap size, which is a major factor in determining gap heat transfer and thus the stored energy, an important quantity for safety analysis.

2.5.1 Summary (FTHEXP)

The function FTHEXP models fuel thermal expansion as a function of temperature, fraction of PuO₂, and the fraction of fuel which is molten. The O/M ratio is not included. When the departure from

stoichiometry, |O/M-2.0|, is greater than 0.2, there is clearly an effect.^{2.5-1} to ^{2.5-3} This effect is ignored in modeling thermal expansion, since typical reactor fuels only deviate about a tenth this much from the stoichiometric composition.

The equations for the thermal expansion of UO_2 and PuO_2 have the same form. In the solid phase, the equation is

$$\frac{\Delta L}{L_0} = K_1 T - K_2 + K_3 e^{\left(\frac{E_0}{kT}\right)}$$
 (2-36)

where

k

$$\frac{\Delta L}{L_0}$$
 = linear strain caused by thermal expansion (equal to zero at 300 K) (unitless)

T = temperature (K)

E_D = energy of formation of a defect (J)

and K_1 , K_2 , and K_3 are constants to be determined. K_1 , K_2 , K_3 , and E_D are given in Table 2-10.

Boltzmann's constant (1.38 x 10⁻²³ J/K)

Table 2-10. Parameters used in UO_2 and PuO_2 solid phase thermal expansion correlations.

Constant	UO ₂	PuO ₂	Units
K ₁	1.0 x 10 ⁻⁵	9.0 x 10 ⁻⁶	K ⁻¹
K ₂	3.0 x 10 ⁻³	2.7 x 10 ⁻³	Unitless
K ₃	4.0 x 10 ⁻²	7.0 x 10 ⁻²	Unitless
E_{D}	6.9 x 10 ⁻²⁰	7.0 x 10 ⁻²⁰	J

For mixed UO₂ and PuO₂, the thermal expansion of the solid is found by combining the contribution from each constituent in proportion to its weight fraction.

During melting, an expansion equal to a linear strain of 0.043 occurs. If the fuel is partially molten, the strain due to thermal expansion is given by

$$\frac{\Delta L}{L_0} = \frac{\Delta L}{L_0} (T_m) + 0.043 \cdot FACMOT \tag{2-37}$$

where

$$\frac{\Delta L}{L_0}(T_m)$$
 = thermal expansion strain of solid fuel from Equation (2-38) with $T = T_m$

 $T_{\rm m}$ = melting temperature of the fuel (K)

FACMOT = reaction of the fuel which is molten (unitless).

If FACMOT = 0.0, the fuel is all solid; if FACMOT = 1.0, the fuel is all molten.

The correlation used to describe the expansion of entirely molten fuel is

$$\frac{\Delta L}{L_0} = \frac{\Delta L}{L_0} (T_m) + 0.043 + 3.6 \times 10^{-5} [T - (T_m + \Delta T_m)] . \qquad (2-38)$$

The solid to liquid phase transition is isothermal only for pure UO_2 or pure PuO_2 . For $(U, Pu)O_2$, the transition occurs over a finite temperature range, denoted in Equation (2-38) by ΔT_m . That is, ΔT_m is the liquidus minus the solidus temperature for the $(U, Pu)O_2$ considered.

The uncertainty of the pooled data was found to be temperature dependent, increasing approximately linearly with temperature. Therefore, a percentage error is given rather than a fixed number. The $\pm \sigma$ limits were found to be within $\pm 10\%$ of the calculated value.

Section 2.5.2 contains a discussion and evaluation of the sources used. Section 2.5.3 presents the development of the model. In Section 2.5.4, the model predictions are compared with data and an uncertainty estimate is given. Implementation of FTHEXP is described in Section 2.5.5. In Section 2.5.6. the subcode FDEN is described.

2.5.2 Literature Review (FTHEXP)

Data were taken from nine sources for UO_2 , $^{2.5-1}$ to $^{2.5-9}$ and two sources for PuO_2 , $^{2.5-3}$, $^{2.5-3}$. For UO_2 , the data cover a temperature range from 300 to 3,400 K; and for PuO_2 , the data cover a range from 300 to 1,700 K.

In four of the UO_2 experiments, $^{2.5-1,2.5-2,2.5-8,2.5-9}$ x-ray measuring techniques were used. This type of measurement gives the change in the lattice parameter rather than the bulk thermal expansion. Several investigators $^{2.5-2,2.5-11,2.5-12}$ have noted that the change in the lattice parameter is appreciably smaller than the bulk thermal expansion measured using dilatometric or interferometric methods, especially at high (> 1,000 K) temperature. In general, the difference is attributed to the creation of Schottky defects. $^{2.5-2,2.5-11,2.5-12}$ Hock and Momin $^{2.5-9}$ obtained results where there was no discrepancy between their x-ray results and bulk results. However, the bulk of the data support the Schottky defect theory, since the x-ray data

consistently fall below other data at high temperatures where defects begin to appear in large numbers. Therefore, x-ray data were used in the data base only at low temperatures (< 800 K).

2.5.3 Model Development (FTHEXP)

While most authors simply fit their data with a polynomial, in this report correlations based on more physical grounds are used.

2.5.3.1 Low Temperature Thermal Expansion. The simplest theory of the linear expansion of a solid near room temperature is found in most elementary physics texts, such as Sears and Zemansky.^{2.5}-13

$$\Delta L = L_0 K_1 (T - T_0) \tag{2-39}$$

or

$$\frac{\Delta L}{L_0} = K_1 T - K_1 T_0 \tag{2-40}$$

where

 ΔL = linear expansion (m)

 K_1 = the average coefficient of linear expansion (K^{-1})

 T_0 = a reference temperature (K)

 L_0 = length at reference temperature (m).

At the reference temperature, $\Delta L = 0$ or, equivalently, $L = L_0$.

The low temperature (< 800 K) data were fit by the method of least-squares to a generalized form of Equation (2-40)

$$\frac{\Delta L}{L_0} = K_1 T - K_2 . {(2-41)}$$

This fit was done separately for UO_2 and PuO_2 , and the coefficients K_1 and K_2 for each material are listed in Table 2-10. The numbers in the table have been rounded off to two significant figures. Comparison of Equations (2-40) and (2-41) shows that $T_0 = K_2/K_1$, which for both fuels is 300 K, a

temperature typical of the reference temperatures where $\Delta L = 0$ in data bases. These correlations describe low temperature thermal expansion within the data scatter.

2.5.3.2 High Temperature Thermal Expansion. For both UO_2 and PuO_2 , Equation (2-41)was inadequate at higher temperatures (T > 1,000 K), most likely due to the formation of Schottky defects. Fenkel defects will also be present but should have no measurable effect on the thermal expansion. ^{2.5-2,2.5-9} The contribution from Schottky defects should be directly proportional to their concentration, which is given by ^{2.5-2,2.5-14}

$$N/N_0 = K_3 e^{-E_D/(kT)}$$
 (2-42)

where

N = number of Schottky defects in the crystal

 N_0 = number of atoms in the crystal

 E_D = energy of formation of a defect (J)

k = Boltzmann's constant $(1.38 \times 10^{-23} \text{ J/K})$

 K_3 = constant to be determined (unitless).

The difference between the thermal strain calculated with Equation (2-41) and each data point was found. These differences were assumed to be the defect contribution to the thermal expansion strain and were fit by the method of least-squares to an equation of the form

$$\left(\frac{\Delta L}{L_0}\right)_{D} = K_3 e^{(-E_D/kT)} \tag{2-43}$$

where $\left(\frac{\Delta L}{L_0}\right)_D$ is the defect contribution to the thermal expansion (unitless).

The values for K₃ and E_D resulting from these fits are given in Table 2-10.

Baldock^{2.5-2} did a similar analysis using UO_2 data and those data of Conway.^{2.5-4} Both the preexponential factor, K_3 , and the energy of formation, E_D , were larger than those listed in Table 2-10 The differences mean that Baldock's Schottky term is smaller than the one found here at low temperatures and

larger at high temperatures. The magnitude of the Schottky term determined this way is strongly dependent on the low temperature correlation used. Since Equation (2-41) has been found using a much broader data base than Baldock's, the values for K_3 and E_D in Table 2-10 should be the more accurate and are the ones used in his model.

2.5.3.3 Mixed Oxide Thermal Expansion. When the fuel is composed of a mixture of UO₂ and PuO₂, the thermal expansion is found by taking a weighted average of the contributions from each component

$$\left(\frac{\Delta L}{L_0}\right)(U, Pu)O_2 = \left(\frac{\Delta L}{L_0}\right)UO_2 \cdot (1 - FCOMP) + \left(\frac{\Delta L}{L_0}\right)PuO_2 \cdot FCOMP$$
 (2-44)

where FCOMP is the PuO₂ weight fraction.

2.5.3.4 Thermal Expansion of Partially Molten Fuel. Christensen^{2.5-6} has determined that UO₂ experiences a linear thermal strain of 0.043 on melting. His measurements show considerable scatter but are the only data available. No comparable measurements exist for PuO₂. The structure of the two fuels is similar enough, however, so that no serious error should be introduced by equating the PuO₂ expansion on melting with that of UO₂. For partially molten fuel, the thermal expansion strain is given by

$$\frac{\Delta L}{L_0} = \frac{\Delta L}{L_0} T_m + 0.043 \cdot \text{FACMOT} . \qquad (2-45)$$

The various terms of Equation (2-37) are defined in Section 2.5.1.

2.5.3.5 Thermal Expansion of Entirely Molten Fuel. The experiment of Christensen on UO_2 again produced the only data available and must be used for all combinations of $(U, Pu)O_2$.

A least-squares fit to his limited data yields

$$\frac{\Delta L}{L_0} = \frac{\Delta L}{L_0} T_m + 0.043 + 3.6 \times 10^{-5} [T - (T_m + \Delta T_m)]$$
 (2-46)

where all the variables have been defined previously in Section 2.5.1.

2.5.4 Model Data Comparison and Uncertainty (FTHEXP)

Figure 2-12 compares the correlation for UO_2 with its data base. The three very low points around 1,500 K are all from Christensen.^{2.5-6} Other data from Christensen fit well to the curve, and there is no obvious reason for the large deviation of these points. At the highest temperatures, there are several data

considerably above the curve. These are also from Christensen. (At these temperatures, the possibility exists that the fuel was melted in the sample.) The large expansion which occurs on melting could easily explain the deviation of these data from the solid UO₂ data.

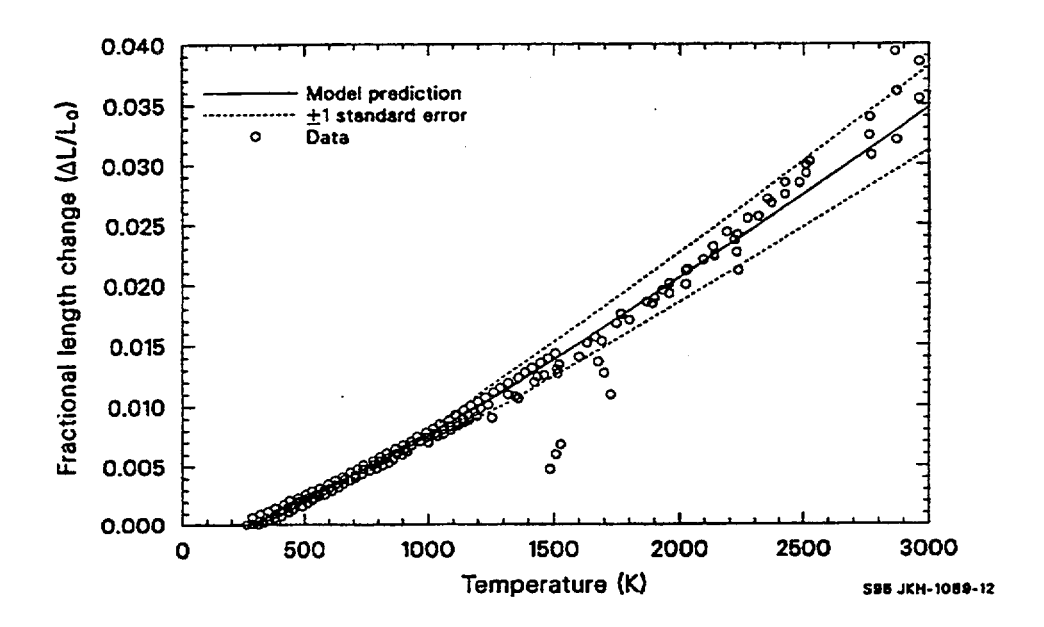


Figure 2-12. Correlation for the thermal expansion strain of UO₂ compared with its data base.

A similar comparison of the correlation and the data is shown in Figure 2-13 for PuO_2 . Figure 2-14 shows a comparison of the expansion curves for UO_2 and PuO_2 and $(U_{0.8}, Pu_{0.2})O_2$. No data are shown on this curve because thermal expansion data for mixed oxides are not available. The figures show that the thermal expansion behavior of the two materials differ, but only slightly.

Error bands, calculated from the sum of the squared residuals, are shown in Figure 2-12 and Figure 2-13 as dotted lines. These reflect a standard error of \pm 10% of the calculated value found from the UO₂ data set. A percentage uncertainty is given because the error increases with temperature. A single-valued uncertainty can lead to a nonphysical possibility in this model. For example, the standard error for UO₂ is \pm 0.0012, which equals the thermal expansion strain at 420 K. Thus, for any temperature less than 420 K, the lower limit implied by the uncertainty would be negative, implying that as the fuel heats from 300 to 400 K, it contracts. A percentage error automatically precludes this.

The error for PuO_2 was somewhat smaller, probably due to the limited number of sources. The \pm 10% error limit is also used for PuO_2 to avoid assigning unrealistic accuracy to these data.

2.5.5 Implementation (FTHEXP)

The function FTHEXP is coded as described in the preceding sections to calculate the thermal expansion strains of UO₂ and PuO₂. As used in SCDAP/RELAP5, this function has the ability to calculate

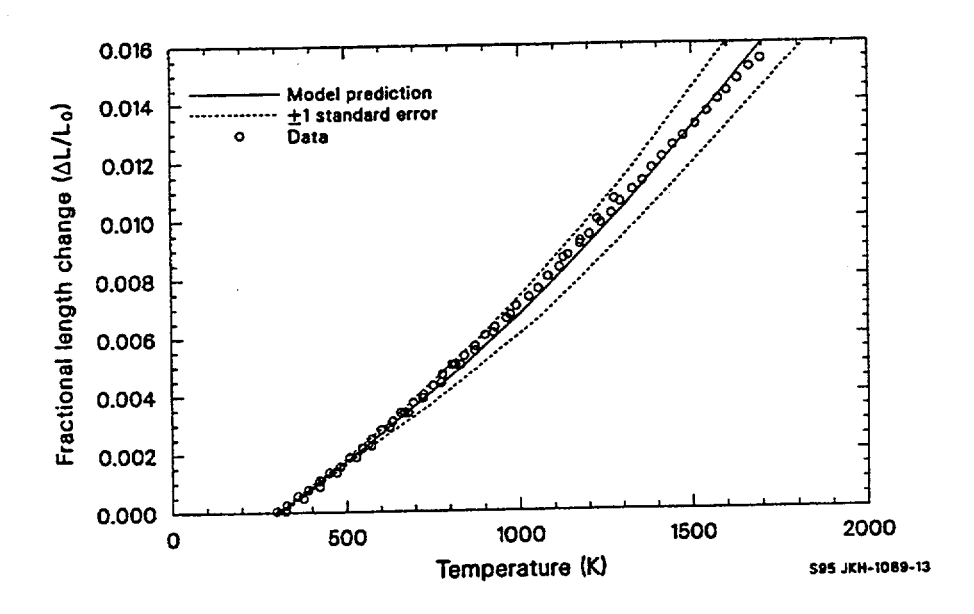


Figure 2-13. Correlation for the thermal expansion strain of PuO₂ compared with its data base.

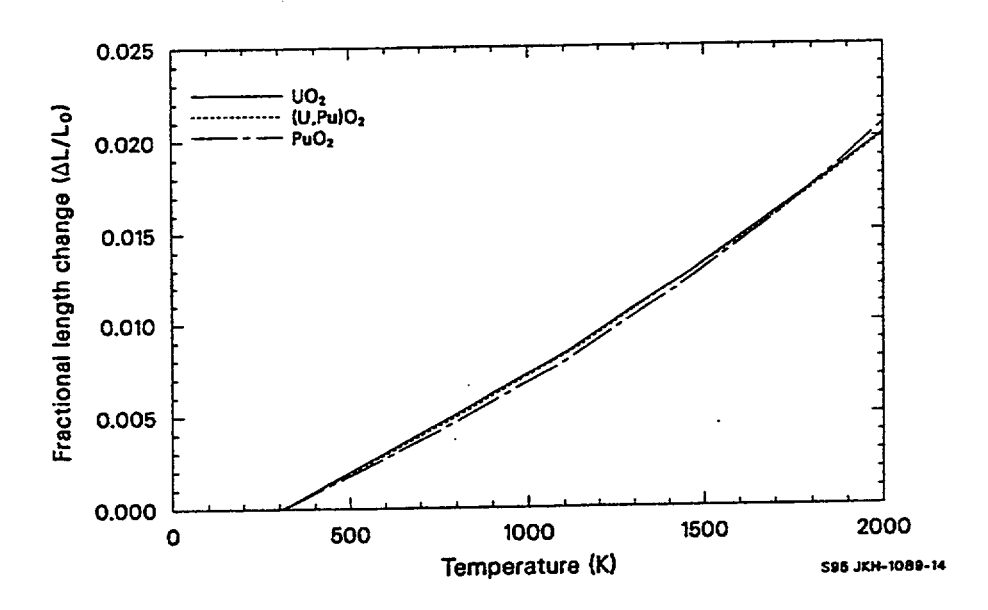


Figure 2-14. Comparisons of the UO_2 , PuO_2 , and $(U_{0.8}, Pu_{0.2})O_2$ correlations from 0 to 2,000 K. the thermal expansion strains with PuO_2 disabled. (A PuO_2 fractional composition of 0.0, making the fuel pure UO_2 , is hard-wired into the coding.) By inputting the PuO_2 composition fraction by argument list or common block, the PuO_2 thermal expansion strain can be restored.

2.5.6 Density (FDEN)

The FDEN function determines the theoretical density of UO₂ using room temperature data and thermal expansion strains calculated by the FTHEXP subcode. The relation used is

$$\rho = \rho_0 (1 - 3\varepsilon_{UO_2}) \tag{2-47}$$

where

 ρ = theoretical density of UO₂ (kg/m³)

 ρ_0 = room temperature density of $UO_2 = 10,980 \text{ (kg/m}^3\text{)}$

 ε_{UO_2} = linear thermal expansion strain calculated for UO_2 , using a reference (zero strain) temperature of 300 K (m/m).

The room temperature density, 10,980 kg/m3, was taken from Olander^{2.5-15} and is accurate to \pm 20 kg/m³. Figure 2-15 shows the theoretical density of uranium dioxide as calculated by FDEN.

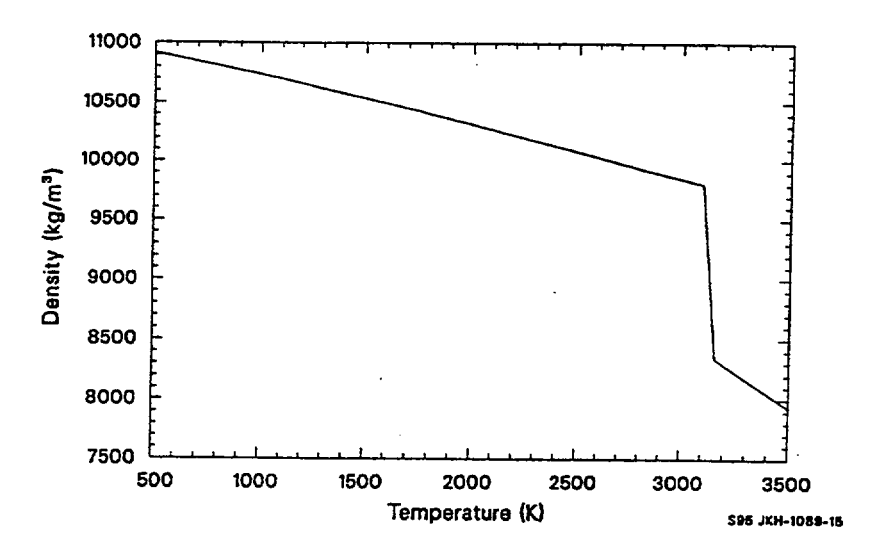


Figure 2-15. Theoretical density of UO_2 .

2.5.7 References

2.5-1 F. Gronvold, "High Temperature X-ray Study of Uranium Oxides in the UO₂-U₃0₈ Region," Journal of Inorganic and Nuclear Chemistry, I, 1955, pp. 357-370.

- 2.5-2 P. J. Baldock et al., "The X-ray Thermal Expansion of Near Stoichiometric UO₂," *Journal of Nuclear Materials*, 18, 1966, pp. 305-313.
- 2.5-3 N. H. Brett and L. E. Russel, "The Thermal Expansion of PuO₂ and Some Other Actinide Oxides Between Room Temperature and 1,000 °C," Proceedings of the Second International Conference on Plutonium Metallurgy, Grenoble, France, April 19-22, 1960, pp. 397-410.
- 2.5-4 J. B. Conway et al., The Thermal Expansion and Heat Capacity of UO₂ to 2,200 °C, TM-63-6-6, 1963.
- 2.5-5 M. D. Burdick and H. S. Parker, "Effect of Particle Size on Bulk Density and Strength Properties of Uranium Dioxide Specimens," *Journal of the American Ceramic Society*, 39, 1956, pp. 181-187.
- 2.5-6 J. A. Christensen, "Thermal Expansion and Change in Volume of Uranium Dioxide on Melting," Journal of the American Ceramic Society, 46, 1963, pp. 607-608.
- 2.5-7 W. A. Lambertson and J. H. Handwerk, *The Fabrication and Physical Properties of Urania Bodies*, ANL-5053, 1956.
- 2.5-8 C. P. Kempter and R. E. Elliott, "Thermal Expansion of UN, UO₂, UO₂-ThO₂, and ThO₂, Journal of Chemical Physics, 30, 1958, pp. 1524-1526.
- 2.5-9 M. Hoch and A. C. Momin, "High Temperature Thermal Expansion of UO₂ and ThO₂," *High Temperature High Pressures*, 1, 1969, pp. 401-407.
- 2.5-10 M. Tokar and A. W. Nutt, "Thermal Expansion of PuO₂ from 25 to 1,420 °C," Transactions of the American Nuclear Society, 10, June 1972, pp. 210-211.
- 2.5-11 M. Tokar et al., "Linear Thermal Expansion of Plutonium Dioxide," Nuclear Technology, 17, 1973.
- 2.5-12 R. W. Siegel, "Vacancy Concentration in Metals," Journal of Nuclear Materials, 69 and 70, 1978, pp. 117-146
- 2.5-13 F. W. Sears and M. W. Zemansky, *University Physics*, 3rd Edition, Reading, MA: Addison-Wesley Publishing Company, 1967, p. 347.
- 2.5-14 C. Kittel, *Introduction to Solid State Physics*, 3rd Edition, New York: John Wiley and Sons, Inc., 1966.
- 2.5-15 D. R. Olander, Fundamental Aspects of Nuclear Reactor Fuel Elements, TID-26711-P1, 1976, p.114.

2.6 Elastic Moduli (FELMOD, FPOIR)

The FELMOD subcode calculates values for Young's modulus for UO₂ and (U, Pu)O₂. An estimate of the standard error expected with FELMOD is also calculated. FELMOD and FPOIR are intended for use with mechanical codes like FRACAS, ^{2.6-1} which predict pellet deformation.

The FELMOD code is discussed in Section 2.6.1 through Section 2.6.4, and the FPOIR code is discussed in Section 2.6.5.

2.6.1 Summary (FELMOD)

The Young's modulus of ceramic fuels is affected by the temperature, density, and, to a lesser extent, the oxygen-to-metal ratio (O/M) and burnup of the fuel. Although published (U, Pu)O $_2$ mixed oxide data are very limited, several authors indicate that the addition of PuO $_2$ to UO $_2$ causes an increase in Young's modulus which is at least as large as the standard error of the UO $_2$ correlation. The increase has therefore been included in the model.

The subcode was constructed by considering values of Young's modulus measured at high temperatures typical of normal and abnormal LWR operation. Extensive room temperature data were available but were used only to help evaluate the uncertainty of the model.

The correlation developed to model Young's modulus for stoichiometric UO_2 fuel below the melting temperature is

$$ES = 2.334 \times 10^{11} [1 - 2.752 (1 - D)] [1 - 1.0915 \times 10^{-4} T]$$
 (2-48)

where

ES = Young's modulus for stoichiometric UO_2 fuel (N/m^2)

D = fuel density (fraction of the theoretical density)

T = temperature (K).

For nonstoichiometric fuel or fuel which contains PuO₂, the Young's modulus below melting temperature is

$$E = ES e^{(-Bx)} [1 + 0.15f]$$
 (2-49)

where

 $E = Young's modulus (N/m^2)$

ES = Young's modulus for stoichiometric UO_2 fuel (N/m^2)

B = 1.34 for hyperstoichiometric fuel or 1.75 for hypostoichiometric fuel

x = the magnitude of the deviation from stoichiometry in $MO_2\pm_X$ fuel

f = PuO_2 content of the fuel (weight fraction).

The estimated standard error^a of FELMOD for stoichiometric fuel is

(1) for temperatures between 450 and 1,600 K,

$$S_{ES} = 0.06 \times 10^{11}$$
 (2-50)

(2) for temperatures between 1,600 and 3,113 K,

$$S_{ES} = 0.06 \times 10^{11} + ES (T-1600)/6052.6$$
 (2-51)

where S_{ES} is the estimated standard error for stoichiometric UO_2 fuel (N/m²) and ES and T were previously defined.

For nonstoichiometric fuel or fuel that contains PuO2, the estimated standard error is

$$S_{E} = [(S_{ES})^{2} + (E - ES)^{2}]^{1/2}$$
(2-52)

where S_E is the estimated standard error (N/m²) for nonstoichiometric fuel and E, ES, and S_{ES} were previously defined.

The following subsection is a review of the available Young's modulus data for UO₂ and (U,Pu)O₂ fuel. Section 2.6.3 describes the approach used to formulate the model, and Section 2.6.4 is a discussion of the uncertainty of the model.

a. The standard error is estimated with a set of data by the expression (sum of squared residuals/number of residuals minus the number of constants used to fit the data)^{1/2}.

2.6.2 Survey of Available Data (FELMOD)

Young's modulus for UO₂ and (U,Pu)O₂ fuel has been measured by bending techniques^{2.6-2,2.6-3} and by resonant frequency methods. The bending techniques measure an isothermal Young's modulus that is more characteristic of reactor operating conditions than the adiabatic Young's modulus measured with resonant frequency methods. However, bending technique measurements are not as accurate as resonance frequency methods and will therefore not be used in the data base for this model. Also, the difference between adiabatic and isothermal Young's moduli is small, only about 0.1% of the measured value.^{2.6-4}

2.6.2.1 Stoichiometric Fuels at Reactor Operating Temperatures. Data from Padel and de Novion, 2.6-5 Belle and Lustman, 2.6-6 and Hall 2.6-7 are most important because they include temperatures characteristic of reactors. Figure 2-16 illustrates values of Young's modulus for stoichiometric UO₂ at several temperatures and densities. The modulus decreases with increasing temperature and decreasing density. Moreover, the temperature dependence of the modulus at each density is nearly linear.

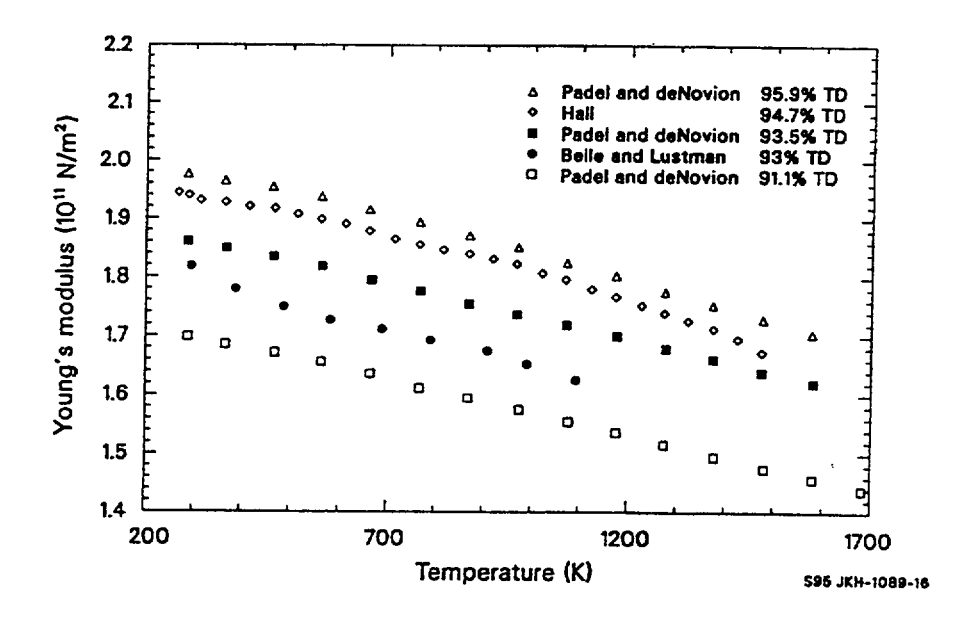


Figure 2-16. Young's modulus for stoichiometric UO_2 fuel at several temperatures and fractions of theoretical density.

Padel and de Novion have reported measurements of mixed oxide (with 20% PuO₂) moduli as a function of temperature and O/M ratio, but their report includes only room temperature data and curves representing the fractional decrease in Young's modulus with increasing temperature on 95% dense fuel. Room temperature, mixed oxide data from Padel and de Novion and from Boocock et al., ^{2.6-8} as well as curves from Padel and de Novion, are shown in Figure 2-17. The effect of temperature on the (U, Pu)O₂ Young's modulus is similar to its effect on UO₂, but the stoichiometric mixed oxide samples have a larger Young's modulus than stoichiometric UO₂ samples.

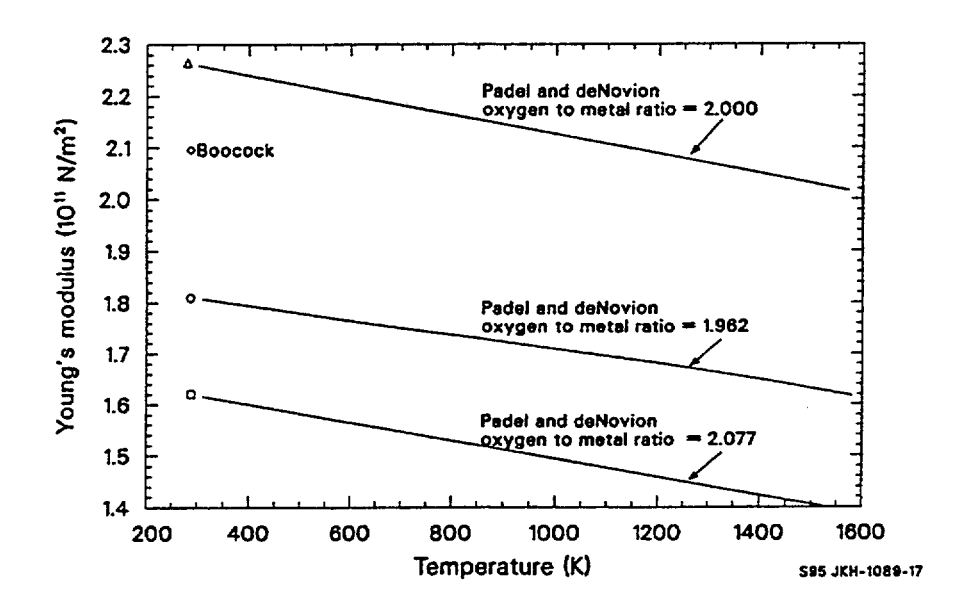


Figure 2-17. Young's modulus for (U, Pu)O₂ with various oxygen-to-metal ratios.

Boocock's results suggest that Padel and de Novion have exaggerated the increase of Young's modulus in mixed oxides. Boocock's measurements are supported by the following observations: (a) plutonium and uranium are transition elements with presumably similar atomic bonding; (b) more recent results that showed a 3% increase in Young's modulus due to the addition of PuO₂ have been quoted elsewhere; ^{2.6-9} and (c) Nutt et al., ^{2.6-10} have published a correlation for the effect of porosity on (U, Pu)O₂ oxides that agrees with Boocock's measurements. The 3% increase due to an addition of 20% PuO₂ to UO₂ is probably the most reliable estimate, since it is based on the more recent data of de Novion. ^{2.6-11}

In-reactor measurements of Young's modulus as a function of neutron fluence^{2.6-12} have indicated that irradiation increases Young's modulus by about 2% at saturation. Since the effect is small and could be explained by in-reactor densification of the fuel, no separate model for such burnup related changes as fission product accumulation and fuel lattice damage appears necessary at this time.

2.6.2.2 Room Temperature Measurements of Young's Modulus. The effect of changes in fuel density shown in Figure 2-16 is confirmed by room temperature measurements of Young's modulus as a function of density. Numerous data obtained with stoichiometric UO₂ fuels between 90 and 100% of theoretical density^{2.6-5} to 2.6-8, 2.6-13 to 2.6-15 are reproduced in Figure 2-18. The data are plotted both as a function of density and porosity (1 minus the density). The room temperature data for porosities between 0 and 0.1 can be described with the least-squares regression line also shown in Figure 2-18. The equation represented by the line is

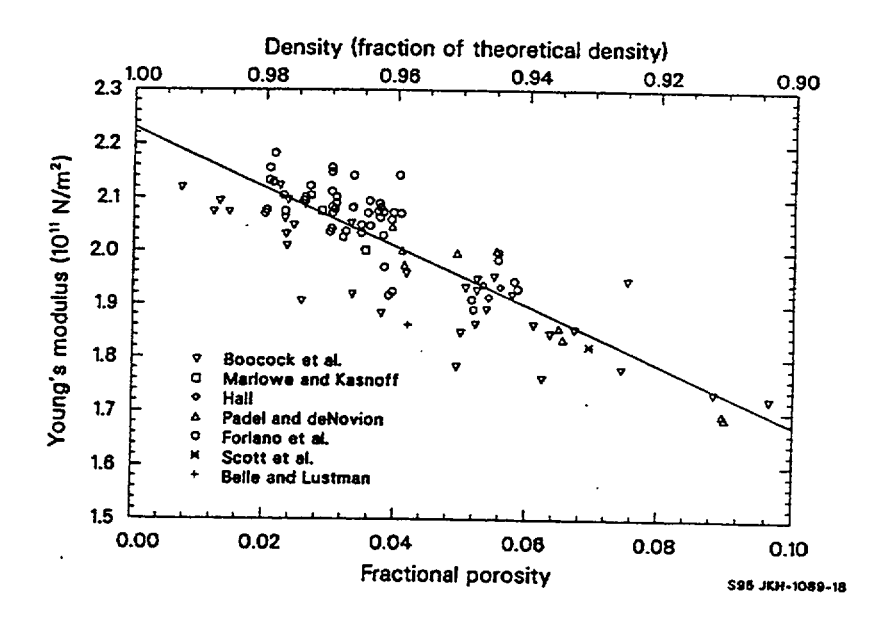


Figure 2-18. Young's modulus data and least-squares linear fit for stoichiometric UO₂ fuel at room temperature and several different densities.

$$ES = 2.334 \times 10^{11} - 5.63 \times 10^{11} P$$
 (2-53)

where

ES = the Young's modulus for stoichiometric UO_2 fuel (N/m^2)

P = porosity (1-D).

The standard deviation of this fit is $\pm 0.6 \times 10^{11} \text{ N/m}^2$.

2.6.2.3 Nonstoichiometric Fuels. The data available to describe the effect of variations in the O/M ratio on Young's modulus are difficult to interpret. For example, the significant variation of Young's modulus with changes in stoichiometry reported by Padel and de Novion (see Figure 2-17) is not seen in low density fuel studies by Nutt et al.^{2.6-10} Data attributed to de Novion et al. by Matthews show an intermediate effect.

Table 2-11 summarizes relevant nonstoichiometric fuel data taken at room temperature.

Table 2-11. Summary of Young's moduli measured in nonstoichiometric fuel at room temperature.

Composition	O/M Ratio	Porosity	Young's modulus (10 ¹¹ N/m ²)	Fraction of stoichiometric value
Padel and de Novion:				
$20\%~{ m PuO}_{2\pm { m X}}$	1.962	0.051	1.808	0.798
20% Pu ${ m O}_{2\pm X}$	2.000	0.050	2.265	1.000
$20\%~{ m PuO}_{2\pm X}$	2.077	0.050	1.620	0.715
Scott et al.:				
$\mathrm{UO}_{2\pm\mathrm{X}}$	2.000	0.042	1.860	1.000
$UO_{2\underline{+}X}$	2.160	0.042	1.240	0.666
de Novion et al. as quoted by Matthews:			·	
$20\%~{ m PuO}_{2\underline{+}{ m X}}$	2.000			1.000
$20\%~{ m PuO}_{2\underline{+}{ m X}}$	1.967		0.926	
$20\%~{ m PuO}_{2\pm { m X}}$	1.963			0.919
$20\%~{ m PuO}_{2\pm { m X}}$	1.926			0.873
$20\%~{\rm PuO}_{2\underline{+}{\rm X}}$	1.911	10 10		0.848
$20\%\mathrm{PuO}_{2\underline{+}\mathrm{X}}$	1.904			0.871
$20\%~{ m PuO}_{2\pm { m X}}$	1.900	*-		0.876
20% Pu ${ m O}_{2\pm { m X}}$	2.022		0.960	
20% Pu ${ m O}_{2\pm { m X}}$	2.050			0.929
20% Pu ${ m O}_{2\pm { m X}}$	2.052			0.915
20% PuO _{2±X}	2.089			0.903
20% PuO _{2±X}	2.111			0.895
20% PuO _{2±X}	2.142			0.816
20% Pu ${ m O}_{2\pm { m X}}$	2.168			0.812
Nutt et al.:				
20% Pu ${ m O}_{2\pm X}$	2.000			1.000

Table 2-11. Summary of Young's moduli measured in nonstoichiometric fuel at room temperature.

Composition	O/M Ratio	Porosity	Young's modulus (10 ¹¹ N/m ²)	Fraction of stoichiometric value
20% PuO _{2±X}	1.968			0.996
$20\%~\mathrm{PuO}_{2\underline{+}\mathrm{X}}$	1.971			0.996
20% Pu ${ m O}_{2\pm { m X}}$	1.982			0.998
20% Pu ${ m O}_{2\pm { m X}}$	2.006			1.006
20% Pu ${ m O}_{2\pm { m X}}$	2.008			1.002
20% Pu $O_{2\pm X}$	2.008			1.005

The ratio (Young's modulus in nonstoichiometric fuel/Young's modulus in stoichiometric fuel) is plotted as a function of the fuel's O/M ratio in Figure 2-19. Most of the points show a decrease in Young's modulus when the fuel is either hypo- or hyperstoichiometric, but there is little agreement about the magnitude of the decrease.

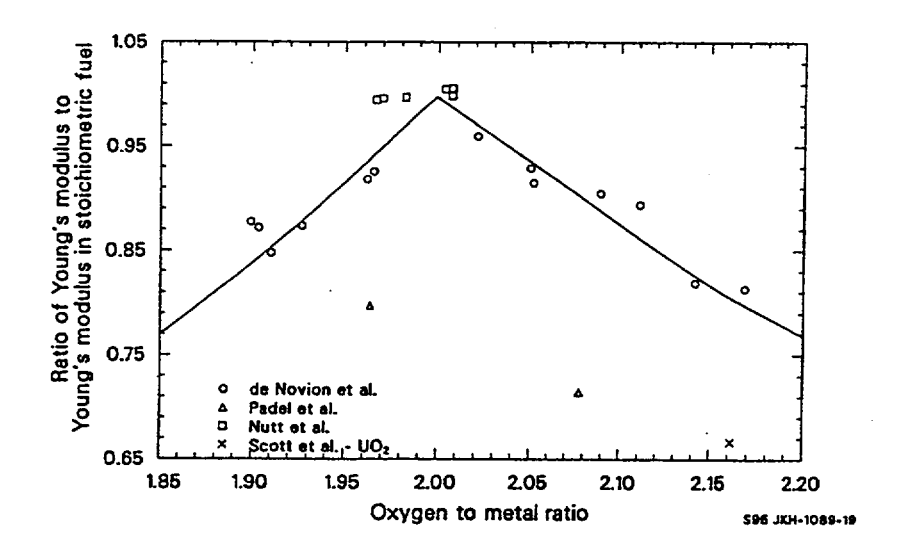


Figure 2-19. Ratio of Young's modulus for stoichiometric and nonstoichiometric fuels measured at room temperature compared to values predicted by de Novion's correlation.

It is possible that the fabrication history of the fuel is more significant than the O/M ratio in determining the Young's modulus. However, the inconsistent data of Nutt et al., are from fuel of uncharacteristically low density (9.5 g/cm³) and may not apply to more dense fuels. Therefore, the correlation selected for modeling the effects of nonstoichiometric fuel is that attributed to de Novion et al. by Matthews.

$$E = ES e^{(-Bx)}$$
 (2-54)

where the terms of the equation were previously defined.

Since typical in-reactor values of the O/M ratio are 1.96 to 2.04, ^{2.6-16} the effect of nonstoichiometry is a reduction of Young's modulus by 0 to 5%.

2.6.3 Model Development (FELMOD)

The model for Young's modulus is based primarily on the available UO₂ fuel data. A correlation for the Young's modulus of stoichiometric UO₂ fuel in the temperature range 450 to 1,600 K was developed first, then extrapolated to the approximate melting temperature and modified to predict a slight increase proportional to the weight fraction of PuO₂. The rate of increase with PuO₂ was set to reproduce the factor of 1.03, which was estimated in Section 2.6.2 for 20% PuO₂. A second modification for the estimated effect of nonstoichiometric fuel was also included in the model. The section describes the development of the model for stoichiometric UO₂ fuel.

The most realistic correlation for the effect of temperature on Young's modulus is the exponential form proposed by Wachtman et al. ^{2.6-17} However, the data in the temperature range 300 to 1,600 K shown in Figure 2-16 can be described with an expression of the form

$$E = a (1 + bT)$$
 (2-55)

where a and b are constants.

A similar approximation is possible to describe the effect of porosity on Young's modulus in the limited range of porosities of interest. The approximation is used because the information necessary to use detailed discussions of the effects of very large porosities^{2.6-18,2.6-19} and pore shape variation^{2.6-8,2.6-20} is most often not available. The room temperature data of Figure 2-18 for porosities between 0 and 0.1 can be described with an expression of the form

$$E = c (1 + dP)$$
 (2-56)

where c and d are constants.

Equation (2-56) was used to describe the effect of porosity on Young's modulus at temperatures above 450 K. However, the constants c and d were not evaluated with the room temperature data because (a) sufficient high temperature data exist to evaluate the effect of porosity in the temperature range of interest and (b) the room temperature data exhibit considerable scatter. The expression used to correlate the combined effects of porosity and temperature on Young's modulus is

$$E = e (1 + fT) (1 + gP)$$
 (2-57)

where E, T, and P have been defined previously and e, f, and g are constants.

The constants e, f, and g were evaluated using a two step fitting procedure. In the first step, least-squares constants a and b of Equation (2-55) were determined for each UO₂ fuel sample shown in Figure 2-16. The result of the fits is summarized in Table 2-12.

Table 2-12. Least squares constants for data of Figure 2-16.

Reference	Fraction of theoretical density	a (10 ¹⁰ N/m ²)	b (10 ⁻⁴ /K)
Padel and de Novion	0.911	17.605	-1.1053
Padel and de Novion	0.935	19.221	-1.0056
Padel and de Novion	0.959	20.549	-1.0665
Belle and Lustman	0.93	18.742	-1.1957
Hall	0.947	20.175	-1.0843

The constant a is equivalent to the product of the factors e (1 + gP) in Equation (2-57) for each UO_2 fuel sample, and the constant b is equivalent to the constant f in Equation (2-57). The second step of the fitting procedure was therefore the determination of a linear least-squares regression equation of constant a on P in order to find the best fit values of e and g. The least-squares fit produced values of $e = 23.34 \times 10^{10}$ N/m² and g = 2.752. These values were combined with the average of the values for f = b from Table 2-12 to produce the correlation

$$E = 23.34 \times 10^{10} (1 - 1.0915 \times 10^{-4} \text{T}) (1 - 2.752 \text{ P})$$
 (2-58)

where the terms have been previously defined. The correlation is equivalent to Equation (2-48).

No data are available for solid UO_2 fuel above 1,500 K. Equation (2-58) was simply extrapolated to estimate Young's modulus between 1,600 K and the approximate melting temperature (3,113 K).

2.6.4 Model Uncertainty (FELMOD)

The standard error of Equation (2-58) with respect to its own data base is $0.021 \times 10^{11} \text{ N/m}^2$ (about 1% of the predicted value), and the standard error of the equation with respect to the room temperature

data of Figure 2-18 is 0.073 x 10¹¹ N/m². These numbers represent lower and upper bounds for the standard error to be expected in applying the model to stoichiometric UO₂ fuel in the range 450 to 1,600 K. The first number does not include possible variations to be expected with samples not in the data base, and the second number was obtained using data taken at a low temperature where the linear expression for the effect of temperature systematically overpredicts Young's modulus. The best estimate for the standard error to be expected with this model is the standard deviation of Equation (2-53). The value, 0.06 x 10⁻¹¹ N/m², includes the effect of sample to sample variation but does not include the artificial error due to the extrapolation of the temperature coefficient.

For temperatures above 1,600 K, there are no data and no rigorous ways to test the model. In Equation (2-51), the standard error estimate for 400 to 1,600 K has been increased by an additive term, which is zero at 1,600 K and increases to one fourth of the predicted value at the approximate melting temperature (3,113 K).

The modifications to the basic UO_2 fuel correlation to predict the effects of nonstoichiometry and PuO_2 additions are based on limited data and are therefore uncertain. The standard error estimate expressed in Equation (2-52) assumes an independent error equal to the change produced by the models for nonstoichiometry and PuO_2 addition. That is, the net estimated standard error is taken to be the square root of the sum of the square of the standard error of the prediction for the stoichiometric UO_2 fuel elastic modulus and the square of the net change produced by the models for nonstoichiometric and PuO_2 fuels.

2.6.5 Poisson's Ratio (FPOIR)

Poisson's ratio for both UO₂ and (U, Pu)O₂ fuels is calculated by the routine FPOIR as a function of fuel temperature and composition.

Poisson's ratio can be related to Young's modulus and the shear modulus as follows: 2.6-21

$$\mu = \frac{E}{2G} - 1 \tag{2-59}$$

where

 μ = Poisson's ratio (unitless)

E = Young's modulus (N/m²)

 $G = shear modulus (N/m^2).$

a. Since three constants were used to fit the stoichiometric UO_2 fuel data base, the number of degrees of freedom is equal to the number of measurements minus three.

Wachtman et al. $^{2.6-22}$ report mean values for the Young's modulus and shear modulus of UO_2 from two experiments as $E=2.30 \times 10^{11} \text{ N/m}^2$ and $G=0.874 \times 10^{11} \text{ N/m}^2$. Consequently, the value of Poisson's ratio is 0.316 and the routine FPOIR returns this value for UO_2 . The Wachtman et al. paper only considers single-crystal UO_2 data at 25 °C. However, Padel and de Novion have reported values of 0.314 and 0.306 for the Poisson's ratio of polycrystalline UO_2 . These values are in reasonable agreement with Wachtman's value of 0.316.

Nutt et al. determined Poisson's ratio for $U_{0.8}Pu_{0.2}O_{2-x}$ at room temperature by determining the Young's modulus and the shear modulus and calculating Poisson's ratio using Equation (2-59). Nutt and Allen's room temperature Poisson's ratio for (U, Pu)O₂ fuel of 0.276 \pm 0.094 was found to be independent of density and is returned by FPOIR for mixed oxides.

Poisson's ratio for the fuel is shown in Figure 2-20 as a function of temperature and fuel composition. As can be seen from the figure, any plutonia content is assumed to reduce Poisson's ratio, which is independent of temperature.

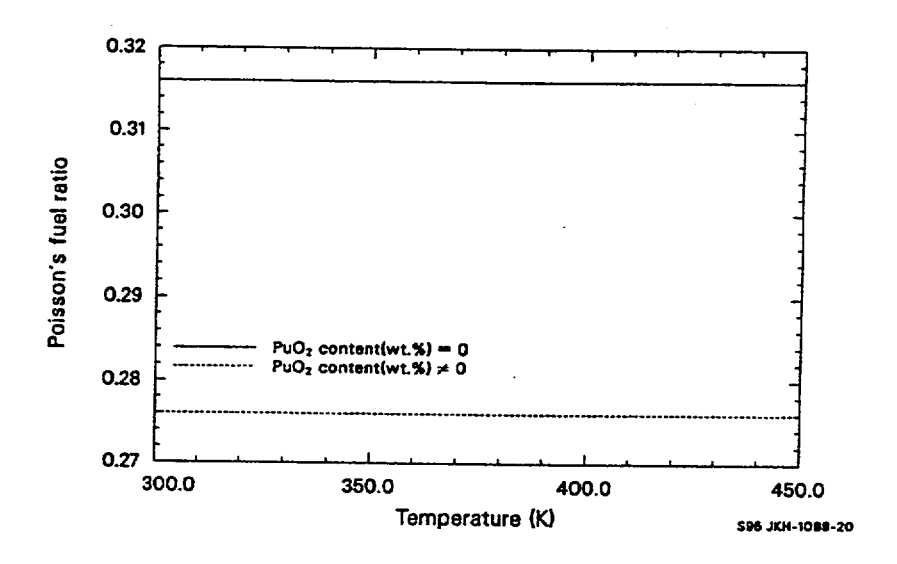


Figure 2-20. Poisson's ratio as a function of temperature.

2.6.6 References

- 2.6-1 M. P. Bohn, FRACAS A Subcode for the Analysis of Fuel Pellet Cladding Mechanical Interaction, TREE-NUREG-1028, April 1977.
- 2.6-2 W. A. Lambertson and J. H. Handwerk, *The Fabrication and Physical Properties of Urania Bodies*, ANL-5053, February 1956.
- 2.6-3 J. T. A. Roberts and Y. Ueda, "Influence of Porosity and Deformation and Fracture of UO₂," Journal of the American Ceramic Society, 55, 1972, pp. 117-124.

- 2.6-4 I. J. Fritz, "Elastic Properties of UO₂ at High Pressure," *Journal of Applied Physics*, 47, 1976, pp. 4353-4358.
- 2.6-5 A. Padel and C. de Novion, "Constants Elastiques des Carbures, Nitures et Oxydes d'Uranium et de Plutonium," *Journal of Nuclear Materials*, 33, 1969, pp. 40-51.
- 2.6-6 J. Belle and B. Lustman, "Properties of UO₂," Fuel Elements Conference, Paris, France, November 18-23, 1957, TID-7546, March 1958, pp. 480-481.
- 2.6-7 A. R. Hall, "Elastic Moduli and Internal Friction of Some Uranium Ceramics," Journal of Nuclear Materials, 37, 1970, pp. 314-323. Also AERE-R 5650, 1967.
- J. Boocock, A. S. Furzer, and J. R. Matthews, The Effect of Porosity on the Elastic Moduli of UO₂ as Measured by an Ultrasonic Technique, AERE-M 2565, September 1972.
- 2.6-9 J. R. Matthews, Mechanical Properties and Diffusion Data for Carbide and Oxide Fuels, Ceramics Data Manual Contribution, AERE-M2643, 1974.
- 2.6-10 A. W. Nutt, Jr., A. W. Allen, and J. H. Handwerk, "Elastic and Anelastic Response of Polycrystalline UO₂-PuO₂," *Journal of the American Ceramic Society*, 53, 1970, p. 205.
- 2.6-11 A. de Novion et al., "Mechanical Properties of Uranium Plutonium Based Ceramics," *Nuclear Metallurgy*, 17, 1970, pp. 509-517.
- 2.6-12 V. M. Baranov et al., "In-Reactor Measurements of the Modulus of Elasticity of Uranium Dioxide," Soviet Atomic Energy, 40, 1976, pp. 37-39.
- 2.6-13 M. O. Marlowe and A. I. Kaznoff, "Elastic Behavior of Uranium Dioxide," *Journal of the American Ceramic Society*, 53, 1970, pp. 90-99.
- 2.6-14 R. J. Forlano et al., "Elasticity and Anelasticity of Uranium Oxides at Room Temperature: I Stoichiometric Oxide," *Journal of the American Ceramic Society*, 50, 1967, pp. 92-96.
- 2.6-15 R. Scott et al., "The Plastic Deformation of Uranium Oxides Above 800 °C," Journal of Nuclear Materials, 1, 1959, pp. 39-48.
- 2.6-16 D. R. Olander, Fundamental Aspects of Nuclear Reactor Fuel Elements, TID-26711-P1, 1976, pp. 160-166.
- 2.6-17 J. B. Wachtman et al., "Exponential Temperature Dependence of Young's Modulus for Several Oxides," *Physics Review*, 122, 6, 1961, pp. 1754-1759.
- 2.6-18 M. O. Marlowe and D. R. Wilder, "Elasticity and Internal Friction of Polycrystalline Yttrium Oxide," Journal of the American Ceramic Society, 48, 1965, pp. 227-233.

- 2.6-19 N. Igata and K. Domoto, "Fracture Stress and Elastic Modulus of Uranium Dioxide Including Excess Oxygen," *Journal of Nuclear Materials*, 45, 1972/73, pp. 317-322.
- 2.6-20 D. P. H. Hasselman and R. M. Fulrath, "Effect of Cylindrical Porosity on Young's Modulus of Polycrystalline Brittle Materials," *Journal of the American Ceramic Society*, 48, 1965, p. 545.
- 2.6-21 I. S. Sokolnikoff and R. D. Specht, *Mathematical Theory of Elasticity*, 2nd Edition, NewYork: McGraw-Hill Book Company, Inc., 1956.
- 2.6-22 J. B. Wachtman, Jr., M. L. Wheat, H. J. Anderson, and J. L. Bates, "Elastic Constants of Single-Crystal UO₂ at 25 °C," *Journal of Nuclear Materials*, 16, 1, 1965, p. 39.

2.7 Creep (FCREEP)

The fuel creep model, FCREEP, calculates creep rate of UO₂ and (U, Pu)O₂ fuels. Fuel creep affects the width of the gap between fuel pellets and cladding and hence the temperature gradient in the fuel rod. FCREEP was developed through use of both out-of-pile and in-pile data. The samples were high density (generally above 95% theoretically dense) and were irradiated to burnups too low for swelling to be a major factor. Therefore, the fuel dimensional changes calculated with the FCREEP subcode should simply be added to the dimensional changes calculated using other MATPRO correlations.

2.7.1 Summary

The FCREEP model calculates creep deformation of UO_2 or mixed oxide fuels. The model includes a time dependent creep rate for UO_2 , valid for both steady-state and transient reactor conditions. Fuel creep is modeled as a function of time, temperature, grain size, density, fission rate, oxygen to metal (O/M) ratio, and external stress.

At a transition stress (σ_t), the creep rate changes from a linear stress dependence to a creep rate proportional to stress to a power n. The transition stress is defined by

$$\sigma_{t} = \frac{1.6547 \times 10^{7}}{G^{0.5714}} \tag{2-60}$$

where

 σ_t = transition stress (Pa)

G = fuel grain size (μm).

The creep function is dependent on an Arrhenius type activation energy. This energy is found to be a function of the fuel O/M ratio. Increasing the O/M ratio increases the creep rate, all other things being constant. The activation energy of UO_2 below the transition stress is given by

$$Q_1 = 17884.8 \left\{ e^{\left[\frac{-20}{\ln(x-2)} - 8\right]} + 1 \right\}^{-1} + 72124.23$$
 (2-61)

where

Q₁ = activation energy below the transition stress (cal/mol)

x = O/M ratio.

The activation energy of UO2 above the transition stress is

$$Q_2 = 19872 \left[e^{\left(\frac{-20}{\ln(x-2)} - 8\right)} + 1 \right]^{-1} + 111543.5$$
 (2-62)

where Q₂ is the activation energy above the transition stress (cal/mol).

The steady-state creep rate of UO2 is determined using

$$\dot{\varepsilon} = \frac{(A_1 + A_2 \dot{F})\sigma e^{\left(\frac{Q_1}{RT}\right)}}{(A_3 + D)G^2} + \frac{(A_4 + A_8 \dot{F})\sigma^{4.5} e^{\left(\frac{Q_2}{RT}\right)}}{A_6 + D} + A_7 \sigma \dot{F} e^{\left(\frac{Q_3}{RT}\right)}$$
(2-63)

where

$$\dot{\epsilon}$$
 = steady-state creep rate (s⁻¹)

$$A_1 = 0.3919$$

$$A_2 = 1.3100 \times 10^{-19}$$

$$A_3 = -87.7$$

$$A_4 = 2.0391 \times 10^{-25}$$

$$A_6 = -90.5$$

$$A_7 = 3.72264 \times 10^{-35}$$

Uranium Dioxide/Mixed Oxides

$$A_8 = 0.0$$

$$\dot{F}$$
 = fission rate (fissions/m² · s)

$$\sigma$$
 = stress (Pa)

$$R = universal gas constant (J/mol \cdot K)$$

$$T = temperature (K)$$

G = grain size
$$(\mu m)$$

Q3 =
$$2.6167 \times 10^3$$
 (J/mol).

For mixed oxides, the steady-state creep rate is found using the equation

$$\dot{\varepsilon}_{s} = \frac{(B_{1} + B_{2}\dot{F})\sigma}{G^{2}} e^{\left[-\frac{Q_{3}}{RT} + B_{3}(1 - D) + B_{4}C\right]} + (B_{5} + B_{6}\dot{F})\sigma^{4.5} e^{\left[-\frac{Q_{4}}{RT} + B_{7}(1 - D) + B_{4}C\right]}$$
(2-64)

where

$$B_1 = 0.1007$$

$$B_2 = 7.57 \times 10^{-20}$$

$$B_3 = 33.3$$

$$B_4 = 3.56$$

$$B_5 = 6.469 \times 10^{-25}$$

$$B_6 = 0.0$$

$$B_7 = 10.3$$

$$Q_3 = 55354.0$$

$$Q_4 = 70451.0$$

$$C = PuO_2$$
 concentration (weight percent)

and the other terms have been previously defined.

When the applied stress (σ) is less than the transition stress (σ_t), the applied stress is used in the first term of Equation (2-63) or (2-64). For stresses greater than σ_t , the transition stress is used in the first term and the external stress is used in the second term of both equations.

When the fuel first experiences stress, usually during initial irradiation, or when a higher stress than in any other time step is applied, the strain rate is time dependent and is calculated using the equation

$$\dot{\varepsilon}_{T} = \dot{\varepsilon}_{S}[2.5e^{(-1.40\times10^{-6}t)} + 1] \tag{2-65}$$

where

 $\dot{\epsilon}_{\rm T}$ = the total strain rate (s⁻¹)

 $\dot{\epsilon}_{\rm S}$ = steady-state strain rate defined by Equation (2-63) (s⁻¹)

t = time since the largest stress was applied (s).

Equation (2-65) is the total creep rate function prescribed by the subcode FCREEP.

2.7.2 Model Development

Fuel deforms through a number of creep mechanisms depending on the stress, density, temperature, O/M ratio, irradiation level, and grain size. The FCREEP model is based on vacancy diffusion at low stress, dislocation climb at high stress, and a time dependent creep rate at all stresses at times less than 300 hours after a stress increase. The time dependent creep increases the creep rate over the steady-state value for times less than 300 hours but contributes little at longer times. Only constant volume creep is modeled in FCREEP, whereas hot pressing processes are being considered separately.

This subcode incorporates the UO_2 steady-state creep model proposed by Bohaboy, $^{2.7\text{-}1}$ with modifications suggested by Solomon $^{2.7\text{-}2}$ for fission enhanced and fission induced creep. The subcode also incorporates the $(U, Pu)O_2$ creep equation proposed by Evans et al. $^{2.7\text{-}3}$ modified in a similar manner to include fission enhanced creep. The constants proposed by Bohaboy and Solomon for UO_2 creep and by Evans for $(U, Pu)O_2$ creep were fit to the data base.

2.7.2.1 Steady-State Creep. Steady-state creep for ceramic fuel can be modeled as a two process phenomenon: (a) low stress creep based on vacancy diffusion and (b) power law creep based on dislocation

climb.

The theoretical model^{2.7-4} to ^{2.7-6} for viscous creep is based upon diffusion of vacancies from grain boundaries in tension to grain boundaries in compression. This model results in a creep rate that is (a) proportional to the vacancy diffusion coefficient, (b) inversely proportional to the square of the grain size, and (c) proportional to stress. Low stress creep can be written as

$$\dot{\varepsilon}_{S} = \left(\frac{A_{1}}{G^{2}}\right) \sigma e^{\left(\frac{Q_{2}}{RT}\right)}$$
 (2-66)

where the terms of the equation have been previously defined.

Equation (2-66) is based upon the assumption that volume diffusion controls the creep rate. Therefore, the creep rate is inversely proportional to the square of the grain size with an activation energy determined for volume diffusion. However, Coble^{2.7-7} has shown that if the diffusion path is along grain boundaries, the creep rate should be inversely proportional to the cube of the grain size with an associated activation energy that corresponds to grain boundary diffusion. Equation (2-66) is derived solely for diffusion of vacancies, but grain boundary sliding has been observed during low stress creep deformation of UO₂. ^{2.7-8,2.7-9} Both grain boundary sliding and diffusional creep have the characteristics of linear stress dependence and an activation energy nearly that of self diffusion. Therefore, it is not possible to distinguish between mechanisms of grain boundary sliding and diffusion. Regardless of which mechanism predominates, the form of Equation (2-66) is still applicable.

At high stresses, the movement of dislocations due to external shear stresses within the crystal structure results in a macroscopic movement of material. At high temperatures, dislocation climb can occur, which results in an increase in deformation rate by allowing dislocations to surmount barriers which normally would restrict movement. Weertman^{2.7-10} has proposed a model based upon dislocation climb which results in a creep rate proportional to stress raised to the 4.5 power. In this case, creep rate is not a function of grain size. This power law model for steady-state creep rate is

$$\dot{\varepsilon}_{S} = A_{2} \sigma^{4.5} e^{\left(\frac{Q_{2}}{RT}\right)} \tag{2-67}$$

where the terms of the equation have been previously defined.

2.7.2.2 Irradiated Fuel Creep. Equations (2-62) and (2-63) were modified to model enhanced creep rate due to irradiation following the method suggested by Solomon. Solomon concluded that inreactor creep of UO₂ is composed of (a) an elevated temperature regime, in which normal thermal creep mechanisms are enhanced, and (b) a low temperature regime, in which the fission process induces fuel creep. At temperatures less than 1,173 K, the creep rate is linearly proportional to fission rate and to stress. All the data appeared to lie within a broad scatter band that is insensitive to temperature. Evidence was insufficient to determine whether scatter is due primarily to variations of material properties (density, grain

size, stoichiometry, and impurity concentration), or test conditions (temperature, stress, and fission rate).

Solomon consolidated the results of Perrin^{2.7-11} and used Bohaboy's equation to arrive at the following expression:

$$\dot{\varepsilon}_{S} = \frac{(A_4 + A_8 \dot{F})}{(A_6 + D)} \sigma^{4.5} e^{\left(-\frac{Q_2}{RT}\right)} + \frac{(A_1 + A_2 \dot{F})}{(A_3 + D)G^2} \sigma e^{\left(\frac{Q_1}{RT}\right)} + Ag\sigma \dot{F}$$
(2-68)

where A_1 , A_2 , A_3 , A_4 , A_6 , A_8 , and A_9 are constants and the other terms of the equation have been previously defined. This equation assumes a fivefold increase in creep rate instead of the fourfold increase reported by Perrin at a fission rate of 1.2×10^{19} fission/m³/s. The five-fold increase is also assumed at higher stresses where dislocation creep occurs but where no experimental data are available.

Brucklacher et al.^{2.7-12} reported an equation for the fission induced creep up to 2.5% burnup of

$$\dot{\varepsilon} = 5.6e^{\left[\frac{2616.8}{T}\right]}\dot{F} \tag{2-69}$$

where $\dot{\epsilon}$ is the creep rate (s⁻¹).

Equation (2-69) is used in place of the last term of Equation (2-68), resulting in the final form of the UO₂ steady-state creep Equation (2-63).

For the creep of mixed oxides, the equation suggested by Evans et al., is adopted with similar modification for fission enhanced creep. The steady-state, mixed oxide creep rate equation is

$$\dot{\varepsilon}_{s} = \frac{(B_{1} + B_{2}\dot{F})}{G^{2}}\sigma e^{\left[-\frac{Q_{1}}{RT} + B_{3}(1-D) + B_{4}C\right]} + (B_{5} + B_{6}\dot{F})\sigma^{4.5}e^{\left[-\frac{Q_{2}}{RT} + B_{7}(1-D) + B_{4}C\right]}$$
(2-70)

where B₁, B₂, B₃, B₄, B₅, B₆, and B₇ are constants and the other terms of the equation have been previously defined.

2.7.2.3 Transition Stress. Wolfe and Kaufman^{2.7-13} pointed out that the stress at which the transition from viscous creep to power law creep occurs is only mildly dependent upon temperature, but more strongly affected by grain size. Seltzeret al.^{2.7-14,2.7-15} performed an analysis of the transition stress that presents circumstantial evidence for a power law creep rate with a 4.5 stress coefficient and a viscous creep rate with an inverse dependence on the square of the grain size. At the transition, Equations (2-66)

Uranium Dioxide/Mixed Oxides

and (2-67) can be equated:

$$\frac{A_1 \sigma}{G^2} e^{\left(\frac{Q_1}{RT}\right)} = A_2 \sigma^{4.5} e^{\left(\frac{Q_2}{RT}\right)}$$
(2-71)

where the terms of the equation have been previously defined.

Solving Equation (2-71) for the stress at the transition (σ_t):

$$\sigma_{t} = \left(\frac{A_{1}}{A_{2}}\right)^{1/3.5} G^{-0.57} e^{\left[\frac{Q_{2} - Q_{1}}{3.5RT}\right]} . \tag{2-72}$$

If the activation energies, Q_2 and Q_1 , are about the same magnitude, then the temperature dependence of σ_t should be minimal and the resulting transition stress is calculated using

$$\sigma_{\rm t} = AG^{-0.57}$$
 (2-73)

2.7.2.4 Time Dependent Creep. The time dependent creep rate is based on an anelastic creep equation and is used in FCREEP to calculate the creep rate of water reactor fuel during the first 300 hours after the stress on the fuel has been increased. The strain resulting from the time dependent stress can be a major portion of the total creep deformation. A number of time dependent creep functions were compared with transient creep data. In particular, time to a power used by other authors to describe UO₂ transient creep. Was tried; but the function found to best predict the transient creep data was the exponential function

$$\dot{\varepsilon}_{t} = 2.5[1 + e^{(-at)}]$$
 (2-74)

where

 $\dot{\varepsilon}_t$ = time dependent creep rate (s⁻¹)

a = constant

t = time(s).

Since this subcode is to be used to calculate both steady-state and transient reactor conditions, the anelastic form of time dependent creep was used because it better predicted the creep data for all times. The anelastic equation is multiplied by the steady-state creep rate to obtain the total creep rate.

$$\dot{\varepsilon}_{T} = [1 + 2.5e^{(-at)}]\varepsilon_{s} \tag{2-75}$$

where $\dot{\epsilon}_T$ is the total creep rate (s⁻¹) and the other terms of the equation have been previously defined.

2.7.3 Evaluation of Constants and Data Comparison

Data selection for code development use was based on the following requirements:

- 1. The data results from compressive creep tests were considered.
- 2. The initial O/M ratio was measured and documented.
- 3. The temperature was measured and documented.
- 4. The grain size was measured and documented.

Requirement (2) prevented the use of some data in determining the constants of FCREEP. These data were used after the creep model was developed (with an assumed O/M ratio) as an extra data comparison, and no significant deviation was noted.

2.7.3.1 Evaluation of Steady-State Creep Constants. The basic form of the steady-state equation of Solomon and Evans et al. was retained, but some of the constants were refit to include the effect of the fuel O/M ratio. The activation energies of Equations (2-61) and (2-62) were determined by calculating the creep rate using the data reported by Burton and Reynolds, ^{2.7-18,2.7-19} Seltzer et al., ^{2.7-15} and Bohaboy et al. ^{2.7-1} These were data of UO₂ under different stresses, temperatures, and O/M ratios. Fitting the equations to the available data gave effective activation energies, which changed less as the O/M ratio increased than is reported in the literature. ^{2.7-15}

Other creep data considered while developing the subcode are Bohaboy and Asamoto, ^{2.7-20} Speight, ^{2.7-21} Brucklacher and Dienst, ^{2.7-22} Solomon, ^{2.7-23} Scott et al., ^{2.7-24} and Armstrong and Irvine. ^{2.7-25}

The activation energies found to give the best fit to the base data were

(1) for low stresses,

$$Q_1 = 17884.8 \left\{ e^{\left[\frac{-20.0}{\log(x-2.0)} - 8.0\right]} + 1.0 \right\}^{-1} + 72124.23 . \tag{2-76}$$

(2) for high stresses,

Uranium Dioxide/Mixed Oxides

$$Q_2 = 19872.0 \left\{ e^{\left[\frac{-20.0}{\log(x-2.0)} - 8.0\right]} + 1.0 \right\}^{-1} + 112142.4 . \tag{2-77}$$

After the approximate activation energies were determined, the equations were further evaluated against the data of Bohaboy et al.^{2.7-1} to refine the constants. Figure 2-21 shows the calculated creep rates plotted against experimental data. Those data which did not have a documented O/M ratio are shown, along with the data used to develop the code. Figure 2-22 shows the calculated creep rates for irradiated fuel compared to the experimental data base. The uncertainty of the FCREEP calculations was determined as the standard deviation of the log of the calculated creep rate compared with the log of the corresponding creep rate. The uncertainty range is shown as dashed lines in Figure 2-21 and Figure 2-22. The uncertainty creep rates can be calculated using the equation:

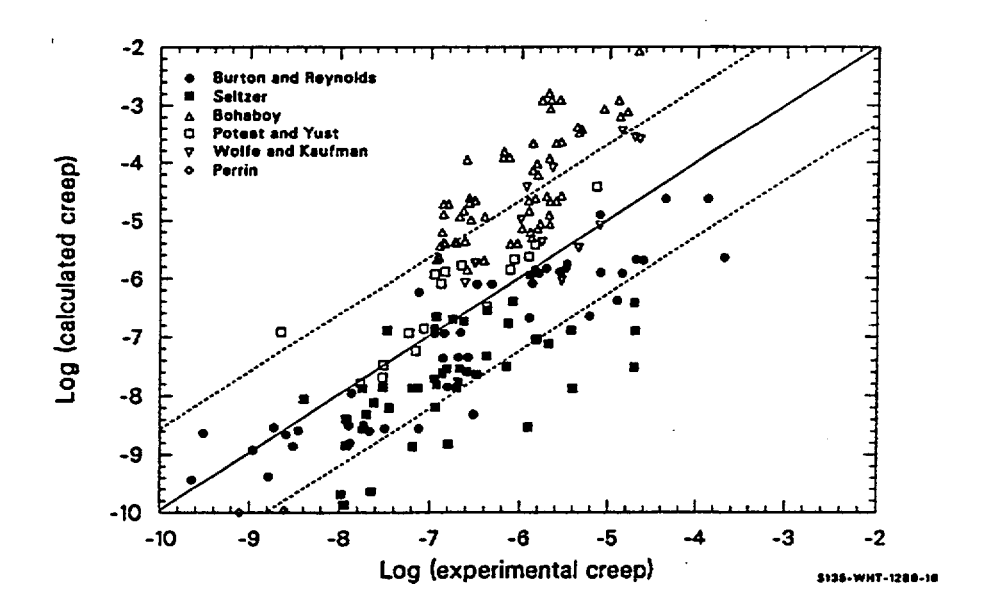


Figure 2-21. Comparison of unirradiated UO₂ experimental data with corresponding calculated values from FCREEP.

$$\dot{\varepsilon}_{\rm u} = \dot{\varepsilon} \times 10^{\rm U} \tag{2-78}$$

where

$$\dot{\epsilon}_u$$
 = upper and lower bounds of creep rate (s⁻¹)

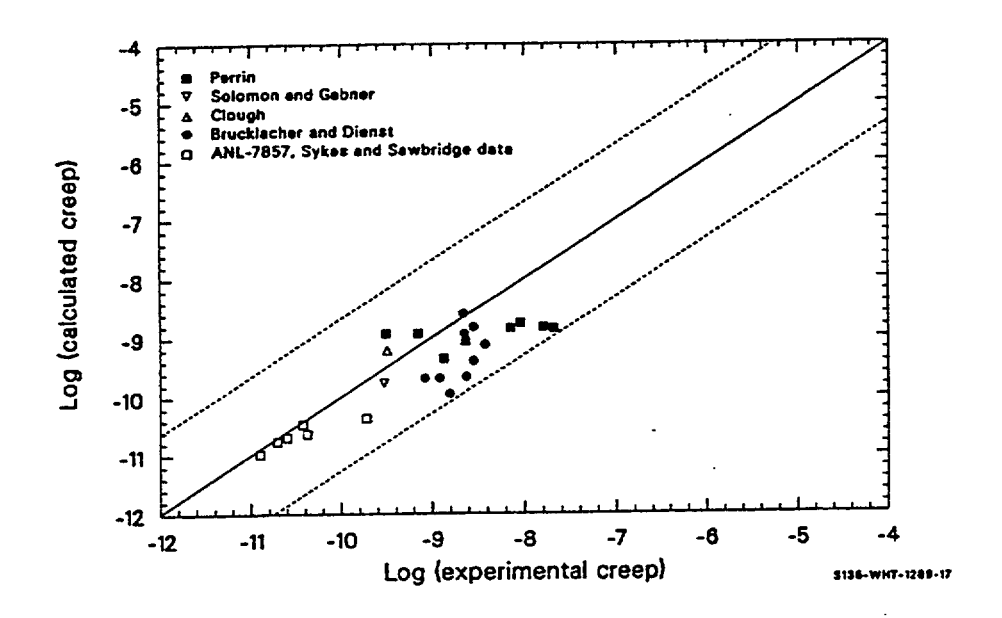


Figure 2-22. Comparison of irradiated UO₂ experimental data with corresponding calculated values from FCREEP.

$$\dot{\epsilon}$$
 = FCREEP calculated creep rate (s⁻¹)

U = ± 1.25 .

2.7.3.2 Evaluation of Constants for Irradiation Enhanced Creep. The data sources used to evaluate the constants for the last term of Equation (2-63) are the fission induced creep tests of Sykes and Sawbridge, Clough, Clough, End Brucklacher and Dienst, and Solomon and Gebner and in-pile creep measurements of Perrin, Vollath, Cloud and Slagle. These data were considered by Solomon, who developed Equation (2-63) except for the last term, which was proposed by Brucklacher et al. 2.7-12

In Figure 2-23, the predictions of FCREEP are compared with mixed oxide creep data selected from compressive experiments with O/M ratios between 1.95 and 1.98. This comparison includes data from Evans et al., 2.7-3 Routbort et al., 2.7-32 and Perrin. 2.7-33 Good agreement is obtained for O/M ratios between 1.95 and 1.96 and grain sizes between 18 and 23 µm. However, measured values for the 4-µm material used by Evans et al. 2.7-3 are one to two orders of magnitude higher than the corresponding values calculated by FCREEP. Also, the high stress data of Routbort 2.7-32 (in the dislocation controlled creep regime) compare favorably with FCREEP calculations even though the O/M ratio is slightly higher than 1.95. The low stress data lie about an order of magnitude higher than calculated by the FCREEP model, indicating the significance of the stoichiometry on the diffusion mechanism in the viscous creep regime. Perrin's 2.7-33 data were used to determine the constants for fission enhanced creep in the linear stress creep

of Equation (2-70). Reasonably good agreement is achieved for the irradiated material, but the calculated values for unirradiated material are about an order of magnitude less than experimental values. The solid line represents perfect agreement between experimental and calculated values.

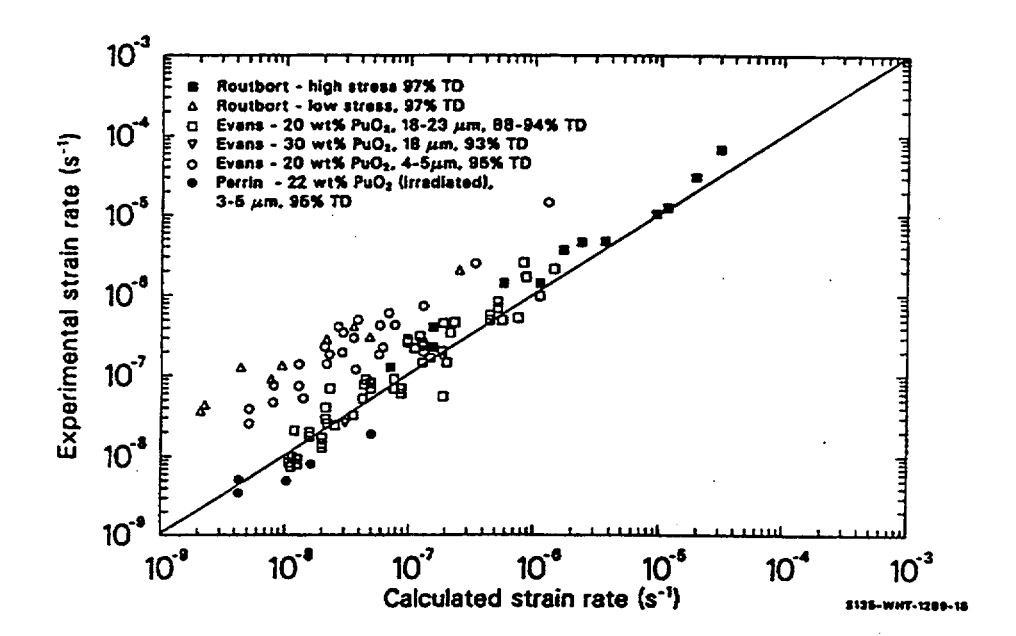


Figure 2-23. Comparison of $(U,Pu)O_2$ experimental data with corresponding calculated values from FCREEP.

2.7.3.3 Evaluation of Constants for Time Dependent Creep. Much of the reported creep rate data do not include the time dependent creep contribution, and the reported steady-state data probably include those contributions, making an accurate analysis difficult. Some excellent creep studies reporting both time dependent and steady-state creep have been reported. A comprehensive study was conducted by Battelle Columbus Laboratories. ^{2.7-11,2.7-34,2.7-35} They evaluated creep of UO₂ under both irradiated and unirradiated conditions. These data were used as the data base, along with the data reported by Solomon, ^{2.7-29,2.7-36} Clough, ^{2.7-37} Dienst, ^{2.7-38} and Brucklacher and Dienst. ^{2.7-22}

Evaluation of the time dependent creep equation was carried out, using the reported steady-state creep rate and then determining the appropriate function to follow the curve and have the appropriate magnitude after a number of iterations. The best estimate equation is

$$\dot{\varepsilon}_{t} = 2.5 e^{(-1.4 \times 10^{-6} t)} \dot{\varepsilon}_{s} \tag{2-79}$$

where the terms of the equation have been previously defined.

Examples of the strain determined using the final strain rate equation are shown in Figure 2-24 and Figure 2-25. They show the FCREEP calculated strain compared with the base data and show a reasonably good fit.

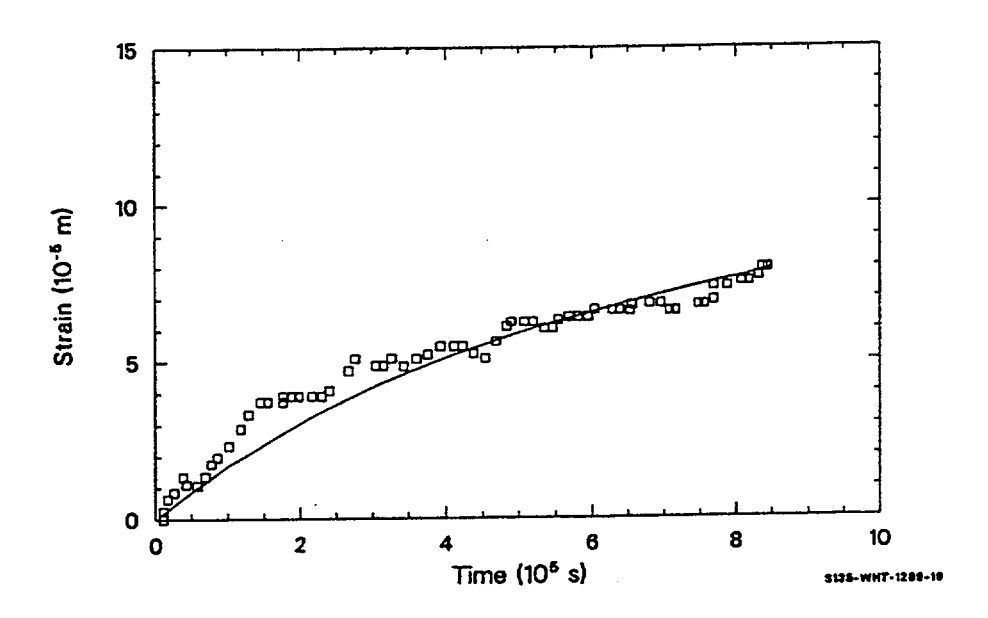


Figure 2-24. Comparison of UO₂ strain data of Rod 3C with corresponding calculated values from FCREEP.

$$\dot{\varepsilon}_{t} = [2.5e^{(-1.4 \times 10^{-6}t)} + 1]\dot{\varepsilon}_{s} . \tag{2-80}$$

2.7.4 References

- 2.7-1 P. E. Bohaboy, R. R. Asamoto, and A. E. Conti, Compressive Creep Characteristics of Stoichiometric Uranium Dioxide, GEAP-10054, May 1969.
- 2.7-2 A. A. Solomon, J. L. Routbort, and J. C. Voglewede, Fission Induced Creep of UO₂ and Its Significance to Fuel Element Performance, ANL-7857, September 1971.
- 2.7-3 S. K. Evans, P. E. Bohaboy, and R. A. Laskiewicz, *Compressive Creep of Urania Plutonia Fuels*, GEAP-13732, August 1971.
- 2.7-4 J. S. Perrin and W. R. D. Wilson, Effect of Irradiation on the Creep of Uranium Dioxide, BMI-1899, March 1971.
- 2.7-5 F. R. N. Nabarro, Report of a Conference on the Strength of Solids, *Physical Society, London, England, 1949*, p. 75.

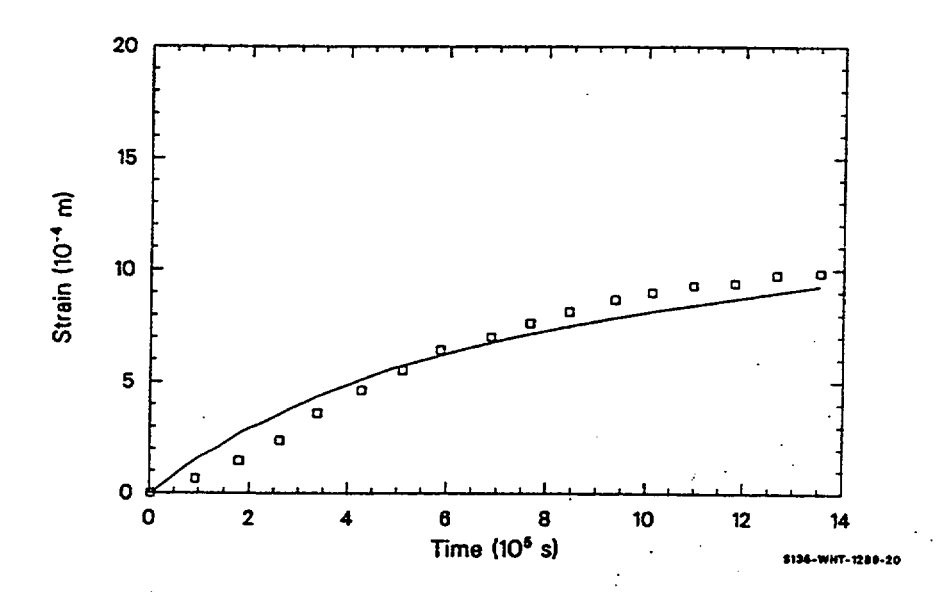


Figure 2-25. Comparison of UO₂ strain data of Capsule 2 with corresponding calculated values from FCREEP.

- 2.7-6 C. Herring, "Diffusional Viscosity of Poly-Crystalline Solid," *Journal of Applied Physics*, 21, 1950, p. 437.
- 2.7-7 R. L. Coble, "A Model for Boundary Diffusion Controlled Creep in Poly-Crystalline Materials," *Journal of Applied Physics*, 34, 1963, p. 1679.
- 2.7-8 W. M. Armstrong, W. R. Irvine, and R. H. Martinson, "Creep Deformation of Stoichiometric Uranium Dioxide," *Journal of Nuclear Materials*, 7, 2, 1962, pp. 133-141.
- 2.7-9 L. E. Poteat and C. S. Yust, Grain Boundary Reactions During Deformation, ORNL-P-2371, 1965.
- 2.7-10 J. Weertman, "Steady-State Creep Based Through Dislocation Climb," *Journal of Applied Physics*, 28, 1957, p. 362.
- 2.7-11 J. S. Perrin, "Irradiation Induced Creep of Uranium Dioxide," *Journal of Nuclear Materials*, 39, 1971, pp. 175-182.
- 2.7-12 D. Brucklacher, W. Dienst, and F. Thummler, Creep Behavior of Oxide Fuels Under Neutron Irradiation, translated from German by J. L. Routbort, Argonne National Laboratory, ANL-Trans-942, May 1973.

- 2.7-13 R. A. Wolfe and S. F. Kaufman, *Mechanical Properties of Oxide Fuels*, WAPD-TM-587, October 1967.
- 2.7-14 M. S. Seltzer, A. H. Clauer, and B. A. Wilcox, "The Stress Dependence for High Temperature Creep of Polycrystalline Uranium Dioxide," *Journal of Nuclear Materials*, 34, 1970, pp. 351-353.
- 2.7-15 M. S. Seltzer, J. S. Perrin, A. H. Clauer, and B. A. Wilcox, "A Review of Creep Behavior of Ceramic Nuclear Fuels," *Reactor Technology*, 14, 2, January 1971, pp. 99-135.
- 2.7-16 J. R. Matthews, Mechanical Properties and Diffusion Data for Carbide and Oxide Fuels, AERE-M-2643, September 1974.
- 2.7-17 R. G. Sachs, Reactor Development Program Progress Report, ANL-RDP-16, April-May 1973.
- 2.7-18 B. Burton and G. L. Reynolds, "The Diffusional Creep of Uranium Dioxide: Its Limitation by Interfacial Processes," *Acta Metallurgical*, 21, August 1973, pp. 1073-1078.
- 2.7-19 B. Burton and G. L. Reynolds, "The Influence of Deviations from Stoichiometric Composition on the Diffusional Creep of Uranium Dioxide," *Acta Metallurgical*, 21, December 1973, pp. 1641-1647.
- 2.7-20 P. E. Bohaboy and R. R. Asamoto, "Compressive Creep Characteristics of Ceramic Oxide Nuclear Fuels: Part I: Uranium Dioxide," American Ceramic Society Nuclear Division, Pittsburgh, PA, October 6-8, 1968.
- 2.7-21 M. V. Speight, Enhancement of Diffusion Creep Under Irradiation, Central Electricity Generating Board, RD/B/N-2402, August 1972.
- 2.7-22 D. Brucklacher and W. Dienst, "Creep Behavior of Ceramic Nuclear Fuels Under Irradiation," Journal of Nuclear Materials, 42, 1972, pp. 285-296.
- 2.7-23 A. A. Solomon, "Effect of c-Radiation on the Deformation of UO₂," Journal of Nuclear Materials, 47, 1973, pp. 345-346.
- 2.7-24 R. Scott, A. R. Hall, and J. Williams, "The Plastic Deformation on Nonstoichiometric Uranium Dioxide," *Journal of Nuclear Materials*, 1, 1959, pp. 39-48.
- 2.7-25 W. M. Armstrong and W. R. Irvine, "Creep Deformation on Nonstoichiometric Uranium Dioxide," *Journal of Nuclear Materials*, 9, 2, 1963, pp. 121-127.
- 2.7-26 E. C. Sykes and P. T. Sawbridge, *The Irradiation Creep of Uranium Dioxide*, Central Electricity Generating Board, RD/BN/1489, November 1969.
- 2.7-27 D. J. Clough, "Irradiation Induced Creep of Ceramic Fuels," Proceedings on Fast Reactor Fuel and Fuel Elements, GFK Karlsruhe, 1970, p. 321.

- 2.7-28 D. Brucklacher and W. Dienst, "Kontinuierliche Messung Des Kriechens von UO₂ Unter Bestrahlung," *Journal of Nuclear Materials*, 36, 1970, pp. 244-247.
- 2.7-29 A. A. Solomon and R. H. Gebner, Instrumented Capsule for Measuring Fission Induced Creep of Oxide Fuels," *Nuclear Technology*, 13, February 1972, p. 177.
- 2.7-30 D. Vollath, "Thermisches Kriechen von Plutonium-Haltigen Oxidischen Kernbrennstoffen," Reactor Meeting, Bonn, Germany, March 30, 1971, pp. 558-561.
- 2.7-31 O. D. Slagle, High Temperature Creep of UO₂-20 wt% PuO₂, HEDL-TME-71-28, August 1971.
- 2.7-32 J. L. Routbort, N. A. Javed, and J. C. Voglewede, "Compressive Creep of Mixed Oxide Fuel Pellets," *Journal of Nuclear Materials*, 44, 1972, pp. 247-259.
- 2.7-33 J. S. Perrin, "Effect of Irradiation on Creep of UO₂-PuO₂," Journal of Nuclear Materials, 42, 1972, pp. 101-104.
- 2.7-34 J. S. Wilson and R. D. William, Effect of Irradiation on the Creep of Uranium Dioxide, BMI-1899, March 1971.
- 2.7-35 W. R. D. Wilson and J. S. Perrin, "Anisothermal Effects During In-Pile Creep Testing of Uranium Dioxide, Nuclear Science and Engineering, 45, 1971.
- 2.7-36 A. S. Solomon, "Radiation Induced Creep of UO₂," Journal of the American Ceramic Society, 56, March 1973.
- 2.7-37 D. J. Clough, "Creep Properties of Oxide and Carbide Fuels Under Irradiation," *Journal of Nuclear Materials*, 65, 1977.
- 2.7-38 W. Dienst, "Irradiation Induced Creep of Ceramic Nuclear Fuels," *Journal of Nuclear Materials*, 65, 1977.

2.8 Densification (FUDENS)

The subcode FUDENS calculates fuel dimensional changes due to irradiation induced densification of UO₂ and (U, Pu)O₂ fuels during the first few thousand hours of water reactor operation. Densification is calculated as a function of fuel burnup, temperature, and initial density. This subcode is based on data of fuel that had small amounts of hydrostatic stress applied. Densification can result from hydrostatic stress on the fuel due to contact with the cladding, which is considered in Section 2.10. Both models describe the same physical process; the model which calculates the greater densification should be used.

The data used to develop FUDENS were taken from irradiated fuel which was also swelling. If fuel densification is much greater than swelling during the first 1,000 hours of irradiation, then, to a first approximation, swelling can be neglected during this period. That was done for the development of the

FUDENS model. A suggested calculation procedure, combining calculations of models given in this section with pressure sintering and fuel swelling models, is discussed in Section 2.9.

2.8.1 Summary

The subcode FUDENS uses one of two methods to calculate the maximum density change during irradiation. The density change observed during a resintering test (1,973 K for more than 24 hours) in a laboratory furnace is the preferred input for the calculation. If a resintering density change is not input, the code uses the initial unirradiated density of the fuel and the fuel fabrication sintering temperature for the calculations. These inputs are used in the following equations to calculate the maximum densification length change during irradiation.

If a nonzero value for the resintering density change is input,

when FTEMP < 1,000 K,

$$\left(\frac{\Delta L}{L}\right)_{m} = -(0.0015)RSNTR \quad . \tag{2-81}$$

When FTEMP $\geq 1,000 \text{ K}$,

$$\left(\frac{\Delta L}{L}\right)_{m} = -(0.00285)RSNTR \quad . \tag{2-82}$$

If zero is input for the resintering density change, when FTEMP < 1,000 K,

$$\left(\frac{\Delta L}{L}\right)_{m} = \frac{-22.2(100 - DENS)}{(TSINT - 1453)}$$
 (2-83)

When FTEMP > = 1,000K,

$$\left(\frac{\Delta L}{L}\right)_{m} = \frac{-(66.6)(100 - DENS)}{(TSINT - 1453)}$$
(2-84)

where

 $\left(\frac{\Delta L}{L}\right)_m$ = maximum possible dimension change of fuel due to irradiation (percent)

RSNTR = resintered fuel density change (kg/m^3)

FTEMP = fuel temperature (K)

DENS = theoretical density (percent)

TSINT = sintering temperature (K).

Densification as a function of burnup is calculated using

$$\frac{\Delta L}{L} = \left(\frac{\Delta L}{L}\right)_{m} + e^{[-3(FBU+B)]} + (2.0e^{[-35(FBU+B)]})$$
 (2-85)

where

 $\left(\frac{\Delta L}{L}\right)$ = dimension change (percent)

FBU = fuel burnup (MWd/kgU)

B = a constant determined by the subcode to fit the boundary condition: $\Delta L/L$ when FBU = 0.

The FUDENS subcode uses Equation (2-85) to calculate total densification and then subtracts the densification from the previous time step to obtain the incremental densification. The incremental densification for the time step being considered is the output of the subcode FUDENS.

2.8.2 Uranium Dioxide and Mixed Oxide Densification Data and Models

The sintering of cold pressed UO₂ powder may be divided usefully into three regimes: (a) the formation of necks between particles, (b) the decrease of interconnected porosity, and (c) the subsequent volume reduction of isolated pores.^{2.8-1} The last stage begins when 92 to 95% theoretical density (TD) is reached. Two types of porosities, open along grain edges and closed along grain boundaries, are present in low density fuels, less than 92% TD, sintered at low temperatures. However, at higher sintering temperatures, accelerated grain growth occurs; and closed porosity may be found inside the grains even in low density fuel pellets.^{2.8-2} In-reactor densification involves the third sintering regime in which fine, isolated, closed porosity (located either at grain boundaries or within the grains) is annihilated.

2.8.2.1 Uranium Dioxide and Mixed Oxide Densification Data. Edison Electric Institute/ Electric Power Research Institute (EEI/EPRI)^{2.8-3,2.8-4} performed a comprehensive study of UO₂ fuel densification. The fuel was tested in the RAFT (Radially Adjustable Facility Tubes) of the General Electric Test Reactor (GETR), located in Pleasanton, CA. Pre- and post-irradiation physical properties were reported on fuel subjected to burnups of up to 3.5 MWd/kgU. It was concluded that irradiation induced

densification can be correlated with fuel microstructure, that is, the largest in-reactor density changes occurred for fuel types having a combination of the smallest pore size, the largest volume percent of porosity less than 1 μ m in diameter, the smallest initial grain size, and the lowest initial density. The volume fraction of porosity less than 1 μ m in diameter contributed significantly to densification of the fuel types studied; and density increases were accompanied by a significant decrease in volume fraction of pores in this size range. The volume fraction of pores ranging in diameter from 1 to 10 μ m initially increased with densification but decreased with continued densification. Significant density increases occurred during irradiation, with only minimal increases in grain size.

Analysis of the EPRI data also shows that pellets in low burnup, low fission rate, and low temperature regions densify less than pellets irradiated to the same burnup but in higher fission rate and temperature positions, as shown in Figure 2-26. At higher fission rates and temperatures, densification occurs rapidly, with pellets approaching maximum densities at a burnup of 1 MWd/kgU. At lower fission rates, densification appears to be increasing with a fuel burnup of 2 MWd/kgU.

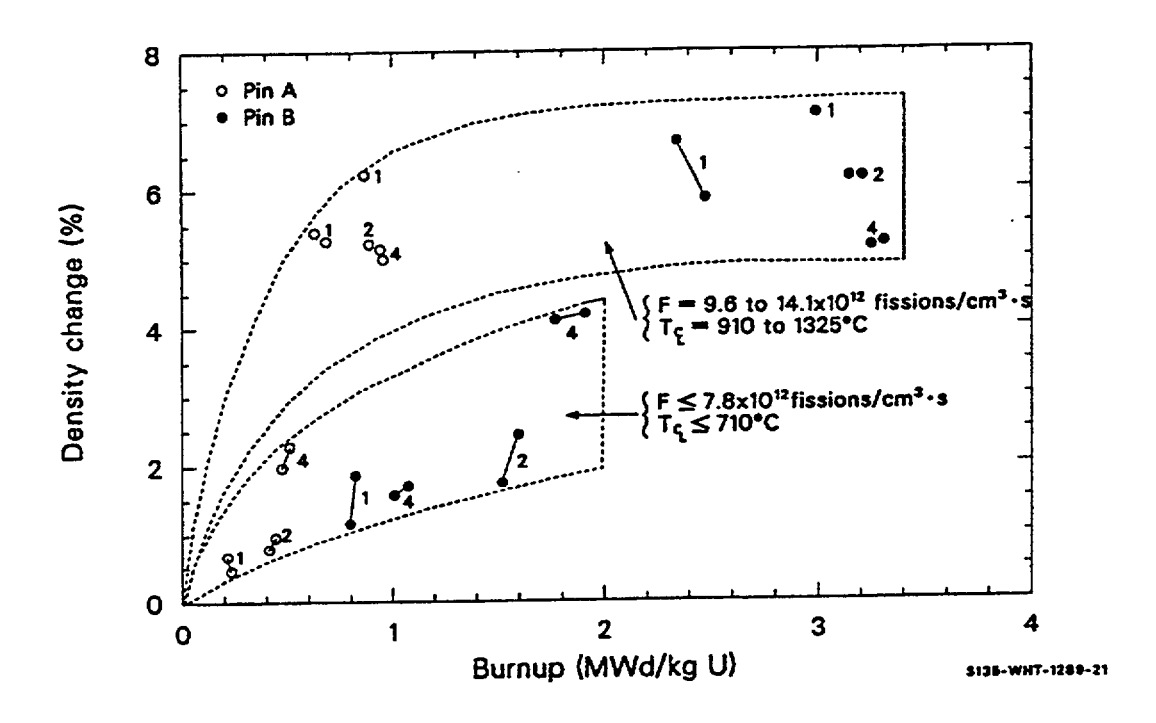


Figure 2-26. The effect of burnup and fission rate on the fuel density change for EPRI fuel types 1, 2, and 4.

Rolstad et al.^{2.8-5} measured the fuel stack length change of UO₂ in the Halden HBWR reactor. Fuel densities (87, 92, and 95% TD), fabrication sintering temperatures, irradiation power levels, and fuel cladding gap sizes were used to study irradiation induced densification. Rolstad found that fuel sintered at the highest temperature densified the least (stable fuel) and fuel sintered at the lowest temperature densified the most (unstable fuel). The axial length change, measured during irradiation and as a function of burnup (Figure 2-27) for different power levels, did not depend on reactor power levels or fuel

temperatures. Hanevik et al.^{2.8-6} proposed that this may be attributed to the fact that temperatures of the outer edges (shoulders) of the pellet would be within 200 to 300 K of each other at both power levels. Since the shoulders of the pellet are much colder than its center, the axial in-reactor length change measurements are probably a measurement of the shrinkage in these regions (low temperature irradiation densification). The amount of fuel stack length change of the Halden fuel was found to depend on out-of-pile thermal fuel stability, initial density, and burnup.

Collins and Hargreaves $^{2.8-7}$ compared measurements of out-of-pile sintering rates at temperatures greater than 1,600 K with the sintering rates of fuel irradiated in the Windscale Advanced Gas Cooled Reactor (WAGR). The observed out-of-pile densification was attributed to the sintering of grain boundary porosity and was characterized by an activation energy of 2.9 x 10^5 J/mol for grain boundary diffusion. Extrapolation of these results to 1,000 K, the approximate temperature of the in-pile material, indicated that negligible thermal sintering would be expected after a few hundred hours at this temperature. In addition, no evidence of sintering was observed in out-of-pile annealing tests conducted at 1,173 K and a pressure of 2.06 MPa. However, fuel irradiated to less than 0.3% burnup at temperatures between 1,000 and 1,100 K experienced significant reduction in diameter. This shrinkage was attributed to irradiation induced sintering, which decreased the initial fuel porosity volume. Pores with diameters less than 3 μ m were reported by Collins and Hargreaves to be the major source of increased density. Pores with diameters greater than 10 μ m were reported stable during irradiation at temperatures below 1,500 K.

Ferrari et al.^{2.8-8} measured UO₂ fuel pellet densification in commercial reactors using both movable in-core flux detectors and post-irradiation examination of selected test rods. The densification rate of the fuel was reported to occur rapidly during the early stages of irradiation and then slow or even stop after about 6 to 10 MWd/kgU, as shown in Figure 2-28. These results are consistent with the measurements of Rolstad et al. For 92% TD, the extent of densification was reported to vary significantly with microstructure, but no microstructure details were reported. Ferrari et al. reported that power levels between 4.9 and 55.8 kW/m did not significantly affect densification. This result is in agreement with Rolstad et al. The axial shrinkage was suggested to be controlled by densification in the shoulder of the fuel pellets, a region of the fuel pellets where the temperature is generally below 1,073 K, a temperature too low for in-pile densification to be attributed to thermal mechanisms. Ferrari et al. proposed that the kinetics of densification are compatible with irradiation enhanced diffusion processes.

Metallographic measurements on the fuel by Ferrari et al., indicated that the irradiation enhanced densification was associated with the disappearance of fine pores and that pore shrinkage significantly decreased with increasing pore size. These results correspond to the EPRI findings. Ferrari et al. suggested that densification could be reduced through both microstructural control of the fuel pellet and a reduction of the fine porosity content. Both of these factors are influenced by the fabrication process, especially the sintering temperature and the use of so called pore formers. Ferrari et al. reported that experimental fuel of 89% theoretical density has been made and demonstrated to be relatively stable in the Saxton reactor.

Heal, et al. $^{2.8-9}$ reported that they have developed UO₂ fuel which does not densify significantly by controlling the pore size. They assumed that shrinkage of the pores would continue until the internal pressure of trapped gas in the pores matched the surface tension forces. Their calculations show shrinkage in pores of diameters greater than 20 μ m and that pores of 10 μ m shrink only to 6 to 7 μ m before gas stabilization occurs, whereas voids of 1.0 μ m or less shrink to 0.2 μ m or less before gas stabilization

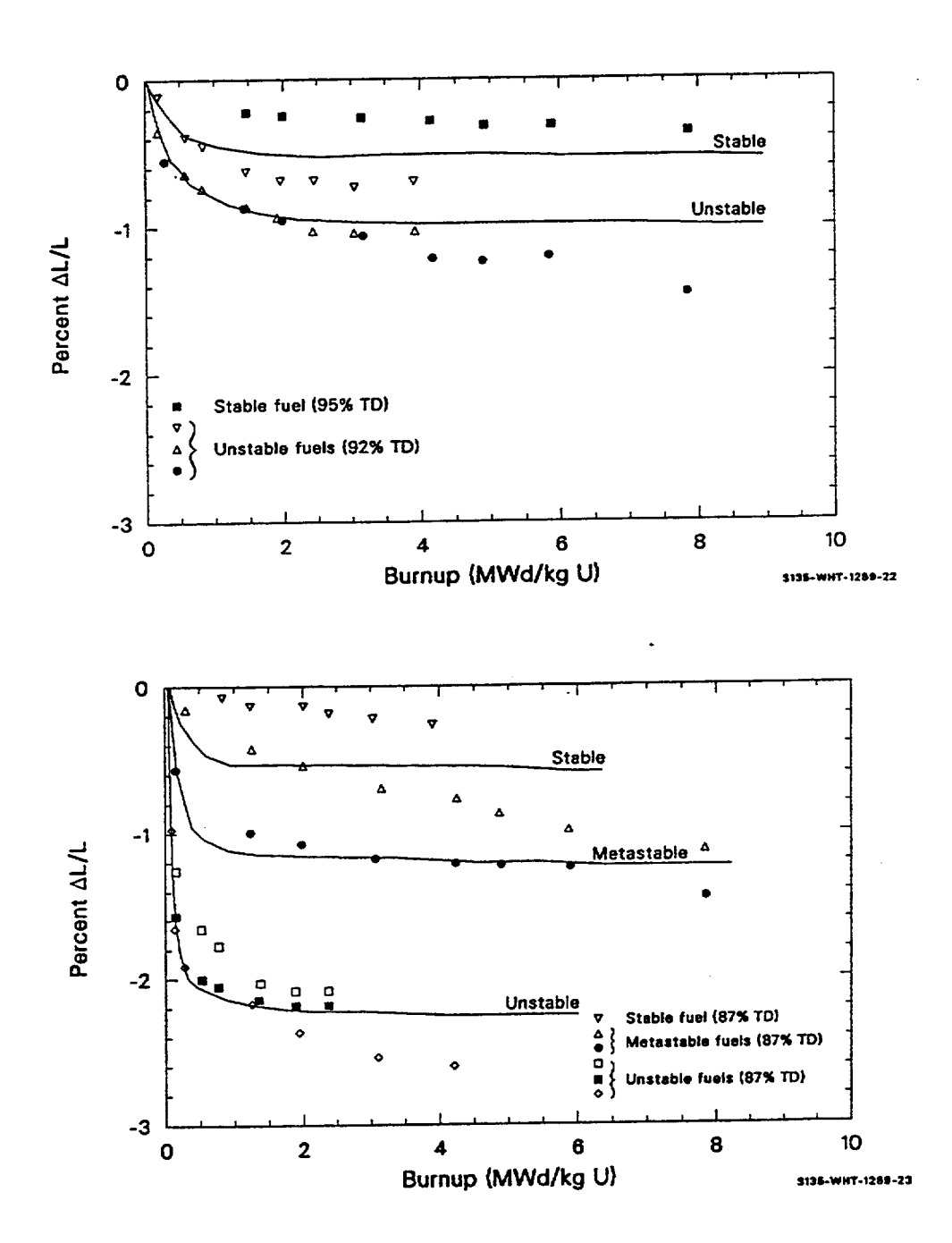


Figure 2-27. Change in fuel stack length of Halden fuel as a function of burnup.

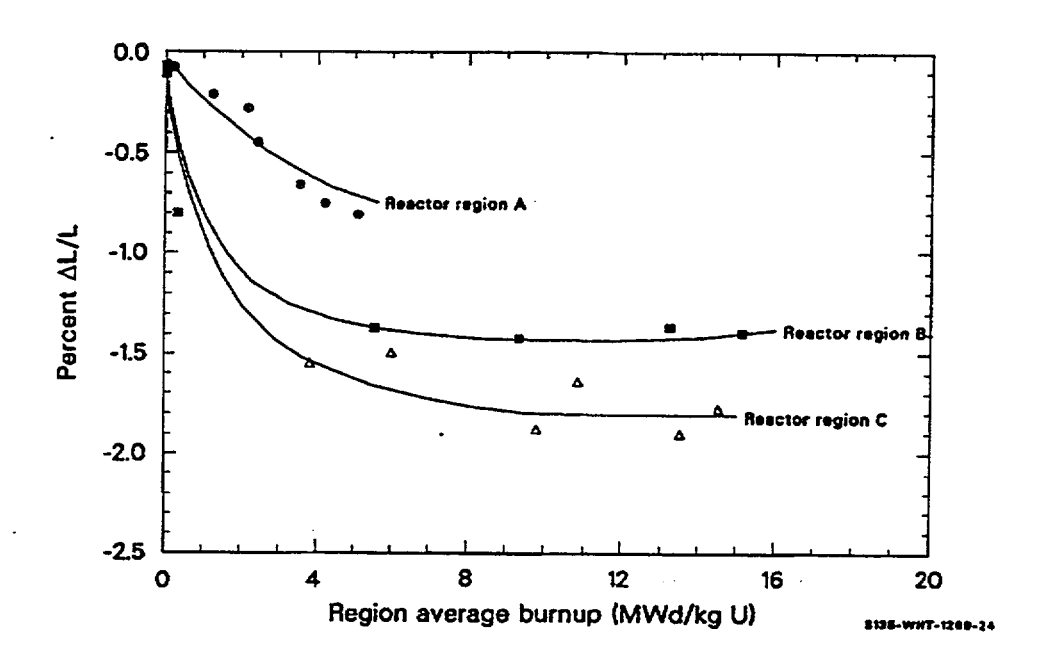


Figure 2-28. Fuel stack length changes for 92% TD UO₂ processed by different techniques. occurs, causing considerable densification. Fuel pellets fabricated with porosity sizes greater than 25 μ m were irradiated by Heal et al. to 1.4 x 10^{26} fissions/m³ with center temperatures up to 1,873 K. Postirradiation examination of these pellets showed significantly less than 1% volume densification.

Ross^{2.8-10} has shown that fuel after an irradiation of 2 x 10^{25} fission/m³ has lost most pores with radii less than 0.5 μ m. He found that fuels with burnups even as low as 2 x 10^{24} fissions/m³ had lost most pores with radii less than 0.3 μ m.

Burton and Reynolds^{2.8-11} measured the shrinkage of three fuel pellets of 96.5% TD UO₂ with isolated porosity at grain boundaries during the final stage of out-of-pile sintering. The densification rate was initially large but decreased with longer sintering times. (The shapes of these curves are very similar to those obtained for the in-pile densification of UO₂; however, in-pile densification occurs at much lower temperatures.) This reduction in the densification rate with time can arise for several reasons: (a) grain boundaries may migrate away from cavities; (b) when significant entrapped gas is present, cavities may shrink until they become stabilized as the internal gas pressure becomes equal to the surface tension of the cavity, as proposed by Heal et al.; and/or (c) the number of cavities can progressively decrease as densification proceeds. The first and second reasons were rejected by Burton and Reynolds because the majority of the cavities in their samples remained on grain boundaries during sintering and smaller cavities centered to closure. Therefore, Burton and Reynolds suggested that the reduction in the densification rate with time is only due to the progressive reduction in the number of cavities.

The reported irradiation induced densification data indicate that it is affected by porosity and pore size distribution, fuel density, and irradiation temperature. The lack of a temperature dependence of the

fuel densification data reported by Ferrari et al. and Rolstad et al. is probably a result of the technique used to measure the length change in the low temperature pellet edges.

2.8.2.2 Survey of Densification Models. Densification models proposed by Rolstad,^{2.8-5} Meyer,^{2.8-12} Collins and Hargreaves,^{2.8-7} Voglewede and Dochwat,^{2.8-13} Stehle and Assmann,^{2.8-14} Marlowe,^{2.8-15} Hull and Rimmer,^{2.8-16} and MacEwen and Hastings^{2.8-17} are reviewed in this section.

Rolstad et al., $^{2.8-5}$ used two equations to correlate their data. In the first, the shortening ($\Delta L/L$)_m is a function of the current theoretical density (DENS) and sintering temperature in degrees centigrade (TSINT) at a burnup of 5,000 MWd/tUO₂:

$$\left(\frac{\Delta L}{L}\right)_{m} = \frac{-22.2(100 - DENS)}{(TSINT - 1453)} . \tag{2-86}$$

The effect of burnup was introduced through the use of a master curve created by shifting all curves vertically to agreement at 5,000 MWd/tU and then horizontally to achieve the best agreement at the low burnup portion of the curve. The master curve is

$$\left(\frac{\Delta L}{L}\right) = -3.0 + 0.93e^{(-BU)} + 2.07e^{(-35BU)}$$
 (2-87)

where

$$\left(\frac{\Delta L}{L}\right)$$
 = the percent shrinkage of the fuel

$$BU = the burnup (MWd/kgU).$$

This equation results in a rapid length change at low burnups (< 1.0 MWd/kgU) and a small length change at higher burnup levels. Very little additional densification is calculated after a burnup greater than 5,000 to 6,000 MWd/kgU.

Meyer developed a conservative model based on resintering of fuel at 1,973 K for 24 hours. The change in density of fuel after resintering was used as an upper limit. Two equations were used to calculate densification, one for fuels that resintered less than 4% and one for fuels which resintered more than 4%. Meyer's model was based on a log function of burnup and the resintering density change. Meyer reports that his model adequately bounds all in-reactor densification data at his disposal.

Collins and Hargreaves developed an empirical densification expression based on the initial porosity and an exponential burnup function. They suggested that a complete description of the densification rate of irradiated uranium dioxide demands a knowledge of the initial porosity size distribution of the as

manufactured UO₂ fuel in addition to the total porosity volume because of the differing sintering rates associated with different pore sizes. However, the pore morphology of their fuel was not determined.

Voglewede and Dochwat developed an equation for final stage densification of mixed oxide fuels based on EBR-II reactor data. It is a semiempirical approach based on porosity, stress, and temperature.

Stehle and Assmann proposed a vacancy controlled densification model as a function of initial fuel porosity, fission rate, initial pore radius, fuel temperature, and vacancy diffusion. Their equation considers pores of only one diameter; therefore, application of this equation to practical engineering problems requires that the equation be integrated over all pore sizes existing in the fuel. Their approach predicts that irradiation induced densification is temperature dependent because of the dependence of the volume diffusion coefficient, D_v , on temperature. The authors used approximate values for D_v and found that the densification rate should change at approximately 1,023 K. This corresponds very well with the experiment results found in the EPRI densification study.

Marlowe proposed a model for diffusion controlled densification and modified the model to include fuel swelling contributions to the density change, as well as an irradiation induced diffusivity, which provides atomic mobility for grain growth densification. This model is based on densification and grain growth rate, which must be determined experimentally for any particular fuel. These rates strongly affect the predicted in-reactor densification behavior through grain size modification. Because the model allows complete pore elimination and, in fact, densities greater than theoretical for the matrix material, an upper limit to the density must be calculated to limit the densification change.

Hull and Rimmer developed an empirical densification equation based on grain boundary diffusion and temperature. They report reasonably good agreement with the Burton and Reynolds data despite the approximations required to evaluate the equation and the errors in determining the porosity distribution of the samples. Both the shape of the predicted curve and the absolute magnitude of the values were reported to be in good agreement with experimental data, demonstrating that the decrease in sintering rate with time is associated only with the progressive reduction in the number of cavities. The calculation assumed a constant cavity spacing for each time step in changing from one volume size to the next. The similarity between out-of-pile and in-pile densification strongly suggests the importance of pore size distribution and volume for in-reactor densification.

MacEwen and Hastings developed a model describing the rate change of pore diameter based on the time dependence of vacancy and interstitial concentrations, fission gas concentrations, and internal pore pressures. Two equations were used, one describing the diametral change of pores on the grain boundaries and the other describing intergranular pore shrinkage. Use of this model also requires vacancy jump frequencies. The model is thus difficult to use in engineering applications with the present in-reactor fuel data base.

Fuel densification models proposed in Reference 2.8-11 and Reference 2.8-13 through Reference 2.8-17 attempted to correlate fuel densification with fundamental material properties. These theoretical or semiempirical approaches will eventually be the preferred modeling techniques, but current versions of these models are based on estimates of material properties such as diffusion coefficients, void concentrations, and jump frequencies. These properties are not sufficiently defined to be used to predict inreactor densification. As Meyer pointed out in his review, the use of complicated theoretical approaches is

not justified unless they can be supported with material property data, which allow significantly better predictions than fully empirical correlations. An empirical approach similar to the Meyer model is best for modeling densification.

2.8.3 Model Development

The relation between densification and burnup suggested by Rolstad et al., Equation (2-87) has been adopted for use in the FUDENS subcode. Densification is assumed to consist of a rapidly varying component, represented by the term $2.0 \, \mathrm{e}^{[-35(FBU\,+\,B)]}$ in Equation (2-85), and a slowly varying component, represented by the term $\mathrm{e}^{[-3(FBU\,+\,B)]}$ in Equation (2-85). The expression was adopted because it successfully describes the burnup dependence of both the original Rolstad et al. data and recent EPRI data.

The Rolstad et al. model, ^{2.8-5} as originally proposed, is solved graphically, as indicated in Figure 2-29. The curves in Figure 2-29a are defined by Equation (2-86) for various sintering temperatures, and the curve in Figure 2-29b is defined by Equation (2-87).

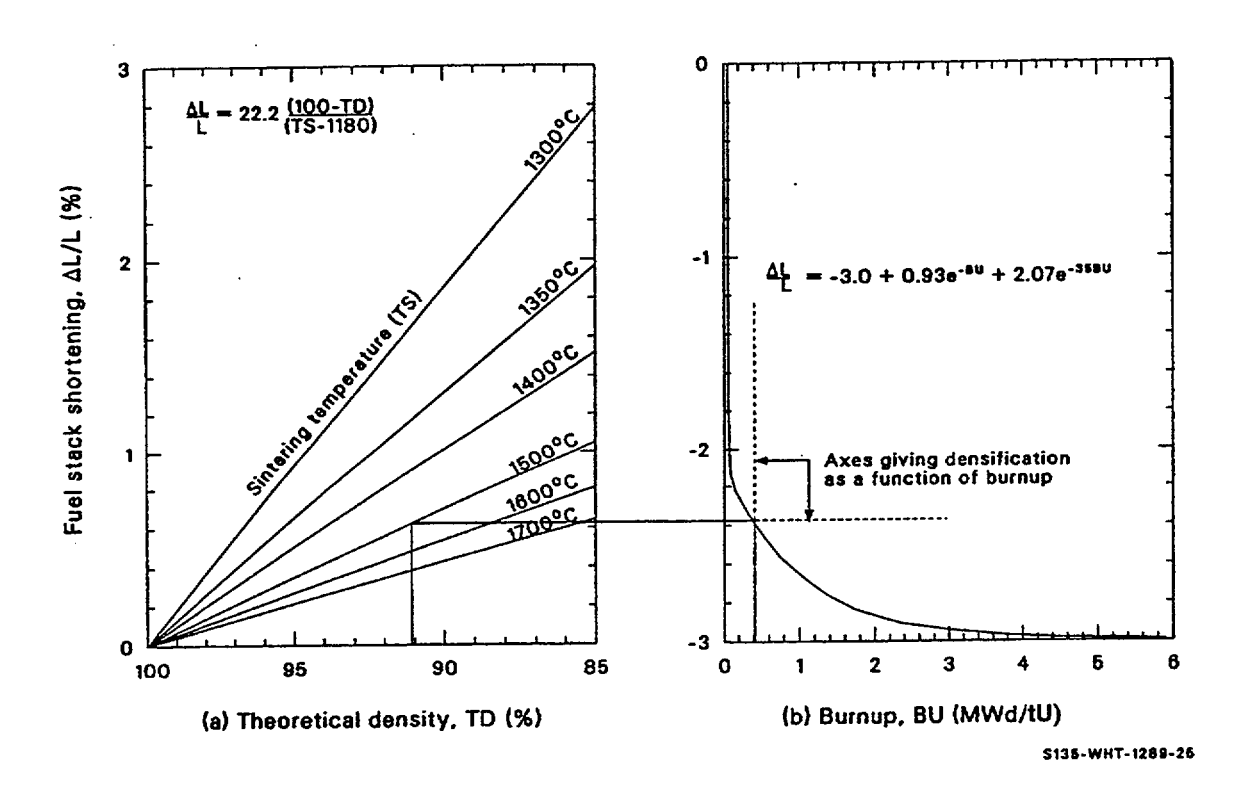


Figure 2-29. Graphical solution of Rolstad's model, where TD is percent of theoretical density, TS is sintering temperature (°C), and BU is burnup.

The use of these equations to find the length change as a function of burnup is also shown in Figure 2-29. For an initial density of 91% TD and sintering temperature of 1,500 °C, the left scale of Figure 2-29

shows that the eventual length change will be about 0.6%. To determine the change as a function of burnup, new axes are drawn in Figure 2-29b, as shown by the dashed lines. With the (x,y) origin of these new axes interpreted to be zero burnup and zero length change, the solid curve in Figure 2-29b then gives $\Delta L/L$ as a function of burnup. The 0.6% fractional length change is then seen to require about 5 MWd/tU burnup.

The numerical equivalent to this graphical solution is incorporated into the subroutine FUDENS. Newton's method^{2.8-18} was selected for the iterative determination of the new origin because of its rapid convergence. Between four and ten iterations are typically required to determine the position of the new axes, with a 0.0002% convergence criterion defined by

$$E = 100 (X - X_1)/X$$
 (2-88)

where

E = calculated convergence

X = current value of burnup in Equation (2-88)

 X_1 = preceding value of burnup in Equation (2-88).

The maximum densification term, (Δ L/L)m in Equation (2-85), determines the in-reactor densification limit. Four different expressions, Equations (2-81) through (2-84), are used by the FUDENS code to determine a number for this term. When a measurement of fuel densification during a resintering test at 1,973 K is available, this measurement is the basis of the model's prediction for the maximum inpile shrinkage. The resintering density change found during a resintering test at 1,973 K for at least 24 hours is appropriate for use in calculating the maximum in-pile densification because in-pile densification and thermal resintering are both dependent on porosity removal. Meyer's assumption that the change in length during a resintering test is equal to the maximum in-pile densification is too conservative for a best estimate code. Therefore, the maximum irradiation induced densification calculated by FUDENS is a fraction of the density change found during a resintering test. If resintering test data are not available, the FUDENS model defaults to the expression suggested by Rolstad et al., Equation (2-83). This provides a reasonable estimate of in-pile densification but cannot account for variations in pore size distribution.

Constants in the expressions used by FUDENS for maximum in-pile shrinkage were determined separately for high (> 1,000 K) and low temperatures. The separate expressions were used because a temperature dependence was found in the EPRI data and because of irregularities between the Halden and the EPRI high temperature data sets. The Rolstad et al. model, which predicts the Halden data well, fits the EPRI low temperature data but not the high temperature EPRI data. Hanevik et al. suggested that the Halden data were probably measurements of the densification of fuel pellet edges, that is, the cooler regions of the pellet. The Rolstad et al. model is assumed by the FUDENS code to apply to low temperature densification, and the high temperature densification is assumed to be three times as large.

The constants in Equations (2-81) through (2-84) were determined by inspection to provide the best fit to the maximum density change of the EPRI data. Model predictions and the data base used are shown in Figure 2-27 and Figure 2-30. Mixed oxide fuel is assumed to densify in the same manner as UO₂ due to lack of data to show otherwise.

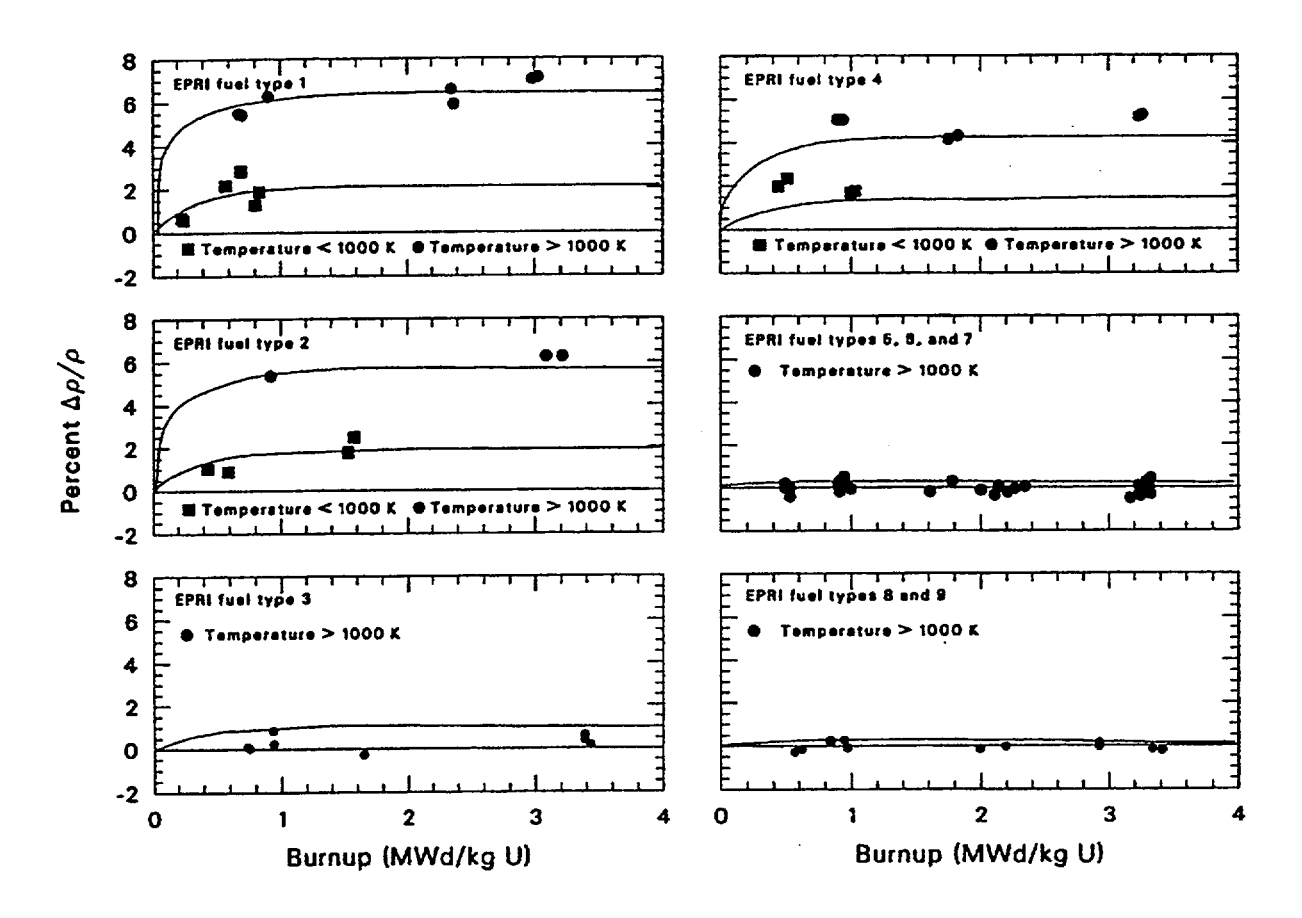


Figure 2-30. FUDENS calculations using EPRI fuel fabrication parameters and resintering values correlated with experimental EPRI in-pile data.

2.8.4 References

- 2.8-1 W. Beere, "The Sintering and Morphology of Interconnected Porosity in UO₂ Powder Compacts," Journal of Materials Science, 5, 1973, pp. 1717-1724.
- 2.8-2 W. M. Armstrong, W. R. Irvine, and R. H. Martinson, "Creep Deformation of Stoichiometric Uranium Dioxide," *Journal of Nuclear Materials*, 7, 1962, pp. 133-141.
- 2.8-3 D. W. Brite et al., EEI/EPRI Fuel Densification Project, Research Project131 Final Report, revised June 1975.

- 2.8-4 M. D. Freshley et al., "The Effect of Pellet Characteristics and Irradiation Conditions on UO₂ Fuel Densification," ANS/CNA Topical Meeting on Commercial Nuclear Fuel Current Technology, Toronto, Canada, April 1975.
- 2.8-5 E. Rolstad et al., "Measurements of the Length Changes of UO₂ Fuel Pellets During Irradiation," Enlarged HPG Meeting on Computer Control and Fuel Research, June 4-7, 1974.
- 2.8-6 A. Hanevik et al., "In-Reactor Measurements of Fuel Stack Shortening," BNES Nuclear Fuel Performance Conference, London, October 15-19, 1973, Paper No. 89.
- 2.8-7 D. A. Collins and R. Hargreaves, "Performance Limiting Phenomena in Irradiated UO₂," BNES Nuclear Fuel Performance Conference, London, October 15-19, 1973, Paper No. 50.
- 2.8-8 H. M. Ferrari et al., "Fuel Densification Experience in Westinghouse Pressurized Water Reactors," BNES Nuclear Fuel Performance Conference, London, October 15-19, 1973, Paper No. 54.
- 2.8-9 T. J. Heal et al., "Development of Stable Density UO₂ Fuel," BNES Nuclear Fuel Performance Conference, London, October 15-19, 1973, Paper No. 52.
- 2.8-10 A. M. Ross, "Irradiation Behavior of Fission Gas Bubbles and Sintering Pores in UO₂," *Journal of Nuclear Materials*, 30, April 1969, pp. 134-142.
- 2.8-11 B. Burton and G. L. Reynolds, "The Sintering of Grain Boundary Cavities in Uranium Dioxide," *Journal of Nuclear Materials*, 45, 1972/73, pp. 10-14.
- 2.8-12 R. O. Meyer, The Analysis of Fuel Densification, NUREG-0085, July 1976.
- 2.8-13 J. C. Voglewede and S. C. Dochwat, *Reactor Development Program Progress Report*, ANL-RDP-33, December 1974, pp. 5-1-5-2.
- 2.8-14 H. Stehle and H. Assmann, "The Dependence of In-Reactor UO₂ Densification on Temperature and Microstructure," *Journal of Nuclear Materials*, 52, 1974, pp. 303-308.
- 2.8-15 M. O. Marlowe, "Predicting In-Reactor Densification Behavior of UO₂," Transactions of the American Nuclear Society, 17, November 1973, pp. 166-169.
- 2.8-16 D. Hull and D. E. Rimmer, "The Growth of Grain Boundary Voids Under Stress," *Philosophical Magazine*, 4, 1959, p. 673.
- 2.8-17 S. R. MacEwen and I. J. Hasting, "A Model for In-Reactor Densification of UO₂," *The Philosophical Magazine*, 31, 1, January 1975, pp. 135-143.
- 2.8-18 R. W. Hamming, *Introduction to Applied Numerical Analysis*, New York: McGraw-Hill Book Company, Inc., 1971.

2.9 Swelling (FSWELL)

The computer subcode FSWELL calculates fuel swelling, which is caused by the buildup of solid and gaseous fission products during irradiation. In order to calculate the overall fuel dimensional changes, fuel swelling (FSWELL) must be combined with the effects of creep induced elongation (FCREEP) and densification due to pressure sintering (FHOTPS) and irradiation (FUDENS).

2.9.1 Summary

The expression used in FSWELL to calculate swelling due to solid fission products is

$$S_s = 2.5 \times 10^{-29} B_s$$
 (2-89)

where

S_s = fractional volume change due to solid fission products (m³volume change/m³ fuel)

 B_s = burnup during a time step (fissions/m³).

The correlation employed for swelling due to gaseous fission products when the temperature is below 2,800 K is

$$S_{g} = 8.8 \times 10^{-56} (2800 - T)^{11.73} e^{[-0.0162(2800 - T)]} e^{[-8.0 \times 10^{-27} B]} B_{s}$$
 (2-90)

where

 S_{σ} = fractional volume change due to gas fission products (fissions/m³)

T = temperature(K)

B = total burnup of fuel (fissions/ m^3).

For temperatures greater than 2,800 K, S_g is zero because the gas that causes swelling is assumed to have been released.

2.9.2 Solid Fission Product Swelling Model

Volume changes caused by the buildup of nongaseous atoms are difficult to measure. However, a number of studies have been undertaken to determine the relative amounts of fission product elements and compounds, as well as their chemical states and locations within the fuel.^{2.9-1} to ^{2.9-15}

Anselin^{2.9-8} calculated swelling as a function of burnup using room temperature data with an assumed fission product yield and chemical state for each element. He found a maximum solid fission product swelling rate of 0.13% Δ V/V per 10^{26} fissions/m³, if the fuel completely utilized the vacancies created during irradiation, and 0.54% Δ V/V per 10^{26} fissions/m³ if none of the vacancies are used. He proposed an average of 0.35% Δ V/V per 10^{26} fissions/m³ for all conditions but cautioned that there is no unique value for the swelling rate, since the irradiation conditions, fuel pin design, and fuel properties all contribute to swelling.

Harrison and Davies $^{2.9\text{-}10}$ calculated solid fission product swelling as a function of thermal neutron flux and concluded that the swelling rate decreases monotonically with increasing flux. They reported swelling rates of 0.45% Δ V/V per 10^{26} fissions/m³ and 0.39% Δ V/V per 10^{26} fissions/m³ for thermal neutron fluxes of 10^{18} and 10^{21} n/m² \cdot s , respectively.

Olander $^{2.9-16}$ obtained a solid fission product swelling rate of 0.32% Δ V/V per atom percent burnup, which corresponds closely to Anselin's average value of 0.35% Δ V/V per 10^{26} fissions/m³. However, this calculation does not account for fission product migration and is influenced by uncertainties in the physical and chemical states of the fission products, leading to an error of \pm 50% in the predicted value. Olander found a minimum swelling rate of 0.16% Δ V/V per atom percent burnup for initially hypostoichiometric UO_2 and a maximum of 0.48% Δ V/V per atom percent burnup for initially hyperstoichiometric fuel or fuel irradiated to high burnups.

Rowland^{2.9-17} conducted an extensive study of oxide fuel swelling and found the maximum total swelling due to both solid and gaseous fission products to be $0.4\% \Delta \text{ V/V}$ per 10^{26} fissions/m³.

Frost^{2.9-18} obtained 0.21% Δ V/V per 10^{26} fissions/m³, and Whapman and Sheldon^{2.9-19} obtained 0.20% Δ V/V per 10^{26} fissions/m³.

The FSWELL model was developed by choosing a swelling rate between Anselin's rate of swelling when vacancies are utilized and General Electric's maximum swelling rate due to both solid and gaseous fission products. The best solid fission product swelling rate at both low burnups and high burnups, where much of the fission gas is released and solid fission product swelling dominates, is $0.25\% \Delta V/V$ per 10^{26} fissions/m³. Thus, the correlation for swelling due to solid fission products is given by Equation (2-89) where the terms are previously defined. This equation has been modified in FSWELL, where burnup is given in terms of MW-s/kg-U. To make the proper conversion between units, the correlation must be

soldsw =
$$7.435 \times 10^{-13}$$
 fdens (bu - bu₁) (2-91)

where

soldsw = fractional volume change due to solid fission products

fdens = initial input density of the fuel (kg/m^3)

bu = input burnup to end of current time step (MW-s/kg-U)

bu₁ = input burnup to end of last time step (MW-s/kg-U).

2.9.3 Fission Gas Swelling Model

Fuel swelling is primarily a result of the increase in fission gas bubbles within the fuel pellets. The physical mechanisms that cause the fuel to swell are complex and are not considered in detail in the FSWELL subcode. Swelling due to fission gas is modeled using a correlation for unrestrained swelling as a function of temperature and burnup. This correlation is based on the data reported by Battelle Columbus Laboratories, ^{2.9-20} to ^{2.9-24} Turnbull, ^{2.9-25} to ^{2.9-27} Kuz'min and Lebedev, ^{2.9-28} and Grando et al. ^{2.9-29} for unrestrained swelling caused by the growth of intergranular gas bubbles and tunnels on the grain boundaries, edges, and corners at temperatures between 1,373 and 1,973 K. The model considers two gross mechanisms, depending on the temperature of the fuel. Above 1,573 K, macropores begin to grow, causing a significant increase in fuel rod swelling. At very high temperatures (1,973 K to the melting point), columnar grains form, fission gas is released, and swelling is reduced.

The fuel volume changes listed by Chubb et al.^{2,9-20} and Turnbull^{2,9-27} were used to correlate the unrestrained isothermal swelling rate. The fission gas swelling rate equation was determined by comparing the calculated swelling curve with the data and adjusting the equation until the predicted values matched the measured data. The shape of the unrestrained isothermal curve was determined by assuming that (a) at temperatures below 1,000 K, the gases remain in very small bubbles and/or as single atoms in the matrix so that little swelling occurs; (b) between 1,000 and 2,000 K, bubbles grow at the grain boundaries, edges, and corners, creating volume changes, and (c) above 2,000 K, dense (98% of theoretical density) columnar grains form and gas is removed, making fission gas swelling insignificant compared to solid fission product swelling. The equation describing this process is

$$F_g = 8.8 \times 10^{-56} (2800 - T)^{11.73} e^{[-0.0162(2800 - T)]}$$
(2-92)

where

 F_g = fractional volume change/burnup (m³/fission)

T = temperature (K).

The unrestrained fuel swelling predicted by Equation (2-92) is shown in Figure 2-31. The values calculated by FSWELL are compared with the data of Turnbull and Chubb et al., in Figure 2-32.

Fission gas swelling must also be modeled as a function of burnup. Data reported by Battelle Columbus Laboratories, Turnbull, and Kuz'min and Lebedev indicate that fission gas swelling saturates at

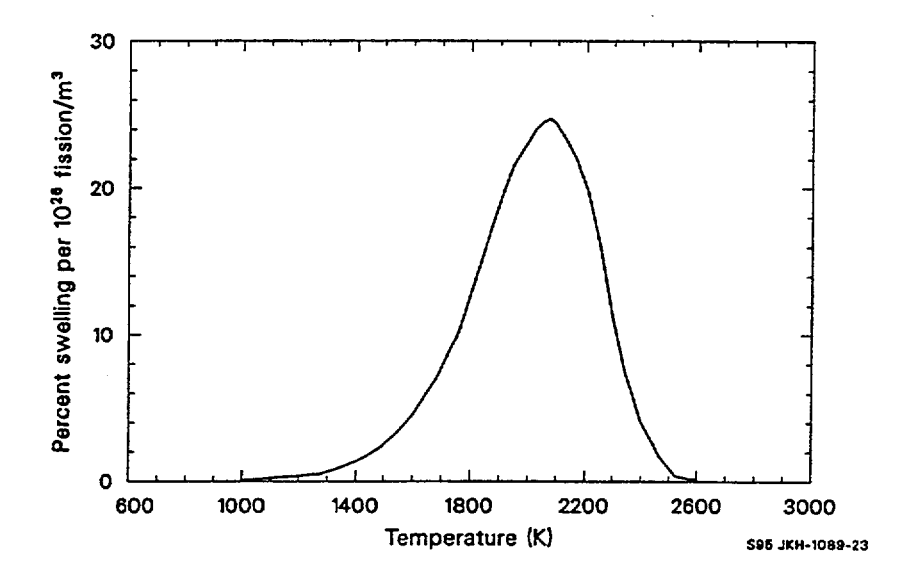


Figure 2-31. Unrestrained fission gas swelling.

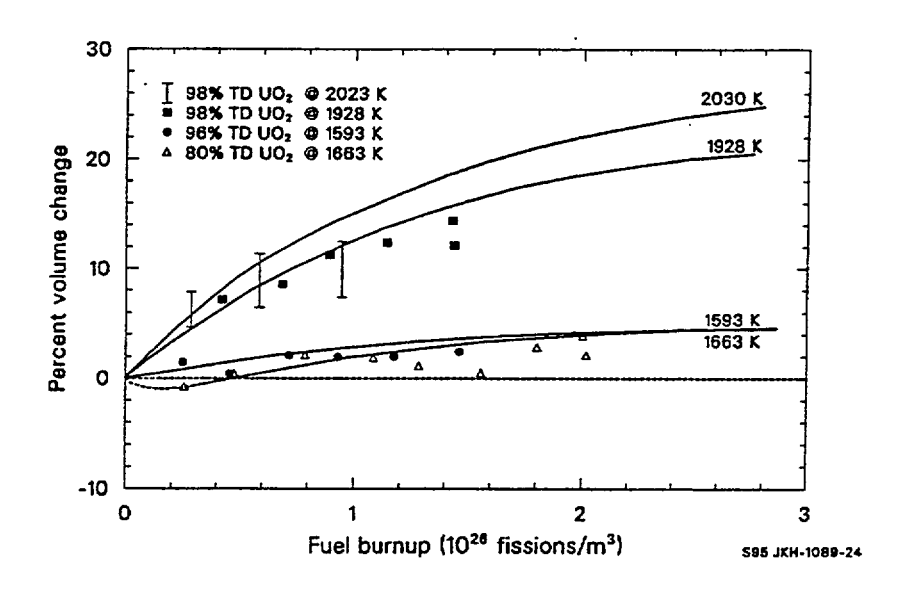


Figure 2-32. Fuel volume changes calculated by FSWELL compared with experimental fuel swelling data.

relatively low burnups ($< 10^{26}$ fissions/m³). An exponential burnup function has been included in the FSWELL model to account for swelling saturation. The swelling dependence on burnup is

$$S_g = F_g B_S e^{(-8.0 \times 10^{-27} B)} B_S$$
 (2-93)

where

 S_g = fractional volume change due to gaseous fission products

B = total burnup (fissions/ m^3).

When Equation (2-92) is substituted into Equation (2-93), the correlation for swelling due to gaseous fission products is given by Equation (2-90)

for T < 2,800 K, and

$$S_g = 0.0$$
 (2-94)

for $T \ge 2,800 \text{ K}$.

Converting fissions/m³ to MW-s/kg-U gives

$$gaswl = 2.617 \times 10^{-39} fdens(bu - bu_1)(2800 - T)^{11.73}$$

$$e^{[-0.0162(2800 - T)]} e^{(-2.4 \times 10^{-10} bu \cdot fdens)}$$
(2-95)

where gaswl is the fractional volume change due to gaseous fission products.

2.9.4 References

- 2.9-1 B. T. Bradbury and B. R. T. Frost, *Studies in Radiation Effects on Solids*, NewYork: Gordon and Breach, 1967.
- 2.9-2 B. T. Bradbury, J. T. Demant, P. M. Martin, and D. M. Poole, *Journal of Nuclear Materials*, 17, 1965.
- 2.9-3 B. T. Bradbury, J. T.Demant, and P. M. Martin, AERE-R-5149, 1966.
- 2.9-4 G. M. Jeffery, Journal of Nuclear Materials, 22, 1964.
- 2.9-5 J. L. Bates, Metallic Uranium in Irradiated UO2, HW-82263, 1964.

- 2.9-6 D. R. O'Boyle, F. L. Prown, and J. E. Saneck, "Solid Fission Product Behavior in Uranium Plutonium Oxide Fuel Irradiated in a Fast Neutron Flux," *Journal of Nuclear Materials*, 29, 1969, pp. 27-42.
- 2.9-7 I. J. Hastings, D. H. Rose, and J. Barid, "Identification of Precipitates Associated with Intergranular Fission Gas Bubbles in Irradiated UO₂ Fuel," *Journal of Nuclear Materials*, 61, 1976, pp. 229-231.
- 2.9-8 F. Anselin, The Role of Fission Products in the Swelling of Irradiated UO_2 and $(U, Pu)O_2$ Fuel, GEAP-5583, January 1969.
- 2.9-9 F. Anselin and W. E. Baily, "The Role of Fission Products in the Swelling of Irradiated UO₂ and (U, Pu)O₂ Fuels," *Transactions of the American Nuclear Society, 10*, 1967.
- 2.9-10 J. W. Harrison and L. M. Davies, "The Variation of Solid Fission Product and Gas Swelling in Uranium Compounds with Thermal Neutron Dose Rate," *Journal of Nuclear Materials*, 27, 1968.
- 2.9-11 B. Lustman, Technical Progress Report, PWR Project, WAPD MRP11, October 1964 January 1965.
- 2.9-12 J. H. Davies, R. F. Boyle, D. Weidenbaum, and J. Hanson, "On the Composition of Metallic Ingots Formed in High Performance Ceramic Fuel Elements," *Transactions of the American Nuclear Society*, 9, 63, 1966.
- 2.9-13 J. H. Davies, Some Considerations Regarding the Behavior of Fission Products in the Fast Ceramic Reactor, GEAP-4872, 1966.
- 2.9-14 M. L. Bleiberg, R. M. Berman, and B. Lustman, Effect of High Burnup on Oxide Ceramic Fuels, WAPD-T-1455, 1962.
- 2.9-15 I. G. Lebedev, V. I., Kuz'min, and A. S. Piskum, "Swelling of Hot Oxide Fuel," *Soviet Journal of Atomic Energy*, 28, 1970.
- 2.9-16 D. R. Olander, Fundamental Aspects of Nuclear Reactor Fuel Elements, TID-26711-P, 1967.
- 2.9-17 T. C. Rowland, M. O. Marlowe, and R. B. Elkins, Fission Product Swelling BWR Fuels, NEDP-20702, November 1974.
- 2.9-18 B. R. T. Frost, "Studies of Irradiation Effects in Ceramic Fuel at Harwell," *Journal of the American Ceramic Society*, 1969.
- 2.9-19 A. D. Whapham and B. E. Sheldon, Electron Microscope Observation of the Fission Gas Bubble Distribution in UO₂, AERE-R-4970, April 1966.

- 2.9-20 W. Chubb, V. W. Storhok, and D. L. Keller, "Observations Relating to the Mechanisms of Swelling and Gas Release in Uranium Dioxide of High Temperatures," *Journal of Nuclear Materials*, 44, 1972, pp. 136-152.
- 2.9-21 W. Chubb, V. W. Storhok, and D. L. Keller, "Factors Affecting the Swelling of Nuclear Fuel at High Temperatures," *Nuclear Technology*, 18, June 1973, pp. 231-255.
- 2.9-22 W. Chubb and D. L. Keller, Implication of High Temperature Irradiation Data for Low Temperature Reactor Design, BMI-1918, July 1971, pp. B98-B112.
- 2.9-23 R. F. Hilbert, W. J. Zielenbach, D. E. Lozier, R. B. Clark, and V. W. Storhok, *Irradiation Behavior of Oxide Fuels at High Temperatures*, BMI-1918, July 1971, pp. B2-B43.
- 2.9-24 R. F. Hilbert, V. W. Storhok, W. Chubb, and D. L. Keller, "Mechanisms of Swelling and Gas Release in Uranium Dioxide," *Journal of Nuclear Materials*, 38, 1971, pp. 26-34.
- 2.9-25 J. A. Turnbull, "The Effect of Grain Size on the Swelling and Gas Release Properties of UO₂ During Irradiation," *Journal of Nuclear Materials*, 50, 1974, pp. 62-68.
- 2.9-26 J. A. Turnbull, "The Mobility of Intragranular Bubbles in Uranium Dioxide During Irradiation," Journal of Nuclear Materials, 62, 1976, pp. 325-328.
- 2.9-27 J. A. Turnbull and M. O. Tucker, "Swelling in UO₂ under Conditions of Gas Release," *The Philosophical Magazine*, 30, July 1974, pp. 47-64.
- 2.9-28 V. I. Kuz'min and I. G. Lebedev, "Effect of Temperature Distribution on the Swelling of UO₂ and UO₂-PuO₂ Cores," *Power Atomic Energy*, 28, January 1975.
- 2.9-29 C. Grando, M. Montgomery, and A. Strasser, "Unrestrained Swelling and Fission Gas Release of Fast Reactor Fuels," *Proceedings of the Conference on Fast Reactor Fuel Element Technology, New Orleans, LA, April 13-15, 1971*, Ruth Farmakes, ed., pp. 771-784.

2.10 Pressure Sintering (FHOTPS)

Urania or mixed oxide fuel pellets densify when exposed to sufficiently high hydrostatic pressures (pressure sintering), high temperatures (thermal sintering), and irradiation. This report discusses a densification model based on published out-of-pile fuel pressure sintering data. The pressure sintering model complements the irradiation dependent densification model described in Section 2.8 of this report.

A summary of the pressure sintering model, FHOTPS, is contained in Section 2.10.1. Section 2.10.2 describes pressure sintering theories and examines their applicability to modeling urania and mixed oxide pressure sintering data. Section 2.10.3 describes the development of the FHOTPS model, provides standard error estimates, and compares FHOTPS calculated results with experimental data, and the references are given in Section 2.10.4.

2.10.1 Summary

Fuel densification in a reactor environment is a function of temperature, stress, and irradiation. Temperature and stress densification mechanisms are driven by a stress, P, expressed by

$$P = P_e - P_i + 2\gamma/a (2-96)$$

where

P_e = external hydrostatic stress (Pa)

P_i = internal pore pressure (Pa)

 γ = surface energy per unit area (J/m²)

a = grain size (m).

Pressure sintering is the dominant densification process if the stress (P_e - P_i) is much larger than the surface energy stress, 2c/a. If an external hydrostatic stress, P_e , is present, it will dominate the densification of in-pile fuel because the internal pore pressure, P_i , and the surface energy stress, 2c/a, are generally much smaller than the externally applied stress. Over an extended irradiation period and at zero P_e , the internal pore pressure, P_i , could cause fuel swelling and the surface energy stress could cause some fuel densification. However, these changes in fuel volume are small compared with densification caused by applied stress and are not considered in the development of the FHOTPS model.

Equation (2-96) does not include an irradiation related driving stress. It is assumed that the irradiation densification driving stress would be added to the right side of Equation (2-96). Since the irradiation densification driving stress is a linear term, it is treated independently as a separate model (the FUDENS model, see Section 2.8). The values calculated with the FUDENS model should, therefore, be added to the FHOTPS model described in this section. The reader should, however, be cautioned that data used to develop the FUDENS model were in-pile data that may include some pressure sintering effects so that combining the two model outputs may be conservative. There are no in-pile data available that will allow separation of these effects.

A lattice diffusion creep equation was fit to the data of Solomon^{2.10-1} to give the equation used for urania in the FHOTPS model

$$\frac{1}{\rho} \frac{d\rho}{dt} = 48939 \left(\frac{1-\rho}{\rho}\right)^{27} \frac{P}{TG^2} e^{\left(\frac{Q_u}{RT}\right)}$$
(2-97)

where

p = fraction of theoretical density (unitless)
t = time (s)

P = hydrostatic pressure (Pa)

T = temperature (K)

G = grain size (μm)

Qu = activation energy (J/mole)

R = 8.314 (J/mole•K).

The activation energy of urania pressure sintering for Equation (2-97) is calculated with the oxygen to metal dependent equation

$$Q_{u} = R \left(\frac{9000}{e^{\left[\frac{20 - 8|\log(x - 1.999)|}{|\log(x - 1.999)|} + 1.0 \right]}} + 36294.4 \right)$$
 (2-98)

where x is the oxygen to metal ratio.

The lattice diffusion creep equation was fit to the mixed oxide data of Routbort^{2.10-2} to give the mixed oxide fuel pressure sintering equation

$$\frac{1}{\rho} \frac{d\rho}{dt} = 1.8 \times 10^7 \left(\frac{1-\rho}{\rho}\right)^{2.25} \frac{P}{TG^2} e^{\left(\frac{450000}{RT}\right)} . \tag{2-99}$$

The estimated standard error of estimate for both equations is $\pm 0.5\%$ of the calculated density.

Care must be exercised when using these models out of the 1,600 - 1,700 K and 2 - 6 MPa data base range. Pressure sintering not represented in the data base may be controlled by a different creep densification mechanism, as discussed below. Pressure sintering rates would then be much different than those calculated by Equations (2-97) or (2-99).

2.10.2 Pressure Sintering Process and Data

Pressure sintering or volume creep consists of several modes of creep. One of these modes of creep mechanisms can dominate the others, depending on the fuel temperature, pressure, porosity, and grain size conditions, as will be discussed below. Equations representing each creep mechanism combined with the

theoretical constants for UO_2 were used by Routbort^{2.10-2} to determine the most probable dominating (contributes the highest densification rate) mechanism under reactor operating conditions. These equations, their use, and the published experimental data used to develop the FHOTPS model are described in this section.

2.10.2.1 Creep Densification. Several distinct mechanisms, such as lattice diffusion (Narbarro-Herring creep) or rate independent plasticity (yielding or dislocation glide), contribute to fuel densification. Each mechanism imposes specific stress porosity temperature dependent functions. One or any combination of these creep mechanisms can dominate densification, depending on the grain size and stress porosity temperature conditions. There is no single mechanism that will always dominate the densification process. Therefore, an equation representing each creep mechanism is presented so that all possible densification parameter dependencies are described.

Pressure sintering by grain boundary diffusion creep (grain boundary acting as a diffusion path) is usually dominant at temperatures less than one half the melting temperature. ^{2.10-3,2.10-4} The densification rate by grain boundary creep is expressed by

$$\frac{d\rho}{dt} = \frac{4.5\delta D_b \Omega}{kTb^3} \frac{P}{1 - (1 - \rho)^{1/3}}$$
(2-100)

where

 δ = grain boundary thickness

D_b = grain boundary diffusion coefficient

 Ω = atomic volume

P = applied stress

k = Boltzman's constant

b = grain size.^a

Pressure sintering by grain boundary diffusion creep can dominate only if the grain sizes remain small, so that the diffusion paths along the grain boundaries are small.

a. It was assumed here and in the following equations that the effective particle radius is the grain size. This is consistent with the model that is based on the assumption of about one pore to every grain in the compact.

Pressure sintering by lattice diffusion creep often dominates at temperatures greater than half the melting temperature and before significant grain growth has occurred. Densification by lattice diffusion creep is expressed by

$$\frac{d\rho}{dt} = \frac{3D_V \Omega P}{kTb^2} \tag{2-101}$$

where D_v is the lattice diffusion coefficient. This equation is used to calculate densification by vacancy flow from the surface of a pore to sinks on nearby grain boundaries.^{2.10-3}

Pressure sintering by power law creep can dominate at high fuel temperatures or pressures. Densification by power law creep (dislocation creep) has been derived by Wilkinson and Ashby^{2.10-4} and by Wolfe and Kaufman.^{2.10-5} The densification rate equation is

$$\frac{d\rho}{dt} = \frac{SA}{T} e^{\frac{Q}{kT} \left(\frac{\rho(1-\rho)}{[1.0-(1-\rho)^{1/n}]^n} \right)} \left(\frac{3|\rho|^n}{2n} \right)$$
(2-102)

where

S = sign of pressure

A = constant

Q = power law activation energy (J/mole)

n = stress and porosity exponent.

Equation (2-102) assumes steady-state creep and densification independent of the grain size and is valid even after extensive grain growth.

The fourth pressure sintering mechanism, plastic flow, operates at low temperatures or very high strain rates and is defined by the expression

if
$$\rho \ge 1 - e^{\left(\frac{-3P}{2\sigma_y}\right)}$$

$$\frac{\mathrm{dq}}{\mathrm{dt}} = 0 \tag{2-103}$$

Uranium Dioxide/Mixed Oxides

else
$$\frac{dq}{dt} = \infty$$
 (2-104)

where σ_y is the yield stress. Densification by the plastic flow mechanism is assumed to occur instantaneously.^{2.10-3}

The stress dependency of the above equations has been shown by Rossi and Fulrath, ^{2.10-6} McCelland, ^{2.10-7} Fryer, ^{2.10-8} and Wolf^{2.10-5} to be dependent on the applied stress and the fuel porosity. Porosity in fuel increases stress in the vicinity of the pores and results in a vacancy concentration difference between the pore surfaces and the grain boundaries. Various porosity dependent functions have been proposed by the above authors, but the porosity dependent function of Fryer^{2.10-8} is the most generally accepted effective stress porosity dependent function. The form of Fryer's expression is

$$P = \left(\frac{1-\rho}{\rho}\right)^n \tag{2-105}$$

where

 ρ = fractional density (unitless)

$$n = 1.0.$$

Routbort^{2.10-2} found that the porosity exponent, n, of Equation (2-105) was not constant for mixed oxides but varied with the pressure sintering temperature. Routbort mapped pressure sintering of mixed oxides (determined the most dominant mechanism using theoretical material properties) using predominantly urania material constants. It was found that the lattice diffusion mechanism dominates under LWR conditions (fuel temperatures between 1,100 and 3,136 K, pressures < 100 MPa, and fuel densities > 0.90% of theoretical density). This conclusion, however, must be exercised with caution because the densification rate equations depend on the grain size and the oxygen-to-metal ratio and neither were included in the pressure sintering map analysis. The oxygen-to-metal ratio has been shown by Seltzer^{2.10-9} to ^{2.10-11} to strongly influence the activation energy and thereby drastically alter the densification rates predicated by Equations (2-100) through (2-102).

The final pressure sintering mechanism is lattice diffusion modified to include an effective applied stress. The expression describing this mechanism is

$$\frac{1}{\rho} \frac{d\rho}{dt} = A \left(\frac{1-\rho}{\rho}\right)^n \frac{P}{TG^2} e^{\left(\frac{Q}{RT}\right)}$$
 (2-106)

where

A = constant

Q = activation energy (J/mole).

2.10.2.2 Pressure Sintering Data. The models presented in Section 2.10.1 are based on data published in the open literature that deal with final stage sintering of urania and mixed oxide fuels. These models are based on the urania pressure sintering data of Solomon^{2.10-1} and the mixed oxide pressure sintering data of Routbort.^{2.10-2} Other data were used as comparison data, but fuel resintering data or final stage sintering data are used because these data most closely resemble what is occurring in a reactor. Measurement techniques and urania and mixed oxide data published in the open literature are presented in this section.

2.10.2.2.1 Measurement Techniques--Immersion density and specimen length change measurements are used to obtain densification data. From the more accurate immersion density measurements, is the more accurate technique, but only the initial and final densities are obtained. Densities from specimen length changes provide time density data and are calculated by density changes determined from length change measurements. These densities have several inherent sources of error. The most critical error is the change in length during the initial densification of the test sample, caused by seating and alignment changes. This strain error affects only the initial 1 to 2% of sample densification. Creep (nonvolumetric strain) of the sample and loading column is another source of error. Routbort measured the final densities using both the immersion and length change techniques and found about a 5% difference.

$$\frac{\rho}{\rho_f} = \left(\frac{l_f}{l}\right)^3 \tag{2-107}$$

where

 ρ = initial fraction of theoretical density (unitless)

 ρ_f = final fraction of theoretical density (unitless)

 l_f = final length (mm)

1 = initial length (mm).

2.10.2.2.2 Urania Densification Data—Pressure sintering data of UO₂ fuel have been published by Solomon, ^{2.10-1} Kaufman, ^{2.10-12} Amato, ^{2.10-13} Hart, ^{2.10-14} Fryer, ^{2.10-8} and Warren and Chaklader. ^{2.10-15} Fuel resintering or final stage sintering data from other sources were used only as

comparison data.

Solomon^{2.10-1} measured pressure sintering rates of UO_2 fuel pellets with pretest theoretical densities between 92 and 94% at 1,673 K for up to 136 hours. A summary of the experimental conditions used by Solomon is provided in Table 2-13. These pressure sintering tests indicate that (a) significant densification occurred prior to the application of pressure, (b) internal pore pressures were possible influences on the densification rate, (c) pressure sintering rates are approximately linear with applied stress ($\sigma^{1.03}$ to $\sigma^{1.2}$), and (d) activation energy for specimens at different temperatures and constant density was 0.290 MJ/g•mole. The activation energy of 0.480 MJ/g•mole obtained from two isothermal tests was reported to be more accurate. Pressure cycling tests showed that the specimens swelled after the applied pressure was removed and that the applied pressure densification and released pressure swelling rates were reversible.

Table 2-13. Pressure sintering data.

	Solomon	Kaufman	Amato	Routbort
O/M ratio	2.004 + 0.001		2.00	$1.98 + 0.01^a$
Presintering				
Temperature (K)	$1,783 \pm 1$	2,023		
Time (h)	3	12 to 24		
Pressure sintering				
Theoretical density (%)	92 to 98	80 to 92	68 to 96	90 to 99
Temperature (K)	1,673 ± 1	2,123	1,373 to 1,473	1598 <u><</u> T <u><</u> 1823
Time (s)	$0 < t < 5 \times 10^5$		900 < t < 3,600	
Pressure (MPa)		3.86 to 3.96x10 ⁷	2.76 to 5.52x10 ⁷	7.6 to 76
Stress exponent	1.03 < n < 1.2			1.33
Porosity exponent	2.7			2.25
Initial Grain size (mm)	3.354	10 to 40		8.0

a. Mixed oxide pellets consisted of 25 wt% PuO₂ and 75 wt% UO₂ (20%²³⁵U enriched).

Kaufman $^{2.10-12}$ reported experimental urania pressure and sintering data of fuel with initial theoretical densities of 80.7 to 83.7%. Immersion densities were taken before and after pressure sintering with a \pm 0.2% accuracy. These data are intermediate sintering data and can only be used to check the FHOTPS model densification rates. Kaufman observed in his experiments that no densification from heating occurred prior to the application of the load. From experimental results, Kaufman determined the stress exponent values for Equation (2-105) to be between 1 and 4.5.

Amato^{2.10-13} used a graphite die plunger lined with alumina to obtain hot pressing data in pressure sintering tests conducted in a vacuum of 10⁻⁵ torr. A summary of test conditions is given in Table 2-13. This intermediate and final stage sintering data is used to check the densification rates and is not part of the FHOTPS data base.

The fabrication pressure sintering data reported by Hart^{2.10-14} and Fryer,^{2.10-8} which include initial, intermediate, and final stage densification, and the chemical reaction sintering data reported by Warren and Chaklader were not useful in the MATPRO modeling effort, since the densification and chemical reaction rate equations change at each stage.

2.10.2.2.3 Mixed Oxide Densification Data--The experimental results of Routbort^{2.10-2} and Voglewede^{2.10-16,2.10-17} were the only mixed oxide pressure sintering data published in the open literature. The test conditions used by Routbort for his experiments are summarized in Table 2-13. Routbort determined a porosity exponent of from 1.5 at 1,673 K to 2.25 at 1,823 K. His results also showed pressure sintering to be a nonlinear function of stress, with a stress exponent of 1.33.

2.10.3 Model Development and Uncertainties

The pressure sintering model, FHOTPS, calculates the volume reduction rate of fuel under hydrostatic pressures and elevated temperatures. The model is based on the urania and plutonia data described above and the semiempirical equation suggested by Solomon, Routbort, and Voglewede. The model simulates the removal of closed porosity developed during fuel pellet fabrication and porosity created by released fission gases.

The appropriate pressure sintering mechanism to model reactor fuel behavior is best determined by comparing the densification rates calculated using the theoretical equations described in Section 2.10.2. The equation indicating the largest densification rate at expected reactor pressures and temperatures is the best model for in-reactor pressure sintering. Both Routbort, from his analysis of mixed oxides using mostly UO₂ physical constants, and Solomon, from his analysis of urania densification rates, determined lattice diffusion to be the controlling mechanism. The lattice diffusion equation is therefore used as the framework for the final FHOTPS model.

The constants used in Equation (2-97) were obtained from the general equation for lattice diffusion, Equation (2-106), and the data of Solomon. Determining constant A of Equation (2-106) constituted equation fitting to the data. Trial and error adjustments of the constant A were made until the standard error of estimate from Equation (2-106) and the data converged to the smallest error possible. The porosity exponent, n, for urania was obtained by using the average slope value of $1/\rho(d/\rho dt)$ plotted versus $\ln[(1-\rho)/\rho]$. The average slope value was determined to be 2.7.

The lattice diffusion equation, Equation (2-106), was fit to the Solomon data using a porosity exponent of 2.7, an initial grain size of 3.5 µm, an assumed activation energy of 0.48 MJ/mole, the reported hydrostatic pressure, and isothermal temperature. This fitted equation calculated a larger densification rate than indicated by the intermediate stage sintering data of Amato. This was opposite to the expected results because intermediate sintering is usually faster than final stage sintering. The lattice diffusion equation was then refit to the Solomon data, using an apparent activation energy closer to 0.290

MJ/mole (apparent activation energy obtained by Solomon from specimen data taken at different temperatures). The activation energy used in the urania pressure sintering model was calculated using Equation (2-98). This activation energy equation and the resulting activation energy were used to be consistent with the FCREEP model of the MATPRO package. With the oxygen-to-metal ratio of 2.004, an apparent activation energy of 0.332 MJ/mole was calculated using Equation (2-98), which is relatively close to the lower Solomon activation energy. Using this activation energy, Equation (2-106) was fit by trial and error adjustments of constants to fit the Solomon data, with a final error estimation of \pm 0.48%. Calculations using Equation (2-97) compared with the Solomon data are shown in Figure 2-33.

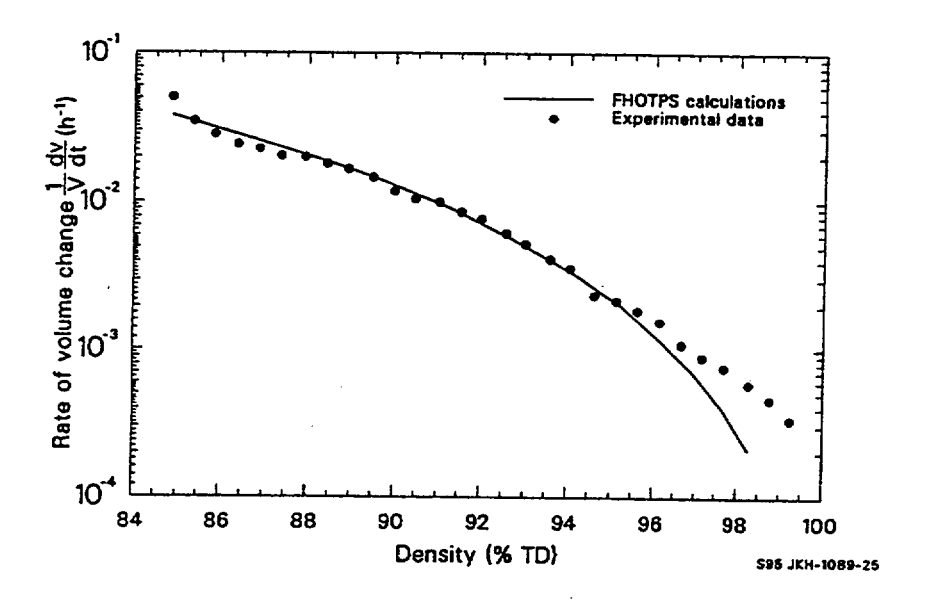


Figure 2-33. Urania pressure sintering rates calculated using the FHOTPS model compared with data.

The mixed oxide pressure sintering rate equation suggested by Routbort was used as the FHOTPS mixed oxide model except with the grain size dependence of the theoretical lattice diffusion equation consistent with the urania model. The 0.4 MJ/mole activation energy for mixed oxides suggested by Routbort, with an oxygen-to-metal ratio of 1.98, was used in the model. This activation energy is assumed not to vary with the oxygen-to-metal ratio because of a lack of data. The porosity exponent is also assumed constant at 2.25, the value determined by Routbort for samples tested at 1,823 K. Although Routbort observed a temperature dependence of the porosity exponent, a model for the dependence was not developed because data on which this conclusion was based were not included in the published report.

Equation (2-106) was fit to the Routbort data using an activation energy of 0.4 MJ/g mole, a porosity exponent of 2.25, and an initial grain size of 9 µm. Constants were adjusted until the smallest standard error estimate was obtained. The final standard error of estimate is 0.5%. Figure 2-34 shows a comparison of the mixed oxide densification rates corresponding to the Routbort data and those calculated with the FHOTPS model.

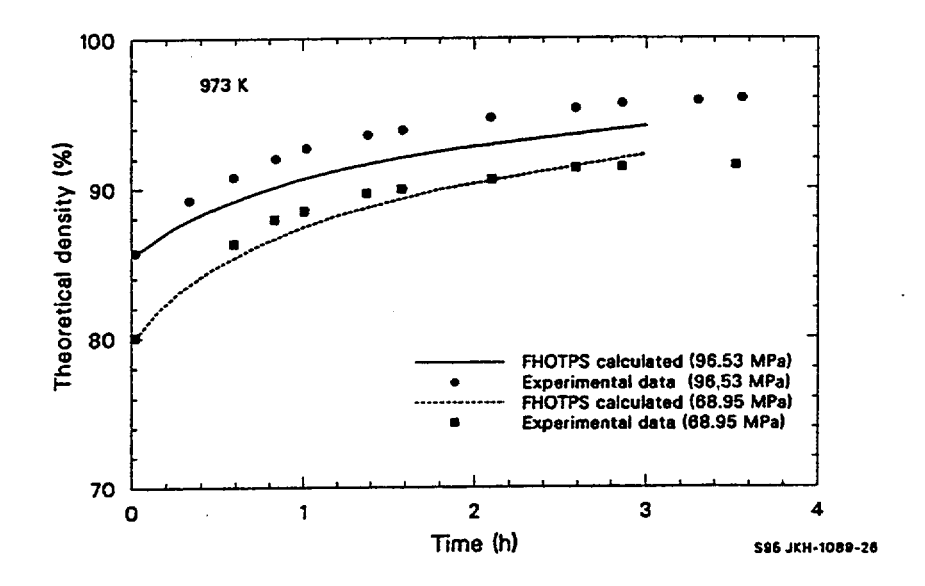


Figure 2-34. Mixed-oxide pressure sintering rates calculated using the FHOTPS model compared with data.

The FHOTPS model calculates a density change rate. These calculations are easily modified to obtain strain rate by multiplying calculational results by -1/3. This is a result of the following analysis. Using a fuel mass, g, a change in density can be expressed.

$$\frac{1}{\rho} \frac{d\rho}{dt} = \frac{\frac{g}{V} - \frac{g}{V_0}}{\frac{g}{V_T}} \frac{1}{\Delta t}$$
 (2-108)

where

$$g$$
 = fuel mass V = final volume V_0 = initial volume V_T = volume of the mass, g , at theoretical density Δt = time step.

Eliminating g and multiplying denominator and numerator by V_T gives

Uranium Dioxide/Mixed Oxides

$$\frac{1}{\rho} \frac{d\rho}{dt} = V_T \left(\frac{V - V_0}{V V_0} \right) \frac{1}{\Delta t} . \tag{2-109}$$

Assuming that $V_T \cong IV$, Equation (2-109) relates a densification strain rate to a volume strain rate by

$$\frac{1}{\rho} \frac{d\rho}{dt} = \left(\frac{V - V_0}{V_0}\right) \frac{1}{\Delta t} \quad . \tag{2-110}$$

This can be reduced to a linear strain rate by using the assumption that

$$\frac{1}{3}\frac{\Delta V}{V_0 \Delta t} = \frac{\Delta L}{L_0} \frac{1}{\Delta t} . \tag{2-111}$$

Equations (2-97) and (2-99) must be used with caution because the models are based on very limited data. Both equations are based on one data set, and these data cover only a small portion of the temperatures, pressures, oxygen to metal ratios, and grain sizes possible in a reactor environment. An additional concern is that a significant change in any one of these parameters could result in a different creep mechanism.

2.10.4 References

- 2.10-1 A. A. Solomon, K. M. Cochran, and J. H. Habermeyer, *Modeling Hot-Pressing of UO*₂, NUREG/CR-2023, March 1981.
- 2.10-2 J. L. Routbort, J. C. Voglewede, and D. S. Wilkinson, "Final Stage Densification of Mixed Oxide Fuels," *Journal of Nuclear Materials*, 80, 1979, pp. 348-355.
- 2.10-3 D. S. Wilkinson and M. F. Ashby, "The Development of Pressure Sintering Maps," *Proceedings of the Fourth International Conference on Sintering and Related Phenomena, May* 26-28, 1975.
- 2.10-4 D. S. Wilkinson and M. F. Ashby, "Pressure Sintering by Power Law Creep," *Acta Metallurgica*, 23, November 1975.
- 2.10-5 R. A. Wolfe and S. F. Kaufman, Mechanical Properties of Oxide Fuels (LSBR/LWB) Development Program, WAPD-TM-58, October 1967.
- 2.10-6 R. C. Rossi and R. M. Fulrath, "Final Stage Densification in Vacuum Hot Pressing of Alumina," Journal of the American Ceramic Society, 48, 1965, pp. 558-564.
- 2.10-7 J. D. McCelland, Kinetics of Hot Pressing, NAA-SR-5591, 1961.

- 2.10-8 G. M. Fryer, "Hot Pressing of Alumina: A New Treatment of Final Densification," *Transactions of the British Ceramics Society, 66,* 1967, pp. 127-134.
- 2.10-9 M. S. Seltzer, A. H. Claver, and B. A. Wilcox, "The Influence of Stoichiometry on Compression Creep of Uranium Dioxide Single Crystals," *Journal of Nuclear Materials*, 44, 1972, pp. 43-56.
- 2.10-10 M. S. Seltzer et al., "A Review of Creep Behavior of Ceramic Nuclear Fuels," Reactor Technology, 14, 2, January 1971, pp. 99-135.
- 2.10-11 M. S. Seltzer, A. H. Calver, and B. A. Wilcox, "The Stress Dependence for High Temperature Creep of Polycrystalline Uranium Dioxide," *Journal of Nuclear Materials*, 34, 1970, pp. 351-353.
- 2.10-12 S. F. Kaufman, The Hot Pressing Behavior of Sintered Low Density Pellets of UO₂, ZrO₂-UO₂, THO₂ and THO₂-UO₂, WAPD-TM-751, May 1969.
- 2.10-13 I. Amato, R. L. Colombo, and A. M. Petrucciolo Balzari, "Hot Pressing of Uranium Dioxide," Journal of Nuclear Materials, 20, 1966, pp. 210-214.
- 2.10-14 P. E. Hart, "Fabrication of High Density UO₂ and (U_{0.75} Pu_{0.25})O₂ by Hot Pressing," *Journal of Nuclear Materials*, 51, 1974, pp. 199-202.
- 2.10-15 I. H. Warren and A. C. D Chaklader, "Reactive Hot Pressing of Nonstoichiometric Uranium Dioxide," *Metallurgical Transactions*, 1, 1970, pp. 199-205.
- 2.10-16 J. C. Voglewede, Reactor Development Program Progress Report, ANL-RDP-26, March 1974.
- 2.10-17 J. C. Voglewede, Reactor Development Program Progress Report, ANL-RDP-29, June 1974.

2.11 Restructuring (FRESTR)

The morphology and structural integrity of oxide fuel changes while power is being produced in LWRs. These changes are a function of time, temperature, burnup, and energy density. These structural changes affect the effective fuel thermal conductivity, fuel swelling, fission gas release, and fuel creep. The structure of irradiated fuel can be grouped into four categories: as-fabricated unrestructured fuel, equiaxial grains which are enlarged fuel grains with all sides approximately the same length, columnar grains that have their long axes parallel to the radial temperature gradient, and shattered or desintered grains consisting of fuel grains which are fractured free of bonds to other grains during high power transients. The physical processes which create restructured fuel and models to predict the modified fuel structures are discussed in the following sections.

2.11.1 Summary

The FRESTR subroutine is used to calculate equiaxial grain size, columnar grain size, and regions of fuel shattering during normal or transient reactor operation. Grain growth is driven by a potential

difference across a curved grain boundary or by a temperature gradient, with the growth rate is controlled by the motion of impurities at the grain boundaries. Since impurities and migration mechanisms are probably the same in UO₂ and (U, Pu)O₂, the model described in the following paragraphs is assumed to apply for both fuel types.

The growth rate of equiaxial fuel grains is calculated using the expression

$$g = \left(\frac{1.0269 \times 10^{-13} \text{te}^{\left(\frac{-35873.2}{T}\right)}}{(1.0 + 5.746 \times 10^{-6} \text{B})^2 \text{T}} + g_0^4\right)^{1/4}$$
(2-112)

where

g = grain size at the end of a time interval (m)

 g_0 = grain size at beginning of the time interval (m)

t = time interval(s)

T = temperature (K)

B = burnup (MWs/kg).

The standard error of Equation (2-112) with respect to its data base is $\pm 8.4 \times 10^{-6}$ m.

Columnar grains form behind lenticular (large lens shaped) pores, moving up the temperature gradient in the fuel at a rate given by the equation

$$V = \frac{49.22\nabla T e^{\frac{44980}{T}}}{T^2}$$
 (2-113)

where

V = rate of pore movement (M/s)

 ∇T = temperature gradient (K/m)

T = temperature (K).

Columnar grain formation is characterized by a threshold temperature and temperature gradient. This threshold temperature is defined by the time, temperature, and temperature gradient combination required

to move a grain boundary or bubble across one-tenth of the pellet diameter (approximately 0.0005 m) during a time step. The long axis of a columnar grain is the smaller of the length of the pore migration during a time step or the distance to the center of the pellet.

Formation of shattered fuel is characterized in FRESTR by an integer switch, NSHATR, which is unity if the fuel is shattered and zero if the fuel is not shattered.

If $E \ge E_0$ and $T < T_m$ and columnar grains have not formed

$$NSHATR = 1$$
 . (2-114)

If $E < E_0$ or $T > T_m$ or columnar grains have formed

$$NSHATR = 0 (2-115)$$

where

E = energy density deposited during a transient (J/m^3)

 E_0 = energy density required to fracture the fuel at the grain boundaries (J/m³)

 $T_{\rm m}$ = fuel melting temperature (K)

T =fuel temperature (K).

The energy density required to fracture the fuel at the grain boundaries is determined by the expression

$$E_0 = \frac{8.64 \times 10^{-14}}{g} (T - 1673) . (2-116)$$

The following paragraphs discuss restructuring data and the code development approach. Section 2.11.2 is a discussion of restructuring data. Section 2.11.3 describes the approach used to develop the FRESTR code. Section 2.11.4 is a list of references.

2.11.2 Restructuring Data

The FRESTR restructuring subcode is based on a fit of equation constants to data available in the literature. A complete data base requires both unirradiated isothermal and irradiated restructuring data, with accompanying well documented temperature profiles. Unirradiated isothermal restructuring data are relatively easy to obtain, and a number of good data sets are available for the data base. Irradiated

restructuring data with well documented temperature and time histories, on the other hand, are difficult to obtain, especially at burnups above 20,000 MWd/t. The following paragraphs discuss data available in the open literature and the merits of those data for the FRESTR code data base.

The data of Ainscough, ^{2.11-1} Singh, ^{2.11-2} MacEwan, ^{2.11-3} Stehle, ^{2.11-4} Brite, ^{2.11-5} and Freshley ^{2.11-6} are useful for equiaxial grain growth model development. Data analysis published by Singh, Michels and Poeppel ^{2.11-7} and Oldfield and Brown ^{2.11-8} show surface diffusion as the mechanism controlling boundary migration; and data published by Gulden, ^{2.11-9} Williamson and Cornell, ^{2.11-10} Brite, ^{2.11-5} and Michels and Poeppel ^{2.11-8} (for fission gas bubbles) show either volume diffusion or vapor transport as the controlling mechanism. Since no data unequivocally demonstrate which mechanism is controlling grain growth and since more available data indicate volume diffusion or vapor transport as the controlling mechanism, volume diffusion equations were used to develop the FRESTR code. A detailed discussion of the data sets used is contained in this section.

Lenticular pore migration velocity data of Kawamata, ^{2.11-11} Oldfield and Brown, ^{2.11-8} and Ronchi and Sari^{2.11-12} were used to develop the FRESTR columnar grain growth model. Other available data sets were used only qualitatively to determine specific mechanisms. These data sets are also discussed in this section. Lenticular pore migration data indicate that the probable diffusion mechanism controlling columnar grain growth rates is volume diffusion or vapor phase transport. Each mechanism results in a velocity migration rate equation of the form discussed in the model development section.

Ainscough^{2.11-1} conducted a thorough investigation of equiaxial grain growth in urania using samples with initial theoretical densities between 0.94 and 0.99%, temperatures between 1,273 and 1,773 K, and times up to 24 weeks (1.45152 x 10⁷ seconds). The densities and the O/M ratios of the samples remained constant during testing and showed little grain growth at temperatures below 1,500 K. Above 1,500 K, the grain growth rate increased rapidly with increasing temperatures. Ainscough also reported some data from irradiated fuel that were received through personal communications. These data had burnup values approaching 14,000 MWd/t at temperatures representative of LWRs. Therefore, the Ainscough data were considered to be the best available for determining the effect of burnup or grain growth rates.

Singh^{2.11-2} measured isothermal grain growth rates of urania at temperatures between 2,073 and 2,373 K for times up to 21 hours (75,600 seconds). Equiaxial grains formed during their experiments, with no accompanying change in O/M ratio. Singh concluded from his data analysis that urania grain growth follows the cubic vapor transport law and determined pore sizes to be at equilibrium with the surface tension. He also observed test sample densities to decrease during the experiments. These observations suggest vapor phase transport growth with a pore size gas pressure equilibrium.

MacEwan $^{2.11-3}$ measured grain growth of urania at constant temperatures between 1,828 and 2,713 K for times up to 700 hours (2.52 x 10^6 seconds). The MacEwan data are excellent for model development because of the long times and appropriate temperatures.

Stehle^{2.11-4} reported grain growth measured at temperatures between 1,823 and 2,373 K and at times up to 120 hours $(4.32 \times 10^5 \text{ seconds})$. These data are also an excellent source for the FRESTR data base.

Hausner^{2.11-13} studied grain growth while sintering green urania pellets (cold pressed and unsintered) and grain growth in some presintered pellets. Grain growth rates in presintered pellets were measured at temperatures between 2,223 and 2,853 K. Sintering grain growth of green pellets is different than the grain growth being modeled in FRESTR, so the Hausner data were not used in the FRESTR data base.

Brite^{2.11-5} reported extensive UO₂ densification, and Freshley^{2.11-6} reported mixed oxide densification grain growth and porosity measurements in both isothermal and in-reactor environments. Although these data were useful for determining the effect of burnup on grain growth rate, they were less useful than desired because most of the data were obtained at temperatures where little grain growth occurs.

Eichenberg^{2.11-14} reported three grain growth data taken from samples at 2,273, 2,473 and 2,573 K and annealed at these temperatures for 900 seconds. These data were used as part of the FRESTR data base.

Runfors^{2.11-15} and Padden^{2.11-16} measured grain growth in UO_2 during sintering from green compacts. These data do not represent growth rates of final sintering or resintering pellets and are, therefore, of no value for FRESTR code development.

Williamson and Cornell^{2.11-10} observed bubble migration rates in single-crystal UO₂. Although the FRESTR code does not consider pore velocities or rates for equiaxial grain growth, these observation are interesting in that they demonstrate possible migration mechanisms of pores or impurities that control the growth rate of equiaxial grains.

Data provided by Kawamata^{2.11-11} dealt with columnar grain formation. His results demonstrated that columnar grains are formed by pores migrating up a temperature gradient with migration velocities between 2.389×10^{-9} and 4.0×10^{-8} m/s.

Buescher and Meyer^{2.11-17} measured migration velocities of 3 x 10⁻¹⁰ m/s for helium gas bubbles in single-crystal urania. Their results were not useful for the FRESTR data base because intragranular bubbles do not control grain boundary movement.

Oldfield and Brown^{2.11-8} published from experimental results lenticular pore migration velocities up to 1.5×10^{-8} m/s and columnar grain growth measurements. These data were used in the data base for the FRESTR grain growth model.

Michels and Poeppel^{2.11-7} measured migration velocities of fission gas bubbles and fission product inclusions in mixed oxides. The migration velocities of fission product inclusions were found to be

dependent on the size of the inclusion. These data were used only to help define maximum and minimum migration rates.

Gulden^{2.11-9} measured bubble migration velocities at the equilibrium pressures of long lived or stable fission gas species, using irradiated fuel with burnups of approximately 10^{26} fissions/m³ (~ 3.0 x 10^{25} krypton and xenon atoms/m³ UO₂). These data are interesting in that they show the probable bubble migration mechanism but were not useful for developing the detailed thermal gradient correlation for bubble migration contained in the FRESTR subcode.

Ronchi and Sari^{2.11-12} measured lenticular pore migration rates and grain boundary migration rates at temperatures between 2,200 and 3,000 K. These data were useful in developing the FRESTR subcode.

In-pile restructuring data from EG&G Idaho, Inc.^{2.11-18,2.11-19,2.11-20} and out-of-pile data from Argonne tests^{2.11-21} were all that are available on fuel shattering. These data were used to determine an approximate fuel shattering model in spite of the large uncertainty of the temperature.

2.11.3 Model Development

An equiaxial grain growth and pore migration model based on theory and a fit of the data, was developed for use in the FRESTR subcode. Many of the material properties used in developing the theoretical equations are not well defined and are, therefore, included in the fitted constants. The theoretical derivation proves very beneficial in that the dependence of restructuring on temperature, time, power density, and impurity particle size can be determined.

The equiaxial and columnar grain growth equations are based on the equations developed in a paper by Shewman, 2.11-22 who considers three possible diffusion mechanisms: surface diffusion, volume diffusion, and vapor transport. These mechanisms describe the motion of impurities, bubbles, or inclusions on the grain boundaries that retard and control the motion of the grain boundaries. As discussed in the previous section, much of the data show volume diffusion as the controlling mechanism for grain boundary migration. The equation Shewman obtained for volume diffusion migration is

$$V = \frac{\alpha D_{V} F_{a}}{T}$$
 (2-117)

where

V = velocity of atom movement (m/s)

 α = constant

 D_v = volume diffusion coefficient (m²/s)

 F_a = force driving atom (N) T = temperature (K).

Equation (2-117) was used for columnar grain growth for the following reasons. The data discussed in Section 2.11.3 indicate volume diffusion or possibly vapor transport at constant pressure as the controlling mechanism for lenticular pores forming large columnar grains. Shewman^{2.11-22} showed that an approach similar to that described previously for vapor transport produced an equation of the same form as Equation (2-117), thus making this equation proper assuming either mechanism.

The approach used by Nichols^{2.11-23} and Shewman^{2.11-22} to relate the force on each atom to the force driving the entire bubble and grain boundary was used to further develop Equation (2-117) into a usable form, resulting in the following equation for equiaxial grain growth

$$\frac{\mathrm{dx}}{\mathrm{dt}} = \frac{\beta D_{\mathrm{V}}}{\mathrm{r}^3 \mathrm{T}} \tag{2-118}$$

where

x = the migration distance (m)

t = time(s)

 β = constant

r = bubble radius (m).

If the migration distance is assumed to be equal to the grain boundary migration distance and the particle radius is assumed to be proportional to the grain size and burnup, then

$$r = \beta'(1 - \beta B)g \tag{2-119}$$

where

 $\beta', \beta = constants$

B = burnup (MWs/kg)

g = grain size (m).

Substitution of Equation (2-119) into Equation (2-118) and use of a common temperature dependent form for the volume diffusion constant results in the expression

Uranium Dioxide/Mixed Oxides

$$\frac{dg}{dt} = \frac{aD_0 e^{(\theta/T)}}{T(1-\beta B)^2 g^3}$$
 (2-120)

where

 D_o = diffusion coefficient (m²/s)

 θ = activation energy divided by the gas constant (K).

Combining the equation constants and integrating gives the final form of the equiaxial grain growth equation

$$g^4 - g_0^4 = \frac{D\Delta t e^{(\theta/T)}}{T(1 - \beta B)^2}$$
 (2-121)

where

g = final grain size (m)

 g_0 = grain size at beginning of increment (m)

D = constant.

The constants D and θ of Equation (2-121) were determined by fitting the data of Singh, $^{2.11-2}$ MacEwan, $^{2.11-3}$ Stehle, $^{2.11-4}$ and Ainscough $^{2.11-1}$ with $\beta=0$ (no irradiation). The constant β was then determined by fitting the equation to the irradiation data of Ainscough. $^{2.11-1}$

The movement of columnar grains can be derived using Equation (2-117). For columnar grain growth, the grain boundary driving force is derived from a temperature gradient in the fuel. This analysis was done by Shewman, who obtained the following expression for the bubble velocity

$$V = \frac{C\nabla T e^{(\theta/T)}}{T^2}$$
 (2-122)

where

V = pore migration velocity (m/s)

C = constant

 ∇T = temperature gradient (K/m).

The constants in Equation (2-122) were then fit to the data of Ronchi and Sari, ^{2.11-12} Michels and Poeppel^{2.11-7} (for upper and lower bounds), Buescher, ^{2.11-17} Oldfield and Brown, ^{2.11-8} and Kawamata. ^{2.11-11}

Equation (2-122) was used to calculate the onset of columnar grain growth. An assumption, suggested by Nichols, ^{2.11-24} that columnar grains form only if lenticular pores are able to migrate one-sixth of the pellet radius, was required to define columnar grain growth in the subcode. On the basis of this criterion, columnar grains form only if the migration distance per time step is greater than 0.0005 m. If this criterion is not met, the grain size is determined by equiaxial grain size calculations and the columnar grain growth switch, NCOLGN, is set to zero. If columnar grains were formed in a previous time step, the preceding calculations are bypassed and NCOLGN remains unity. If columnar grains are formed, their length is the smaller of the migration distance during the time step or the distance from the ring edge to the center of the fuel pellet. Figure 2-35 shows typical columnar growth threshold as a function of time and temperature with an average temperature gradient of 4.0 x 10⁵ K/m.

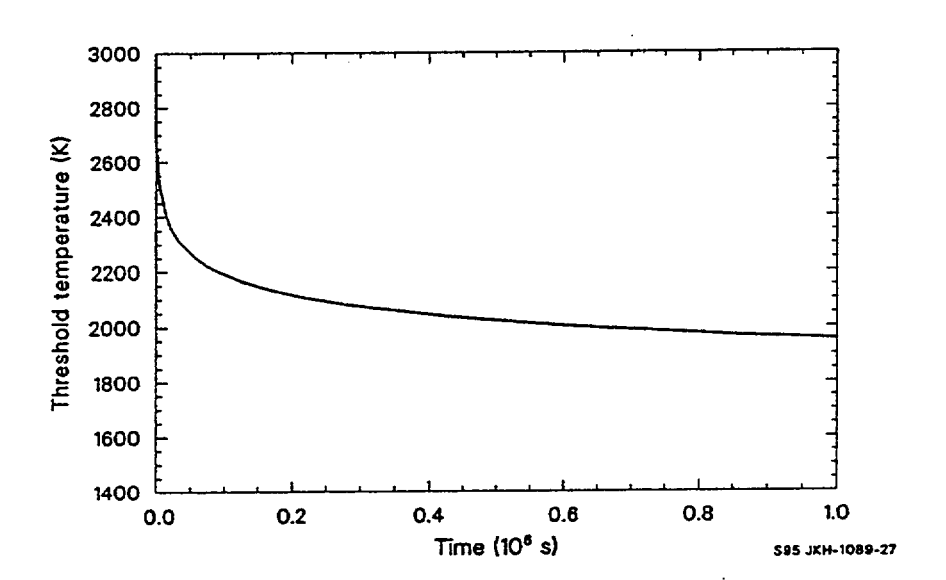


Figure 2-35. Threshold of columnar grain growth with temperature gradient of 4.0 x 10⁵ K/m.

The model for fuel shattering is taken from a study of this effect by Cronenberg and Yackle, ^{2.11-25} using data from the reactivity initiated accident (RIA) tests by EG&G Idaho and direct electrical heating tests by Argonne. They found the fuel shattered at the grain boundaries when the stress resulting from the deposited energy is greater than the fracture strength. Their expression for the energy density at fracture is

$$E = \frac{8.64 \times 10^{-14} (T - 1673)}{g} . (2-123)$$

The FRESTR subcode uses Equation (2-123) to determine whether the fuel in the region of fuel being considered has fractured at the grain boundaries. If the input energy density is greater than E, the fuel temperature is less than melting, and columnar grains have not formed, the fuel is assumed to be shattered and the shattering parameter, NSHATR, is set to unity.

2.11.4 References

- 2.11-1 J. B. Ainscough, B. W. Oldfield and J. O. Ware, "Isothermal Grain Growth Kinetics in Sintered UO₂ Pellets," *Journal of Nuclear Materials*, 49, 1973/74, pp. 117-128.
- 2.11-2 R. N. Singh, "Isothermal Grain Growth Kinetics in Sintered UO₂ Pellets," *Journal of Nuclear Materials*, 64, 1977, pp. 174-178.
- 2.11-3 J. R. MacEwan, Grain Growth in Sintered Uranium Dioxide, AECL-1184, 1961.
- 2.11-4 V. H. Stehle, "Kornwachstrum von UO₂," Bericht der Deutschen Keramische Gesellshaft, 1963, pp. 129-135.
- 2.11-5 D. W. Brite et al., EEI/EPRI Fuel Densification Project 131-Final Report, 1975.
- 2.11-6 M. D. Freshley et al., Plutonia Fuel Study, EPRI NP-637, 1978.
- 2.11-7 L. C. Michels and R. B. Poeppel, "In-Pile Migration of Fission Product Inclusions in Mixed Oxide Fuel," *Journal of Applied Physics*, 44, 1973.
- 2.11-8 W. Oldfield and J. B. Brown, Jr., "Bubble Migration in UO₂-A Study Using a Laser Image Furnace," *Material Science and Engineering*, 6, 1970, pp. 361-370.
- 2.11-9 M. E. Gulden, "Migration of Gas Bubbles in Irradiated Uranium Dioxide," *Journal of Nuclear Materials*, 23, 1967, pp. 30-36.
- 2.11-10 G. K. Williamson and R. M. Cornell, "The Behavior of Fission Product Gases in Uranium Dioxide," *Journal of Nuclear Materials*, 13, 1974, pp. 278-280.
- 2.11-11 H. Kawamata, H. Kaneko, H. Furuya, and M Koizumi, "Migration Rate of Lenticular Voids in UO₂ Under the Influence of Temperature Gradient," *Journal of Nuclear Materials*, 68, 1977, pp. 48-53.
- 2.11-12 C. Ronchi and C. Sari, "Properties of Lenticular Pores in UO₂, (U, Pu)O₂" Journal of Nuclear Materials, 50, 1974, pp. 91-97.
- 2.11-13 H. Hausner, "UO₂ Grain Growth and Melting Studies," High Performance Quarterly Progress Reports, GEAP-3771-5, 3771-6, 3771-7, 1962, 1963.
- 2.11-14 J. D. Eichenberg, Effects of Irradiation on Bulk UO2, WAPD-183, 1957.

- 2.11-15 U. Runfors et al., "Sintering of Uranium Dioxide," Proceedings of 2nd International Conference on Peaceful Uses of Atomic Energy, 6, Paper P/142, September 1958, p. 605.
- 2.11-16 T. R. Padden, "Behavior of Uranium Oxide as a Reactor Fuel," *Proceedings of 2nd International Conference on Peaceful uses of Atomic Energy, 6*, Paper P/2404, September 1958, pp. 569-586.
- 2.11-17 B. J. Buescher and R. O. Meyer, "Thermal Gradient Migration of Helium Bubbles in Uranium Dioxide," *Journal of Nuclear Materials*, 48, 1973, pp. 143-156.
- 2.11-18 P. E. MacDonald et al., Response of Unirradiated and Irradiated PWR Fuel Rods Tested Under Power Cooling Mismatch Conditions, TREE-NUREG-1196, January 1978.
- 2.11-19 R. W. Garner et al., Gap Conductance Test Series-2, Test Results Report of Tests GC2-1, GC2-2, and GC2-3, NUREG/CR-0300, TREE-1268, 1978.
- 2.11-20 R. J. Buckland, C. E. White, and D. G. Abbott, Experimental Data Report for Test RIA1-1 (Reactivity Initiated Accident Test Series), NUREG/CR-0516, TREE-1236, 1979.
- 2.11-21 R. G. Sachs and J. A. Kyger, Light Water Reactor Safety Research Program: Quarterly Progress Report, ANL-77-59, April-June 1977, pp. 76-111.
- 2.11-22 P. G. Shewman, "The Movement of Small Inclusions in Solids by a Temperature Gradient," Transactions of the Metallurgical Society of AIME, 230, 1964.
- 2.11-23 F. A. Nichols, "Theory of Grain Growth in Porous Compacts," *Journal of Applied Physics*, 37, 1966, pp. 4599-4062.
- 2.11-24 F. A. Nichols, "Theory of Columnar Grain Growth and Central Void Formation in Oxide Fuel Rods," *Journal of Nuclear Materials*, 22, 1977, pp. 214-222.
- 2.11-25 A. W. Cronenberg and T. R. Yackle, An Assessment of Intergranular Fracture Within Unrestructured UO₂ Fuel Due to Film Boiling Operation, NUREG/CR-0595, TREE-1330, March 1979.

2.12 Fracture Strength (FFRACS)

FFRACS calculates the UO_2 fracture strength as a function of fuel temperature and fractional fuel density.

2.12.1 **Summary**

FFRACS calculates the fracture strength of UO₂ as a function of fractional fuel density and temperature up to 1,000 K, the lowest temperature at which plasticity has been observed in-pile. For temperatures above 1,000 K, a constant value is used for the in-pile fracture strength of plastic UO₂. The UO₂ fracture model is given by the following equations:

For $273 < T \le 1,000 \text{ K}$.

$$\sigma_{\rm F} = 1.7 \times 10^8 [1 - 2.62(1 - D)]^{1/2} e^{\left(-\frac{1590}{8314\text{ T}}\right)} . \tag{2-124}$$

For T > 1,000 K,

$$\sigma_{\rm F} = \sigma_{\rm F} (1000 \,{\rm K})$$
 (2-125)

where

 $\sigma_{\rm F}$ = fracture strength (Pa)

D = fraction of theoretical density

T = temperature (K)

 $\sigma_{\rm F}(1000~{\rm K}) =$ fracture strength found with T = 1,000 K.

Equation (2-124) is based upon out-of-pile UO_2 data and describes the behavior of brittle UO_2 . Because no in-pile measurements of fracture strength have been made, Equation (2-125) is based upon theoretical considerations and fragmentary out-of-pile data and applies to plastic UO_2 . The transition from brittle to ductile material is accompanied by a discontinuity in fracture strength and occurs at temperatures below the usual out-of-pile brittle ductile transition temperature due to fission induced plasticity. Equation (2-124) has a standard deviation with respect to experimental data of 0.19 x 10^8 Pa. The uncertainty in Equation (2-125) is not estimated because of lack of in-pile data.

2.12.2 Out-of-Pile Uranium Dioxide Deformation

The out-of-pile deformation of UO₂ exhibits either elastic or elastic plastic behavior. Elastic behavior is characterized by stress being linearly proportional to strain up to the fracture point.^{2.12-1} to ^{2.12-5} Elastic plastic behavior is characterized by the stress strain curve, which is initially elastic (to the elastic proportional limit) and which then exhibits plastic behavior.^{2.12-1} to ^{2.12-5}

2.12.2.1 Review of Out-of-Pile Uranium Dioxide Elastic Behavior Data and Theory. At temperatures below a ductile brittle transition temperature, T_c , UO_2 deforms elastically up to the fracture point. $^{2.12-1}$ to $^{2.12-5}$ In such cases, the fracture strength, σ_F , is much less than the yield strength, σ_y , so that no yielding occurs prior to fracture. The fracture topography of near theoretically dense UO_2 exhibits the cleavage fracture mode of a brittle material. However, this fracture mode is affected by the amount of porosity and grain size, where, in general, the relative proportion of brittle to ductile fracture decreases

with an increase in porosity and a decrease in grain size. 2.12-6

The crack initiator^{2.12-1},^{2.12-2},^{2.12-4},^{2.12-6} has been suggested as the largest pore. The Griffith fracture theory^{2.12-7} can be applied to theoretically examine the parameters that affect the fracture strength. Griffith showed that the fracture stress or critical stress required to propagate an elliptical crack of length 2c with an infinitely small radius of curvature is given by Equation (2-126):

$$\sigma_{\rm F} = \left(\frac{2\gamma E}{\pi c (1 - v^2)}\right)^{1/2} \tag{2-126}$$

where

E = elastic modulus (Pa)

 γ = surface energy (J/m²)

 $c = \operatorname{crack} \operatorname{length} (m)$

 ν = Poisson's ratio (unitless).

This equation applies to planar strain conditions and to an infinitely thick section of purely elastic material.

In Equation (2-126), the fracture strength is proportional to the square root of the elastic modulus, which, in turn, linearly decreases with porosity and temperature, as discussed in Section 2.6.1 of this report. Therefore, the fracture strength should decrease with increasing temperature. However, the fracture strength of UO_2 has been observed to increase slightly with temperature. These measurements can be explained by the fact that γ in Equation (2-126) probably increases with temperature $^{2.12-4}$ at a faster rate than the rate of decrease of E with temperature.

Hasselman^{2.12-8} has shown that when a material contains numerous elliptical cracks of length 2c spaced a distance 2h from each other. Equation (2-126) becomes for planar strain conditions

$$\sigma_{\rm F} = \left(\frac{\rm E\gamma}{2(1-v^2)h}\right)^{1/2} \cot\left(\frac{\pi c}{2h}\right) \tag{2-127}$$

where the terms are previously defined.

Equation (2-127) and Equation (2-126) both predict a UO_2 fracture strength that is dependent on porosity because of the effect of porosity on the elastic modulus. Equation (2-127) also predicts a crack spacing effect upon fracture strength, which, in turn, depends upon both the pore size and volume of

porosity. A fracture strength dependence upon the pore morphology (size, shape, and distribution) has also been observed by Roberts and Ueda.^{2.12-1}

2.12.2.2 Out-of-Pile Elastic Models. Experimental data^{2.12-1,2.12-2,2.12-6,2.12-9,2.12-10} for fracture strength in the brittle region were fit to Equation (2-128) using a linear least-squares regression analysis [after reducing Equation (2-128) to a linear form] to determine the coefficients A, m, and Q

$$\sigma_{\rm F} = A \left[1 - 2.62 (1 - {\rm D})\right]^{1/2} {\rm G}^{-m} {\rm e}^{(-{\rm Q/RT})}$$
 (2-128)

where

$$G = grain size (\mu m)$$

R = gas constant
$$(8.314 \text{ J/mol} \cdot \text{K})$$

and the other terms of the equation have been previously defined. The following values of A, m, and Q were determined:

A =
$$1.70 \times 10^8 \text{ Pa}$$

$$m = 0.047$$

$$Q = 1,590 \text{ J/mol}.$$

The expression $[1-2.62 \ (1-D)]^{1/2}$ arises from the proportionality between σ_F and \sqrt{E} in Equations (2-126) and (2-127) and the relation between E and D (see Section 2.6.1). The expression between fracture strength and grain size was based upon the suggestion of Orowan^{2.12-11} and Petch^{2.12-12} and the data of Igata and Domoto, ^{2.12-13} which relate the strength of a material to $G^{-1/2}$. In general terms, this factor is written G^{-m} . The Boltzmann factor was selected to represent the temperature dependence. The effects of pore morphology have been ignored because of a lack of appropriate data. In Figure 2-36, Equation (2-128) is compared with experimental data normalized to a 10- μ m grain size and to 95% TD using Equation (2-128).

Knudsen^{2.12-14} proposed the following empirical equation relating fracture strength to grain size and porosity:

$$\sigma_{\rm F} = AG^{\rm -m} \, e^{[-b(1 - D)]}$$
 (2-129)

where

$$1 - D = porosity$$

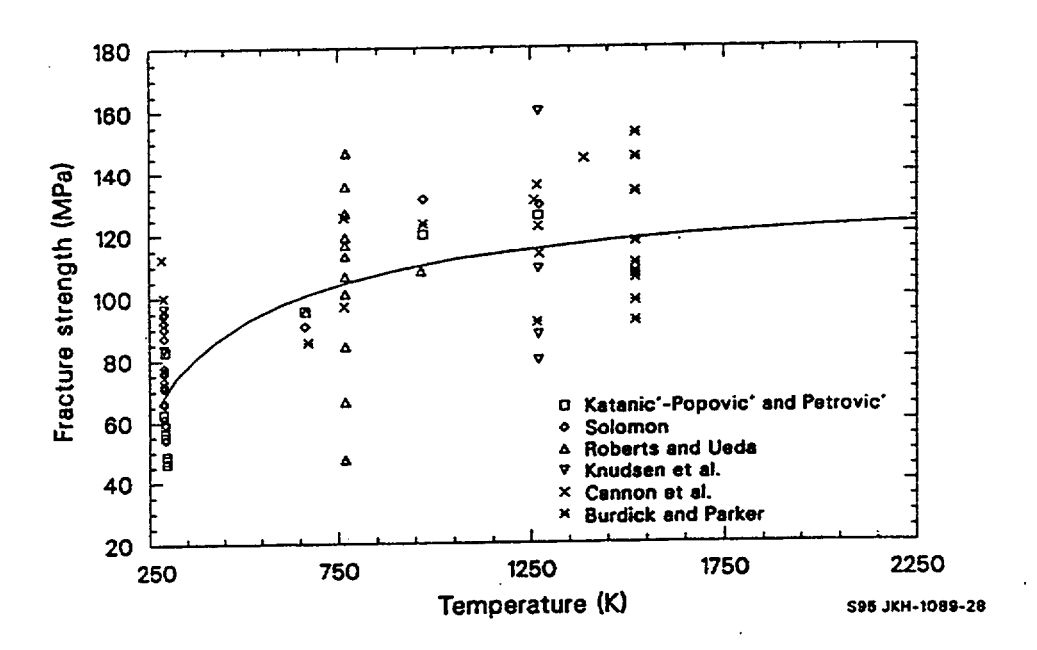


Figure 2-36. Comparison of Equation (2-128) in the elastic behavior regime with out-of-pile UO₂ fracture strength data normalized to 10-μm grain size and 95% TD.

the other terms have been previously defined, and constants are given below.

Knudsen suggested that this relation describes the strength of chromium carbide and thoria reasonably well. This expression was fit to UO₂ fracture strength data, except that the Arrhenius term from Equation (2-128) was added to provide a temperature dependence. The resultant expression was reduced to a linear form; and a linear, multiple variable regression analysis was used to determine the coefficients A, m, b, and Q. The results are:

A =
$$1.7108 \times 10^8 \text{ Pa}$$

m = 0.05136
b = 2.412
Q = 1649 J/mol.

Equation (2-129) is compared with experimental data in Figure 2-37.

Both Equations (2-128) and (2-129) indicate a very small effect of grain size upon the fracture strength. Values of m on the order of 0.5 are expected theoretically; ^{2.12-11,2.12-12} but values of 0.05 were

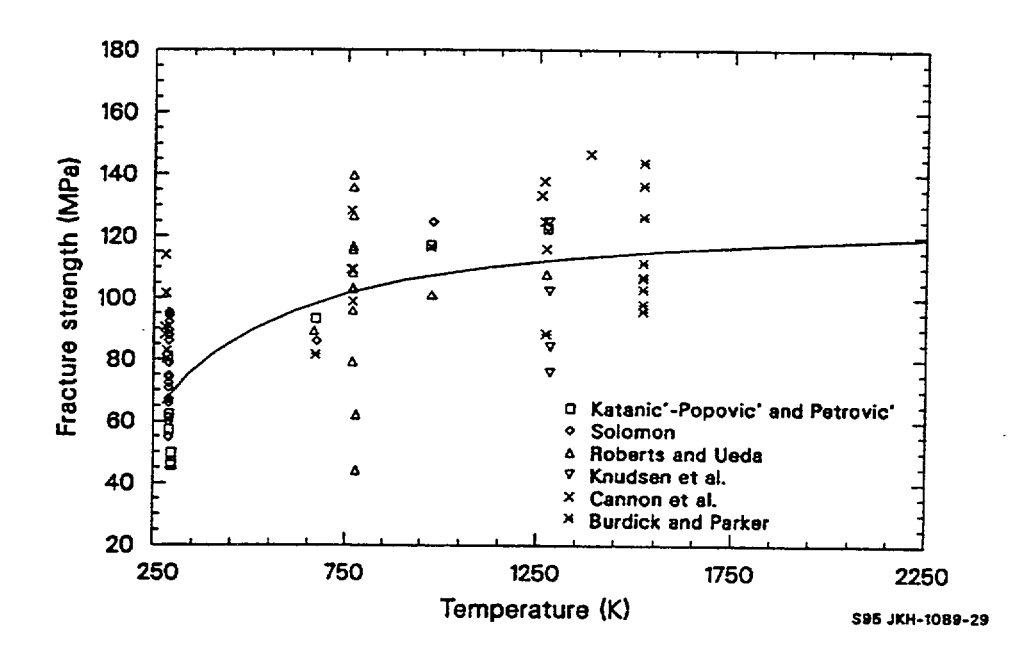


Figure 2-37. Comparison of Equation (2-129) in the elastic behavior regime with out-of-pile UO_2 fracture strength data normalized to 10- μ m grain size and 95%TD.

obtained, indicating a very insignificant effect of grain size on UO_2 fracture strength. Much scatter exists in the data with respect to Equations (2-128) and (2-129) and is attributed to differences in pore morphology not accounted for in these equations and also not reported with the data.

In some cases, porosity has not been the initiator of cracks in UO_2 . Instead, silica or alumina^{2.12-12} precipitated at grain boundaries has considerably reduced the fracture strength, whereas small additions of titania increased the fracture strength of UO_2 .^{2.12-9} These additions are not normally part of the fabrication process and were not considered in the UO_2 fracture strength model.

2.12.2.3 Out-of-pile Transition Temperature. The transition temperature, T_c , is defined to be the temperature at which the stress strain curve departs from (linear) elastic to plastic behavior. Density, grain size, and strain rate are expected to affect this transition temperature, but data are insufficient to obtain a precise relationship.

Cannon et al. $^{2.12-2}$ reported out-of-pile transitions at 1,100, 1,375, and 1,450 °C for strain rates of 0.092, 0.92, and 9.2/h, respectively, in material with an 8 m average grain size. Transitions at 1,050 and 1,100 °C occurred for a strain rate of 0.092/h in material with 15 and 3 μ m average grain sizes, respectively. Evans and Davidge $^{2.12-4}$ reported transition temperatures of 1,200 and 1,300 °C for 8 and 25 μ m materials. A transition temperature of 1,250 °C is assumed for FFRACS, since that is the midpoint of the 1,050 to 1,450 °C range.

2.12.2.4 Out-of-pile Uranium Dioxide Elastic Plastic Behavior. At temperatures above the transition temperature, the deformation of UO₂ exhibits plastic behavior after some elastic deformation has occurred. The fracture mode is mostly intergranular, and a significant contribution to the deformation arises from grain boundary sliding. Figure 2-38 shows the fracture strength of UO₂ as a function of temperature. At temperatures above T_c, the ultimate tensile strength decreases with increasing temperature. The effect of strain rate is significant, but the effect of grain size is negligible for grain sizes up to about 30 µm. Strain rate effects and grain boundary sliding strongly suggest that creep plays a dominant role at these temperatures. When the creep rate for a given temperature is nearly the same order of magnitude as the strain rate, stress relaxation reduces the fracture stress. This effect is shown in Figure 2-38 by the increase in fracture strength with the increase in strain rate.

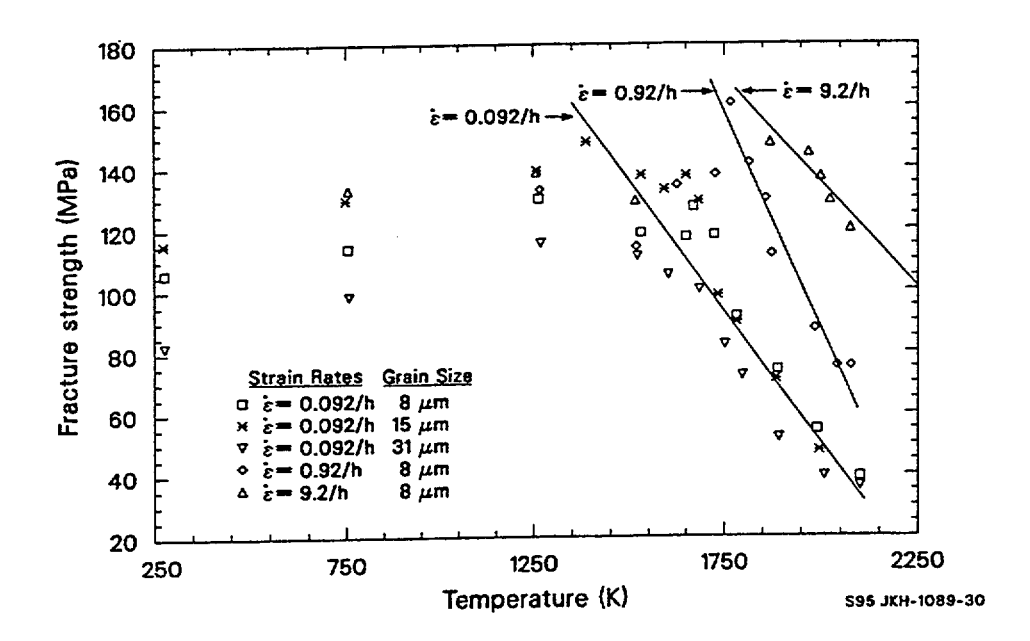


Figure 2-38. Least squares regression fit of UO₂ fracture strength in the elastic plastic regime to out-of-pile data of Cannon et al.

2.12.3 Uranium Dioxide Fracture Strength Model

Irradiation substantially reduces the ductile brittle transition temperature. As discussed in Section 2.7, in-pile creep measurements show that plasticity exists in UO_2 at temperatures as low as 1,000 K. UO_2 is assumed to be brittle below this temperature, and Equation (2-128) (without the grain size term) is selected for the low temperature fracture strength model for UO_2 . Equations (2-128) and (2-129), each with a standard deviation of about 1.9 x 10^7 Pa, predict the experimental out-of-pile fracture strength about equally well; but Equation (2-128) has more theoretical foundation.

Above 1,000 K, irradiation and thermal effects enhance the plasticity of UO_2 so that a decrease in fracture strength with increasing temperature may not occur. A strain rate effect may also exist, but the experimental data available are not sufficient to quantify a strain rate effect. Therefore, the in-pile fracture strength for plastic UO_2 at temperatures higher than 1,000 K is taken to be that found with the low temperature correlation at 1,000 K. This ensures calculational continuity between the two correlations.

The in-pile UO₂ fracture strength model is summarized by Equations (2-124) and (2-125).

Equation (2-124) can be used for temperatures up to about 1,323 K for out-of-pile use. The predictions of FFRACS for two different fuel densities as a function of temperature are shown in Figure 2-39.

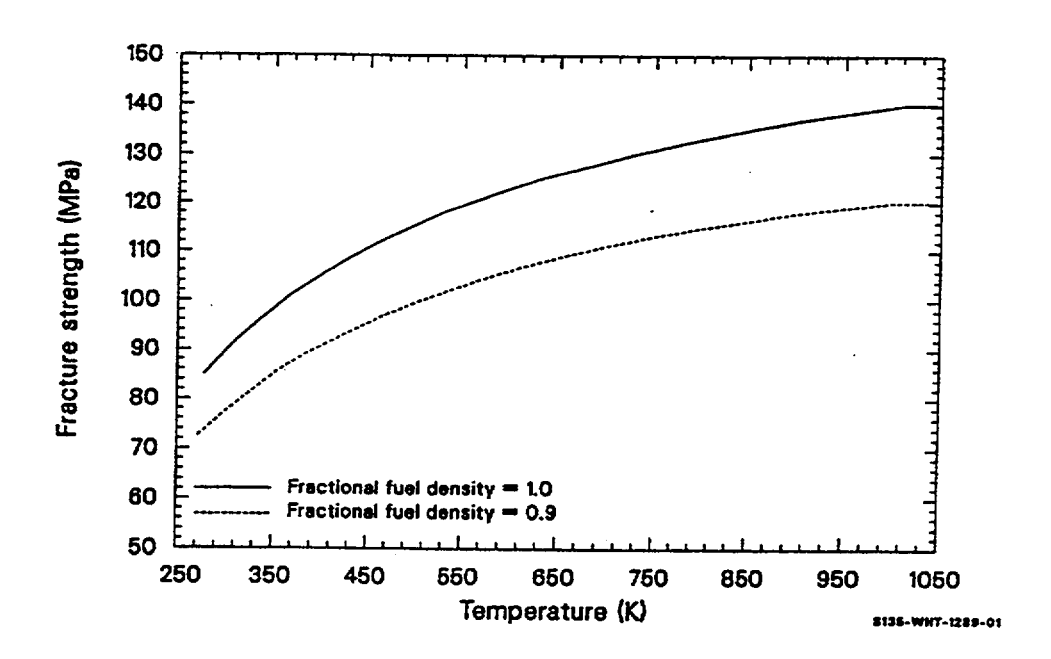


Figure 2-39. Calculated curves showing the predictions of FFRACS as a function of temperature for two fuel densities.

2.12.4 References

- 2.12-1 J. T. A. Roberts and Y. Ueda, "Influence of Porosity on Deformation and Fracture of UO₂," Journal of the American Ceramic Society, 55, 3, 1972, pp. 117-124.
- 2.12-2 R. F. Cannon, J. T. A. Roberts, and R. J. Beals, "Deformation of UO₂ at High Temperatures," Journal of the American Ceramic Society, 54, 1971, pp. 105-112.
- 2.12-3 Y. Guerin, "Etude par Compression a Hautes Temperatures de la Deformation Plastique du Bioxyde d'Uranium Polycristallin," *Journal of Nuclear Materials*, 56, 1975, pp. 61-75.

- 2.12-4 A. G. Evans and R. W. Davidge, "The Strength and Fracture of Stoichiometric Polycrystalline UO₂," *Journal of Nuclear Materials*, 33, 1969, pp. 249-260.
- 2.12-5 C. R. Tottle, Mechanical Properties of Uranium Compounds, ANL-7070, November 1965.
- 2.12-6 J. Katanic'-Popovic' and V. Petrovic', "Strength Dependence on Microstructure Characteristics of Sintered UO₂," *Physics Sintering*, 5, 2, 1973, pp. 95-105.
- 2.12-7 A. Tetelman and A. McEvily, Jr., *Fracture of Structural Materials*, New York: John Wiley and Sons, 1967, p. 53.
- 2.12-8 D. Hasselman, "Analysis of the Strain at Fracture of Brittle Solids with High Densities of Microcracks," *Journal of the American Ceramic Society*, 52, 1969, pp. 458-459.
- 2.12-9 F. P. Knudsen, H. S. Parker, and M. D. Burdick, "Flexural Strength of Specimens Prepared from Several Uranium Dioxide Powders: Its Dependence on Porosity and Grain Size and the Influence of Additions of Titania," *Journal of the American Ceramic Society*, 43, 1960, pp. 641-647.
- 2.12-10 M. C. Burdick and H. S. Parker, "Effect of Particle Size on Bulk Density and Strength Properties of Uranium Dioxide Specimens," *Journal of the American Ceramic Society*, 39, 1956, pp. 181-187.
- 2.12-11 E. Orowan, "Die Erhohte Festigkeit Dunner Faden, die Joffe-Effekt, und Verwandte Erscheinungen vom Standpunkt der Griffithschen Bruchtheorie," Zeitschrift Fuer Physik, 3/4, pp. 195-213.
- 2.12-12 N. J. Petch, "Cleavage Strength of Polycrystals," *Journal of the Iron Steel Institute, 174*, Part I, 1953, pp. 25-28.
- 2.12-13 N. Igata and K. Domoto, "Fracture Stress and Elastic Modulus of Uranium Dioxide Including Excess Oxygen," *Journal of Nuclear Materials*, 45, 1972/73, pp. 317-322.
- 2.12-14 F. P. Knudsen, "Dependence of Mechanical Strength of Brittle Polycrystalline Specimen on Porosity and Grain Size," *Journal of the American Ceramic Society*, 42, 1959, pp. 376-387.
- 2.12-15 A. A. Solomon, "Influence of Impurity Particles on the Fracture of UO₂," *Journal of the American Ceramic Society*, 55, 1972, pp. 622-627.

2.13 Viscosity (FVISCO)

The function FVISCO calculates the dynamic viscosity of UO₂. The viscosity is one of the parameters needed to model the motion of fuel during severe core damage.

The effects of departure from stoichiometry and the range of temperatures where liquid and solid UO₂ can coexist are not modeled. Also, the model does not consider any possible contamination of the molten UO₂. Uncertainty estimates are provided based on the data used in the model.

2.13.1 **Summary**

Viscosity of UO_2 is modeled as a function of temperature, melting temperature (solidus), and the fraction of the fuel that has liquefied. Input arguments describing the oxygen-to-metal ratio and PuO_2 content are not used in the current correlations for viscosity.

Viscosity is calculated by one of three equations, depending on whether the temperature is below the melting point for UO₂, in the range of temperatures where liquid and solid UO₂ can coexist, or above this range.

The equation used to model the viscosity of completely liquefied fuels is

$$\eta_e = 1.23 \times 10^{-2} - 2.09 \times 10^{-6} \text{ T}$$
 (2-130)

where

 η_e = dynamic viscosity of the liquid (Pa•s)

T = temperature (K).

For solid UO2, the viscosity is modeled with the expression

$$\eta_s = 1.38e^{(4.942 \times 10^4/T)} \tag{2-131}$$

where η_s is the dynamic viscosity of the UO₂ for temperatures below melting (Pa•s).

In the temperature range where liquid and solid UO_2 phases can both exist, the viscosity is modeled with the expression

$$\eta = \eta_S (1 - f) + \eta_e f$$
 (2-132)

where

 η = dynamic viscosity of the liquid solid mixture (Pa•s)

f = fuel fraction that is liquid (unitless).

The estimated uncertainty of the values computed with Equations (2-130) through (2-132) is computed with the FVISCO subcode but not returned as an output argument. The expressions used for this uncertainty are

$$U = \eta A (1 + |\gamma - 2|) \tag{2-133}$$

where

U = estimated uncertainty (Pa•s)

A = 0.33 for temperatures above melting 0.67 for temperatures below melting

Y = oxygen to metal ratio of the fuel (unitless).

Details of the development of the fuel viscosity model used in the FVISCO function are presented in the following sections. Section 2.13.2 is a review of the data, and Section 2.13.3 is a discussion of the model development.

2.13.2 Fuel Viscosity Data

Viscosities for solid UO₂, UO_{2.06}, and UO_{2.15} have been reported by Scott, Hall, and Williams.^{2.13-1} Viscosities for the nonstoichiometric oxides are lower than the viscosity of UO₂ at corresponding temperatures and could be measured over a sufficient range to establish the following relation for nonstoichiometric UO₂:

$$g_s = A e^{(-B/T)}$$
 (2-134)

where A and B are material constants. The viscosity of UO₂ was determined to be 2 x 10¹¹ Pa•s at 1,923 K and to be in excess of 10¹⁷ Pa•s at 1,273 K.

Viscosity data at much higher temperatures were obtained by Nelson. ^{2.13-2,2.13-3} An early measurement (0.145 Pa•s at a temperature of 3,028 K) was reported to correspond to incomplete melting of the sample. Subsequent data (0.045 Pa•s at 3,028 K and 0.036 at 3,068 K) represent a viscous fluid at temperatures below the melt temperature used in this report. ^a These data are not suitable for use in the viscosity model because all three measurements have indicated viscosities well above the more extensive viscosity measurements at temperatures where the UO₂ is known to be completely liquefied.

Two useful sources of data with completely molten UO_2 were available. Tsai and Olander^{2.13-4} published data from two samples, and Woodley^{2.13-5} published more extensive data from a single sample.

a. The melt temperature for UO2 is given as 3,113 K in the PHYPRP subcode of the MATPRO package.

The data are tabulated in Table 2-14 and Table 2-15 and plotted in Figure 2-40. The precision of the data by Woodley is noticeably higher than the precision of the other data, but there is a larger difference between the two experiments than can be explained by random measurement error. This difference is discussed by Woodley, but no definite reason for it was found. The model developed in the next section therefore contains the assumption that the difference between the data of Tsai and Olander and the data of Woodley is caused by some material parameter that has not been considered (oxygen to metal ratio, for instance).

Table 2-14. UO₂ viscosity data from Tsai and Olander. ^{2.13-4}

	Temperature (K)	Viscosity (Pa•s)
Sample 1	3,153	0.00583
	3,153	0.00739
	3,153	0.00594
	2,333	0.00514
	3,113	0.00628
	3,113	0.00686
	3,173	0.00762
Sample 2	3,083	0.00921
	3,188	0.00869
	3,188	0.00771
	3,138	0.00781
	3,328	0.00602
	3,328	0.00602
	3,328	0.00765
	3,248	0.00808
	3,248	0.00682

Table 2-15. UO₂ viscosity data from Woodley. ^{2.13-5}

Temperature (K)	Viscosity (Pa•s)
3,143	0.00425
3,148	0.00365
3,148	0.00326

Table 2-15. UO_2 viscosity data from Woodley.^{2.13-5} (Continued)

Temperature (K)	Viscosity (Pa•s)
3,193	0.00441
3,193	0.00434
3,193	0.00444
3,258	0.00420
3,258	0.00417
3,258	0.00415
3,213	0.00426
3,213	0.00428
3,218	0.00427
3,178	0.00432
3,183	0.00436
3,183	0.00434
3,163	0.00424
3,163	0.00420
3,163	0.00423
3,158	0.00418
3,158	0.00428
3,163	0.00425
3,198	0.00417
3,208	0.00418
3,198	0.00419
3,263	0.00399
3,263	0.00405
3,263	0.00402
3,298	0.00398
3,298	0.00395
3,303	0.00394
3,273	0.00399

Table 2-15. UO₂ viscosity data from Woodley.^{2.13-5} (Continued)

Temperature (K)	Viscosity (Pa•s)
3,273	0.00398
3,273	0.00397
3,218	0.00409
3,213	0.00406
3,218	0.00404
3,178	0.00412
3,178	0.00406
3,178	0.00413

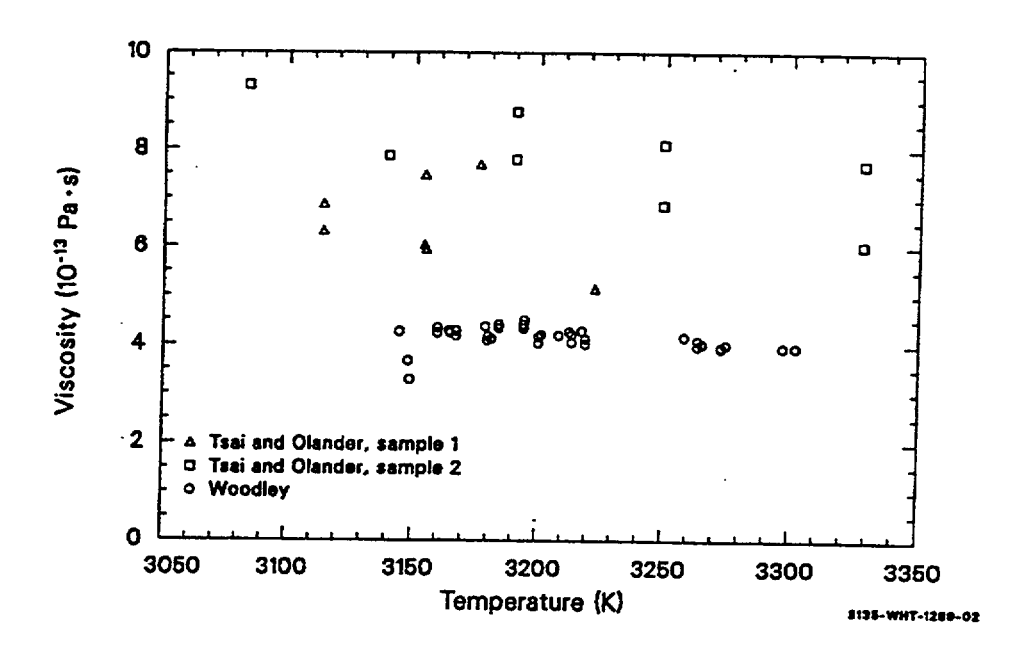


Figure 2-40. Uranium dioxide viscosities measured as a function of temperature.

2.13.3 Model Development and Uncertainty

The correlation for the viscosity of UO_2 below the melt temperature was obtained by solving Equation (2-134) for the values of the two material constants that reproduce the viscosity measured by Scott, Hall, and Williams at 1,273 K and the minimum viscosity reported by these authors for UO_2 at 1,273 K. The fact that this procedure produces only a crude engineering estimate of viscosity is expressed by assigning a large fractional uncertainty, two thirds, to the predicted viscosity of solid UO_2 .

Equation (2-130), the correlation for viscosity of liquid UO₂, was obtained from the data of Tsai and Olander and the data of Woodley. The less precise data of Tsai and Olander were used because Woodley used only one sample and the viscosities measured by Tsai and Olander with their samples differ from Woodley's data by more than the scatter of their measurements.

The traditional Arrhenius relation [Equation (2-134)] was not used to correlate the liquid viscosities because a simpler linear expression fits the data as well as the exponential form. A linear least-squares fit to the data of Woodley (with the two anomalously low viscosities at 3,148 K omitted) produced the equation

$$\eta_e = 1.09 \times 10^{-2} - 2.09 \times 10^{-6} \,\mathrm{T}$$
 (2-135)

The data of Tsai and Olander yielded the following correlation

$$\eta_e = 1.60 \times 10^{-2} - 2.77 \times 10^{-6} \text{ T}$$
 (2-136)

The viscosities predicted by Equations (2-135) and (2-136) are compared with the data in Figure 2-41. By inspection of this figure, it was concluded that the best mathematical description of the difference in the viscosities measured for the different lots of UO₂ is to assume that the viscosities of the two different lots differ by an additive constant.^a

To recognize the more precise measurements of Woodley, yet account for the probable lot-to-lot variation indicated by the data of both authors, the least-squares fit to the data of Tsai and Olander was repeated with the added constraint that the slope of the correlation match the slope obtained from the data of Woodley. The resultant correlation for the data of Tsai and Olander is

$$\eta_e = 1.38 \times 10^{-2} - 2.09 \times 10^{-6} \text{ T}$$
 (2-137)

The final step in the derivation of Equation (2-130) was to average Equations (2-137) and (2-135). With a lot to lot variation present, this step assumes that each lot of UO_2 is equally probable.

The estimated uncertainty of the values of viscosity computed with Equation (2-137) was determined using the assumption that the important difference in the measurements of the two references is the unknown difference in the two lots of UO₂. The resultant standard deviation is

$$\sigma = 2 \times 10^{-3} \text{ Pa} \cdot \text{s}$$
 (2-138)

a. The interpretation corresponds to the assumption mentioned at the end of Section 2.13.2; the difference in viscosities is caused by some unknown material parameter of the UO₂.

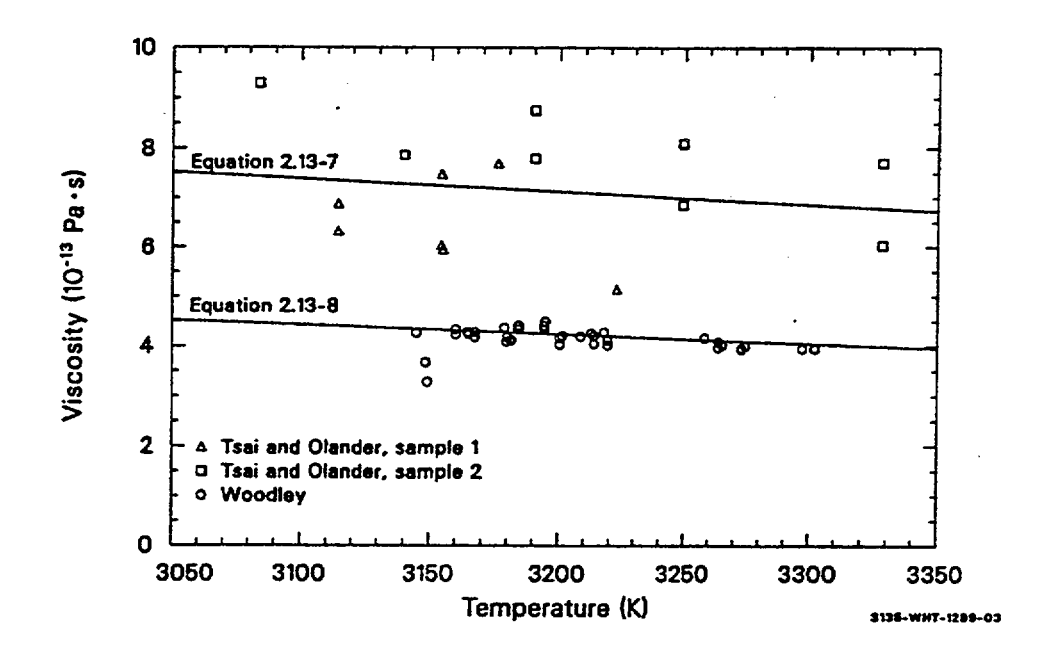


Figure 2-41. Data from uranium dioxide samples compared with least-squares fit.

which is approximately one-third the predicted value of the viscosity. The increased uncertainty for nonstoichiometric UO₂ shown in Equation (2-133) is simply an estimate that has been included to indicate that the model contains no dependence on the oxygen-to-metal ratio of the fuel.

Figure 2-42 illustrates the viscosities calculated with Equation (2-130) for liquid UO_2 . The dashed lines are the upper and lower uncertainty limits obtained by adding \pm 1/3 of the predicted viscosity and an assumed melt temperature of 3,113 K.

Equation (2-132), which is employed only in the temperature range where liquid and solid can both exist (for temperatures between the fuel melting temperature and the melt temperature plus the liquid solid coexistence temperature range), is obtained from the assumption that the viscosity is the volume weighted average of the solid and liquid viscosities in this temperature range.

2.13.4 References

- 2.13-1 R. Scott, A. R. Hall, and J. Williams, "The Plastic Deformation of Uranium Oxides Above 800 K," *Journal of Nuclear Material*, 1, 1959, pp. 39-48.
- 2.13-2 W. F. Sheely ed., Quarterly Progress Report, July-September, 1969, Reactor Fuels and Materials Development Programs for Fuels and Materials Branch of USAEC Division of Reactor Development and Technology, BNWL-1223, November 1969.

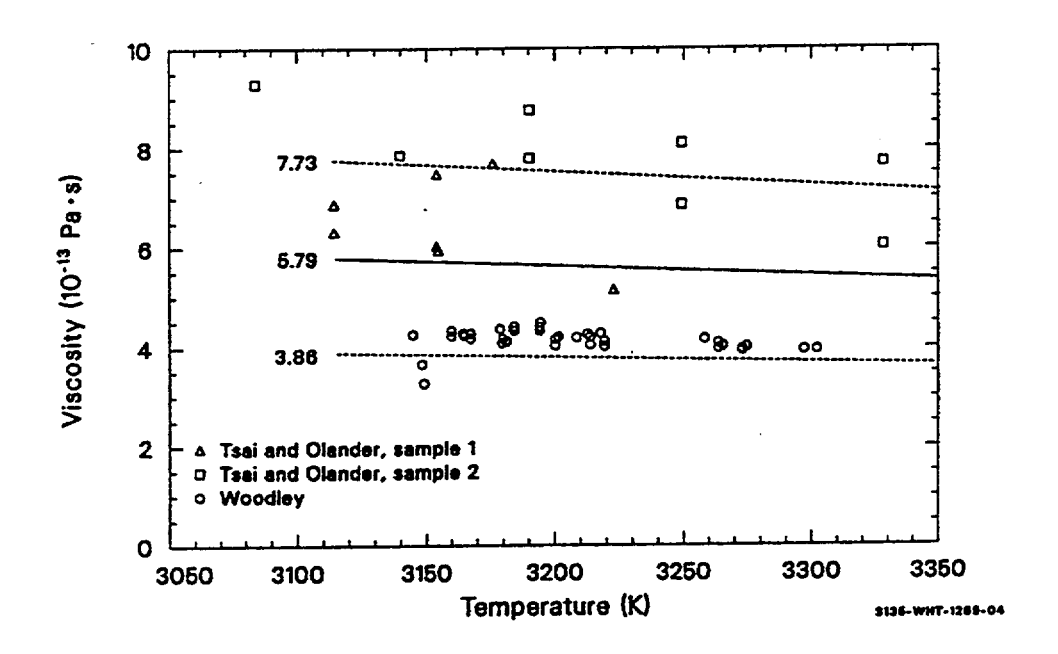


Figure 2-42. Viscosities calculated with Equation (2-130) (solid line) and upper and lower uncertainty estimates (dashed lines) compared with data.

- 2.13-3 W. F. Sheely ed., Quarterly Progress Report, October-December, 1969, Reactor Fuels and Materials Development Programs for Fuels and Materials Branch of USAEC Division of Reactor Development and Technology, BNWL-1279, February 1970.
- 2.13-4 H. C. Tsai and D. R. Olander, "The Viscosity of Molten Uranium Dioxide," *Journal of Nuclear Materials*, 44, 1972, pp. 83-86.
- 2.13-5 R. E. Woodley, "The Viscosity of Molten Uranium Dioxide," *Journal of Nuclear Materials*, 50, 1974, pp. 103-106.

2.14 Vapor Pressure (FVAPRS)

During very high temperature excursions, evaporating reactor fuel (urania or plutonia urania mixtures) can create pressures that equal or exceed plenum gas or fission gas pressures in the fuel rod. This pressure will influence the failure mechanism of the cladding and may cause the melted portion of the fuel to froth and swell. Significant volume changes of the fuel may also result from phase changes due to noncongruent evaporation (composition of the vapor phase being different than that of the fuel). A number of compounds are present in fuel vapors. These are actinide and actinide oxide vapors (UO₂, UO₃, UO₄, U, PuO₂, PuO, Pu) and oxygen vapors (O to O₂). The total pressure (sum of all partial pressures) of the actinides and actinide oxides is calculated.

The vapor pressure equations described in this section are to be used in transient fuel codes, mechanistic gas release codes, or restructuring codes that require vapor pressures of calculate bubble migration by evaporation condensation.

2.14.1 Summary

The FVAPRS model determines the saturated actinide vapor and oxygen vapor pressures over urania, plutonia, and mixed oxides as a function of fuel O/M ratio and temperature. Semi-empirical equations based on the Clausius-Clapeyron equation are used. The standard error of estimate (SEOE) with respect to the log of the data base is given for each equation.

For urania,

$$\log_{10}(P) = -11191/T + 9.9932 \ln(T) - 0.00132 T - 69.174$$
(2-139)

and SEOE (\log_{10} P) = ± 0.206 .

For plutonia,

$$\log_{10}(P) = (-5404.1 + 6854.6x)/T + 18.166 \ln(T) - 0.003389 T - 130.65$$
(2-140)

and SEOE $(\log_{10}P) = \pm 0.559$

where

P = vapor pressure (Pa)

x = deviation from stoichiometry (absolute value of O/M-2)

T = temperature (K).

Equation (2-139) is used to calculate the vapor pressure of urania at all O/M ratios. Plutonia vapor pressures are calculated in the FVAPRS code for hypostoichiometric fuel using Equation (2-140). Because it is improbable that plutonia or mixed oxides will be hyperstoichiometric, the FVAPRS code uses a default value of 2.0 for all O/M ratios greater than 2.0. Mixed oxide vapor pressures are obtained by multiplying the plutonia and urania equations by the weight fraction of each material and adding the two resulting calculated pressures.

Similar equations are used for the oxygen vapor pressure [P(O₂) or P(O)] over urania.

For O/M ratios > 2.004,

$$\log_{10}(P(O_2)) = -14638.2/T + 21.7752x + 6.2062$$
 (2-141)

and SEOE $(\log_{10} P(O_2)) = +0.545$.

For O/M ratios < 1.999,

$$\log_{10}(P(O)) = -(49535 + 1418.1 \ln x)/T + 15.181$$
 (2-142)

and SEOE $(\log_{10} P(O)) = +0.801$.

For O/M ratios < 2.004 but > 1.999,

$$\log_{10}(P'(O_2)) = -\frac{14638}{T} + 1.8036\ln(x + 0.004) + 6.2933$$
 (2-143)

and SEOE $(\log_{10}P'(O_2)) = \pm 9.0$

where $P'(O_2)$ is the diatomic oxygen pressure for 1.999 < O/M < 2.004.

The rapid decrease of the pressure predicted by Equation (2-143) as stoichiometric composition is approached is limited by imposing the following restrictions:

If $-52708/T + 23.32 \ge \log_{10} [P'(0_2)]$,

$$\log_{10} [P(O_2)] = -52708/T + 23.32 . (2-144)$$

If $-52708/T + 23.32 < \log_{10} [P'(0_2)]$,

$$\log_{10}[P(O_2)] = \log_{10}[P'(O_2)] . (2-145)$$

The following sections contain a discussion of the information and techniques used to develop Equations (2-139) through (2-145). Section 2.14.2 is a discussion of data described in the literature and methods used by each investigator to obtain those data. Section 2.14.3 is a discussion of vapor pressure theory, FVAPRS subcode development, and comparisons of the FVAPRS subcode with literature data. Section 2.14.4 contains references.

2.14.2 Vapor Pressure Data

Vapor pressure data for urania, plutonia, and mixed oxides are obtained, using a number of different experimental techniques, such as transpiration, effusion, Knudsen effusion, laser heating, electron beam heating, free evaporation, static testing, and boiling point pressures. Of these techniques, transpiration, Knudsen effusion, static testing, and laser heating are most widely used. Reported vapor pressures are generally determined indirectly, calculated from measurements of sample weight loss, sample momentum, weight of deposit on a target, or by analysis of the ions in a gas stream. Techniques such as coulorimetric or x-ray analysis are used to determine vapor pressure when the O/M ratio of the sample is known. These measurement techniques are discussed in the following text in enough detail to indicate their advantages or disadvantages.

The transpiration technique is one of the techniques that can be used to measure vapor pressure in the presence of large concentrations of other gases. It is most accurate at temperatures where the confining material does not contribute significantly to the measured vapor pressure. Since it is not limited by the pressure of the gas being measured, a distinct advantage of this technique is that a carrier gas can be used to control the composition of the sample. Using this technique, the vapor pressure of a sample is determined from measurements of sample weight loss, weight of vapor condensed in a cold trap, or by monitoring molecular species in the carrier gas. A disadvantage of the technique is that vapor pressure is independent of the carrier gas flow rate in only a narrow band of flow rates which depend on other experimental conditions.

The Knudsen effusion technique^{2.14-1} and a similar technique, the Langmuir free evaporation technique, are good measurement methods for vapor pressures below 15 Pa. An advantage of the Knudsen technique to measure vapor pressure is that there are very small temperature gradients in the sample and its surroundings.

The application of lasers or electron beams to heat the surface of materials that melt at very high temperatures has provided an experimental method to study materials at temperatures above those that would melt the retaining crucibles. Vapor pressure data gathered when intense pulses of laser or electron beams impinge on the surface of the samples are derived from sample weight loss, evaporation depth, recoil momentum, torsion, or by mass spectrometry ion intensity measurements. These experiments must be analyzed with caution because equilibrium vapor pressure may not be the pressure measured.

2.14.2.1 Urania Vapor Pressure. The measurement techniques described previously have been used to measure urania vapor pressures discussed in the following paragraphs.

Szwarc and Latta^{2.14-2} reported total equilibrium vapor pressure data of hypostoichiometric urania, using the transpiration technique with the oxygen potential of the carrier gas controlled with H_2/H_2O mixtures. They found that the initial O/M ratios remained stable to within \pm 0.005 but that the vapor pressure changed an order of magnitude as the O/M ratio varied between 1.88 to 1.94.

Bober^{2.14-3} measured urania vapor pressure, using the laser heating technique to attain temperatures between 4,100 and 4,400 K and found vapor pressures between 0.608 and 1.01 MPa.

Reedy and Chasanov^{2.14-4} used the transpiration technique to obtain total vapor pressure data. They determined the O/M ratio of remaining residues and found final O/M ratios to be dependent on the testing temperatures.

Ackermann^{2.14-5} determined the vapor pressure of hypostoichiometric urania between 1,580 to 2,400 K, using effusion rate measurements, with an assumed vapor of UO. Mass spectrometric measurements on the system found the UO vapor pressure to be about 10 times greater than the UO₂ and U vapor pressures.

Tetenbaum and Hunt^{2.14-6} measured total vapor pressure of hypostoichiometric and nearly stoichiometric urania, using the transpiration technique. The O/M ratio of their samples increased with increasing temperatures, and the fuel vapor pressure increased as the O/M ratio approached the hypostoichiometric phase boundary. Their reported vapor pressure data are in very good agreement with those of Szwarc and Latta for UO_{1.88} but are approximately 1.5 to 2 times greater for UO_{1.92} and UO_{1.94}. They also reported an order of magnitude pressure change as the O/M ratio of the samples changed.

Benezech $^{2.14-7}$ used the transpiration technique to obtain urania vapor pressure data at temperatures between 2,200 and 2,600 K with O/M ratios varying between 2.0 and 2.15. He reported large temperature gradients in the crucible and found the dominant vapor species (UO₂ or UO) to be dependent on the composition of the carrier gas.

Ohse^{2.14-8,2.14-9} reported vapor pressures of urania at temperatures up to 4,710 K, using the laser heating technique. These data are important because they were taken at temperatures above melting and show the vapor pressure at very high temperatures to increase with increasing temperature at a much slower rate than it does below the melting temperatures.

Alexander^{2.14-10} measured total vapor pressure and oxygen dissociation pressures of urania, thoria, zirconia, and combinations of the three, using the transpiration technique at temperatures between 2,000 and 3,000 K. They reported vapor pressures of thoria urania mixtures to be an order of magnitude less than urania vapor pressures.

Ackermann^{2.14-11,2.14-12} reported vapor pressures for urania at temperatures between 1,600 and 2,800 K, using the Knudsen effusion technique. These data were later revised and reported after the results of later experiments were analyzed.^{2.14-13} Their reported results, urania vapor pressure invariant to 2,700 K and melting at 2,678 K, conflict with results previously discussed by other investigators. Their sample composition probably varied from pure urania, containing impurities that affected the measured vapor pressures and the melting point. However, the magnitude and the slope of the pressure as a function of temperature are within the data scatter bands of other investigators' data.

Chapman and Meadows^{2.14-14,2.14-15} investigated nonstoichiometric urania of compositions between $UO_{2.02}$ and $UO_{2.63}$ in the UO_{2+x} and U_3O_{8-x} and U_3O_{8-y} phase regions at temperatures between 1,273 and 1,873 K, using a thermogravimetric technique to obtain the vapor pressure data. They reported evidence of UO_4 vapor instead of UO or UO_2 and an equilibrium O/M ratio, in a vacuum at temperatures above 1,973 K, to be less than the ratio 2.0 obtained by other investigators.

Ohse $^{2.14-16}$ measured urania vapor pressures between 1 x 10 $^{-6}$ and 3.4 x 10 $^{-4}$ MPa in an effusion cell at temperatures between 2,278 and 2,768 K.

Benson $^{2.14-17}$ investigated vapor pressures of urania, using an electron beam to heat the samples to temperatures between 4,500 and 7,200 K.

Babelot^{2.14-18} reported urania vapor pressure data obtained at temperatures between 3,300 and 4,700 K, using a laser to heat the samples. The slope and magnitude of these data agree very well with those reported by Benson.

The literature data discussed in this section generally indicate that urania evaporates bivariantly as a function of O/M ratio and temperature. A composition change from stoichiometry can, at temperatures less than 2,500 K, cause the vapor pressure to increase 10 times or more as the urania becomes increasingly hypostoichiometric. The data are insufficient to determine how much effect deviation from stoichiometry has on vapor pressures in the hyperstoichiometric region. Tetenbaum and Hunt observed little effect of urania nonstoichiometry on the vapor pressure at temperatures near melting with hypostoichiometric fuel. Data at temperatures above melting and not having O/M ratios reported can therefore be used. There is no observed discontinuity of vapor pressure at the urania melting temperature, although the temperature dependence does begin to decrease. The early data of Ackermann^{2.14-12} are considered in error by the authors^{2.14-15} and are therefore not useful for model development. Also, the Chapman and Meadows data are not applicable for model development because the scatter is large due to unreported O/M ratios much greater than 2.0. All the rest of the data discussed are amenable to model development, although some scatter between data sets occurs. Data discussed in this section are displayed in Figure 2-43. The urania vapor pressure as a function of temperature can be seen in each figure. The decreasing rate of change at temperature above 3,000 K can also be seen.

2.14.2.2 Plutonia Vapor Pressure. Plutonia (PuO_2) is very similar to urania in many of its material properties. The plutonia vapor pressure data presently available in the literature are briefly discussed in the following paragraphs.

Ohse and Ciani^{2.14-19} reported vapor pressures of urania, at 1,800, 2,000, and 2,200 K, and plutonia, with O/M ratios between 1.51 and 1.61, based on effusion cell measurements. They found it very difficult to obtain good data with O/M ratios greater than 1.94 due to rapid change of fuel O/M ratios, or vapor O/M ratios, or both.

Ackermann^{2.14-20} measured plutonia vapor pressures of hypostoichiometric plutonia in effusion cells. Investigating the effects of both temperature and composition on the total vapor pressures, he found the evaporation rate to decrease more than 30% from the initial rate after 8 hours and found the composition to change with time. Chemical and x-ray analyses determined the O/M ratios to be 1.923 to 1.916 and 1.90 to 1.93, respectively.

Phipps^{2.14-21} used the Knudsen effusion method to measure vapor pressures between 1,589 and 2,060 K. The vapor pressure data reported were derived from radiochemical analysis of the deposit on the

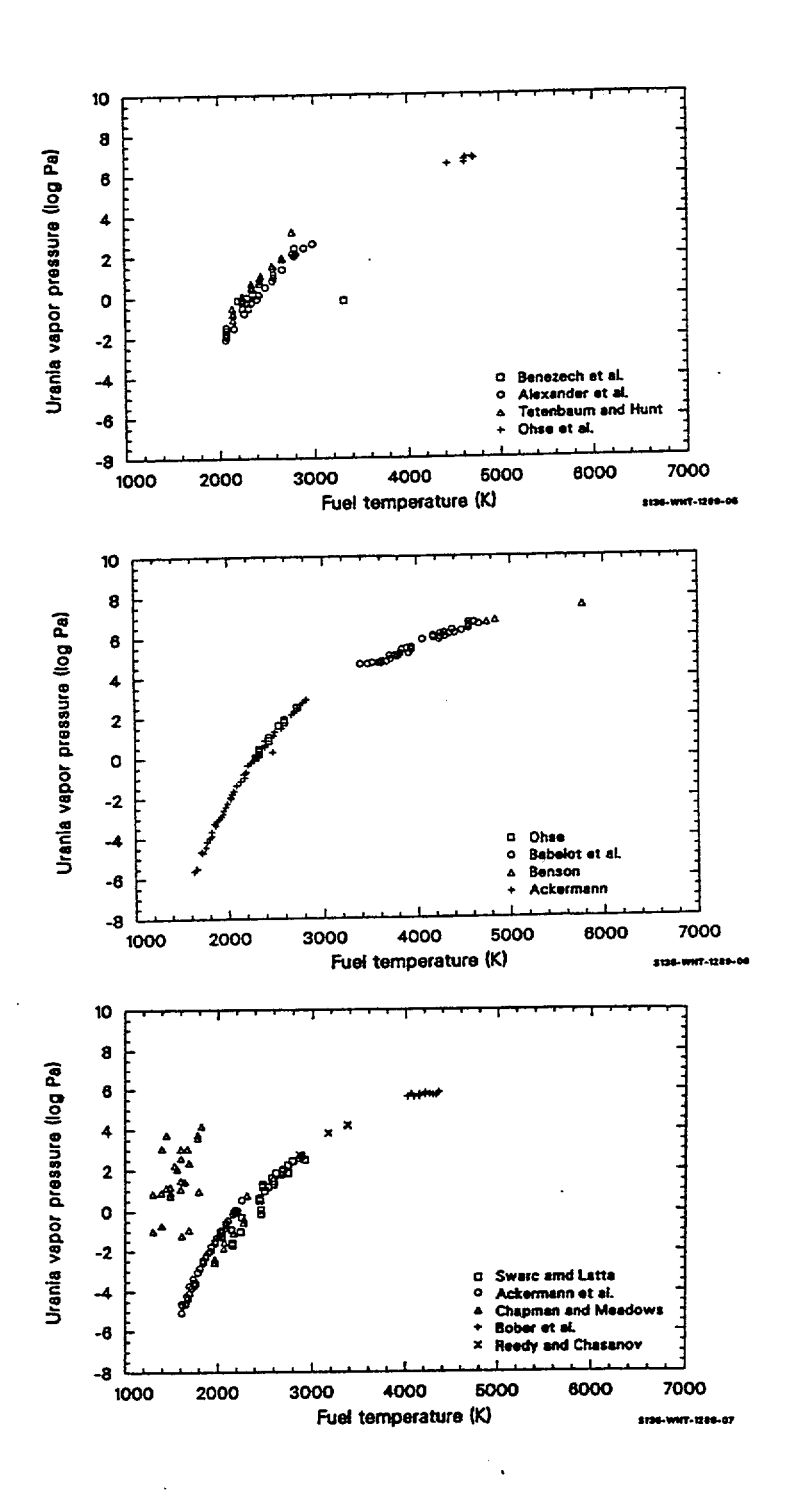


Figure 2-43. Urania vapor pressure data.

effusion target. Phipps reported that oxygen reacted with the vapor flow and, therefore, had to be included in the vapor pressure calculations.

Pardue and Keller^{2.14-22} measured the vapor pressure of plutonia in three atmospheres of air, argon, and oxygen at temperatures between 1,723 and 2,048 K, using the transpiration technique to obtain their data.

Mulford and Lamar^{2.14-23} reported plutonia vapor pressure data measured at temperatures between 2,000 and 2,400 K, using the Knudsen effusion technique, that were significantly different than those observed by Phipps.

The plutonia data reviewed include vapor pressures of plutonia between 1,600 and 2,500 K and O/M ratios between 1.5 and 2.0. These data are shown in Figure 2-44. Vapor pressures of plutonia decrease as the hypostoichiometric phase boundary is approached. Vapor pressures were observed between 10⁻⁶ and 10 Pa. Large scatter in the data can be seen in Figure 2-44, partially a result of O/M ratio effects not recorded by many of the investigators. Therefore, only the data of Ackermann^{2.14-20} and Ohse and Ciani^{2.14-19} are used for model development.

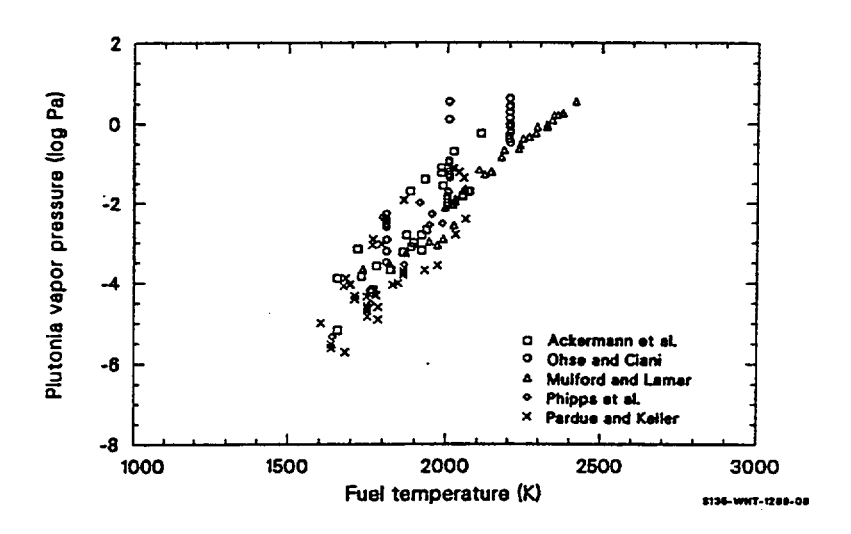


Figure 2-44. Plutonia vapor pressure data.

2.14.2.3 Mixed Oxide Vapor Pressure. Some mixed oxide data have appeared in the literature. These are discussed briefly.

Tetenbaum^{2.14-24} reported the results of an investigation of total vapor pressure of actinide bearing species over the U-Pu-O system, using the transpiration technique. The data indicate that mixed oxides of composition $(U_{0.8}, Pu_{0.2})0_{2-x}$ have vapor pressures between 0.1 and 1Pa at temperatures between 2,150 and 2,450 K. Analysis of these data shows the urania vapor pressure to be approximately 0.85 of the total vapor pressure and plutonia is approximately 0.15 of the total.

Ohse and Olson $^{2.14-25}$ reported the vapor pressures of coprecipitated mixed oxide with a composition of $(U_{0.85} \, Pu_{0.15})O_{2-x}$ obtained in a tungsten effusion cell heated by an electron beam. The measurements were taken at temperatures between 1,800 and 2,350 K, with the O/M ratios varying between 2.0 and 1.94. Ohse and Olson observed urania vapor pressures to be about 10 times greater than for any of the other oxides present.

Battles $^{2.14-26}$ reported vapor pressures of mechanically mixed urania and plutonia ($U_{0.8}$ $Pu_{0.2}$) O_{2-x} with the O/M ratio between 1.92 and 2.01 and the temperature approximately 2,240 K. They used the Knudsen effusion technique with a mass spectrometer to determine the vapor pressure. They reported the urania vapor pressure to be much greater than the plutonia vapor pressure.

Ohse^{2.14-8,2.14-9} reported mixed oxide data measured at very high temperatures (4,000 to 7,000 K), using the laser heating technique. These test samples were melted prior to laser heating and vapor pressure measurements.

The four data sets just reviewed all show the vapor pressure of urania to be on the order of 10 times greater than the pressure of other chemical species present. The O/M ratios between 1.91 and 2.00 were investigated at temperatures between 2,100 and 2,500 K. Vapor pressures ranged from approximately 0.01 Pa at 2,150 K to approximately 12 MPa at 7,000 K. Figure 2-45 shows the mixed oxide data just discussed. The high temperature data show a significant decrease in the rate of vapor pressure increase. The data also show scatter bands of about an order of magnitude at temperatures below 3,000 K.

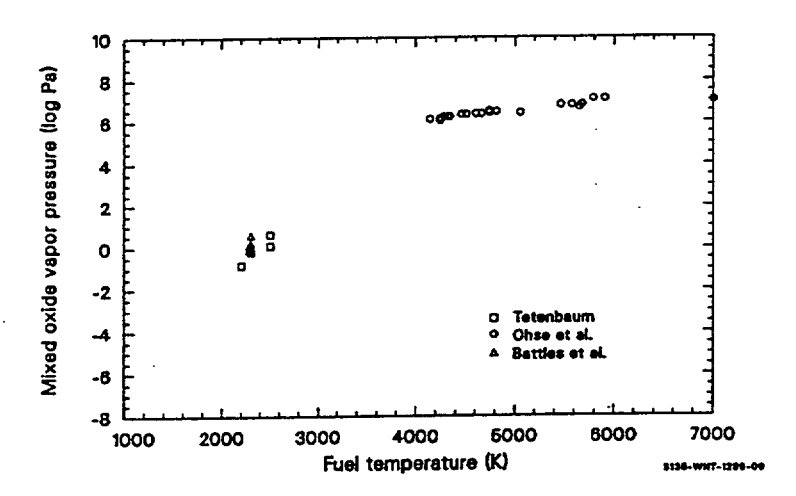


Figure 2-45. Mixed oxide vapor pressure data.

2.14.2.4 Oxygen Vapor Pressure. Although actinide oxide vapors constitute the most prominent vapors evolving from reactor fuels, oxygen vapors (O and O₂) do evaporate and thereby change the chemical composition of the fuel. A number of investigators have found metallic uranium in otherwise pure urania after heating above 2,073 in a vacuum. For example, Aitken^{2.14-27} found both hypo- and hyperstoichiometric urania to change with time and temperature until an O/M ratio of 1.88 was reached.

Vaporization of oxygen from the fuel not only changes the composition of the fuel but is directly related to the oxidation of the internal surfaces of the cladding. Oxygen vapor pressures have been determined for urania up to approximately 2,900 K. Most of this oxygen data is derived from measurement of moisture content of carrier gases, sample weight, or composition changes. Only one set of oxygen vapor pressure data for plutonia^{2.14-28} was found. This data set was at temperatures too low (less than 1,323 K) and is inefficacious until more data are available. Modeling of plutonia oxygen pressures was therefore not attempted. Data reported for oxygen pressures over urania are described in the following paragraphs.

Tetenbaum and Hunt^{2.14-29} used the transpiration technique to measure the oxygen partial pressure of hypostoichiometric urania. Monatomic oxygen pressures were determined up to 2,700 K. Vapor pressure measurements were determined for compositions ranging from UO_{2.0} to approximately UO_{1.86}. Their data show oxygen vapor pressure to increase sharply near the stoichiometric composition at the lower temperatures measured. This pressure increase near the stoichiometric composition is not as steep at the higher temperatures.

Markin $^{2.14-30}$ used a unique method (sample composition measurements after equilibrium was reached) to obtain monatomic oxygen vapor pressure data for hypostoichiometric and hyperstoichiometric urania. The O/M ratios reported are accurate to within \pm 0.005. Measurements were obtained for hypostoichiometric urania between 2,000 and 2,400 K and for hyperstoichiometric urania between 1,600 and 1,700 K. Their data agree will with that of Tetenbaum and Hunt.

Wheeler $^{2.14-31}$ measured the monatomic oxygen vapor pressure of urania between 1,800 and 2,000 K. He used a technique of equilibrating UO_{2-x} in an oxygen atmosphere controlled by the equilibrium reaction

$$C + O_2 = CO_2$$
. (2-146)

Data were obtained from urania with O/M ratios between 2.0 and 1.98. These data agree well with both data sets just described.

Javed^{2.14-32} reported diatomic oxygen vapor pressure data of urania, using the transpiration technique at temperatures between 1,873 and 2,173 K. The O/M ratios were obtained from chemical, x-ray, and metallographic techniques. These oxygen vapor pressure data tend to be higher than those of Tetenbaum and Hunt, Marken, and Wheeler.

Aitken^{2.14-27} used free evaporation and flowing gas transpiration techniques to obtain the oxygen pressure of urania between 2,023 and 2,223 K. These data were reported as diatomic oxygen pressures. Aitken observed the O/M ratio of the urania to approach 1.88 for both hypo- and hyperstoichiometric urania when the samples were heated above 2,000 K. The oxygen vapor pressure implied by these data is approximately two to ten times that of the Tetenbaum and Hunt data. Tetenbaum and Hunt suggest that the discrepancy is a result of the Aitken data not having reached equilibrium pressures.

Roberts and Walter $^{2.14-33}$ investigated diatomic oxygen equilibrium vapor pressure of urania with compositions between $UO_{2.00}$ and $UO_{2.3}$ and at temperatures between 1,273 and 1,723 K. Temperature measurements were obtained, using a tensimetric technique (direct measurement of pressure). The technique is crude, and there was no control of the sample O/M ratio. The investigators found deposits of mixtures of the U_4O_9 and $UO_{2.61}$ phases in cooler parts of the furnace, indicating that the O/M ratio of the samples was changing. The authors also suggest that an equilibrium vapor pressure may not have been obtained. These data were therefore not used as part of the data base for model development.

Hagemark and Broli^{2.14-34} conducted an extensive investigation of diatomic oxygen pressures of urania with O/M ratios between 2.0 and 2.25 and at temperatures between 1,173 and 1,773 K. Oxygen vapor pressure measurements were obtained from thermobalance measurements during testing.

Alexander $^{2.14-10}$ used the transpiration technique to determine the oxygen dissociation pressure of urania. They investigated oxygen vapor pressures of urania compositions of $UO_{2.03}$, $UO_{2.0}$, and $UO_{1.97}$ with compositions accurate to \pm .01 units at temperatures between 1,950 and 2,720 K.

Blackburn^{2.14-35} used the Knudsen effusion technique to measure the diatomic oxygen vapor pressure of urania. He obtained oxygen vapor pressure data for O/M ratios between 2.1 and 2.6 at temperatures between 1,263 and 1,400 K. For purposes of the FVAPRS code and this report, only the data of O/M ratios less than 2.2 can be used. This is roughly the boundary of urania-oxygen solid solution at temperatures above 1,273 K. These data are in fair agreement with those reported by other investigators.

Aronson and Belle^{2.14-36} used an electrochemical measurement technique (emf measurements on urania half cells) to measure the diatomic oxygen vapor pressure of urania. Vapor pressures for urania compositions between $UO_{2.0}$ and approximately $UO_{2.5}$ at temperatures between 1,150 and 1,350 K were investigated. Only the urania data with O/M ratios below 2.2 were considered for model development.

Kiukkola^{2.14-37} used emf measurements from galvanic cells to obtain diatomic vapor pressures over urania. Vapor pressure measurements of urania at compositions of UO_{2.01} to UO_{2.67} were obtained at temperatures between 1,073 and 1,473 K. Here again, only those data points with urania O/M ratios less than UO_{2.0} were considered.

Markin and Bones^{2.14-38} used emf measurements of urania with O/M ratios between 2.00 and 2.003 in a high temperature galvanic cell. Diatomic oxygen pressures of urania between the temperatures of 973 and 1,673 K were investigated. The O/M ratios were controlled and determined by coulorimetric titration of oxygen ions, using NiO as a source of oxygen. The main purpose of their investigations was to obtain thermodynamic functions and not oxygen vapor pressures, so there is very little discussion of the vapor pressure data. Their data indicate a steep slope (decrease in vapor pressure) as the composition of the urania approaches stoichiometry. This is consistent with other data in this composition range. These data are therefore useful in the modeling effort.

Aukrust^{2.14-39} determined equilibrium oxygen pressures over hyperstoichiometric urania. The O/M ratios were determined by a thermogravimetric method, and oxygen pressures were determined from

known CO₂/CO or O₂/Ar gas mixtures and O/M ratio measurements. Data were obtained at temperatures between 1,373 and 1,673 K. They report O/Mratios accurate to within + 0.0002 and the $log_{10}P_{O2}$ accurate to \pm 0.02.

The data discussed in this section must be divided into two groups; hypostoichiometric and hyperstoichiometric. For hypostoichiometric fuel, the data of Tetenbaum and Hunt, Markin, Wheeler, and Alexander are the best available. The data of Javed and Atkins were probably measured under nonequilibrium conditions and should not be used. For hyperstoichiometric fuel and oxygen pressure, data of Hagemark and Broli are the most extensive and are the best. The rest are within an order of magnitude of these data and have been used.

2.14.3 Model Development

The equations used in FVAPRS are based on thermodynamic equations fitted to the data. The following section is a discussion of thermodynamic and chemical theory and the technique used to develop the FVAPRS correlations.

2.14.3.1 Review of Basic Theory. Evaporation is a change in chemical state obeying the law of conservation of mass. Equations can therefore be used to show which elements or compounds could be expected to be present in the vapor phase above a fuel substrate. Possible reactions of urania are 2.14-12

$$UO_{2(\beta)} \to UO_{(g)} + \frac{(1-\alpha)}{2}O_{2(g)} + \alpha O_{(g)}$$
 (2-147)

$$UO_{2(\beta)} \to \frac{1}{2}UO_{2(g)} + \frac{(2-3\alpha)}{4}O_{2(g)} + \alpha \frac{3}{2}O_{(g)} + \frac{1}{2}U_{(\beta)}$$
(2-148)

$$UO_{2(\beta)} \to \frac{1}{2}UO_{(g)} + \frac{1}{2}UO_{3(g)}$$
 (2-149)

$$UO_{2(\beta)} \to \frac{1}{3}U_{(g)} + \frac{2}{3}UO_{3(g)}$$
 (2-150)

$$UO_{2(\beta)} \to UO^{+}_{2(g)} + e^{-}_{(g)}$$
 (2-151)

$$UO_{(\beta)} \rightarrow UO_{(g)}$$
 (2-152)

$$2UO_{2(\beta)} \to (UO_2)_{2(g)}$$
 (2-153)

where β denotes that the material is in the solid or liquid phase and g denotes the gas phase. These equations apply only in the oxygen solid solution regions of solid and liquid urania. Of these possible compounds, one is usually much more prominent than the others. Analysis of the data indicates that for substrate temperatures < 2,000 K, the magnitude of the actinide oxide vapors follow the order, $P_{UO} > P_{UO_2} > P_{UO_3}$, where P is the vapor pressure. At about 3,000 K, the order of partial pressures is $P_{UO_2} \approx P_{UO} > P_{UO_3}$, $\approx P_U$; and at temperatures > 3,500 K, the partial pressure order is $P_{UO_2} > P_{UO_3} > P_{UO} > P_U$. The oxygen partial pressure at all temperatures is generally much smaller than the combined vapor pressure of the actinide oxides.

For plutonia, the chemical reactions are similar to those of urania

$$PuO_{2(\beta)} \to PuO_{(g)} + \frac{(1-\alpha)}{2}O_{2(g)} + \alpha O_{(g)}$$
 (2-154)

$$PuO_{2(\beta)} \to \frac{1}{2} PuO_{2(g)} + \frac{(2-3\alpha)}{4} O_{2(g)} + \alpha \frac{3}{2} O_{(g)} + \frac{1}{2} Pu_{(\beta)}$$
 (2-155)

$$PuO_{2(\beta)} \to \frac{1}{2}PuO_{(g)} + \frac{1}{2}PuO_{3(g)}$$
 (2-156)

$$PuO_{2(\beta)} \to \frac{1}{3}Pu_{(g)} + \frac{2}{3}PuO_{3(g)}$$
 (2-157)

$$PuO_{2(g)} \to PuO^{+}_{2(g)} + e^{-}_{(g)}$$
 (2-158)

$$PuO_{(\beta)} \to PuO_{(g)} \tag{2-159}$$

$$2PuO_{2(8)} \to (PuO_2)_{2(9)}$$
 (2-160)

It is experimentally determined that PuO is the prominent species of plutonia up to an O/M ratio of approximately 1.99, where PuO₂ becomes more prominent.

Evaporation can be described by simple thermodynamic considerations of a first order phase transition of a pure substance, solid to vapor or liquid to vapor, at constant temperature and pressure. At the phase transition

$$dG_{\beta} = dG_{g} \tag{2-161}$$

Uranium Dioxide/Mixed Oxides

where

 dG_{β} = change in Gibbs free energy for the solid or liquid

 dG_g = change in Gibbs free energy for the gas.

Since the process is reversible for a first order phase transition at constant temperature and pressure,

$$dG_{\beta} = V_{\beta}dp - S_{\beta}dT \tag{2-162}$$

$$dG_g = V_g dp - S_g dT (2-163)$$

where

 V_{β} = molar volume of solid or liquid

 V_g = molar volume of gas

p = pressure (Pa)

 S_{β} = entropy of solid or liquid

 S_g = entropy of gas

T = temperature (K).

Combining Equations (2-161) through (2-163) and rearranging gives

$$(S_g - S_\beta) dT = (V_g - V_\beta) dp$$
 (2-164)

Since \boldsymbol{V}_g is generally much greater than $\boldsymbol{V}\boldsymbol{\beta},$ Equation (2-164) can be reduced to

$$\Delta S/V_g = dp/dT . (2-165)$$

From the second law of thermodynamics, we know that

$$\Delta S = \int_{\beta}^{g} \frac{dQ}{T}$$
 (2-166)

where dQ is the differential of heat for a reversible phase transition proceeding at constant temperature and pressure.

The first law and the definition of system enthalpy can be used to relate dQ to enthalpy. From the first law,

$$dU = dQ - pdV (2-167)$$

where U is the internal energy and V is the volume. The differential of the system enthalpy for a reversible process is

$$dH = dU + pdV + Vdp (2-168)$$

At constant pressure, Equations (2-167) and (2-168) imply

$$dQ = dH (2-169)$$

The change of enthalpy can then be written as

$$\Delta S = \int_{\beta}^{g} \frac{dH}{T} . \qquad (2-170)$$

Integrating Equation (2-170) at constant temperature gives

$$\Delta S = \frac{\Delta H}{T} \tag{2-171}$$

where ΔH is the enthalpy change of the phase transition.

Since the enthalpy change of the phase transition is a function of heat capacity, which is different for solids and gases at different temperatures, the temperature dependence of ΔH must be taken into account for the vapor pressure to be evaluated accurately. The temperature dependence of ΔH can be approximated by the second order empirical equation

$$\Delta H = a + f(x) + bT + cT^2$$
 (2-172)

where

Uranium Dioxide/Mixed Oxides

f(x) = a function of composition

a,b,c = constants.

Substituting Equation (2-172) into Equation (2-171) and the resultant expression into Equation (2-165) gives

$$\frac{\mathrm{dp}}{\mathrm{dT}} = \left[\frac{a + f(x)}{T} + b + cT\right] V_g^{-1} \quad . \tag{2-173}$$

If the vapor behaves as an ideal gas,

$$V_g = RT/p \tag{2-174}$$

where R is the universal gas constant (m³Pa/mole•K). Equation (2-173) reduces to

$$\frac{dp}{p} = \left[\frac{a + f(x)}{T^2} + \frac{b}{T} + c \right] R^{-1} dT$$
 (2-175)

and integrating gives

$$\ln(p) = \left[-\frac{a + f(x)}{T} + b\ln(T) + cT + D \right] R^{-1}$$
 (2-176)

where D is a constant of integration.

2.14.3.2 Evaluation of Constants. Constants used in Equation (2-139) were obtained from fitting Equation (2-176) to literature data. Hyperstoichiometric and hypostoichiometric data were fit separately.

The urania model is based on the data discussed in Section 2.14.2.1 except for that of Chapman and Meadows^{2.14-14} and Ackermann,^{2.14-12} for the reasons discussed in that section. The data of Tetenbaum and Hunt indicate the urania total pressure to be dependent on the urania O/M ratio, but this dependence diminishes near the melting temperature. Since many of the data have been obtained at temperatures where the O/M ratio seems to have little effect and most of the data do not include the O/M ratio, the FVAPRS urania correlation was developed disregarding the vapor pressure dependence on the fuel composition. The low temperature data of Ackermann,^{2.14-5} Alexander,^{2.14-10} and Benezech^{2.14-7} were used, assuming that their test samples did not deviate greatly from stoichiometry. The best fit correlations prediction (solid line) is shown in Figure 2-46 compared to the urania data in Section 2.14.2.1. The standard error of estimate of the FVAPRS equation and log of the data is ± 0.206.

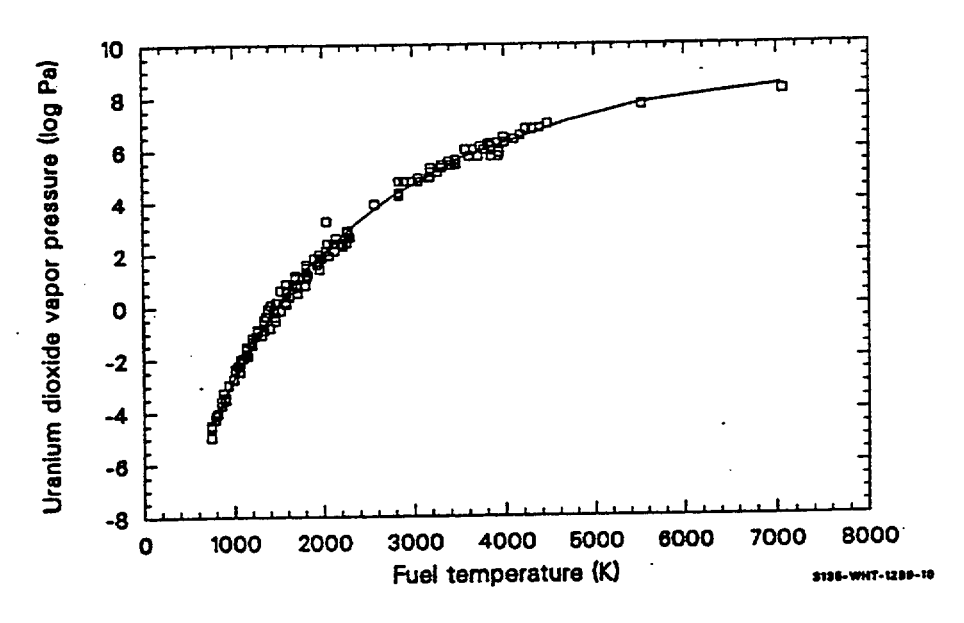


Figure 2-46. FVAPRS calculations (solid line) compared to urania data.

Material constants of Equation (2-139) for hypostoichiometric plutonia were obtained by fitting the vapor pressure data of Ackermann^{2.14-20} and Ohse and Ciani.^{2.14-19} The data of Mulford and Lamar,^{2.14-23} Phipps,^{2.14-21} and Pardue and Keller^{2.14-22} were not used because these data did not include O/M ratios. As a result of the vapor pressure studies of mixed oxides at temperatures between 4,000 and 7,000 K (which indicate maximum pressures of 100 MPa), the data of Ohse^{2.14-8} were modified and used to find the plutonia constants for temperatures above 4,000 K. The data of Ohse were modified by multiplying by the weight fraction of plutonia in the samples. This modification of observed vapor pressure approximates the ratios of urania and plutonia vapor pressures over the mixed oxides observed in the Tetenbaum^{2.14-24} data. The fitting method followed this sequence.

Data in a narrow O/M ratio band near stoichiometry were used to determine a normalization curve. The resulting equation was then used with all applicable data to normalize the data with respect to temperature, while a best fit slope as a function of deviation from stoichiometry was determined. This O/M dependent function was then used to determine the final equation as a function of temperature and O/M ratio. Figure 2-47 shows FVAPRS plutonia subcode predictions, using O/M ratios of 2.0 (bottom curve) and 1.5 (top curve). The data with O/M ratio between 1.5 and 2.0 are seen to lie between the two lines.

The FVAPRS correlation for mixed oxide vapor pressure was obtained by combining the equation calculations of urania and plutonia. This is accomplished by multiplying the weight fraction of urania and plutonia times the calculated vapor pressure of urania and plutonia, respectively. This approach was used rather than modeling the mixed oxide directly because mixed oxide data at typical mixture ratios (< 10%) have not been investigated and Tetenbaum's^{2.14-24} plutonia pressures are roughly the same fraction of the total pressure as the weight fraction. A comparison of the FVAPRS mixed oxide predictions (VAPMIX) to data is shown in Figure 2-48. The fit is good at temperatures below 5,000 K but becomes too large by

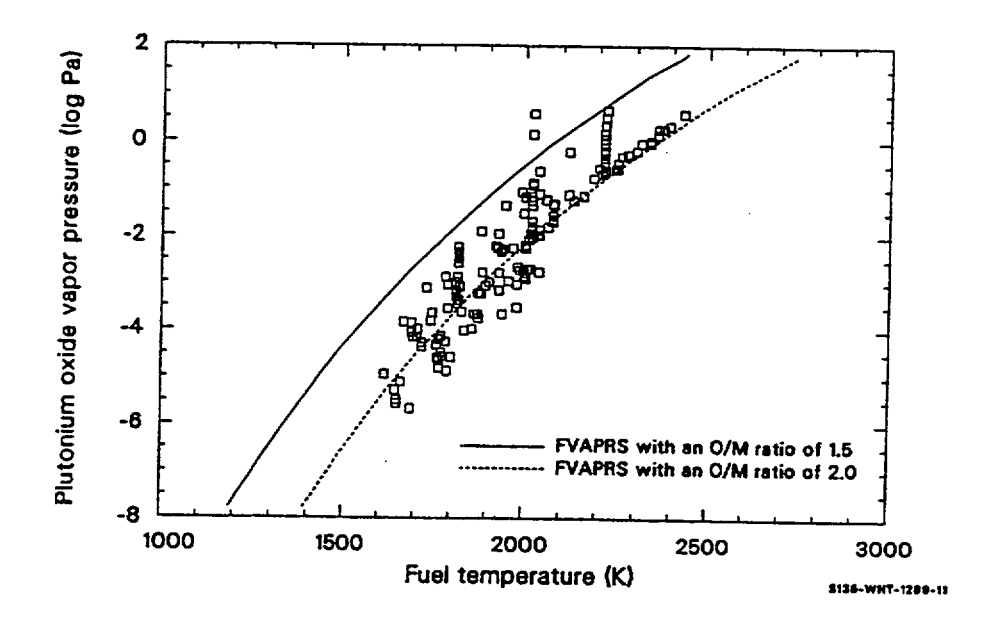


Figure 2-47. FVAPRS calculations (solid line) compared to plutonia data. about an order of magnitude at 6,000 K, well above the temperatures for which this subcode will usually be used.

FVAPRS oxygen vapor pressure calculations for hypostoichiometric urania are for monatomic oxygen up to O/M ratios of 1.999. Because of the scatter in the data, a simplified form of Equation (2-175) was used. The resultant expressions are Equations (2-141) through (2-145). The constants of the equations were obtained by a simple least-squares fit technique. A log function of the deviation from stoichiometry is reported to describe the oxygen vapor pressure for hypostoichiometric fuel. This was used in Equation (2-142) with good results. The fit procedure was to first determine a composition normalization factor from a narrow range of temperature (1,300 to 1,400 K). This was then used to normalize the data and develop the temperature dependent function. The data of Tetenbaum and Hunt, ^{2.14-29} Markin, ^{2.14-30} Wheeler, ^{2.14-31} and Alexander ^{2.14-10} were used to develop the equation constants.

FVAPRS oxygen vapor pressure for hyperstoichiometric urania is defined in two composition regimes, 1.999 to 2.004 and 2.004 to 2.2. Data, especially those of Hagemark and Broli, ^{2.14-34} show an approximately linear increase in pressure as the O/M ratios increase from 2.004 to 2.2; they show an exponential increase as O/M ratios increased from 1.999 to 2.004. Equations (2-141) and (2-143) were developed by determining a composition normalization factor, using the data of Hagemark and Broli. ^{2.14-34} These normalization factors were then used in a least-squares fit subroutine, using the data of Hagemark and Broli, Blackburn, ^{2.14-35} Aronson and Belle, ^{2.14-36} and Markin and Bones ^{2.14-38} to obtain the final Equations (2-141) and (2-142).

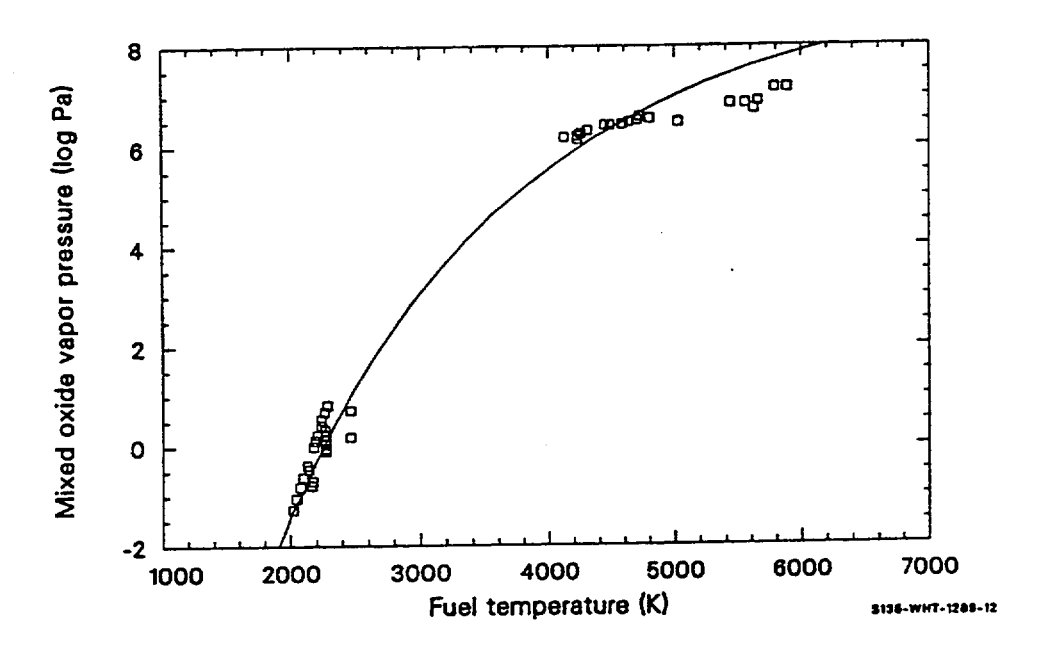


Figure 2-48. FVAPRS calculations (solid line) compared to mixed oxide data. An oxygen-to-metal ratio of 2.0 was used in the FVAPRS calculations.

To ensure that no discontinuity exists between the hyperstoichiometric and hypostoichiometric calculations, thermodynamic equations must be applied. At equilibrium, the reaction $O_2 \leftrightarrow 2O$ implies that

$$2\mu_{\rm O} = \mu_{\rm O_2} \tag{2-177}$$

where

 μ_{O} = monatomic oxygen chemical potential

 μ_{O_2} = diatomic oxygen chemical potential.

For ideal gases at equilibrium, the chemical potentials are

$$\mu_{\rm O} = \Delta G^{\circ}_{0} + RT \ln[P(O)] \tag{2-178}$$

$$\mu_{O_2} = \Delta G^{\circ}_{0_2} + RT \ln[P(O_2)]$$
 (2-179)

where

 ΔG°_{O} = heat of formation of monatomic oxygen (J)

 $\Delta G^{\circ}_{O_{1}}$ = heat of formation of diatomic oxygen (J)

R = universal gas constant (J/K)

T = temperature (K)

P(O) = monatomic vapor pressure (Pa)

 $P(O_2)$ = diatomic vapor pressure (Pa).

Since $\Delta G^{\circ}_{O_2}$ is defined as zero, combining Equations (2-177) through (2-179) and solving for $\log P(O_2)$ gives

$$1/2 \log P(O_2) - \Delta G^{\circ}_{O} (2.303RT)^{-1} = \log P(O)$$
 (2-180)

The heat of formation, or ΔG°_{O} , of Equation (2-180) has been reported by Markin^{2.14-30} and Breitung^{2.14-40} among others. For the FVAPRS code, the Markin value was used

$$\Delta G^{\circ}_{O} = 61250 - 16.1 \text{ T}$$
 (2-181)

which gives the following expression when substituted into Equation (2-179):

$$\log[P(O_2)] = 2.0 \left[\log(P(O)) + \frac{13384.57}{T} + 3.52 \right] . \tag{2-182}$$

Equation (2-182) is used with Equation (2-142) to find the diatomic pressure and limits the calculation of Equation (2-142) to the maximum calculated by Equation (2-141) at an O/M ratio of 1.999. Equation (2-182) does not always produce reasonable results (especially at low temperatures) when used to compare different data sets. It should, therefore, be used with caution except in this case of defining continuity of equations.

Figure 2-49 shows the FVAPRS hypostoichiometric oxygen vapor pressure correlation (UOXVAP) predictions compared to the literature data. The FVAPRS predictions, using O/M ratios of 1.8 and 2.0 (solid lines) show fair agreement, and the correlation predictions bound vapor pressure data having O/M ratios between 1.6 and 2.0. Figure 2-50 compares the FVAPRS hyperstoichiometric oxygen vapor pressure calculation (DIOVAP) at O/M ratios of 2.004 and 2.2 to the literature data having O/M ratios greater than 2.004. These calculations are also seen to yield pressures in the same range as the data. Because of the

large scatter in the data, the standard error of estimate of the log of the data is large, \pm 0.545 in the case of hyperstoichiometric oxygen pressures and \pm 0.806 for hypostoichiometric oxygen pressures.

Correlations for urania (UO2VAP), plutonia (PUOVAP), mixed oxide (VAPMIX), and monatomic oxygen (UOVAP) are compared in Figure 2-51. The calculated urania vapor pressures are the largest, with plutonia vapor pressures about an order of magnitude less and the oxygen vapor pressures (for O/M ratios less than 2.0) even smaller. Oxygen vapor pressure calculations are probably not accurate above 4,000 K (much above the data base temperatures), and the plutonia vapor pressure calculations are useful only to about 5,500 K.

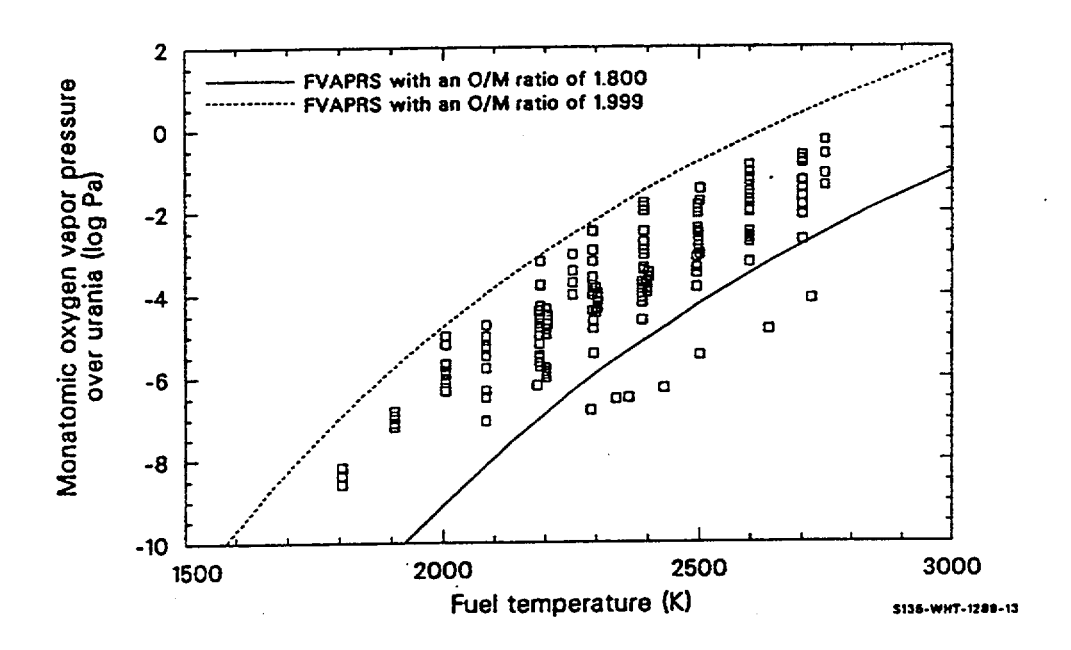


Figure 2-49. FVAPRS hypostoichiometric oxygen vapor pressure calculations (UOXVAP) compared to the data.

2.14.4 References

- 2.14-1 T. E. Phipps, G. W. Sears, and O. C. Simpson, "The Volatility of Plutonium Dioxide," *Journal of Chemical Physics*, 8, 1950.
- 2.14-2 R. Szwarc and R. E. Latta, "Vapor Pressure of Hypostoichiometric Urania as a Function of Composition," *Journal of the American Ceramic Society*, 51, 1968.
- 2.14-3 M. Bober, H. U. Karow, and K. Schretzmann, "Vapor Pressure Measurements of Oxide Fuel Between 3,000 and 5,000 K Using Laser Heating," *Nuclear Technology*, 26, 1975.

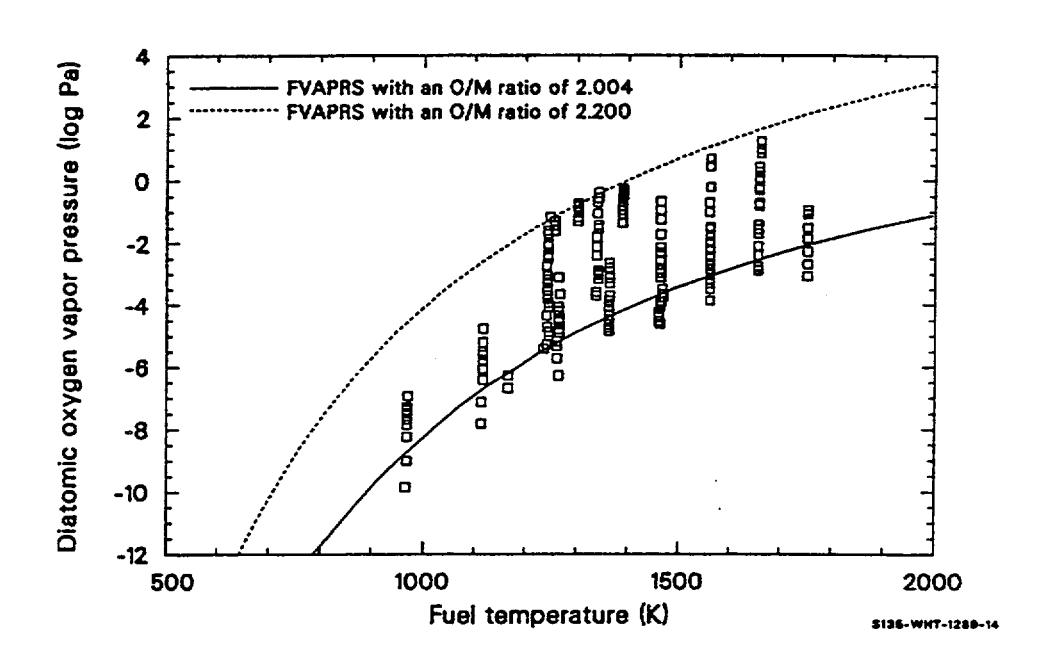


Figure 2-50. FVAPRS hyperstoichiometric oxygen vapor pressure calculations (DIOVAP) compared to the data

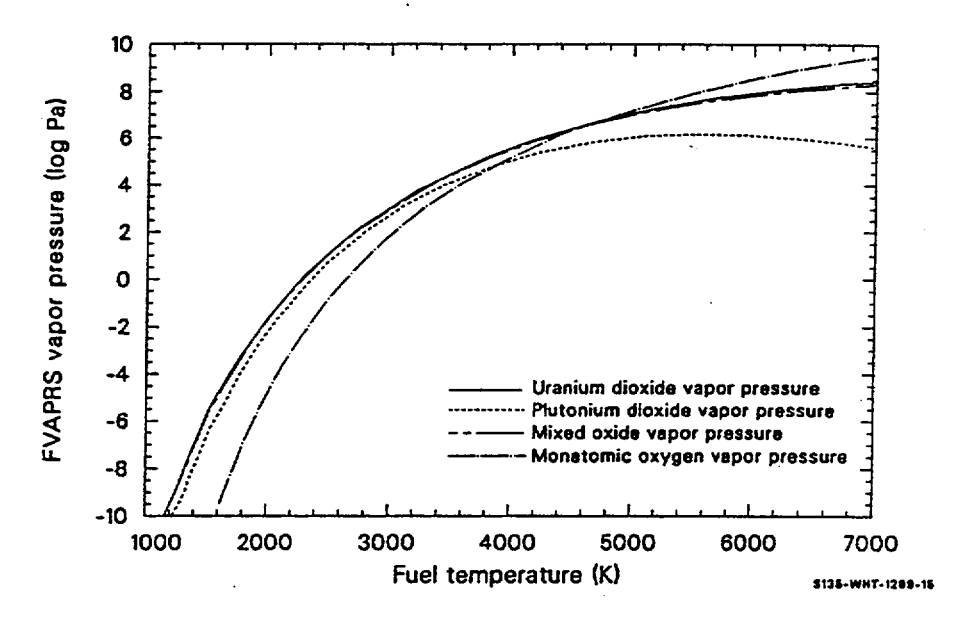


Figure 2-51. FVAPRS vapor pressure calculations of plutonia (PUOVAP), urania (UO2VAP), mixed oxides (VAPMIX), and monatomic oxygen over urania (UOXVAP), using an oxygen-to-metal ratio of 2.0.

- 2.14-4 G. T. Reedy and M. G. Chasanov, "Total Pressure of Uranium Bearing Species Over Molten Urania," *Journal of Nuclear Materials*, 42, 1972, pp. 341-344.
- 2.14-5 R. J. Ackermann, E. G. Rauh, and M. S. Chandrasekharaish, "A Thermodynamic Study of the Urania-Uranium System," *Journal of Physical Chemistry*, 73, 1969, pp. 762-769.
- 2.14-6 M. Tetenbaum and P. D. Hunt, "Total Pressure of Urania Bearing Species Over Oxygen Deficient Urania," *Journal of Nuclear Materials*, 34, 1970, pp. 86-91.
- 2.14-7 G. Benezech, J. P. Coutures, and M. Fox, Transpiration Study of Uranium Dioxide Vaporization Processes Between 2,200 and 2,600 K, ANL-TRANS-972, 1974.
- 2.14-8 R. W. Ohse, P. G. Berrie, H. G. Bogensberger, and E. A. Fischer, "Extension of Vapor Pressure Measurements of Nuclear Fuels (U, Pu)O₂ and UO₂ to 7,000 K for Fast Reactor Safety Analysis," *Journal of Nuclear Materials*, 59, 1976, pp. 112-124.
- 2.14-9 R. W. Ohse, P. G. Berrie, H. G. Bogensberger, and E. A. Fischer, "Measurement of Vapor Pressure of (U, Pu)O₂ and UO₂ to 5,000 K for Fast Reactor Safety Analysis and the Contribution of the Radial Cs Distribution to Fuel Pin Failure," *Thermodynamics of Nuclear Materials*, 1, IAEA-SM-190/8, Vienna 1975.
- 2.14-10 C. A. Alexander, J. S. Ogden, and G. W. Cunningham, *Thermal Stability of Zirconia and Thoria Based Fuels*, BMI-1789, 1967.
- 2.14-11 R. J. Ackermann, The High Temperature, High Vacuum Vaporization and Thermodynamic Properties of Uranium Dioxide, ANL-5482, 1955.
- 2.14-12 R. J. Ackermann, P. W. Gilles, and R. J. Thorn, "High Temperature Thermodynamic Properties of Uranium Dioxide," *Journal of Chemical Physics*, 25, 1956.
- 2.14-13 R. J. Ackermann et al., Journal of Chemical Physics, 49, 1968) p.4739.
- 2.14-14 A. T. Chapman and R. E. Meadows, "Volatility of UO₂+x and Phase Relations in the System Uranium Oxygen," *Journal of the American Ceramic Society*, 47, 1964.
- 2.14-15 A. T. Chapman and R. E. Meadows, The Volatility of UO₂+x and Phase Relations in the Uranium Oxygen System, ORNL-3587, 1964.
- 2.14-16 R. W. Ohse, "High Temperature Vapor Pressure Studies of UO₂ by the Effusion Method and Its Thermodynamic Interpretation," *Journal of Chemical Physics*, 44, 1966.
- 2.14-17 D. A. Benson, Application of Pulsed Electron Beam Vaporization to Studies of UO₂, SAND-77-0429, 1977.

- 2.14-18 J. R. Babelot, G. D. Brumme, P. R. Kinsmann, and R. W. Ohse, "Vapor Pressure Measurement Over Liquid UO₂ and (U, Pu)O₂ by Laser Surface Heating up to 5,000 K," *Atomwirtschaft*, 1977.
- 2.14-19 R. W. Ohse and C. Ciani, "Evaporation Behavior and High Temperature Thermal Analysis of Substoichiometric Plutonium Oxide for 1.51 < O/Pu < 2.00," *Thermodynamics of Nuclear Materials*, Vienna: IAEA, 1968.
- 2.14-20 R. J. Ackermann, R. L. Faircloth, and M. H. Rand, "A Thermodynamic Study of the Vaporization Behavior of the Substoichiometric Plutonium Dioxide Phase," *Journal of Physical Chemistry*, 70, 1966.
- 2.14-21 T. E. Phipps, G. W. Sears, and O. C. Simpson, "The Volatility of Plutonium Dioxide," *Journal of Chemical Physics*, 8, 1950.
- 2.14-22 W. M. Pardue and D. L. Keller, "Volatility of Plutonium Dioxide," *Journal of Chemical Physics*, 8, 1950.
- 2.14-23 R. N. R. Mulford and L. E. Lamar, "The Volatility of Plutonium Oxide (31)," Plutonium 1960— The Proceedings of the Second International Conference on Plutonium Metallurgy, Grenoble, France, 1960, pp. 411-429.
- 2.14-24 M. Tetenbaum, "Total Pressures of Uranium and Plutonium Bearing Species Above the U-Pu-O System," *Transactions of the American Nuclear Society*, 23, 1976.
- 2.14-25 R. W. Ohse and W. M. Olson, "Evaporation Behavior of Substoichiometric (U, Pu)O₂," Proceedings of the 4th International Conference on Plutonium and Other Actinides, Santa Fe, NM, 1970.
- 2.14-26 J. E. Battles, W. A. Shinn, P. E. Blackburn, and R. K. Edwards, "A Mass Spectrometric Investigation of the Volatization Behavior of (U_{0.8} Pu_{0.2})O_{2-x}," Proceedings of the 4th International Conference on Plutonium and Other Actinides, Santa Fe, NM, 1970.
- 2.14-27 E. A. Aitken, H. C. Brassfield, and R. E. Fryxell, "Thermodynamic Behavior of Hypostoichiometric UO₂," *Thermodynamics*, Vienna: IAEA, 1966.
- 2.14-28 T. L. Markin and M. H. Rand, "Thermodynamic Data for Plutonium Oxides," *Thermodynamics*, Vienna: IAEA, 1965, pp. 145-156.
- 2.14-29 M. Tetenbaum and P. D. Hunt, "High Temperature Thermodynamic Properties of Oxygen Deficient Urania," *Journal of Chemical Physics*, 49, 1968.
- 2.14-30 T. L. Markin, V. J. Wheeler, and R. J. Bones, "High Temperature Thermodynamic Data for UO_{2+x}," *Journal of Inorganic Nuclear Chemistry*, 30, 1968.

- 2.14-31 V. J. Wheeler, "High Temperature Thermodynamic data for UO_{2-x}," *Journal of Nuclear Materials*, 39, 1971, pp. 315-318.
- 2.14-32 N. A. Javed, "Thermodynamic Study of Hypostoichiometric Urania," *Journal of Nuclear Materials*, 43, 1972, pp. 219-224.
- 2.14-33 L. E. J. Roberts and A, H, Walter, "Equilibrium Pressures and Phase Relations in the Uranium Oxide System," *Journal of Inorganic Nuclear Chemistry*, 22, 1961, pp. 213-229.
- 2.14-34 K. Hagemark and M. Broli, "Equilibrium Oxygen Pressures Over Nonstoichiometric Uranium Oxides Between UO_{2+x} and U₃O_{8-z} at Higher Temperatures," *Journal of Inorganic Nuclear Chemistry*, 28, 1966.
- 2.14-35 P. E. Blackburn, "Oxygen Dissociation Pressures Over Uranium Oxides," *Journal of Physical Chemistry*, 8, 1958, pp. 897-902.
- 2.14-36 S. Aronson and U. Belle, "Nonstoichiometry in Uranium Dioxide," *Journal of Chemical Physics*, 29, 1958.
- 2.14-37 K. Kiukkola, "High Temperature Electrochemical Study of Uranium Oxides in the UO_{2-x} Region," *Acta Chemical Scandinavica*, 16, 1962, pp, 327-345.
- 2.14-38 T. L. Markin and R. J. Bones, The Determination of Some Thermodynamic Properties of Uranium Oxides with O/U Ratios Between 2.00 and 2.03 Using a High Temperature Galvanic Cell, AERE-R 4178, 1962.
- 2.14-39 E. Aukrust, T. Forland and K. Hagemark, "Equilibrium Measurements and Interpretation of Nonstoichiometry in UO_{2+x}," *Procedures of the IAEA Symposium on Thermodynamics of Nuclear Materials, Vienna, 1962.*
- 2.14-40 W. Breitung, Calculation of Vapor Pressures of Oxide Fuels up to 5,000 K for Equilibrium and Nonequilibrium Evaporation, KfK-2091, 1975.

2.15 Fuel Oxidation (FOXY, FOXYK)

The fuel oxidation models, FOXY and FOXYK, calculate UO₂ oxygen uptake in steam for UO₂ temperatures above 1,150 K. The UO₂ oxidation weight gain is modeled using parabolic kinetics. Oxidation of UO₂ affects its chemical composition, which, in turn, significantly affects most of the other material properties of the fuel (i.e.,thermal conductivity and melting temperature).^{2.15-1} Changes in the material properties of the UO₂ may have an impact on core behavior during severe reactor accidents involving potential liquefaction of the fuel matrix.^{2.15-2}

2.15.1 Summary

The equation used to model UO2 oxygen uptake in steam is

$$W^{2} = 24.4e^{\left(\frac{-26241}{T}\right)} \Delta t + W_{0}^{2}$$
 (2-183)

where

W = oxidation weight gain at end of time step (kg/m^2)

T = temperature of the UO_2 surface (K)

 Δt = oxidation time (s)

 W_o = initial oxidation weight gain (kg/m²).

The standard error^a of the model with respect to its data base is 0.027 kg/m², or 21% of the average measured weight gain.

An estimate of the power resulting from the oxidation of UO2 is given by the equation

$$P = \frac{(W - W_0)(1.84 \times 10^5)}{\Delta t}$$
 (2-184)

where P is the rate of heat generation (W/m²).

2.15.2 Review of Literature

The only published data for UO_2 oxygen uptake are provided by Bittel et al.^{2.15-3} The constants used in Equation (2-183) came from this source. The data represent temperatures from 1,158 to 2,108 K. These constants appear to be independent of fuel density and surface to volume ratio. However, additional data are needed for oxidation at UO_2 temperatures in excess of 2,108 K and, in particular, for molten UO_2 .

a. Standard error =
$$\left[\sum_{i=1}^{n} \frac{(C_i - M_i)^2}{n-1}\right]^{1/2}$$

where

C_i = calculated weight gain

M_i = measured weight gain

n = number of data points.

2.15.3 Model Development

The model for UO_2 oxygen uptake is based on parabolic kinetics. That is, the rate of oxygen weight gain is inversely proportional to the amount of excess oxygen present, or

$$\frac{\mathrm{dW}}{\mathrm{dt}} = \frac{\mathrm{k}}{\mathrm{W}} \tag{2-185}$$

where

$$t = time(s)$$

$$k = rate constant (kg^2/m^4 \cdot s).$$

Solution of this differential equation yields

$$W^2 - W_0 = 2k\Delta t = K_p \Delta t (2-186)$$

where

$$K_p = 2k (kg^2/m^4 \cdot s).$$

Equation (2-187) is equivalent to Equation (2-183). The parabolic rate constant, K_p , was determined in Reference 2.15-3 using a least-squares data fit. Table 2-16 contains a list of the data used to determine K_p , along with the corresponding calculated value of W.

Table 2-16. Measured and calculated weight gain.

Test time (s)	Test weight gain (kg/m²)	Correlation weight gain (kg/m²)
600	0.2313	0.2397
600	0.2036	0.2125
600	0.1679	0.1674
600	0.1401	0.1646
1,200	0.1636	0.1703
1,200	0.1904	0.1611
1,800	0.2574	0.1901
1,200	0.1117	0.1136
	600 600 600 600 1,200 1,200 1,800	(kg/m²) 600 0.2313 600 0.2036 600 0.1679 600 0.1401 1,200 0.1636 1,200 0.1904 1,800 0.2574

Table 2-16. Measured and calculated weight gain. (Continued)

Temperature (K)	Test time (s)	Test weight gain (kg/m²)	Correlation weight gain (kg/m²)
1,773	1,140	0.1170	0.1019
1,768	2,400	0.1351	0.1448
1,768	4,740	0.1672	0.2035
1,678	3,600	0.1897	0.1191
1,673	6,900	0.1365	0.1611
1,668	5,700	0.1619	0.1430
1,663	2,400	0.1004	0.09065
1,478	7,020	0.07352	0.05775
1,478	11,800	0.08825	0.07487
1,373	11,860	0.02577	0.03807
1,368	10,500	0.04287	0.03459
1,273	24,480	0.02373	0.02582
1,158	17,400	0.01445	0.00782

Although experimental data were recorded only for temperatures ranging from 1,158 to 2,108 K, the correlation of Equations (2-183) and (2-187) is used for any temperature up to the melting temperature of UO_2 (3,100 K). When the fuel temperature exceeds 3,100 K, oxidation is assumed to continue at a temperature of 3,100 K.

As an estimate of the heat of reaction for oxidation of UO₂, one percent of the heat of reaction per kg of oxygen in the oxidation of zircaloy was used. The correlation for the rate of heat generation is

$$P = \frac{(W - W_0)(0.01)(6.45 \times 10^6)(2.85)}{\Delta t}$$
 (2-187)

where

6.45 x
$$10^6$$
 = heat of reaction per kg Zr(J/kg)
2.85 = ratio of weight of Zr to O₂ in ZrO₂.

Equation (2-187) is equivalent to Equation (2-184).

A standard error of 0.027 kg/m² was calculated using the measured and calculated values of oxygen weight gain given in Table 2-16. This number was converted to a fraction of the measured value of oxygen uptake because the fractional error was more nearly constant over the temperature range of the data than the absolute error. The standard error of 0.027 kg/m² is about 21% of the mean measured oxygen uptake (0.1306 kg/m²).

Development of the model is based on the following assumptions:

- 1. Enough oxygen is always available for the oxidation process.
- 2. The correlation [Equations (2-183) and (2-185)] applies for UO₂ temperatures below 1,158 K and above 2,108 K up to 3,100 K, where no data exist.
- 3. For UO₂ temperatures above 3,100 K, oxidation will continue at the rate corresponding to a UO₂ temperature of 3,100 K.

Figure 2-52 and Figure 2-53 show the computed weight gain as functions of temperature and time, respectively. In Figure 2-52, the UO₂ temperatures range from 1,158 K to 3,400 K at a constant oxidation time of 60 seconds. The exponential nature of the curve can be seen up to temperatures of 3,100 K. Above this temperature, weight gain calculations are constant using temperature of 3,100 K. Figure 2-53 shows the weight gain for times ranging from 1 to 200 seconds at a constant UO₂ temperature of 1,600 K. This curve is parabolic in shape.

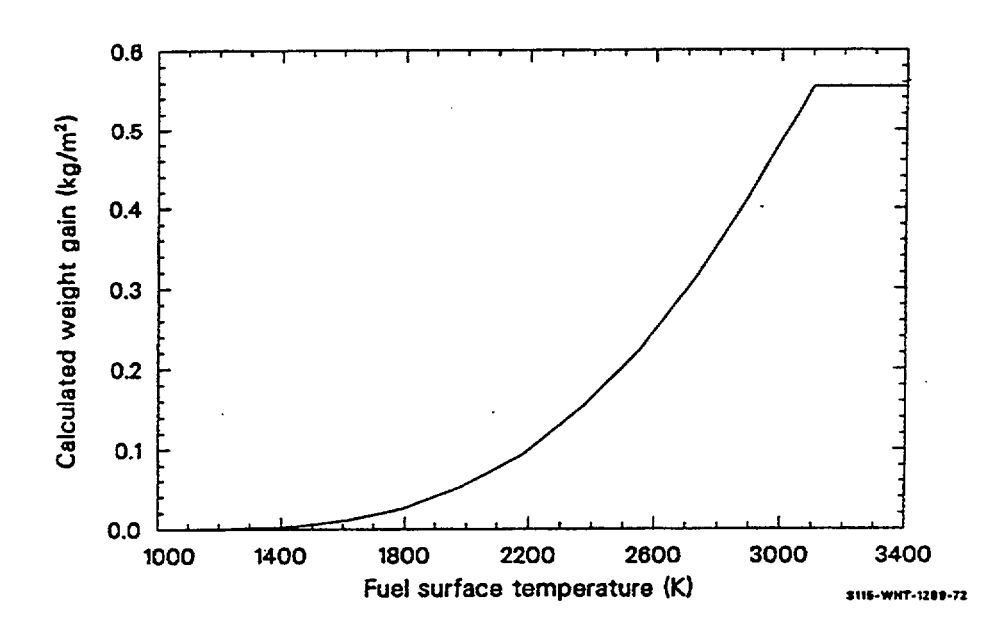


Figure 2-52. Computed weight gain as a function of temperature for constant time step size.

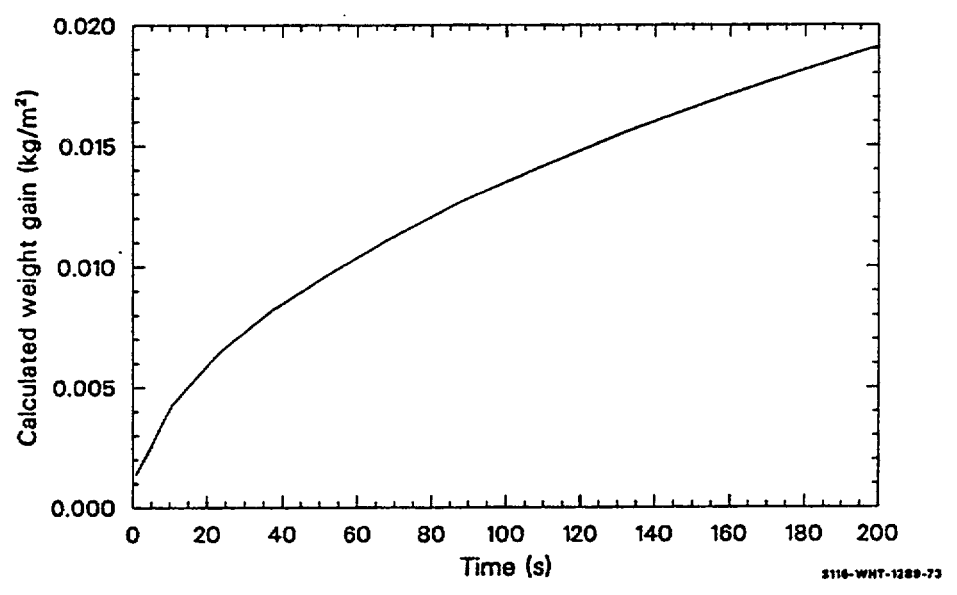


Figure 2-53. Computed weight gain as a function of time step size for constant temperature.

2.15.4 Description of the FOXY and FOXYK Subcodes

The following input variables or information are needed for FOXY: the time duration of oxidation(s), fuel temperature (K), and initial oxidation weight gain (kg/m²). The FOXY subcode will output the total oxide weight gain at the end of the time step and a preliminary estimate of the power generated from this oxidation (W/m²). Also, the value of the parabolic rate constant, [K_p in Equation (2-185)] is made available by FOXYK. Table 2-17 is a list of the FORTRAN names for these variables.

Table 2-17. Glossary of FORTRAN names.

Variable	Input or output	Definition	Units
FTEMP	Input	Fuel surface temperature	K
DT	Input	Time step	s
UO2OXI	Input	Initial oxide weight gain	kg/m ²
UO2OXF	Output	Final oxide weight gain	kg/m ²
P	Output	Power generated by oxidation	W/m^2
FOXYK		Parabolic rate constant	kg ² /m ⁴ •s

The input will be accepted in the following ranges:

FTEMP \geq 0
DT > 0

UO2OXI > 0.

Whenever the fuel temperature is nonpositive or the time step size or initial oxide weight gain is negative, the final oxide weight gain and the power are set to one. A diagnostic message is printed if any one of these input errors is noted but was not noted during the previous execution of FOXY. This message states, "Input Error in FOXY." The entire input is then printed.

2.15.5 References

- 2.15-1 D. L. Hagrman, Melting Temperatures of Uranium-Zirconium-Oxygen Compounds (PSOL and PLIQ) and Uranium Dioxide Solubility in Zircaloy (PSLV), EGG-CDAP-5303, January 1981.
- 2.15-2 C. M. Allison et al., Severe Core Damage Analysis Package (SCDAP), Code Conceptual Design Report, EGG-CDAP-5397, April 1981.
- 2.15-3 J. T. Bittel, L. H. Sjodahl, and J. F. White, "Steam Oxidation Kinetics and Oxygen Diffusion in UO₂ at High Temperatures," *Journal of the American Ceramic Society*, 52, 1969, pp. 446-451.

3. URANIUM ALLOYS

As the need for uranium metal materials properties became apparent, correlations for the specific heat capacity (UCP), enthalpy (UENTHL), thermal conductivity (UTHCON), thermal expansion (UTHEXP), and density (UDEN) were developed for the MATPRO package of materials properties subcodes. Descriptions of these subcodes and required input are given in this section.

3.1 Specific Heat Capacity and Enthalpy (UCP, UENTHL)

The function UCP calculates the specific heat capacity of uranium metal as a function of temperature. The function UENTHL calculates the enthalpy of uranium metal as a function of temperature and a reference temperature (for which the enthalpy change will be zero).

3.1.1 Specific Heat Capacity (UCP)

The function UCP calculates the specific heat capacity of uranium metal from equations derived from data reported by Touloukian^{3.1-1} and listed in Table 3-1 through Table 3-3. Specific heat capacity data for the alpha phase ($300 \le T < 938$ K) were approximated using a least squares fit to a second degree polynomial. An average of the data for the beta ($938 \le T < 1,049$ K) and gamma ($1,049 \le T < 1,405.6$ K) phases was used to determine a constant specific heat capacity for these phases because sample to sample variation was greater than variation with temperature. Since no data were found for the liquid specific heat capacity, the gamma phase specific heat capacity was used as an estimate.

Table 3-1. Alpha phase uranium specific heat capacity data.

Temperature (K)	Specific heat capacity (cal/g•K)	
300.104	0.02779	
307.465	0.02793	
327.514	0.02834	
337.489	0.02853	
347.549	0.02868	
304.95	0.02789	
314.904	0.02806	
323.15	0.0268	
373.15	0.0284	
573.15	0.0345	
623.15	0.0362	
673.15	0.0378	

Table 3-1. Alpha phase uranium specific heat capacity data. (Continued)

Temperature (K)	Specific heat capacity	
	(cal/g•K)	
723.15	0.0394	
773.15	0.041	
823.15	0.0425	
873.15	0.044	
298.	0.02758	
300.	0.0276	
400.	0.0295	
500.	0.0323	
600.	0.03543	
700.	0.03873	
800.	0.04212	
900.	0.0455	
935.	0.04676	
373.15	0.0278	
473.15	0.0296	
573.15	0.0324	
673.15	0.0353	
773.15	0.0392	
873.15	0.0437	
933.15	0.0466	
323.15	0.0283	
373.15	0.02919	
423.15	0.03022	
473.15	0.03135	
523.15	0.03257	
573.15	0.03388	
623.15	0.03529	
673.15	0.03681	

Table 3-1. Alpha phase uranium specific heat capacity data. (Continued)

Temperature (K)	Specific heat capacity (cal/g•K)	
723.15	0.03846	
773.15	0.04031	
823.15	0.04253	
873.15	0.04521	
923.15	0.04818	
941.15	0.0493	

Table 3-2. Beta phase uranium specific heat capacity data.

Temperature (K)	Specific heat capacity (cal/g•K)	
935	0.0436	
950	0.0436	
1,000	0.0436	
1,045	0.0436	
953.15	0.0394	
973.15	0.0396	
1,043.15	0.0397	
1,063.15	0.034	
1,073.15	0.034	
941.15	0.04262	
973.15	0.04262	
1,023.15	0.04262	
1,047.15	0.04262	

Table 3-3. Gamma phase uranium specific heat capacity data.

Temperature (K)	Specific heat capacity (cal/g•K)	
1,045	0.03822	
1,100	0.03822	

Table 3-3. Gamma phase uranium specific heat capacity data. (Continued)

Temperature (K)	Specific heat capacity (cal/g•K)	
1,200	0.03822	
1,300	0.03822	
1,047.15	0.03843	
1,073.15	0.03843	
1,123.15	0.03843	
1,173.15	0.03843	

The following expressions were used to calculate the specific heat capacity of uranium metal:

For solid:

T < 938 K,

$$C_p = 104.82 + 5.3686 \times 10^{-3} \text{ T} + 10.1823 \times 10^{-5} \text{ T}^2$$
 (3-1)

 $938 \le T < 1049 \text{ K},$

$$C_p = 176.41311$$
 (3-2)

For liquid:

 $T \ge 1049 \text{ K}$,

$$C_p = 156.80756$$
 (3-3)

where

 C_p = uranium metal specific heat capacity (J/kg•K)

T = uranium metal temperature (K).

The first two equations represent the alpha, beta, and gamma solid phases of uranium, while the third equation represents the liquid phase.

Figure 3-1 is a plot of the specific heat capacity for uranium metal calculated by the function UCP.

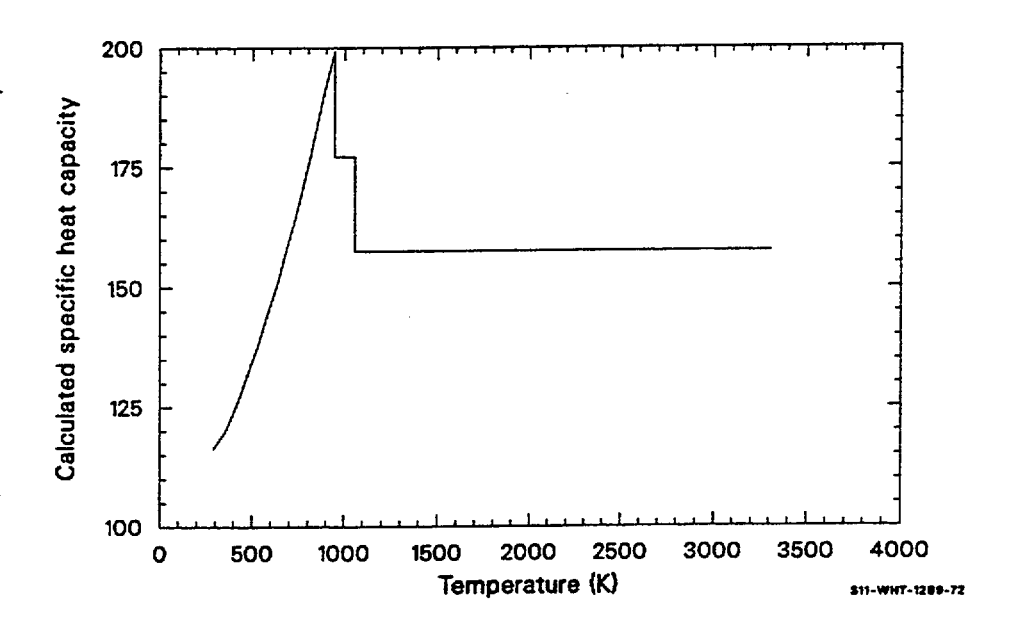


Figure 3-1. Specific heat capacity for uranium metal calculated by the function UCP.

3.1.2 Enthalpy (UENTHL)

The function UENTHL calculates the change in enthalpy of the uranium metal during a constant pressure change from the reference temperature of 300 K to the temperature of the uranium metal. The uranium specific heat capacity equations calculated in UCP were integrated piecewise over the alpha, beta, and gamma temperature ranges to determine the uranium enthalpy. A constant of integration was determined to force an enthalpy of zero at 300 K. (This number will not affect code calculations because the subroutine UENTHL uses a reference temperature of 300 K and subtracts the calculated enthalpy at this reference temperature from the calculated enthalpy at the temperature of interest.) Heats of transformation taken from Tipton^{3.1-2} were:

alpha-to-beta 12,500 J/kg beta-to-gamma 20,060 J/kg gamma-to-liquid 82,350 J/kg.

The expressions used to calculate the enthalpy of the uranium metal in this function are as follows:

For 300 < T < 938 K,

$$H_{\rm u} = 3.255468 \times 10^4 + T[1.0482 \times 10^2 + T(2.685 \times 10^{-03} + 3.394 \times 10^{-05} \, \text{T})] . \tag{3-4}$$

For $938 \le T < 1049 K$,

$$H_u = -6.9385273 \times 10^4 + 1.7641311 \times 10^2 \text{ T}$$
 (3-5)

For $1,049 \le T < 1405.6 \text{ K}$,

$$H_{\rm u} = -4.88190504 \times 10^4 + 1.5680756 \times 10^2 \, {\rm T} \ . \tag{3-6}$$

For $T \ge 1,405.6 \text{ K}$,

$$H_u = 6.177850 \times 10^5 + 1.602 \times 10^2 T$$
 (3-7)

where

 H_u = uranium metal enthalpy (J/kg)

T = uranium metal temperature (K).

The first three equations represent the alpha, beta, and gamma solid phases of uranium, while the fourth equation represents the liquid phase.

Figure 3-2 is a plot of the specific heat capacity for uranium metal calculated by the function UCP.

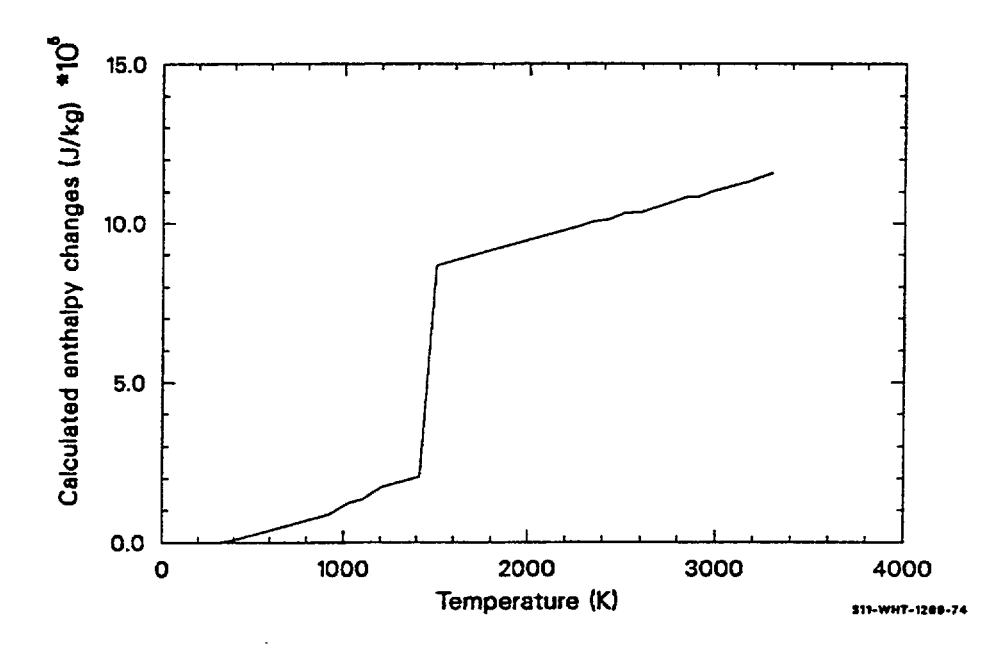


Figure 3-2. Enthalpy change for uranium metal calculated by UENTHL.

3.1.3 References

- 3.1-1. Y. S. Touloukian and E. H. Buyco, Thermal Physical Properties of Matter, V4, Specific Heat Metallic Elements and Alloys, New York: IFI/Plenum, 1970, p. 270.
- 3.1-2. C. R. Tipton, Jr., Reactor Handbook, New York: Interscience Publishers, Inc., 1960, p. 113.

3.2 Thermal Conductivity (UTHCON)

The thermal conductivity of uranium metal as a function of temperature is calculated by the function UTHCON. The only input required is the temperature of the uranium metal (UTEMP).

3.2.1 Model Development

Since the thermal conductivity of uranium metal is not significantly affected by the phase changes that take place during the heating of uranium metal, the single equation used to calculate the thermal conductivity of uranium metal for temperatures less than the melting point (1,405.6 K) is obtained from a polynomial fit of the temperatures and thermal conductivity values.^{3,2-1} These values are shown in Table 3-4. The correlation used to calculate the thermal conductivity is as follows:

Table 3-4. Uranium metal thermal conductivity from Touloukian et al.

Temperature (K)	Thermal conductivity [W/(m•K)]	
255.4	21.4	
255.4	22.6	
310.9	22.4	
310.9	23.5	
311.2	25.5	
318.2	25.5	
323.2	24.3	
353.2	26.4	
353.2	24.5	
358.2	25.9	
383.2	26.8	
398.2	. 28.5	
408.2	27.2	
422.1	24.4, 25.4	

Table 3-4. Uranium metal thermal conductivity from Touloukian et al. (Continued)

Temperature (K)	Thermal conductivity [W/(m•K)]	
423.2	30.1	
458.2	29.3	
469.2	27.5	
473.2	28.6	
533.2	26.5, 27.4	
548.2	34.7	
567.9	29.5	
573.2	30.9	
644.3	28.6, 29.3	
673.3	33.1	
755.4	31.1, 31.1	
773.2	35.4	
866.5	33.6, 33.2	
873.2	37.3	
933.2	34.8	
949.9	35.9	
973.3	40.0	
977.6	36.9	
1,002.6	37.4	
1,005.4	37.9	
1,033.2	38.9	
1,073.2	42.3	
1,173.2	44.6	

$$K_s = 20.457 + 1.2047 \times 10^{-2} \text{ T} + 5.7368 \times 10^{-6} \text{ T}^2$$

(3-8)

where

 K_s = uranium metal thermal conductivity (W/m \bullet K)

T = uranium metal temperature (K).

The expected standard error of the predicted conductivities is ± 0.2 times the calculated conductivity. A plot of the thermal conductivities calculated by UTHCON is shown in Figure 3-3.

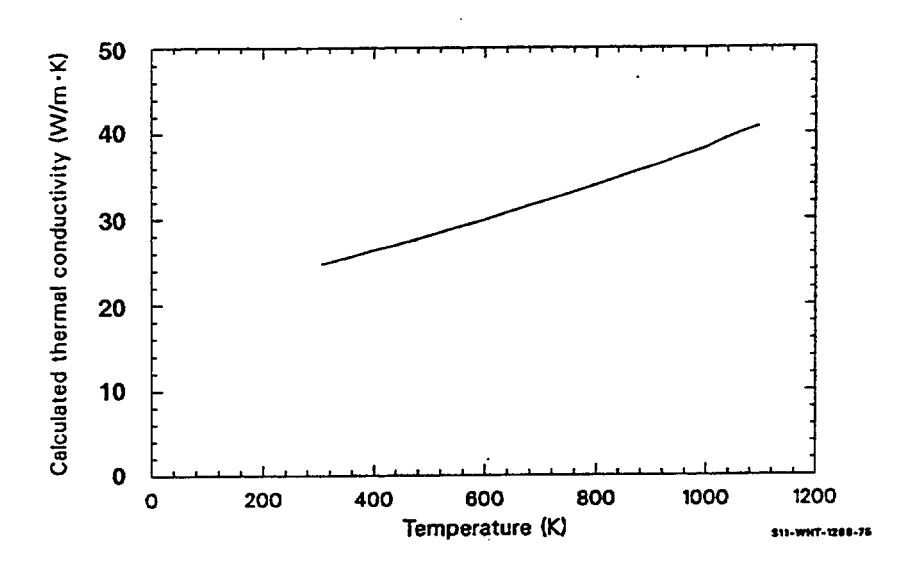


Figure 3-3. Thermal conductivities calculated by UTHCON.

3.2.2 References

3.2-1. Y. S. Touloukian, R. W. Powell, C. Y. Ho, and P. G. Klemens, *Thermal Physical Properties of Matter, V1, Thermal Conductivity Metallic Elements and Alloys*, New York: IFI/Plenum, 1970, pp. 429-440.

3.3 Thermal Expansion and Density (UTHEXP, UDEN)

The function UTHEXP calculates the polycrystalline uranium metal thermal expansion strain, and the function UDEN computes the density from 300 K to the melting point of the uranium metal, 1,132.3 K. Input values required for UTHEXP are the uranium metal temperature and a reference temperature (for which the thermal strain will be zero), while UDEN requires only the uranium metal temperature.

3.3.1 Thermal Expansion (UTHEXP)

The expressions used to calculate the uranium metal thermal expansion strains are:

For 300 < T < 942 K,

$$\varepsilon_{\rm u} = [-0.30667 + T(7.6829 \times 10^{-4} + 9.5856 \times 10^{-7} \text{T})]/100 . \tag{3-9}$$

For $942 \le T < 1045$ K,

$$\varepsilon_{\rm u} = (-0.28340 + 1.9809 \times 10^{-3} \text{ T})/100$$
 (3-10)

For $1,045 \le T \le 1132.3 \text{ K}$,

$$\varepsilon_{\mathbf{u}} = (-0.27120 + 2.2298 \times 10^{-3} \,\text{T})/100$$
 (3-11)

where

 ε_{u} = uranium metal thermal strain (m/m)

T = uranium metal temperature (K).

At the present time, the phase change to liquid is not modeled.

A polynomial fit of the thermal expansion data from Touloukian^{3,3-1} shown in Table 3-5 yields an expression that can be integrated to produce Equation (3-9). Equations (3-10) and (3-11) are derived by using a linear fit of the thermal expansion rates given in Table 3-6 and Table 3-7, respectively. The constant of integration is ignored because the quantity returned by UTHEXP is the strain calculated by Equations (3-9), (3-10), or (3-11) at the given temperature minus the strain calculated at the reference temperature (300 K).

Table 3-5. Uranium thermal expansion data from Touloukian et al., 3.3-1 for temperature < 942 K.

Temperature (K)	Thermal strain (10 ⁻³ m/m)		
0	263	18	
20	267	184	265
40	312	257	
60	306	258	296
80	302	237	280
100	259	215	258
120	233	192	234
140	206	170	207
160	179	148	180
180	159	126	153
200	123	104	126

Table 3-5. Uranium thermal expansion data from Touloukian et al., $^{3.3-1}$ for temperature < 942 K.

Temperature (K)	Thermal strain (10 ⁻³ m/m)		
220	095	081	099
240	068	059	072
260	179	148	180
273	022	022	
280	013	015	018
291	0032		
293	0.00		
300	.014	.009	.008
373	.127	.118	
473	.306	.268	
573	.424	.506	
673	.728	.594	
773	.972	.780	
873	1.238	1.000	

Table 3-6. Uranium thermal expansion data from Touloukian et al., $^{3.3-1}$ 942 K \leq T < 1,045 K.

Temperature (K)	Thermal strain (10 ⁻³ m/m)	
935 ·	1.618	
942	1.515	
948	1.643	
973	1.577	
973	1.685	
998	1.731	
1,000	1.629	
1,023	1.743	
1,045	1.813	

Table 3-7. Uranium thermal expansion data from Touloukian et al., $^{3.3-1}$ T \geq 1,045 K.

Temperature (K)	Thermal strain (10 ⁻³ m/m)	
1,045	2.061	
1,073	2.116	
1,123	2.232	
1,173	2.347	
1,223	2.457	
1,273	2.572	
1,323	2.679	
1,373	2.786	

Uranium metal goes through two phase changes, one at approximately 942 K and another at approximately 1,045 K. The discontinuous change in thermal strain at these phase changes is the reason three different equations are used to calculate ε_u . Each equation calculates the thermal expansion strain of one phase. (The expected standard error for these curves is about 0.1 times the calculated value).

3.3.2 Density (UDEN)

The function UDEN uses the general relation between density and thermal strain, together with a reference density of 1.905 x 10⁴ kg/m³, the density of uranium at 300 K.^{3.3-1} The thermal expansion strain as a function of temperature calculated by UTHEXP using a reference temperature of 300 K is illustrated in Figure 3-4, and the density calculated by UDEN using the thermal strain calculated by UTHEXP is shown in Figure 3-5. The equation used to calculate density is

$$\lambda = 1.905 \times 10^4 \times 1 - 3 \text{xeps}) \tag{3-12}$$

where

eps = predicted thermal expansion strains.

3.3.3 Reference

3.3-1. Y. S. Touloukian, R. K. Kirby, R. E. Taylor, and P. D. Desai, *Thermal Physical Properties of Matter, V12, Thermal Expansion - Metallic Elements and Alloys*, New York: IFI/Plenum, 1970, pp. 336-372.

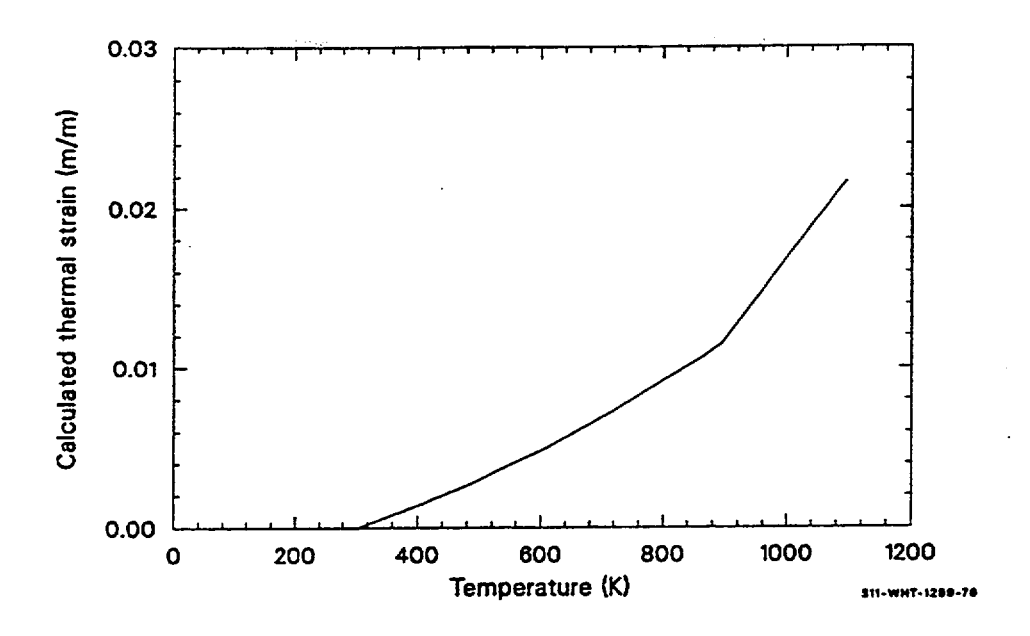


Figure 3-4. Thermal expansion strain as a function of temperature calculated by UTHEXP.

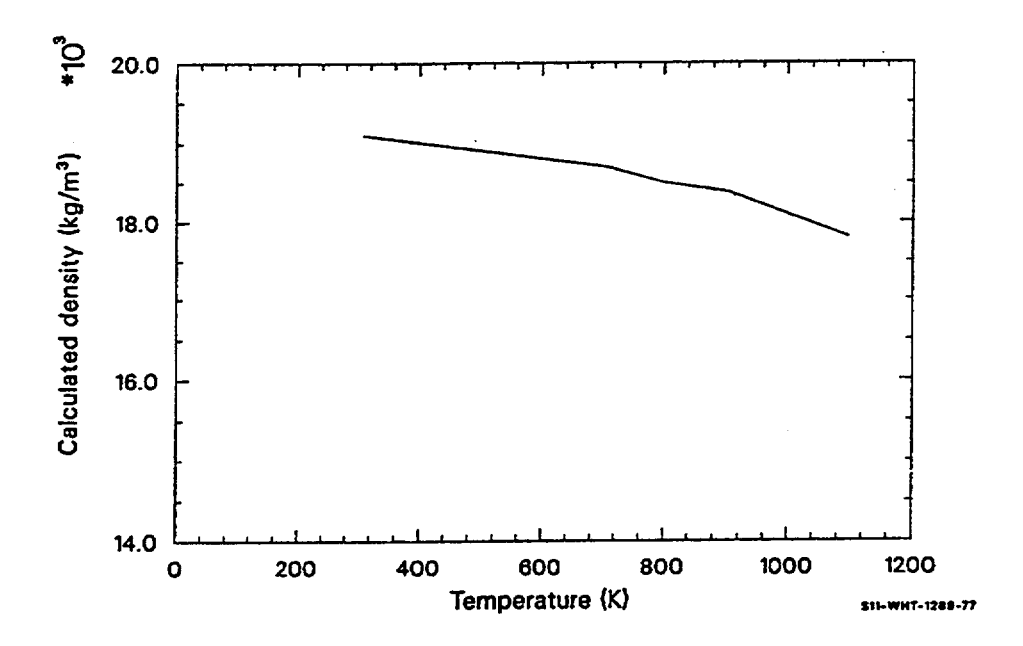


Figure 3-5. Density calculated by UDEN using the thermal strain calculated by UTHEXP.

3.4 Metallic Uranium Oxidation (UOXD, UOXWTK)

3.4.1 Model Development

To calculate the oxidation rates for metallic uranium, the subroutines UOXD and UOXWTK were developed from analytical data reported by Wilson et al.^{3.4-1} Subroutine UOXWTK returns the parabolic oxidation constant while UOXD will calculate oxygen weight gain, steam removal rate, hydrogen generation rate, and oxidation heat generation. These subroutines describe the following reaction:

$$U + 2H_2O \rightarrow UO_2 + 2H_2 + \Delta H_U . \tag{3-13}$$

In UOXWTK, the parabolic rate constant for uranium at a given temperature is calculated using the following expression:

For T > 1,473 K,

$$K_{UO} = 1.3503 \exp(-25000/(R \text{ UTEMP}))$$
 (3-14)

For $T \le 1,473 \text{ K}$,

$$K_{UO} = 0.1656 \exp(-18600/(R \text{ UTEMP}))$$
 (3-15)

where

R = the gas constant 1.987kcal/(mole deg K)

 K_{UO} = the parabolic rate constant for the oxidation of uranium (kg²/m⁴ s)

UTEMP = temperature of the uranium (K).

The oxygen weight gain, uwg, is evaluated by:

$$uwg = \sqrt{uwg0^2 - K_{UO} \times deltc}$$
 (3-16)

where

uwg0 = weight gain from previous time step (kg/m²)

deltc = time step (s).

The oxygen weight gain is limited by the availability of metallic uranium and steam.

The hydrogen generation rate (h2uox), steam removal rate (sroux), and oxidation heat generation (quox) are calculated as follows:

$$h2uox = \frac{(uwg - uwg0) \times slbwd \times dzcond}{8 \times deltc}$$
(3-17)

$$quox = \frac{\left(\frac{238}{32}\right) \times uheat \times (uwg - uwg0) \times slbwd}{deltc}$$
(3-18)

$$sruox = h2uox x 9 (3-19)$$

where

slbwd = fuel element width (m)

dxcond = axial node height (m)

uheat = heat of reaction for uranium reacted (J/kg).

3.4.2 Comparison With Data

The original work by Wilson was measured in volume of hydrogen produced at STP. The conversions to more usable units for MATPRO have been done above, but the data here will be presented in original form. Parabolic rates for the uranium steam reaction are shown in Table 3-8, and a plot of the data versus the calculations is shown in Figure 3-6.

Table 3-8. Parabolic rate law constants for the uranium steam reaction.

Temperature °C	Parabolic rate K [ml H ₂ (at STP)/cm ²] ² /min	Error (±)
500	4.5	1.1
600	3.36	0.33
700	15.6	1.9
900	67	14
1,000	120	11
1,200	341	1
1,300	504	49
1,400	848	18
1,500	1335	55
1,600	1976	122

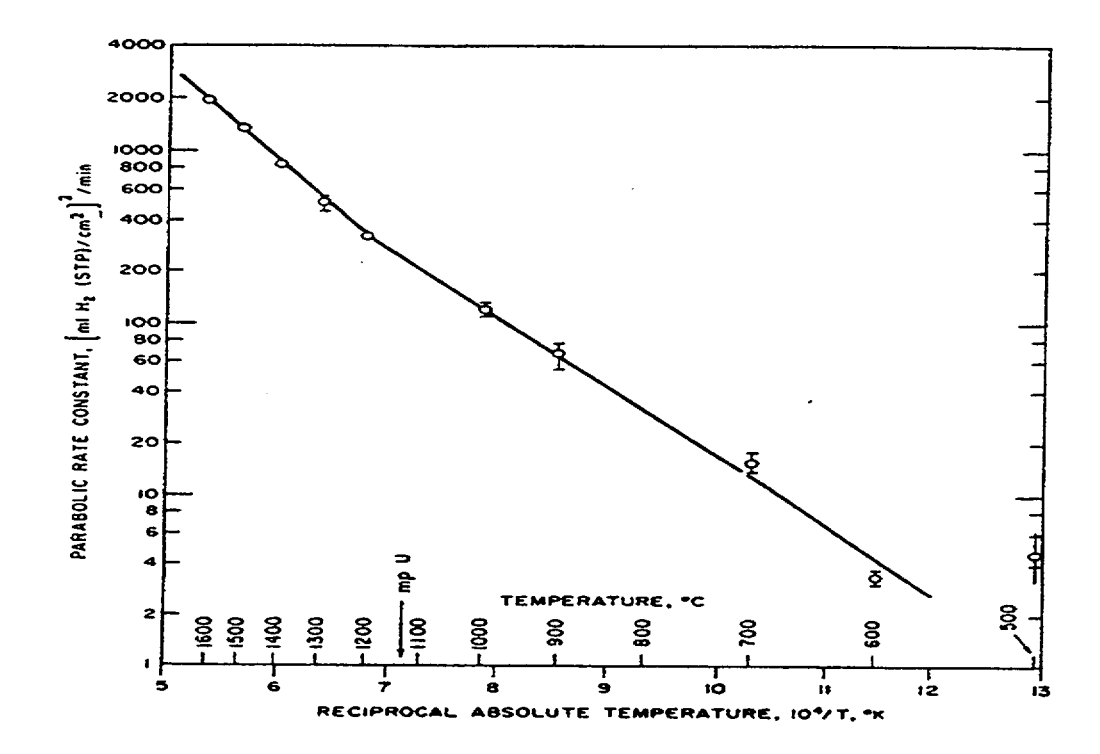


Figure 3-6. Parabolic rate constant for the uranium-steam reaction as a function of temperature.

3.4.3 Summary

According to Wilson,^{3.4-1} the oxide produced at high temperatures exhibited no tendency to leave the surface of the uranium at reaction temperatures, and remained quite adherent until cooling to temperatures of approximately 570 K when it would audibly "ping" and flake off. The flakes were of large size and may contribute to blockage. Under these flakes the original metal was shiny and exhibited no visible oxidation. The oxides formed in these reactions were nearly pure UO₂.

Oxides produced at lower temperature (T < 773 K) did not exhibit the same adherence as the higher temperature UO_2 and it is likely that these were categorized by the formation and rapid oxidation of uranium hydrides. These oxides continually flaked off the metal, and offered no protection to the metal below.

3.4.4 References

3.4-1. R. E. Wilson et al., "Isothermal Reaction of Uranium with Steam between 400 and 1,600 °C," Nuclear Science and Engineering, 25, 1966, pp. 109-115.